Understanding the first formation stages of (Y,Ti) nano-oxides in Oxide Dispersion Strengthened (ODS) steels

Martin Owusu-Mensah

université PARIS-SACLAY

NNT : 2019SACLS310

Thèse de doctorat

UNIVERSITÉ PARIS SUD
Comprendre le monde, construire l'avenir

Understanding the first formation stages of (Y,Ti) nano-oxides in Oxide Dispersion Strengthened (ODS) steels

Thèse de doctorat de l'Université Paris-Saclay
préparée à l'Université Paris-Sud

École doctorale n°576 Particules, Hadrons, Énergie, Noyau, Instrumentation, Imagerie, Cosmos et Simulation (PHENIICS)
Spécialité de doctorat : Energie Nucléaire

Thèse présentée et soutenue à Orsay, le 26 septembre 2019, par

Martin OWUSU-MENSAH

Composition du Jury :

Frédérico Garrido Professeur, CSNSM, Université Paris-Sud, France	Président
Michel Perez Professeur, INSA & Université de Lyon, France	Rapporteur
Robin Schaüblin Professeur, ETH Zurich, Switzerland	Rapporteur
Marie-France Barthe Chercheure, CEMHTI, CNRS, Orléans, France	Examinatrice
Yann de Carlan Chercheur, CEA Saclay, DEN/SRMA, France	Examinateur
Aurélie Gentils Chercheure, CSNSM, CNRS, France	Directrice de thèse
Stéphanie Jublot-Leclerc Chercheure, CSNSM, CNRS, France	Co-Directrice de thèse
Joël Ribis Chercheur, CEA Saclay, DEN/SRMA, France	Invité
Vladimir Borodin NRC Kurchatov Institute, NRNU MEPhI, Moscow, Russia	Invité

Acknowledgements

Albert Einstein once said “if we knew exactly what we were doing, it would not be called research”. This presupposes that there is a wealth of knowledge out there to be discovered. Reminiscing this journey, which began with a Master’s degree, five very wonderful years have quickly flown by and I could not agree more that indeed sometimes it is the journey that teaches you a lot more about the destination. I have been fortunate enough to have encountered wonderful people along the way all of whom have been extremely helpful. The list of people to whom I am most grateful to could go on and on but that does not go by without mention.

First and foremost, I owe my deepest gratitude to my thesis director Dr Aurelie Gentils for giving me the opportunity to initially work on an internship and onwards to the realization of this thesis. She has not only played the role of a supervisor but also as an advisor and a role model. I have learnt so much from her, which has enabled me to grow not only as a researcher but also as a person.

Playing this role alongside her was my thesis supervisor Dr Stephanie Jublot-Leclerc. Most of all the things I have learnt relating to technical and experimental techniques mainly in TEM were acquired during my study by her due diligence. The discussions, analysis and comments have been critical in arriving at this point and I could not have made it without her. I also would like to express my gratitude to my co-supervisor Dr Joel Ribis with whom I carried out most of my HRTEM experiments at CEA/DEN/SRMA as well as some technical training and discussions, which were always helpful.

I would like to sincerely appreciate the effort of my other co-supervisor and visiting researcher from the Kurchatov Institut and MEPhI University, Moscow, Russia for the theoretical analysis, calculations and discussions. All the fruitful discussions relating to the simulations and theoretical details were extremely helpful.

Another person whom to whom I extend my deepest gratitude is Dr Cedric Baumier who is the technical responsible of the TEM at CSNSM/JANNuS-Orsay. He took me through many TEM investigations and always gave me access to the microscope even in the tightest of schedules. All his efforts are deeply appreciated.

Special appreciation also goes to Drs. Djamel Kaoumi, Ce Zheng and Ryan Schoell from North Carolina State University, USA, for the assistance and effort in characterization of samples by ChemiSTEM. They dedicated part of their precious time to the realization of some very vital and useful elemental information.

I also acknowledge Drs Marion Descoins and Dominique Mangelinck from IM2NP, Marseille, for the assistance and contributions through the METSA network during my Atom Probe Tomography (APT) investigations. They not only helped me to perform this experiment but also helped me in the reconstruction, analysis and discussion of the results.

To the SEMIRAMIS team at the JANNuS-Orsay/SCALP facility, I would like to extend my gratitude. Notable mention is given to Cyril Bachelet, Stephane Renouf, Jerome Bourcois and Sandrine Picard who conducted all my ion implantations and thermal annealing experiments even when some conditions appeared quite challenging. They also had a soft spot when it came to my schedules without whom my experiments would not have been possible.

I would like to express my gratitude to Dr Nicolas Nuns (UCCS, Lille) with whom I conducted all the SIMS experiments. He dedicated some of his precious time towards the realization of the SIMS experiments. Similarly I would like to express my gratitude Dr Bertrand Poumellec (ICMMO, Orsay), Dr David Longuevergne and Antoine Luboz (IPNO, Orsay) who all assisted at different times for the profilometry and confocal microscope measurements relating to the SIMS data.

Appreciation also goes to Dr Nicolas Troadec (IEMN, Lille) who was always available when it came to preparation of the samples by FIB thanks to the Renatech network. The received TEM thin foils were the best we could expect and received always ahead of time. His dedication towards the prepared samples will always be appreciated. In addition regarding the preparation of samples, I would like to thank Lucie Delauche and Florent Pallier who are in charge of the sample preparation in CSNSM. They helped me in the initial stages by introducing all the equipment to me and were they always when the need be.

I found myself in the mist of the staff of CSNSM and mostly members of two wonderful groups namely the "Physico Chimie de l'Irradiation" and the "Matière Condensée et Irradiation". I am grateful to Drs Olivier Plantevin, Andres Santander, Frank Fortuna, Aurelien Debelle, Emmanouil Frantzeskakis, Shamashis Sengupta and Frederico Garrido for creating a wonderful working atmosphere not just for me but also all the other students. Not forgetting the administrative staff including Rejane Bodson, Sonia Martineau and Patricia Duarte for all the help and assistance relating to the administrative issues and the missions undertaken in the period of study.

Notable mention is also made of my colleagues both PhD students and internship students including Ji Dai, Olga Emilianova, Marie-Jose Saleh-Afif, Maximilian Thees, and the many others with whom I share some unforgettable memories.

I would like to thank the PHENIICS Doctoral School (Université Paris-Sud/ Université Paris-Saclay) the Ph.D. funding received for the duration of the thesis.

This work has been carried out within the framework of the French Research Federation for Fusion Studies and EUROfusion Consortium and has received funding from the Euratom research and training programme 2014–2018 under grant agreement No. 633053. The views and opinions expressed herein do not necessarily reflect those of the European Commission.

Table of contents

Abstract

Oxide Dispersion Strengthened (ODS) steels, that is steels reinforced with a homogeneous distribution of (Y,Ti) oxide nanoparticles, are advanced structural materials for nuclear applications. The oxide particles serve as point defect recombination centres and obstacles to dislocation motion thereby improving radiation resistance and high-temperature strength of these steels making them perfect candidate materials for future fusion and fission nuclear reactors. The conventional fabrication of ODS steels is achieved by mechanical alloying followed by thermomechanical heat treatments. This way of ODS steel production seems complicated to understand the physical mechanisms leading to the precipitation of nano-oxide particles. The kinetics of nanoparticle formation can be much better studied using an alternative technique of nanoparticle growth, namely Ion Beam Synthesis (IBS). This approach has many advantages including the precise control of experimental parameters and the ability to de-correlate various factors contributing to precipitation kinetics. A better knowledge gained in this way would be potentially helpful for optimization of ODS steel production routines.

In the course of this PhD study, the IBS approach was applied to investigate the co-precipitation of metal (Y and/or Ti) and oxygen ions implanted into a model Fe-Cr alloy with the composition close to those typical for commercial ODS steels. Following the standard IBS schedule, consisting of ion implantation followed by high-temperature heat treatment, ions of Y, Ti and O at low energies were implanted into high-purity Fe10wt%Cr alloy samples at room temperature. The implanted samples were then annealed at various temperatures ranging from 600 to 1100°C to promote the precipitation of nano-oxide particles. A range of Transmission Electron Microscopy techniques were used to characterize the crystallographic structure and chemical composition of the nanoparticles. The study has been performed following three sets of experiments. First of all, the sequential implantation of Ti and O ions was implemented. Subsequent annealing at temperatures below 1000°C revealed that precipitation of titanium oxide was suppressed. Instead, chromium-rich nano-oxide particles with corundum hexagonal structure were found to precipitate. At sufficiently high temperatures these corundum particles were found to contain certain amount of Ti. Only after annealing at the highest temperature of 1100°C, particles of another type with Ti enriched core and Cr enriched shell were additionally fixed. Secondly, sequential Y and O ion implantation resulted in the formation of presumable yttrium-rich oxides at 800°C. Annealing at 1100°C promoted their growth to larger sized yttria (Y_2O_3) particles with a Cr enriched shell. Finally, sequential ion implantation of both metal ions (Y and Ti) was performed, followed by O implantation. The order of metal ion implantation has been found to be crucial for subsequent oxide precipitation at the annealing stage. With the Ti implantation first in the sequence, the precipitation of corundum hexagonal chromium-rich oxide was observed, very similar to the case of Ti and O implantation. In contrast, implantation starting with Y produced yttrium-titanium oxide particles with unidentifiable structure.

Summing up, the study has clarified the details of the formation of Y, Ti and (Y,Ti) oxides by ion implantation. The thesis presents the detailed characterization of the nanoparticles, as well as the discovered specific features of precipitated particles, such as the presence of orientation relationships between the particles and the FeCr matrix, which was observed even for the case of Cr-rich corundum particles. Finally, the implications of the obtained results, in conjunction with the already known data from the existing literature, for the better understanding of the mechanisms involved in the formation of nano-oxide particles in ODS steels are discussed.

Keywords: Fe-Cr alloys, Ion Implantation, Ion Beam Synthesis, Oxide Dispersion Strengthened (ODS) steels, Oxide nanoparticles, Precipitation, Thermal annealing, Transmission Electron Microscopy (TEM).

Résumé en français

Les aciers appelés ODS (pour Oxide Dispersion Strengthened), renforcés par une dispersion homogène de nano-oxydes, sont des matériaux de structure avancés pour les futurs réacteurs nucléaires de fusion et de fission. En effet ces nano-oxydes, à base d'Y et Ti, servent comme centres de recombinaison de défauts ponctuels et d'obstacles aux mouvements des dislocations, améliorant de ce fait leur résistance aux radiations et aux températures élevées. La fabrication conventionnelle des aciers ODS est réalisée par broyage mécanique suivi de traitements thermo-mécaniques, et ne permet pas facilement de comprendre les mécanismes physiques conduisant à la précipitation des nano-oxydes, ce qui serait potentiellement utile pour optimiser leur production. La cinétique de formation de ces nano-oxydes peut être étudiée en utilisant une technique alternative, à savoir la synthèse par faisceaux d'ions, qui présente de nombreux avantages, notamment le contrôle précis des paramètres expérimentaux et la possibilité de décorréler divers facteurs contribuant à la cinétique de précipitation.

Au cours de cette thèse, cette technique a été utilisée pour étudier la coprécipitation d'ions métalliques (Y et/ou Ti) et d'oxygène implantés dans un alliage modèle Fe-Cr de composition proche de celle typique des aciers ODS commerciaux. Des ions de Y, Ti et O à basse énergie ont été implantés dans des échantillons d'alliage Fe10wt%Cr de haute pureté à température ambiante. Les échantillons implantés ont ensuite été recuits à diverses températures entre 600 à 1100°C pour favoriser la précipitation de nano-oxydes, conformément au principe de cette technique. La microscopie électronique à transmission a été utilisée pour caractériser la structure cristallographique et la composition chimique des nano-oxydes formés lors de trois séries d'expériences. Tout d'abord, l'implantation séquentielle d'ions Ti et O a été mise en œuvre. Un recuit ultérieur a révélé qu'il n'y avait pas de précipitation d'oxyde de titane jusqu'à des températures inférieures à 1000°C, mais la présence de nano-oxydes riches en chrome avec une structure hexagonale de type corundum, qui contiennent une certaine quantité de Ti à des températures suffisamment élevées. Ce n'est qu'après le recuit à 1100°C que des nano-oxydes d'un autre type à cœur enrichi en Ti et coquille enrichie en Cr ont également été observés. Deuxièmement, l'implantation séquentielle d'ions Y et O a entraîné la formation à 800°C de nano-oxydes probablement riches en yttrium. Le recuit à 1100°C a favorisé la croissance des particules identifiées comme étant des nano-oxydes d'yttrium avec une coquille enrichie en Cr. Enfin, une implantation ionique séquentielle de deux ions métalliques (Y et Ti) a été réalisée, suivie d'une implantation d'O. L'ordre d'implantation des ions métalliques s'est révélé crucial pour la précipitation de nano-oxydes lors du recuit ultérieur. Lors de la séquence avec une implantation de Ti en premier, une précipitation d'oxyde riche en chrome de structure corundum hexagonale a été observée, très similaire au cas de l'implantation d'ions Ti et O. En revanche, la séquence avec une implantation d'ions Y en premier a produit des nano-oxydes d'yttrium-titane qui possèdent une structure non identifiable.

En résumé, l'étude a clarifié les détails de la formation de nano-oxydes de Y, Ti et (Y, Ti) par implantation ionique. La thèse présente la caractérisation détaillée de ces nano-oxydes, ainsi que certaines de leurs caractéristiques spécifiques, telles que la présence de relations d'orientation entre les nano-oxydes et la matrice FeCr, qui ont été observées même dans le cas de nano-oxydes de type corundum riches en Cr. Enfin, les résultats obtenus, combinés avec les données de la littérature, sont discutés pour une meilleure compréhension des mécanismes impliqués dans la formation des nano-oxydes dans les aciers ODS.

Mots-clés: alliages Fe-Cr, implantation ionique, synthèse par faisceaux d'ions, aciers renforcés par dispersion d'oxydes (ODS), nano-oxydes, précipitation, recuit thermique, microscopie électronique en transmission (MET).

List of abbreviations

APT	Atom Probe Tomography
bcc	body-centred cubic
BF	Bright Field
DF	Dark Field
DP	Diffraction Pattern
dpa	Displacements per atom
EDX	Energy Dispersive X-Ray Spectroscopy
EELS	Electron Energy Loss Spectroscopy
EFTEM	Energy Filtered Transmission Electron Microscopy
F/M steels	Ferritic/ Martensitic Steels
fft	Fast Fourier Transform
fcc	face-centred cubic
FIB	Focused Ion Beam
HAADF	High Angle Annular Dark Field
hcp	hexagonal closed packed
HE	Hot Extrusion
HIP	Hot Isostatic Pressing
HRTEM	High Resolution Transmission Electron Microscopy
IBS	Ion Beam Synthesis
JANNuS	Joint Accelerators for Nano-science and Nuclear Simulation
MA	Mechanical Alloying
NDS	Nitride Dispersion Strengthened Steels
NFA	Nano-reinforced Ferritic Alloys
ODS	Oxide Dispersion Strengthened steels
RED	Radiation Enhanced Diffusion
RT	Room Temperature
RTA	Rapid Thermal Annealing
SAED	Selection Area Electron Diffraction
SFR	Sodium Cooled Fast Reactor
SIA	Self Interstitial Atom
SIMS	Secondary Ion Mass Spectroscopy
SPS	Spark Plasma Sintering
SRIM	Stopping and Range of Ions in Matter
STEM	Scanning Transmission Electron Microscopy
TEM	Transmission Electron Microscopy
Tof-SIMS	Time-of-Flight Secondary Ion Mass Spectroscopy

Introduction

Global modernization and urbanization have resulted in a high-energy demand. World energy forecast predicts the global energy consumption as compared to present is expected to double by the mid of the 21st century [U.S. DOE, 2002]. Increasing the capacity of nuclear power is anticipated as one of the measures to address this growing demand and could play a vital role in achieving an environmentally friendly society. Nuclear power technology has evolved in time from previous generations to current (mostly Generation II, III and Generation III+ systems) in operation. The future of advanced nuclear technology systems leads to Generation IV technology of advanced fission technology and fusion technology [Abram 2008, Mazen 2009]. While the safety of nuclear systems has been questioned due to the few catastrophic nuclear power accidents, these advanced technologies seek to provide sustainable, economically healthy, safe, and reliable energy as well as proliferation resistance to the reactors in future [Goldberg 2011, Smith 2005]. The unique feature concerning these technologies is the fact that they are expected to operate at higher operating temperatures (500-1000°C) as compared to the current fission reactor operating temperatures (≈300°C) while increasing their service lifetime to over 120 years. The neutron displacement damage is estimated to increase significantly up to a maximum 200 dpa (displacement per atom) [Yvon 2009, Lindau 2005] as compared to a few tens of dpa for current reactors. The development of materials to withstand these extreme operating conditions therefore becomes imperative.

Candidate structural materials for the generation IV fission reactors include the austenitic and ferritic/martensitic (F/M) steels [Yvon 2009, Zinkle 2009]. The austenitic steels possess good corrosion resistance and thermal creep resistance but exhibit significant void swelling under irradiation. The F/M steels on the other hand possess better properties as they exhibit higher swelling resistance, high thermal conductivity and low thermal expansion. The weak point of these steels is the limitation to creep resistance at the high temperature operating conditions [Garner 2000, Klueh 2007]. To improve the creep resistance of these Ferritic/Martensitic steels, they can be reinforced with fine particles of metallic oxides, composed usually of Y and Ti, to produce the so-called oxide dispersion strengthened (ODS) steels. The nano-oxide particles serve as recombination sites for point defects, traps for He bubbles as well as impediments to any mobile defects such as dislocations, thereby improving the creep resistance and irradiation resistance at these high temperatures. Such properties make these steels ideal candidates for structural materials of the Generation IV Sodium Fast Reactors [Murty 2008, Cheon 2009] as well as for the first wall and blanket applications for fusion reactors [Klueh 2002a, Murty 2008, Zinkle 2005, 2009]. These steels and their improved properties make them applicable for use in any high temperature and extreme conditions relating to corrosion and irradiation.

ODS steels have been extensively investigated for decades and continues to be the topic of an advancing research, predominantly in the field of materials for nuclear application. The fabrication of the steels conventionally has been performed by powder metallurgy using ball milling. This technique involves mechanical mixing of fine Y_2O_3 and steel powders followed by consolidation at high temperatures using hot isostatic pressing or hot extrusion. Ukai *et al.* were the first to recognise the importance of dissolved Ti in refining the obtained Y_2O_3 precipitates [Ukai 2002]. Since then, detailed characterization of the microstructure of the ODS steels has been performed. The nanoparticles are generally classified according to two main forms. The typical Y-Ti-O features with larger sizes (>10nm) are reported to match that of

Y_2O_3, $Y_2Ti_2O_7$ and Y_2TiO_5 compounds. Other Y-Ti-O smaller features (<10 nm), usually 1-3 nm in diameter, identified by Atom Probe Tomography are described as non-stoichiometric [Sakasegawa 2009]. The microstructure of these steels before and after irradiation has also been extensively reported. The nature and composition of these clusters usually depend on the alloy composition and the exact fabrication route.

The global formation steps of these oxides have been reported by Hsuing *et al.* [Hsuing 2010] and Alinger *et al.* [Alinger 2009]. This oxide formation can be summarized into three main steps involving the fragmentation of the initial Y_2O_3 powder in the early milling stage, agglomeration and amorphization of the Y_2O_3 fragments in the later milling stage and a crystallization of amorphous agglomerates to form larger oxide nanoparticles with a core/shell structure during consolidation at 1150°C [Hsuing 2010]. Several attempts have also been made by using calculations [Gopejenko 2010, Jiang 2009, Murali 2010] to understand the mechanisms involved in the formation of the nanoparticles at the atomic scale. In addition, remarkable efforts have also been made by experimental investigations to fully characterize the oxide nanoparticles at different stages of ODS production, i.e., before and after thermal treatments, to obtain some valuable information for the understanding of the underlying mechanisms [He 2014, Ribis 2017, Williams 2013]. In spite of all these attempts, however, the general consensus remains the fact that the exact precipitation mechanism is yet to be fully established.

This PhD study is motivated by the aim of understanding the mechanisms leading to the precipitation of oxide nanoparticles in ODS steels by using an experimental technique known as ion beam synthesis (IBS) contrary to the conventional ball milling techniques to produce nano-metallic oxide particles. This approach, which involves ion implantation of the desired ions into the matrix followed by a subsequent high-temperature thermal annealing, is advantageous because the ions can be introduced into the matrix in a controllable way while the implantation parameters, such as the temperature and implantation profile, can be tuned independently. A first attempt to create nano-oxide particles by ion implantation in a ferritic-martensitic steel (with chemical composition unspecified) has been reported by Sakuma *et al.* [Sakuma 2004]. In their study, consecutive implantation of Y and O ions was performed at room temperature and fine nano-oxide particles appeared already after the room temperature implantation. The nanoparticles were observed to grow in size after high temperature annealing, but their exact chemical composition was not reported. Recently, Zheng *et al.* [Zheng 2014, 2015, 2017] undertook the feasibility of Al-based oxide precipitation in Fe-10wt%Cr alloy by ion implantation at JANNuS/SCALP, Orsay. Al and O ions with high contents have been implanted into a high purity Fe-10wt%Cr alloy at room temperature and characterised by the use of Transmission Electron Microscopy (TEM) and Atom Probe Tomography (APT). Interestingly, particles forming (Al,Cr,O) clusters at the nanoscale were observed at the ion implantation stage, prior to any annealing, similar to the case for Sakuma. The nanoparticles appeared to grow significantly after annealing at 500°C for 2 hours.

The investigations performed in this study were aimed at creating nano-oxide particles with a composition similar to the particles obtained by the conventional fabrication route by the implantation of Ti, Y, and O ions into a high purity Fe10%wtCr alloy at room temperature followed by thermal treatments. Characterizations of the implanted and annealed material were performed mainly by Transmission Electron Microscopy (TEM) techniques together with complementary investigations by time-of-flight Secondary Ion Mass Spectroscopy (ToF-SIMS) and Atom Probe Tomography (APT). The investigations were performed following three different sequential ion implantation experiments: the first involves implantation of Ti and O

ions, the second involves implantation of Y and O ions, and the third involves implantations of Ti, Y and O ions in two different sequential orders. In all these conditions, as-implanted as well as annealed samples with annealing temperatures in the range 600 – 1100°C were investigated. The results and deductions from each of these investigations are presented in this manuscript with the intention of understanding the mechanisms involved in the nanoparticle precipitation.

The Chapter 1 looks at the future nuclear reactors and material requirements, the concept of ODS steels, their method of fabrication and some existing studies that seek to understand the mechanisms involved in the nano-oxide formation. The aim and the experimental approach of ion implantation are also briefly mentioned. The second chapter looks at the chosen material, experimental techniques with a focus on ion implantation method and the various TEM-related techniques, which are the main characterisation methods employed. The principles of APT and ToF-SIMS methods are also presented. In the Chapter 3, we address the results obtained by experimental characterisation for the as-implanted as well as annealed specimens for all the various ion implantation and annealing conditions. The imports of the results are made in the Chapter 4 whilst comparing with the literature on ODS produced by the conventional fabrication route. Finally, a few conclusions and perspectives are given at the end.

The manuscript is a detailed work of the PhD thesis of Martin Owusu-Mensah in partial fulfilment of the doctoral thesis study performed at the Centre de Sciences Nucléaires et de Sciences de la Matière (CSNSM), a joint research unit between Université Paris-Sud/Université Paris-Saclay and Centre National de la Recherche Scientifique (CNRS) within the framework of the Particules, Hadrons, Énergie, Noyau, Instrumentation, Imagerie, Cosmos and Simulation (PHENIICS) doctoral school.

Chapter 1: Bibliographic review

1. Bibliographic review

1.1 Future Nuclear Power Technology (Generation IV fission and fusion reactors)

Nuclear power technology has been developed for decades and is envisaged as a potential power source to address some of the issues relating to increasing energy demand. This technology has evolved from Generation I through to Generation III and Generation III+ reactors. The future looks at the development of Generation IV fission as well as fusion reactors. In the next sections, a review of this technology is presented as well as their general requirements and candidate structural materials.

1.1.1 Review of Nuclear Fission Generation Technology

According to recent studies [U.S. DOE. 2002], the population of the world currently standing at close to 7 billion is expected to increase rapidly to about 10 billion by the year 2050. Similarly, a review by oil giants BP [BP review 2017] perceives the world economy to almost double over the next 20 years. Accompanying this rapid growth is a high demand for energy, which is expected to increase by up to about 50% during this period. The demand for energy is expected to increase significantly not only due to the increase in population, but also the demand for improved standards of living. Global efforts seek to address this demand as well as the issue of carbon dioxide emissions and green house gas emissions. The importance of nuclear energy becomes even more critical for the future. It is therefore no surprise that there is a gradual transition in the fuel mix with renewables, hydroelectric power and nuclear expected to account for about half of the growth in the energy supplies over the next 20 years. The world is therefore smiling at the sharp decline in coal consumption to about 0.2% p.a. (per anum) as compared to about 2.7% over the past 20 years [BP review 2017].

Nuclear power generation advanced in the 1950s and 1960s with the first generation reactors, which were the early prototype reactors such as the Shippingport and Magnox reactors. The second-generation reactors began the large commercial reactors in the 1970s. Some of these reactors still operate today as the service life of some reactors has been extended to 60 years. Even with this extension most of these ageing plants are being decommissioned especially in Europe. The third generation (Gen III) reactors produced more advanced and improved designs in the 1990s with the advances geared towards safety and economic benefits. The advanced generation III reactors, which are the Generation III+ reactors resulted due to evolutionary designs from the Gen III reactors as well as enhanced safety features, generation capacity and reliability as well as the competitive price as compared to other power generation technologies. These reactors have been constructed in several countries and some are still being constructed. The evolution of the nuclear power technology since its inception is illustrated in the *Figure 1.1.* There are currently about 430 nuclear plants in operation contributing just under 15% to the world's electricity and still remains the largest contributor by a non-greenhouse gas emitting source. Nuclear plants generation capacity is however declining. Looking into the future is the concept of innovative designs through renewed R&D, which constitute the Generation IV nuclear technology. The Generation IV Forum (GIF) is a consortium of countries namely; Argentina, Brazil, Canada, France, Japan, the Republic of Korea, the

Republic of South Africa, Switzerland, the United Kingdom, and the United States of America who met and agreed on a framework for international cooperation in research for a future generation of nuclear energy systems. The Gen IV Forum signed in January 2000 established four-themed goal to advance nuclear technology; (i) Sustainability, (ii) Economics, (iii) Safety and Reliability and (iv) Proliferation Resistance and Physical protection.

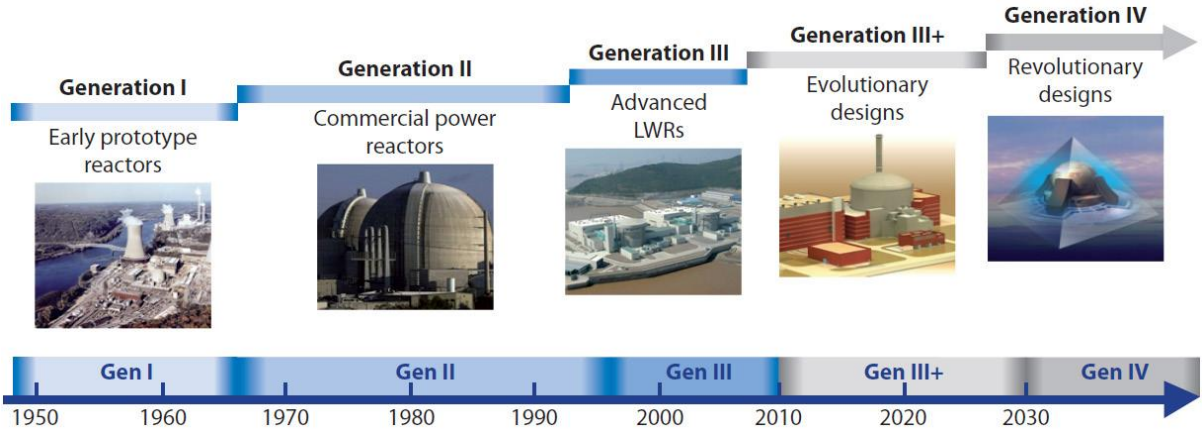

Figure 1.1 Generations of nuclear power: Time ranges correspond to the design and first deployments of different generations of reactors [Gen IV Technology roadmap, 2014].

1.1.2 Future Fission and Fusion reactors

Nuclear Gen IV fission reactor technology is not a logical evolution of previous nuclear reactor technologies but innovative new designs with the aim of achieving the four-themed goal outlined in the Gen IV Forum. To be able to not only compete economically with LWRs but also other electricity generation sources, these reactor systems have been optimized to operate at higher temperatures and this enables up to 40% improvement in the thermodynamic efficiency [Kelly 2014]. Another enhanced feature of these reactor systems is the fact that they are being designed with a high conversion ratio in the utilization of uranium. This would enable an improvement of up to two orders of magnitude in the utilization of uranium sources. From the over 100 proposals received by the Gen IV scientific committee, six reactor systems have been accepted and adopted by the members of the Gen IV Forum for multinational collaboration on research and development. The six reactor systems include the Sodium Fast Reactor (SFR), Gas-cooled Fast Reactor (GFR), Lead-cooled Fast Reactor (LFR), Molten Salt Reactor (MSR), Very High Temperature Reactor (VHTR) and the Super Critical Water-cooled Reactor (SCWR). The features of the various reactor systems can be found in the *Table 1.1*.

Reactor system	Coolant	Neutron spectrum	Core Outlet temperature (°C)	Size(s) (MWe)
Sodium-cooled fast reactor (SFR)	Liquid metal (Na)	Fast	~550	50, 1700
Gas-cooled fast reactor (GFR)	Gas (e.g. He)	Fast	~850	300, 1500
Lead-cooled fast reactor (LFR)	Liquid metal (e.g. Pb, Pb-Bi)	Fast	550 – 800	10-100, 600
Molten salt reactor (MSR)	Molten salt (fluoride salts)	Thermal	700 – 800	1000
Very high temperature reactor (VHTR)	Gas (e.g. He)	Thermal	>900	275
Super critical water-cooled reactor (SCWR)	Water	Thermal/Fast	350 – 620	1700

Table 1.1 Nuclear Generation IV fission reactor systems and their features.

The uniquely important factor concerning all these six reactor technologies is the fact that they are operated at significantly higher temperatures compared to the current Gen II and Gen III reactor operating conditions (300 – 400°C). These reactors are expected to have operating temperatures ranging between 500 and over 1000°C. The neutron radiation dose for most of these reactors is also expected to be significantly higher (up to a maximum of 200 dpa) than the currently operating reactors.

In the context of nuclear power generation, nuclear fusion power is envisaged to be hugely advantageous as compared to the fission reactors. These advantages include very little nuclear waste produced, improved safety and adequate fuel supplies. This form of energy, which involves combining two lighter atomic nuclei to form heavier nuclei whilst producing heat for electricity generation, requires high temperature and pressure within a confined volume to generate a plasma for the fusion to occur. One main challenge, which has hindered the realization of fusion power, is the ability to produce a system, which can confine and sustain these extreme conditions long enough for the fusion reaction to occur. The progress of fusion research over the last couple of decades has been remarkable and has brought fusion researches onto the cusp of demonstrating the plasma physics feasibility of fusion energy via magnetically-confined [Goldston 2002, Lackner 2002, Smith 2005] and inertially-confined [Goldston 2002, Moses 2009] concepts. It is hoped that any remaining key plasma physics issues relating to the operating conditions would be resolved. The completion of breakthrough facilities such as the National Ignition Facility (NIF) [Moses 2009] and ongoing construction of the ITER [Holtkamp 2009] is advancing the fusion power technology greatly. In the design of the fusion reactors, the fusion reactions are expected to occur inside a vacuum chamber to prevent atmospheric contamination. This vacuum is surrounded by a first wall, blanket and divertor components [Zinkle 2009] to absorb the heat and energetic neutrons, and transfer the heat to a coolant for electricity production. The development of high performance structural materials will be a key issue for the success of nuclear fusion reactors. These materials will be subjected to unprecedented fluxes of high-energy as well as intense thermomechanical stresses and high temperature coolants that could lead to corrosion [Smith 1998, Giancarli 2006]. Also, deuterium-tritium fusion reactions resulting in a high average neutron energy as compared to nuclear fission generated significantly higher levels of transmutant solutes such as H and He

in the structural materials which in tend heightens the radiation-induced degradation processes [Zinkle 2009]. The lifetime doses to be experienced for the first wall and blanket structural materials are about five times higher in the fusion reactors as compared to the internal structures for the Generation III fission reactors [Zinkle 2009].

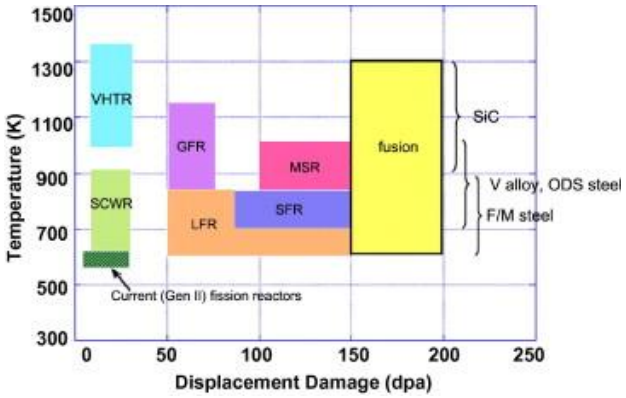

Figure 1.2 Operating temperatures for the different nuclear reactor systems (including the Gen III and various Gen IV fission reactors as well as fusion reactors) as a function of displacement dose [Yvon 2009].

A major issue therefore that arises for both the future fission and fusion reactors is that current structural materials become inefficient to support the extreme operating temperatures and irradiation damage as illustrated in the *Figure 1.2*. It is therefore imperative for the development of enhanced material to support the extreme operating conditions associated with these reactors. For each of these technologies, several materials are envisaged as potential structural materials. A summary of the candidate structural material for the various technologies can be found in [Murty 2008].

A look at the GEN IV designs reveals that the SFR is the most advanced technology and closest to realization. Significant experiences have been obtained relating to the development of SFR reactors from already developed prototypes such as the Joyo and Monju from Japan, the BN600 from Russia and the Phénix and Super Phénix from France. The SFR has also advantages related to actinide management and its closed fuel cycle. Hence, from the Gen IV framework, several countries including France have prioritized this technology.

Just like the other Gen IV designs, SFR have operating temperatures above 500°C and neutron doses up to 200 dpa. In addition, the coolant for this reactor is liquid sodium (a strong corrosive reactant with metals) and hence must be adequately isolated from the fuel core with the pins and fission products. The fuel cladding, which is the outer layer of the fuel rods, standing between the coolant and the fuel components need to be strong enough to resist the nuclear irradiations and corrosion mechanisms over the years. Hence, the functionability of SFR like most Gen IV reactors depends on the structural materials.

1.1.3 Material Requirements

Materials are expected to satisfy the conditions for Gen II and III reactors and more. The efficiency of the material is expressed not only in its ability to meet the requirements in normal operating conditions, but also accidental conditions. All candidate structural materials for SFR

as well as other reactors for structures such as the cladding materials are expected to meet these requirements [Kaloktina 2012]:

- mechanical properties of material (tensile strength, ductility, creep resistance, fracture toughness) should remain acceptable after ageing;
- dimensional stability under irradiation, whether under stress (irradiation creep or relaxation) or without stress (swelling, growth);
- physical and chemical compatibility with the coolant;
- other criteria for the materials are their costs to fabricate and to assemble.

The potential materials for Generation IV fission reactors most notably the Sodium Fast Reactor (SFR) include the Austenitic steels and the Ferritic steels.

The material requirement for the fusion reactors is not significantly different. The materials are expected to withstand the high temperature and radiation damage levels as stated in the section 1.1.2 as well as high thermomechanical loads that produce significant primary and secondary stresses. In addition the materials are expected to experience a high production of transmutant elements (i.e. H and He). These high H and He products generation in the materials by fusion neutron absorption will demand special mitigation techniques to as much as possible minimize the cavity swelling and embrittlement not required in previous nuclear generation reactors [Zinkle 2005].

1.1.3.1 Austenitic Steels

Austenitic steels were the first type of materials, which were designed for the cladding of the first generation of fast reactors [Cheon 2009]. Two types were used: 304 and 316. The 300 series austenitic steels gain their austenitic structure primarily by addition of nickel. The choice of these steels for use was based on the good corrosion resistance and thermal creep resistance of these steels. Other advantages of these steels include high temperature mechanical strength, good fabrication technology and abundant experience. The side effect of these steels is that they exhibit excessive swelling under high radiation doses [Cheon 2009]. The induced swelling was decreased by the addition of stabilizing elements, by adjusting the chemical composition, and by introducing cold work.

Advanced and optimized versions of these steels have been developed within a framework of European Collaboration [Rouxel 2016] such as the 15-15Ti steels. These steels are estimated to be limited up to a maximum of about 130 dpa [Cheon 2009] or else could eventually fail above these conditions. Several other advanced austenitic cladding materials 12-15Cr/20-25 Ni have been proposed, investigated and continue to be investigated as potential cladding materials for fast reactors. These steels are expected to be used up to a maximum of about 160 dpa.

The *Figure 1.3* demonstrates austenitic steels 316 Ti and 15/15 Ti with both showing significantly high swelling under radiation even though 15/15 Ti has a much better swelling resistance. The use of these steels is seen to be limited to the range of relatively low doses of radiation. Another essential factor is the fact that there is Cr depletion suspected at grain

boundaries under high doses of irradiation, which could be a factor in irradiation-assisted stress corrosion cracking.

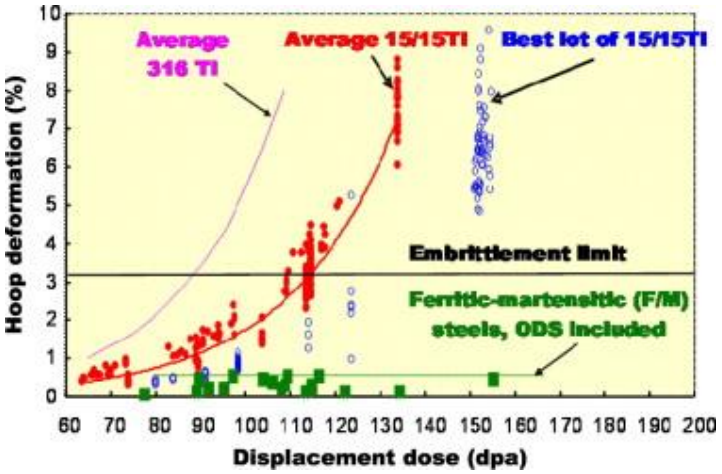

Figure 1.3 The maximum hoop deformation of different grades of austenitic Phenix claddings and ferritic-martensitic materials as a function of the displacement dose at temperatures between 675 and 825 K [Yvon 2009].

1.1.3.2 Ferritic/ Martensitic Steels

Ferritic/ Martensitic steels are envisaged as one of the primary candidate structural materials for the cladding and core components of SFR and the other Gen IV designs due to the various advantages they possess. Their applications in the first wall and blanket of fusion reactors are also envisaged. These have a core composition between 9-20% Cr to provide enough passivation layer against corrosion. Commercial F/M steels are based on 9-12%Cr or a maximum of 16%Cr. Details regarding the effects of Cr are given in section 1.2.2. The property, which sets F/M steels apart from austenitic steels, is the high swelling resistance. The *Figure 1.3* shows the high swelling resistance of F/M steels compared to the 316 Ti and 15/15 Ti austenitic steels. Also, these steels have a high thermal conductivity and low thermal expansion. The main drawback associated with the F/M is the limitation in its creep resistance at elevated temperatures. This makes these steels not ideal materials for various Gen IV systems operating between 400 and 1000°C and specifically the SFR. Klueh *et al.* [Klueh 1992, 2002a] investigated the promises and challenges of F/M steels stating that these steels had low swelling rates. The tensile and fracture properties remain adequate but an increased helium content negatively affects the swelling, tensile behaviour and impact toughness. A means of improving the creep resistance at high temperatures to make them ideal candidate structural materials is by reinforcing them by stable dispersion of nanoparticles. Such steels reinforced by a stable nanoparticle dispersion are referred to as Nano-reinforced Ferritic Steels (NFAs). There are two prominent types of NFAs, namely: Nitride Dispersion Strengthened (NDS) and Oxide Dispersion Strengthened (ODS) steels.

1.1.3.3 Nitride Dispersion Strengthened (NDS) steels:

NDS steels are produced by Gas Nitriding powders (which involves the diffusion of nitrogen into the surface and near the surface layers of low carbon steels usually at very high temperatures to produce nitride compounds) of steels composed of alloying elements capable of forming nitrides such as Cr and Ti [Fischer 1978]. NDS steels may also be produced by

mechanical alloying followed by thermomechanical treatments. The fabrication of these steels have been known to produce an inhomogeneous distribution of titanium nitrides within the matrix due to their stability in the liquid domain of steel [Mathon 2015] which does not make them ideal structural materials. The investigation of these steels was performed mostly in the 1980's. Recently, [Mathon 2015] have attempted to resurrect these studies by improving the fabrication technique using co-milling of powders Fe-18Cr1W0.14N and TiH_2 as well as plasma nitriding at low temperature of a powder of Fe-18Cr1W0.8Ti. It was found that the nano-nitrides could be produced in denser distribution with a size close to 2 nm together with mechanical properties exhibiting a pronounced ductility at high temperature, which is yet to be explained. The plasma nitriding at low temperature of powders has to be optimized to avoid oxygen contamination. Until the issues regarding this technique are fully resolved, this technique may not be fully implementable on the fabrication in large scale.

1.2 Oxide Dispersion Strengthened (ODS) steels

ODS steels are ferritic/ martensitic alloys reinforced by densed nano-oxide particles. The densed nano-oxide particles formed in these steels are quite stable, while serving as point defect recombination sites, He traps and obstacles to dislocation motion. These properties improve their creep resistance and thermal resistance at high temperatures making these steels quite ideal as primary candidate structural material for the cladding of SFR as well as candidate materials for fusion technologies (first wall). The *Figure 1.4* is a comparison between ODS steels and other candidate structural materials such as Austenitic and Ferritic steels in the operating conditions of Generation IV fission and fusion reactors.

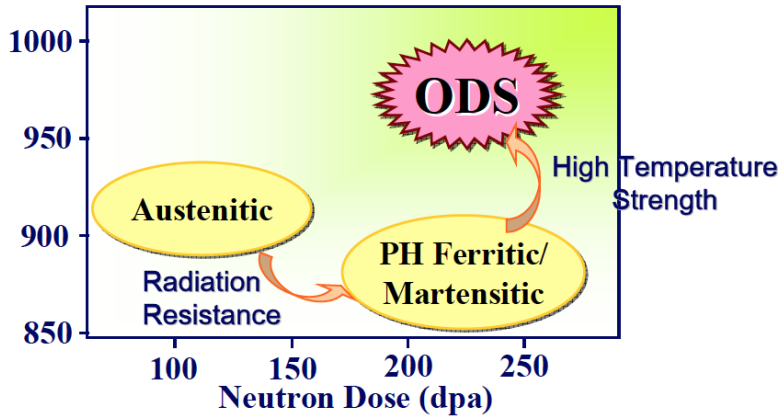

Figure 1.4 Comparison of the maximum temperature strength of Austenitic, Ferritic-Martensitic and ODS steels as a function of neutron irradiation dose [Inoue 2007].

1.2.1 ODS Steels Development

In the early development of nuclear reactor technologies from the 1960s, SCK.CEN (Belgium) began research and development into ferritic stainless materials within the framework of sodium-cooled fast breeder reactors because of the specific properties of these materials. These materials were envisaged to have a higher thermal conductivity, lower thermal expansion, lower tendency to He embrittlement and a lower swelling than austenitic stainless steels. In order to improve their lower creep resistance at high temperatures such as 700°C, oxide dispersions strengthening of the microstructure was conceived [Bremaecker 2012]. An optimized matrix composition of 13%Cr, 3.5%Ti, 2%Mo and the remaining being Fe was arrived at. For such steels, the goal is to create nanoscale oxide dispersions. Two theories

based on the matrix composition have been tested. An internal oxidation of the matrix composition and a direct mixing of the alloy components together with oxide powders (Al_2O_3, MgO) subsequently followed by a hot consolidation method which comprised of pressing, sintering and extrusion. The compression and extrusion were performed at 1050°C. An intermediate and final annealing was performed at 1050°C and a final straightening and aging at 800°C. Early work by Fischer and researchers from the US in the late 1970's [Fischer 1978] led to the idea of precipitation hardening of oxides formed in ferritic/ martensitic steels for use in Liquid-Metal Fast breeder reactors. It was established that mechanical alloying (MA) of Fe-14Cr-1Ti-0.3Mo powders together with $0.25Y_2O_3$, followed by hot extrusion at high temperatures results in the formation of fine nanometre scale oxide particles where these precipitates or clusters yield a high temperature creep strength as well as resistance to radiation damage.

1.2.2 Effects of alloying elements

Keeping in mind the purpose for which ODS steels are being fabricated, a high Cr content steel is preferred. For the Cr together with the other alloying elements, the main aim is to prevent the formation of long life radioactive nuclides. Hence, low activation elements such as W, Ta are preferred. Alloying elements such as Ni, Cu, and Co should be kept as low as possible. Due to the fact that the least amount of C may eventually lead to the formation of an austenitic phase at high temperatures, the least possible amount of C should be maintained.

Effects of Cr: Ferritic-martensitic (F-M) steels properties are largely dependent on the chromium content of the steel. The relationship between the Cr content and the strength of ODS steels is not proportionate [Li 2014]. The various ODS steels fabricated have a Cr concentration ranging between 9 and 18wt%. It is known that, the higher the Cr content, the higher the resistance to corrosion. A minimum Cr content of about 11% is required to form an effective passivation layer on the surface of the steels [Lo 2009]. Elsewhere, a 9% Cr content is also required for the minimum DBTT (Ductile-Brittle Transition Temperature) shift [Kohyama 1996]. Therefore, it could be thought that the highest concentration of Cr must be chosen. However, the microstructure of the steels should be optimized to meet all other requirements for the intended application. Fe-Cr steels containing 9-12 wt%Cr have a martensitic structure which can be used in different applications in a temperature range below 800°C to ensure that the high temperature phase transformation into austenitic is avoided. The martensitic structure of the steels is formed after the quench from the austenitic phase (γ phase) as illustrated in the phase diagram for binary Fe-Cr. The steels with more than 12 wt%Cr show a ferritic matrix and could be used in applications with a maximum temperature of 1100°C. Such high Cr ferritic steels in the range of 14-22 wt%Cr could be however subjected to hardening and embrittlement after ageing in the region of 400-550°C which are in this case very crucial temperatures for future fission and fusion reactor technology applications [Lee 2007, Capdevila 2010, Chen 2015 FED]. Hence, in this study, we chose a material of about 10%Cr to optimize the various requirements to meet conditions for future nuclear reactor applications. For these steels, the transformation from the alpha-Fe to the gamma-phase occurs at approximately 880°C as illustrated in the *Figure 1.5*.

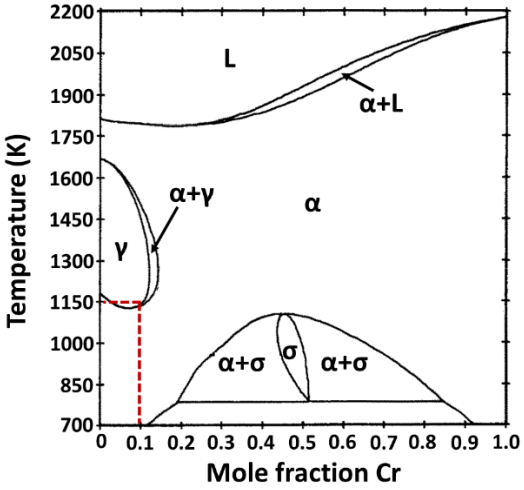

Figure 1.5 The Fe-Cr phase diagram [Andersson 1987].

Effects of Yttria (Y_2O_3): Yttria is described as one of the most stable oxides with a very high negative heat of formation of 1906.7 kJ.mol^{-1}. This is much higher as compared to the heats of formation of other similar oxides such as Al_2O_3, ThO_2 and TiO_2 of 1678.2, 1227.6 and 944.1 kJmol^{-1} respectively at 25°C [Gale 2004]. The fact that yttrium is immiscible in Fe could enforce the stability of Y_2O_3 in Fe-Cr alloys. In a study on the role of yttria content on the strength properties and ductility of ODS steels, Ukai *et al.* [Ukai 2000] demonstrated that the tensile strength along the extruded direction together with the creep rupture strength increase with an increase in the content of Y_2O_3 while the total elongation decreased. The creep rupture strength saturated at about 0.4 wt% of Y_2O_3. It was recommended that in order to optimize both the strength and ductility properties of these steels, the Y_2O_3 content should range between 0 and 0.56 wt%. Most studies use a yttria content of 0.25-0.50 wt%.

Effect of Ti: Formation of finer distribution of nanoparticles is desirable in ODS steels. Ti addition into ODS steels has been reported to produce a fine distribution of nanoparticles during MA [Ukai 1993]. Ti precipitated with yttrium oxide leading to the formation of Y-Ti-O complex oxides with a with very fine distribution. The *Figure 1.6* displays the role of Ti addition in the formation of smaller and more homogeneous nanopartcles in conventional ODS steels where as compared to the other alloying elements, Ti refines the sizes of the nanoparticles formed. The formation of finer nanoparticles distribution has been widely reported [Ukai 2002, Williams 2012, London 2015, Li 2017]. The nano-phases formed in the powders containing the Ti are also said to be more resistant to the phases without any Ti presence [Ratti 2009].

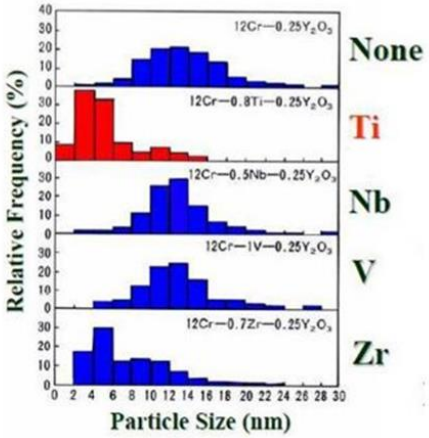

Figure 1.6 The size distribution of oxide particles as determined by TEM in 12CrODS steels with a varying elemental content addition [Ukai 1993].

Effect of Al: The presence of Al in ODS has been widely reported to improve the corrosion resistance of ODS steels [Asteman 2008, Lee 2011, Takaya 2012, Takaya 2009, Airiskallio 2010, Kimura 2011]. Different types of Al oxides including Al_2O_3 [Zhang 2009, Zhao 2017], $YAlO_3$ (YAP) [Zhao 2017, Zhang 2011, Zhang 2015, Zhou 2019], $Y_3Al_5O_{12}$ (YAG)[Zhang 2015, Zhao 2017, Zhou 2019] and $Y_4Al_2O_9$ (YAM)[Hsiung 2010, Hsiung 2011, Zhang 2015, Zhao 2017, Zhou 2019] have been reported. These oxides are predicted to be able to replace the conventional Y-Ti-O for improving the mechanical properties of ODS steels.

Effect of Zr: Binding energy of the cluster increases when Ti is replaced by Zr leading to higher stability [Murali 2010]. The higher stability of the clusters formed could have a hand in the enhanced nucleation rate, which may give rise to a finer dispersion of the nanoclusters. Zr has been reported to suppress the formation of Y-Al-O nanoparticles [Dou 2014]. Near-stoichiometric $Y_4Zr_3O_{12}$ oxide are mostly found with a few orthorhombic Y_2TiO_5 oxide ocassionally reported for an SOC-14 alloy containing Fe-14.85Cr-1.84W-0.09Ti-3.73Al-0.63Zr (wt%). The relative importance of Zr in the nanoparticle formation continues to be investigated [Kimura 2011].

Effects of C: Carbon introduction into the steels leads to the formation of different types of metallic carbides of the form $M_{23}C_6$ [Klimiankou 2007, Castro 2009, Castro 2011, Klimenkov 2012, Tan 2013] and M_3C [Castro 2009] (where M = Cr, Fe, W, V, Ta). Here, the main consequence of the precipitation of the $M_{23}C_6$ phase is the significant degradation of tensile ductility and impact properties as well as a reduction in the corrosion resistance. The presence of the carbide precipitation may be dependent of the sizes of the grains, as nanograin sized structures may show no presence of these carbides [Ramar 2009].

Other alloying elements:
Hafnium (Hf) addition to the alloy composition such as SOC-16 (Fe-15Cr-2W-0.1Ti-4Al-0.62Hf-0.35Y_2O_3) has been reported to suppress the formation of Y-Al-O oxide particles whilst enhancing the formation of a much denser distribution of $Y_2Hf_2O_7$ [Dou 2017, Zhang 2009]. The Hf addition may therefore be eventually useful in improving the creep strength of Al added ODS steels [Kimura 2011]. Tungsten (W) addition has been reported to also responsible for the improved high temperature mechanical properties of ODS steels [Miller 2003]. Elsewhere, the improvement in properties of ODS steels by Vanadium addition has also been reported [Muroga 2014].

1.2.3 Elaboration process of ODS

The fabrication of ODS steels conventionally is achieved by the powder metallurgy technique of mechanical alloying (MA). The process of fabrication involves pre-alloying powders of (Fe, Cr, Ti etc.) together with yttria or yttrium compounds under hydrogen or inert atmosphere such as argon in a high energy ball mill or attrition ball mill for hours. After mechanical alloying, the powders are canned, degassed, sealed and consolidated conventionally by powder metallurgy processes such as Hot Isostatic Pressing (HIP/HIPing) and Hot Extrusion (HE). Finally, cold or warm rolling together with thermo-mechanical heat treatments are performed to produce the final form of these steels. A schematic representation of the steps leading to the production of ODS steels is shown in *Figure 1.7*.

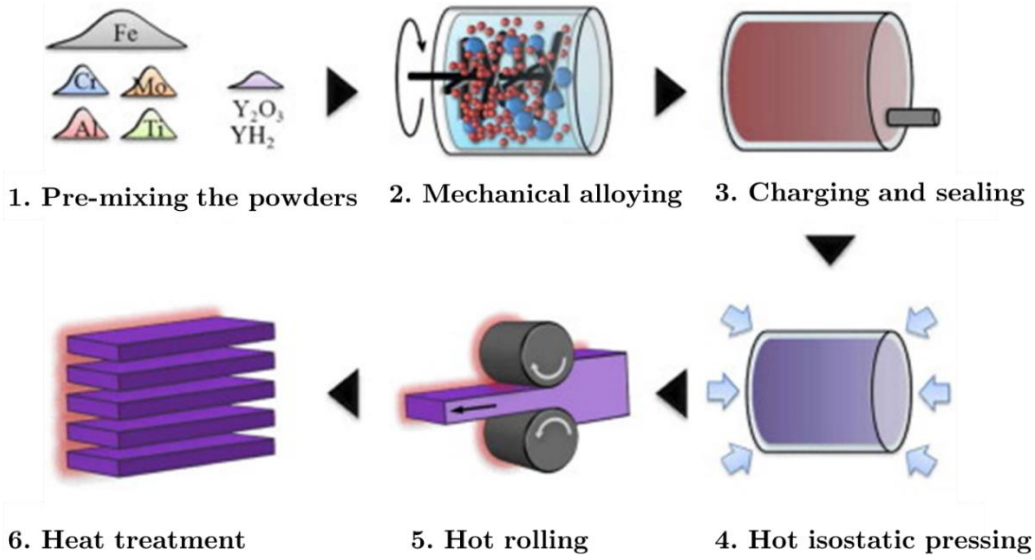

Figure 1.7 Basic scheme on the elaboration of ODS steels [Noh 2014]

1.2.3.1 Mechanical Alloying:

In the ball milling alloying process, steel balls used in the milling are in constant motion. When the steel balls collide, some amount of the alloying powder can be trapped between them. During this collision, the force of the impact deforms plastically the powder particles leading to work hardening and fracture. There are new surfaces created which enable the particles to weld together and ensure an increase in particle size. A steady state equilibrium is eventually reached after a certain period of milling where a balance is attained between the rate of welding, which tends to increase the average particle size and the rate of fracturing, which tends to decrease the average composite particle size [Suryanarayana 2001]. The sizes of both the small and larger particles are driven towards an intermediate size due to the fact that the smaller particles are able to withstand deformation without fracturing and tend to be wielded into larger pieces. A large amount of deformations is introduced into the particles in the form of a variety of crystal defects such as dislocations, vacancies, stacking faults, and increased number of grain boundaries. These defects enhance the diffusivity of the solute elements within the matrix. It is possible to have a slight increase in temperature during the milling process, which may enhance the diffusion of the constituent elements. The milling is usually conducted at room temperature and therefore annealing of the powders at elevated temperatures is required to enhance the formation of new intermetallic phases.

The milling conditions and the parameters of the equipment used may influence the structure and composition of the nanoparticles formed. The duration of the milling process is a crucial factor that affects the final characteristics. It is always necessary that the duration of the milling ends when a steady state is achieved between fracture and cold welding of the powder particles. Milling of the powders for much longer times may lead to the formation of undesirable phases as well as an increase in the level of contamination. In the milling processes of conventional ODS, the mechanical alloying is usually done within 48 hours. Two main high energy milling equipment are often employed in the conventional fabrication of ODS steels and these are the attritor ball mill and the planetary ball mill. The attritor uses a vertical drum with impellors located at right angle to each other. A motor is responsible for rotating the impellors, which move the balls and impact the balls with the powder to lead to powder reduction. The planetary ball mill uses vials (container) based on a mechanism where the vials rotate around their own axis and a rotating disc impacts on the powder in the mill. The forces ensuring the impact on the powder results in the powder size reduction.

Optimization and improvements in the annealing conditions are updated from time to time. Laurent-Brocq *et al.* [Laurent-Brocq 2012] suggested two means of improving the usual milling conditions to promote the formation of nanoparticles with a fine distribution in size. The first mode is to perform a long and/or intense ball milling with limited overheating and also to anneal the as-milled powder at 800°C before performing the thermo-mechanical treatment. Another important factor during the milling is the milling atmosphere. To eliminate the contamination, which may result from air, inert atmospheres such as argon are always preferable. Hydrogen is also used in certain cases. The powders after MA are canned, degassed and sealed before the consolidation.

1.2.3.2 Consolidation of powder and thermo-mechanical heat treatments:

As mentioned, the consolidation of the powders is performed by either of two main modes, which are the hot extrusion (HE), and the hot isostatic pressing (HIP/HIPing).

The hot extrusion technique (HE) begins by pre-heating the sealed powders to a temperature between 850 and 1150°C. Exact temperatures of 850 and 1150°C are more often used. The heated piece is forced through a reduced slit enduring compaction and a reduction in size (see *Figure 1.7*). Extrusion leads to compressive forces and high amount of stresses, which ensures densification of the material.

In the alternative hot isostatic pressing, the canned and sealed powders are heated to the temperature range between 850 and 1150°C where an isostatic pressure is applied. Dense forms of powders are formed after HIP similar to the HE. Ideally, the HIP technique is preferred but not economical when producing these materials in mass quantities. The lower cost of the HE technique makes it more attractive. The challenge however associated with the hot extrusion technique is the fact that the grains may be elongated along the extruded direction. This eventually leads to anisotropy in the mechanical properties. The thermo-mechanical heat treatments become necessary at this stage to reduce such anisotropy by processes involving cold and warm working of the material. Recrystallization of the anisotropic grains eventually occurs to produce a more desirable material.

ODS steels as stated above have been fabricated for decades using different fabrication schemes, different milling equipment, milling atmospheres, time and most importantly compositions. There are therefore possibly hundreds of different kinds of ODS steels fabricated and under production. A few well known ODS steels produced and under investigation are listed in *Table 1.2*.

Alloy	Composition (wt%)				
	Cr	Y_2O_3	Ti	W	Others
12YWT [Klueh 2002b]	12	0.25	0.4	2.5	
14YWT [Miller 2006]	14	0.25	0.4	3.0	
1DK [Yamashita 2002]	13	0.34	0.6	2.8	0.05C
1DS [Yamashita 2002]	11	0.63	0.4	2.7	0.09C
DY [Lescoat 2011]	13	0.50	2.2	-	1.5Mo
Eurofer-97 [Schaublin 2006]	9	0.3	-	1.1	0.11C, 0.47Mn, 0.2V, 0.14 Ta,
F94 [Ukai 2000]	12	0.24	0.3	2.0	0.06C
F95 [Yamashita 2004]	12	0.25	0.3	2.0	0.06C
Fe-14Cr-Y_2O_3 [Steckmeyer 2010]	14	0.30	0.3	1.1	0.3Mn, 0.15Ni, 0.3Si
K1 [Kasada 2007]	18	0.37	0.3	0.3	
K3 [Yutani 2007]	16	0.30	0.3	2.0	4Al
K4 [Kasada [2007]	19	0.37	0.3	1.8	4.6Al
MA965 [Chao 1998]	20	0.50	0.5	-	5Al
MA957 [Miller 2004]	14	0.25	0.9	-	0.1Al, 0.3Mo
PM2000 [Alinger 2009]	20	0.5	0.5	-	5.5Al
U14YT [Alinger 2009]	14	0.25	0.4	-	
U14YW [Alinger 2009]	14	0.25	-	3	
U14YWT [Alinger 2009]	14	0.25	0.4	3	
U14WT [Alinger 2009]	14	0.25	0.4	3	

Table 1.2 Some of the many different types of ODS steels produced

1.2.4 ODS production by alternative processes

The HIP and HE techniques for the conventional fabrication of ODS steels are not without challenges. Hence, Spark Plasma Sintering (SPS) is a developing novel powder consolidation technology applicable for the fabrication of ODS steels [Heintze 2012, Sun 2012, Zhang 2015]. The advantage of the SPS with respect to HIP and HE techniques is that, much less time is spent in the heating and cooling during the consolidation process. The SPS process is mainly based on passing a pulsed current through the compact powder by the sintering process. The heat is applied directly to the powders, which ensures a fast heating as compared to hot pressing where the heat is generated externally. During such very high fast heating at temperatures below the melting point, diffusion of atoms take place. The individual powder particles can then be bonded to each other to create a denser compact form made up of the bonded particles. It is this sintering process which involves compacting and forming of a solid body by heat and/pressure which allows clusterization to occur. This has been employed in

several fabrication modes of ODS steels. Xie *et al.* [Xie 2017] revealed the formation of a dense distribution of $Y_2Ti_2O_7$ nano-oxide particles as well as some large $Cr_2Mn(Ti)O_4$ particles after MA and consolidation by SPS. In a very recent study, Li *et al.* [Li 2018] demonstrated the formation of $Y_4Zr_3O_{12}$ nano-oxide particles in alloys containing 0.3%Zr as well as a few $CrTiO_5$ oxide nanoparticles.

1.2.5 Characterization of ODS steels

ODS steels are usually characterized based on the mechanical properties of these steels. Such characterizations are performed on the ODS fabricated alloys and compared with conventional ferritic-martensitic steels. For these steels, the characterization of the nature, composition and structure of the nanoparticles are also performed. After different kinds of irradiation schemes (i.e. neutron and ion), the microstructural properties and the nanoparticles can be compared to the non-irradiated specimen.

1.2.5.1 Mechanical properties of ODS steels

The characterization of the microstructure of ODS steels are performed to verify the homogeneity of the material and the sizes of the grains as well as other properties. The sizes of the grains can range from several microns to as low as a few nanometres. However, it is possible for ODS steels to possess a bimodal grain size distribution, in which the micron-sized coarse grains provide high ductility whereas the nanometer-sized grains are responsible for enhanced tensile strength [Dapeng 2011]. The tensile properties are very common properties of ODS steels usually determined [Klueh 2002b, Klueh 2005, Auger 2011, Kasada 2011]. This expresses the maximum amount of tensile stress or input force that the material can take before the eventual failure of the material. Such tensile tests have been conducted by various groups and one such test is by Carlan *et al.* [Carlan 2009] where the tensile properties of Fe-18Cr1W ODS steel is compared to MA957. The tests were performed using a strain rate of $7x10^{-4}$ s^{-1} at temperature ranging from 20 to 750°C. Both the MA957 and the Fe-18Cr1W materials have similar property behaviours in that the tensile strength is quite very high at room temperatures and decreases to reach about 400 MPa at 750°C. Such behaviour is very typical for ODS steels. A typical resume of the microstructural properties of ODS steels is presented by *Dade et al.* [Dade 2017] as given in the *Figure 1.8* where different steels are compared. They include an un-strengthened material (US) with no addition of Ti or Y, a low strengthened material (LS) with a low addition of oxides, a high-strengthened material (HS) with a higher amount of oxide addition and a reference material (Ref) with an addition of oxides typical of most studies of the literature. The ductility also reaches a few percent at high temperature, which is usual for these types of steels. Two other materials produced by HIPPing with thr same Ti,Y and O as the reference material, one with coarse precipitates (CP) and and the other a recrystallized material (Rc) as well as a hot extruded material (HE) were investigated. The higher the volume fraction of oxide precipitates, the higher the yield strength and the therefore the high-strengthened materials possess the highest yield strength whilst the un-strengthened material has the lowest yield strength. Regarding the evolution of the total elongation, the US material increases monotonically with temperature with the material becoming soft. On the contrary, all the other oxide reinforced materials showed a non-monotonic evolution of the total elongation where the maximum of the ductility ranged between 500 and 650°C.

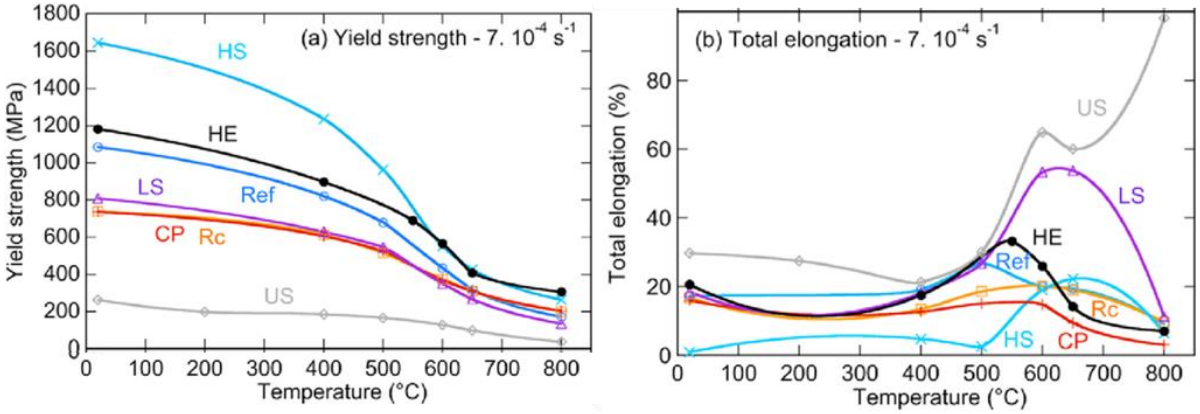

Figure 1.8 The evolution of (a) the yield strength, and (b) total elongation with temperature for the un-strengthened (US), low-strengthened (LS), high-strengthened, Reference (Ref), Coarse Precipitates (CP), Recrystallized (Rc) and Hot extruded (HE) material at a strain rate of 7.10^{-4} s^{-1} [Dade 2017].

The high strength of the materials with the nano-oxide dispersions have just been demonstrated. However, the significant increase in the yield strength is associated with a large decrease in the ductility. Hence, the *Figure 1.9* shows the stress-strain curves for the various materials at RT with a strain rate of $7.10^{-4}s^{-1}$. The low strengthened materials such as the LS and the Ref materials still demonstrate a reasonably large ductility at RT as compared to the HS material which already demonstrates a brittle nature at RT. Hence, even though the high strengthened materials are relatively stronger they could be quite brittle and therefore the need to control the nano-oxide formation in ODS steels.

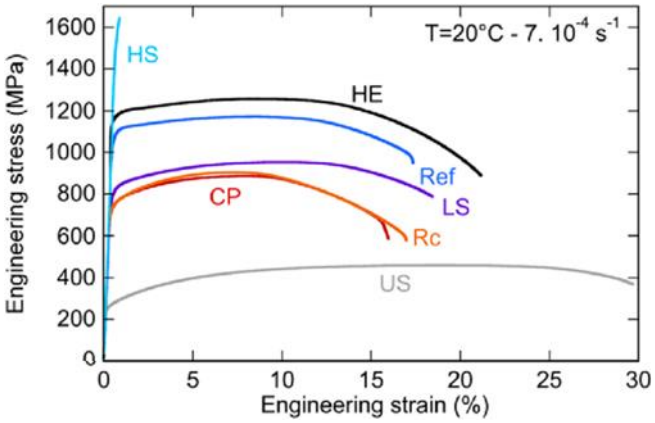

Figure 1.9 The engineering strss-strain curves for the US, LS, HS, Ref, CP, Rc, and HE materials tested at room temperature with a strain rate of $7.10^{-4}s^{-1}$ [Dade 2017].

1.2.5.2 Microstructural characterization based on the nanoparticle formation

The characterization of the microstructure of ODS steels has been performed by various techniques including X-ray Diffraction (XRD), Transmission Electron Microscopy (TEM), Atom Probe Tomography (APT), Electron Holography, Atomic Force Microscopy (AFM), X-ray Absorption Fine Structure Spectroscopy (XAFS) and many others. The two main methods of characterization upon which most literature is based are the TEM and APT techniques. The nature of the nanoparticles formed is found to hugely depend on the composition of the alloy, the fabrication route and the conditions used. The sizes of the nanoparticles range from a few nanometres to several tens of nanometres. To simplify the various kinds of nanoparticles that are formed, the nanoparticles are usually classified into two main types. There are the

non-stoichiometric Y-, Ti-, O- enriched clusters with a size ranging from 1 to 10 nm mostly characterized by APT and much larger stoichiometric Y-, Ti-, O- clusters characterized by TEM.

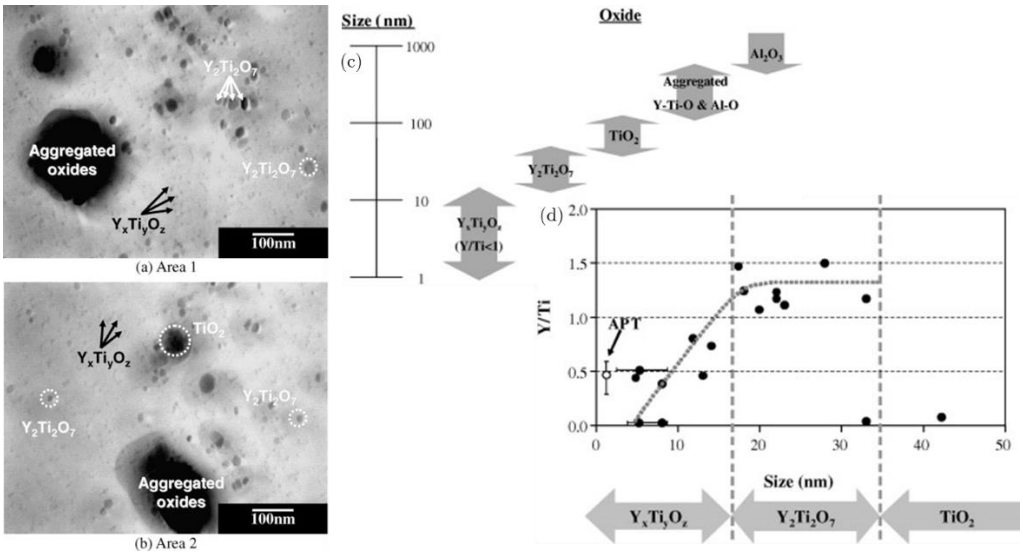

Figure 1.10 The analysis of particles observed in ODS MA957 (a) and (b) TEM images of the extracted replica (c) the size distribution of the identified oxides and (d) the correlation between chemical composition and size of oxide particles [Sakasegawa 2009].

An example of the different kinds of particles that can be obtained as a function of size is given in a study by Sakasegawa *et al.* [Sakasegawa 2009] on MA957 ODS steels. In this study, three types of phases are observed by means of TEM, XRD and EDX: (i) non-stoichiometric Y-, Ti-, O- enriched clusters with a size of 2-10nm, (ii) stoichiometric $Y_2Ti_2O_7$ particles with a size of 15 to 35 nm and (iii) large aggregated nanoparticles greater than 50 nm such as Al-enriched and Ti-enriched oxides. As seen in the *Figure 1.10*, the ratio of the Y to that of Ti increases with an increase in the size of particles up to 15 nm and then saturates after 20 nm. The ratio of Y/Ti in many of the small particles is less than 0.5. It is a good indication that appropriate increase of the titanium compared to the yttrium could be an effective means to increase the number of very small oxide particles. The large TiO_2 particles observed are believed to hardly contribute to oxide dispersion strengthening. Such TiO_2 particles are reported to be formed in the grain boundaries in many studies. There is no consensus yet on exactly when these particles form during the fabrication process. It is predicted that the nanoclusters may form directly after milling [Brocq 2011] or after the thermal treatment.

1.2.5.3 Stoichiometric Y-, Ti-, O- enriched nanoclusters

There are three widely known stoichiometric Y-, Ti-, O- enriched nanoparticles formed in ODS steels. They include Y_2O_3, $Y_2Ti_2O_7$ [Cayron 2010, London 2014, London 2015] and Y_2TiO_5 [Cayron 2010, London 2014, London 2015]. The Y_2O_3 are usually identified in Ti free steels whilst the $Y_2Ti_2O_7$ and Y_2TiO_5 are found in Ti added steels. For cases where Cr appears to play a role in the formation of nanoparticles, a $YCrO_3$ phase is formed [Castro 2011]. Several other different types of oxides can be found in ODS steels such as YAG (Yttrium Aluminium Garnet) for the Al added steels and Zr enriched particles ($Y_4Zr_3O_{12}$ [Dou 2014], $Y_2Zr_2O_7$) for the Zr added steels as mentioned in section 1.2.2.

The elemental composition of the nanoparticles are performed using various analytical TEM characterization techniques as well as APT techniques. The *Figure 1.11* shows typical ODS particles in the order of a few nanometers to tens of the nanometers in a RAFM-ODS alloys by Klimiankou *et al.* [Klimiankou 2004] using EFTEM. The nanoparticles display a yttrium-titanium-oxygen composition.

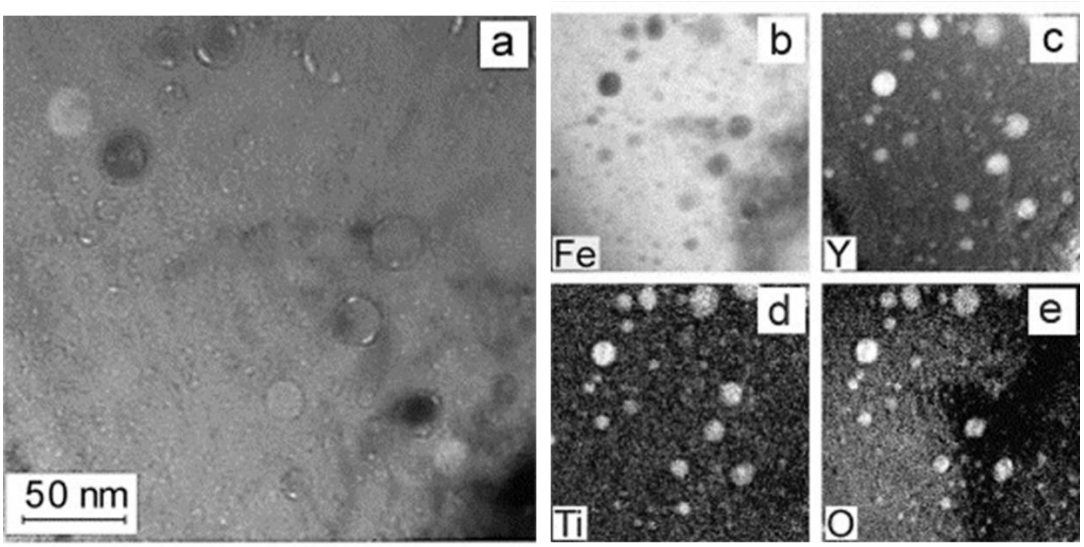

Figure 1.11 (a) Bright field image and (b) EFTEM elemental images (b) to (e) of $Y_2Ti_2O_7$ ODS nanoparticles in the reduced activation ferritic-martensitic steel. The bright field image was taken slightly defocused in order to enhance the particle contrast. The EFTEM elemental images were acquired using Fe-$L_{2,3}$, Y-$M_{5,6}$, Ti-$L_{2,3}$ and O-K EELS edges [Klimiankou 2004].

The Figure 1.12 shows examples of stoichiometric particles observed by HRTEM in ODS steels. Particles of Y_2O_3 (*Figure 1.12(i)*) and $Y_2Ti_2O_7$ *(ii)* are observed in the RAFM ODS Ti free steels [Klimiankou 2004]. The *Figure 1.12(iii)* is a HRTEM image of a Y_2TiO_5 particle observed in SOC-14 (Fe-15Cr-2W-0.1Ti-4Al-0.63Zr-0.35Y_2O_3) studied by Dou *et al.* [Dou 2014]. They also demonstrated the formation of $Y_4Zr_3O_{12}$ in these SOC-14 (Fe-15Cr-2W-0.1Ti-4Al-0.63Zr-0.35Y_2O_3) ODS steels.

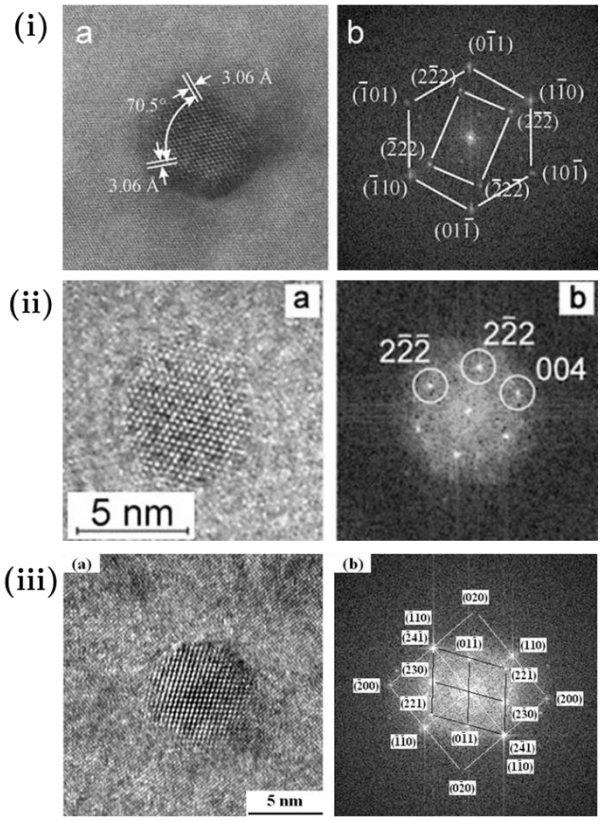

Figure 1.12 HRTEM imaging of typical stoichiometric ODS particles for: [i] Y_2O_3 nanoparticle showing (a) nanoparticle embedded in the matrix with an orientation B=[110] (b) and the corresponding *fft*. [ii] $Y_2Ti_2O_7$ nanoparticle showing (a) nanoparticle embedded in the matrix with an orientation B=[110] and the (b) corresponding *fft* [iii]. Y_2TiO_5 nanoparticle showing (a) nanoparticle embedded in the matrix and the corresponding *fft* (b).

The orientation relationships between these stoichiometric nanoparticles and the base matrix was first reported by Mujahid *et al.* [Mujahid 1994] where they stated that the lattice continuity between the oxide and the matrix implies a presence of a degree of coherency of the interface. Shortly after, Inkson *et al.* [Inkson 1996] also reported that Y_2O_3 particles were observed with facets and these facets coincide with the {100}, {110} and {112} planes of the surrounding matrix. Also, uncoupled ½<111> FeAl superpartial dislocations were found laying a few nanometers from some of the FeAl-Y_2O_3 interfaces. In an opposing view, Yamashita *et al.* [Yamashita 2004] suggested that there may be no specific existence of orientation relationship or coherence between Y_2O_3 nanoparticles and the matrix in 12Cr ODS steel. The investigations by Yamamoto *et al.* [Yamamoto 2011] and Yazawa *et al.* [Yazawa 2004] appeared to back the work by Yamashita *et al.* [Yamashita 2004] where it is reported that phase transformation and recrystallization processes by Yamamoto *et al.* [Yamamoto 2011] and Yazawa *et al.* [Yazawa 2004] respectively induce the loss of interference coherence between nanoparticles and the matrix in ODS steels. The contrasting results may be due to the conditions and processes of fabrication of these steels where such coherence or ORs are affected. However, several investigations have indeed confirmed an orientation relationship does exist between the matrix and the nanoparticles [Klimiankou 2003 and 2004, Ramar 2009, Cayron 2010, Dou 2011, Hsiung 2011, Ribis 2011, 2012 and 2013, Bhattacharyya 2012, Mao 2015]. The orientation relationship between the oxide nanoparticles and the matrix is dependent on the particle size [Hsiung 2011]. The small sized particles < 10 nm are usually coherent or semi-coherent and possess faceted interfaces while the larger sized particles >20 nm are mostly incoherent. The reasoning attached to this is the fact that the nanoparticles lose coherency

with the introduction of dislocations. This is plausible in the bigger sized particles. With ODS nanoparticles quite small in most investigations; the coherency between the particles and the matrix is conceivable. Klimiankou *et al.* [Klimiankou 2003, 2004] suggested that a parallel orientation between Fe(110) and Y_2O_3(111) atomic plane directions is observed in Ti free RAFM ODS alloys. Bhattcharyya *et al.* [Bhattacharyya 2012] and Cayron *et al.* [Cayron 2010] have reported the possible orientation relationships between the matrix and observed particles. For Bhattacharyya *et al.* [Bhattacharyya 2014], some new orthorhombic Y-,Ti- phases were observed, which were semi-coherent to the base matrix. Orientation relationships only between types of particles (i.e. Y_2TiO_5 and $Y_2Ti_2O_7$) were reported in the case of Cayron *et al.*. More detailed information on these ORs have been demonstrated by Ribis *et al.* [Ribis 2012] where ODS materials developed at CEA were investigated. Both $Y_2Ti_2O_7$ and Y_2O_3 nanoparticles were found. The $Y_2Ti_2O_7$ nanoparticles were found to be cubical particles embedded in the matrix with a cube-on-cube orientation relationship with the matrix. The other Y_2O_3 nanoparticles demonstrated both a cube-on-cube and cube-on-edge orientation relationship with the matrix.

The *Table 1.3* illustrates the conditions of fabrication, composition, size and crystallographic structure of nanoparticles found in some of the common ODS alloys. For most of these investigations, the particles >5 nm are characterized based on their crystallographic structure. The structure of most of the nanoparticles <5 nm which have been described as non-stoichiometric is unidentifiable.

Alloy		Characterization method	Consolidation treatment	Composition	Structure	Particle size (nm)
12YWT	2002 Klueh 2003Miller 2007 Pareige	TEM APT APT	HE at 1150°C, 200 Mpa, Ann 1 h at 1050°C HE at 1150°C	Y-Ti-Cr-O and Fe? Y-Ti-O Y-Ti-O		2.6 nm 4 nm 4 nm
MA957	2004 Miller 2011 Miller 2014 Ribis 2016 Wu	APT, TEM APT TEM TEM Cs corrected	HE, Ann 24 h at 1300°C HE HE 850°C, Ann 1 hr at 1000°C	Y-Ti-O Y-Ti-O Y-Ti-O Y-Ti-O	Pyrochlore *fcc* structure $Y_2Ti_2O_7$ pyrochlore	2 nm 2 nm 1-5 nm
14YWT	2006 Miller 2012 Brandes	APT TEM	HE 850°C, Ann 1 hr at 1000°C HE 850°C, Ann 1 hr at 1000°C	Y-Ti-O Y-Ti-Cr-O	Inconsistent with any known O	2 nm 2-4 nm
ODS EUROFER97	2002 Lindau 2003 Klimiankou 2004 Klimiankou 2007 Klimenkov 2009 Ramar	TEM TEM TEM TEM TEM	HIP HIP at 1050°C HIP at 1050°C HIP HIP at 980°C	Y-O Y-O Y-Ti-O Y-O Y-Ti-O	Y_2O_3 Y_2O_3 $Y_2Ti_2O_7$ Y_2O_3 Y_2O_3	2-10 nm, avg 4 3-45 nm, avg 12 ≈ 5 nm 5 nm 5-10 nm
ODS EUROFER	2007 Klimenkov 2009 Klimenkov	TEM TEM	HIP HIP	Y-O Y-O with a Cr shell	Unidentified Y_2O_3	5-18 and 5 nm Bimodial grains 8 nm
Fe12Cr	2009 Castro 2011 Brocq	APT TEM. APT	HIP at 1100°C for 2h, Ann 4 h at 800°C	Y-Ti-O Y-Ti-O		3-10 nm 5 nm
U14YWT	2012 Bhattacharrya	MA – TEM	HIP, 850°C 200 Mpa, 3 h	Y-Ti-O	Possible distorted $Y_2Ti_2O_7$	<5 nm
Fe14CrWT	2009 Oksiuta 2010 Steckmeyer 2012 Olier 2014 London	TEM TEM TEM, SNAS APT, TEM	HE at 1100°C, Ann 1050°C 1 hr HE at 1100°C, Ann 1050°C 1 hr HE at 1150°C, Ann 1200°C 1 hr HE at 1050°C and 1150°C	Y-T-O Y-Ti-O Y-Ti-O	<2nm unidentified, $Y_2Ti_2O_7$ and Y_2TO_5	5 nm 2.3 nm 3 nm
Fe18Cr-Y_2O_3	2010 Cayron 2014 Lescoat	APT APT, TEM	HE HE at 1100°C, Ann 1 hr at 1050°C	Y-O, Y-Ti-O Y-T-Cr-O	Y_2O_3, Y_2TiO_5, $Y_2Ti_2O_7$ Pyrochlore type structure	<2 nm at 850°C, 20 nm at 1000°C > 2 nm

Table 1.3 Different characterizations of the size, structure and compositions of some standard ODS steels

1.2.5.4 Non-stoichiometric Y-, Ti-, O- enriched nanoclusters

The non-stoichiometric Y,Ti,O nanoparticles are usually relatively small in the range <5 nm. The resolution and imaging of such small nanoparticles has remained challenging for most TEMs. On the other hand, Bhattacharrya *et al.* [Bhattacharrya 2012] found the presence many small clusters <5 nm in U14YWT alloy HIP-ed at 850°C. They suggest that these particles correspond to a distorted $Y_2Ti_2O_7$. Elsewhere, Brandes *et al.* [Brandes 2012] also investigated 14YWT by HRTEM and found very small nanoclusters of the size ranging between 2 and 4 nm with a composition of Ti, O, Y and Cr. These clusters had a structure inconsistent with any known oxide structures. The ability to resolve the structure of such small nanoclusters by TEM remains a well known difficulty. However, modern TEMs are being equipped with Cs and double Cs-aberration correctors. Such TEMs can be used to obtain resolutions down until 1 Å. This will be ideal in characterizing in detail the structure of such very small nanoparticles formed. Promising results have therefore been already obtained by Hirata *et al.* [Hirata 2011] using a state-of-the-art Cs-corrected TEM. Their study revealed enough information to show that nanoclusters have a defective NaCl structure with a high lattice coherency with the *bcc* steel matrix. Vacancies are recognized to have an important role in the stabilization of nanoclusters. Various pairwise systems such as Ti-(O,N), Fe-(O,N) and Y-N have the ability to form a NaCl-type structure. This structure has a good flexibility and high vacancy capability to form nanoclusters with multiple constituent elements. The lattice coherency between the oxide nanoclusters and the steel matrix produce a very low interface energy, which can effectively prevent the coarsening of the oxide precipitates. This unique property means therefore that ODS steels possessing a high number of defective nanoprecipitates could be the ideal material state, which is quite different from the conventional nano-phase material, which is susceptible to coarsening at elevated temperatures.

Atom Probe Tomography (APT) has been used extensively to characterize these small non-stoichiometric Y-, Ti-,O- enriched nanoparticles. The compositions of such clusters are usually similar to the composition of much larger clusters with a yttrium-oxygen composition [Miller 2003, 2004, 2006, Bhattacharrya 2012]. Others have a yttrium-titanium oxide composition [Brandes 2012, Lescoat 2014]. In the case where alloys are free of Ti, yttrium oxides are reported [Miller 2003] and similarly in cases of Y free alloys, titanium oxides are found [Miller 2006]. The *Figure 1.13* shows typical clusters in ODS steels as portrayed by APT investigation technique.

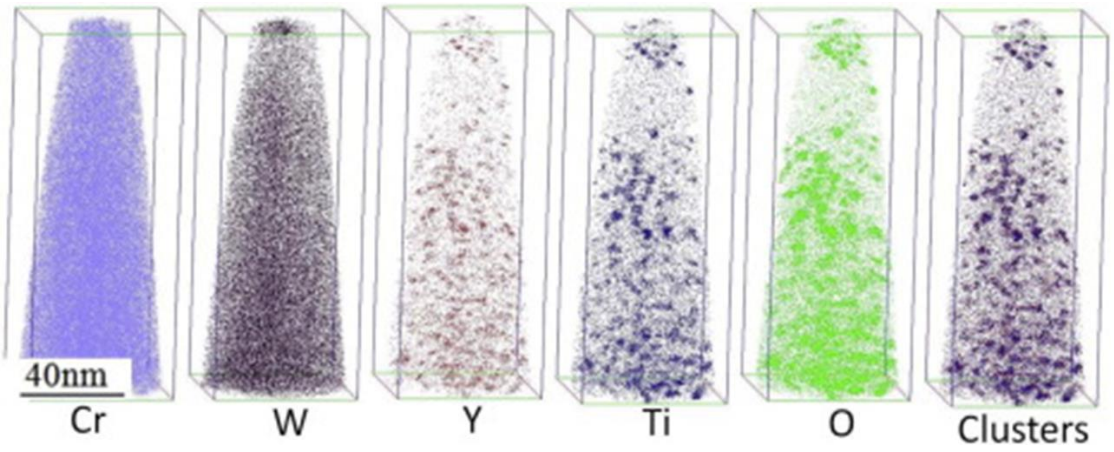

Figure 1.13 APT 3D reconstruction of 14YWT ODS samples showing the distribution of various elements present [Miller 2003].

The two main characterization techniques are therefore complementary to each other. London *et al.* [London 2014] compared TEM and APT for analysing the nanoparticles in ODS steels. The TEM technique is recognized to accurately measure the size of any oxide particles whilst the APT remains ideal for characterization of the sub 1.5 nm particles.

The formation of complex carbides $M_{23}C_6$ (M= Fe,Cr) have also been evidenced in ODS steels [Ramar 2009, Olier 2012]. Such precipitates of carbides are found mainly at the grain boundary of ODS steels. The carbon apparently appears to come from the contamination probably during the MA process. However, Klimiankou *et al.* [Klimiankou 2007] have shown that the presence of carbide $M_{23}C_6$ can be eliminated if an adequate heat treatment is applied to ODS steels.

1.2.5.5 Core/shell structure of nanoparticles in ODS steels

Investigations into the formation of Y,Ti,O nanoparticles have been conducted for decades. A couple of studies [Marquis 2008, 2009, Klimenkov 2009] have proposed the formation of a core/shell structure for the nanopartcles. Marquis *et al.* [Marquis 2008] investigated three different types of ODS alloys namely: MA957 *Figure 1.14(a)*, ODS Fe-12 *Figure 1.14(b)* and ODS Eurofer97 *Figure 1.14(c)* by APT technique. The *Figure 1.14* shows slices through 3D reconstruction showing the evaporation structures of nanoclusters (both small and large nanoclusters). In the left column can be seen small nanoclusters of sizes less than 4 nm and in the right column are much bigger nanoclusters of sizes greater than 8 nm for the three different ODS alloys mentioned. What appears evident is that the nanoparticles are enriched in Y and O for both the small and large clusters. In addition Ti enrichment is observed in the clusters for the MA957 ODS alloy. The profiles for all the particles indicate a shell formation with Cr enrichment. V enrichment in the shell is observed in ODS alloys containing V i.e. ODS Eurofer97. The investigations therefore conclude the formation of Y and O rich nanoclusters with a Cr shell or a Cr,V if V is present in the ODS alloys.

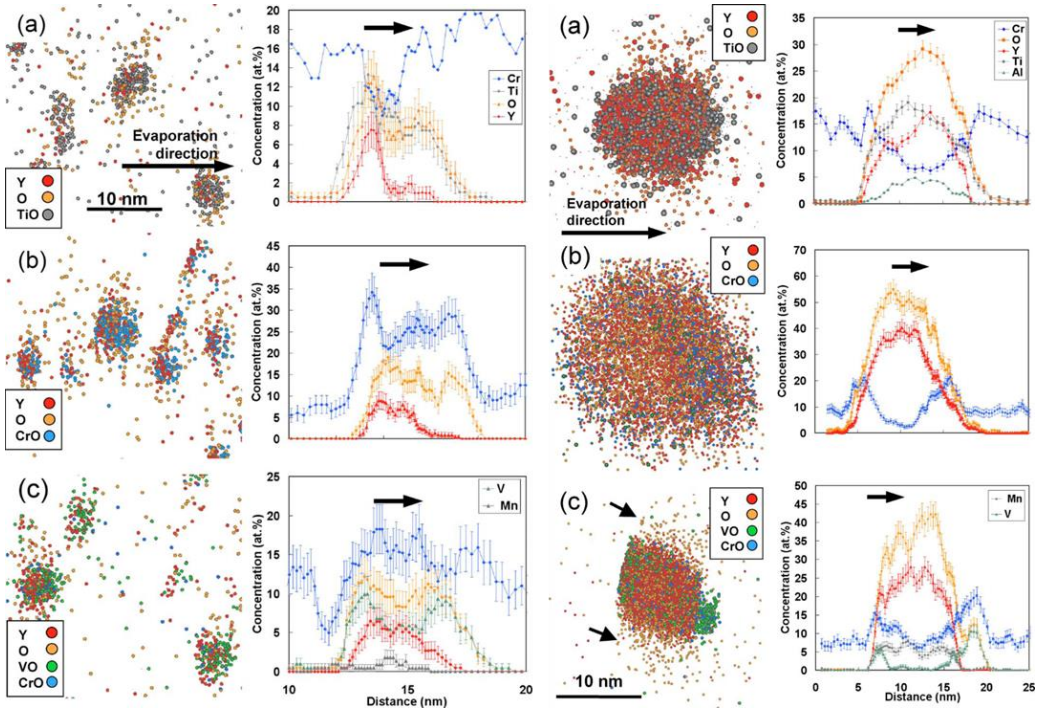

Figure 1.14 Slices made through the 3D reconstruction indicating the evaporation structures of large oxide particles (found in the left column) in (a), ODS Fe-12Cr alloy found in (b) and (c) ODS Eurofer97 alloy. All the samples were analysed by APT in laser pulsing mode [Williams 2010].

Elsewhere, Klimenkov *et al.* [Klimenkov 2009] managed to identify nanoparticles with the core/shell structure in ODS Eurofer97 by TEM investigations. The *Figure 1.15* shows elemental maps of two distinct particles observed in their investigation. The core of the nanoparticles illustrates darker contrasts for Fe, Cr as well as V indicating a deficiency of these elements. Brighter contrasts for Y and O were observed indicating the presence of these elements in the core and therefore the formation of a Y-O nanoparticle. In addition, brighter contrasts were observed on the shell of these particles for the V and Cr maps. This investigation therefore revealed the formation of a V-Cr-O shell with a typical thickness ranging between 0.5 and 1.5 nm around Y,O nanoparticles. The above results confirm the core/shell structure of nanoparticles as proposed by Marquis *et al.* [Marquis 2008].

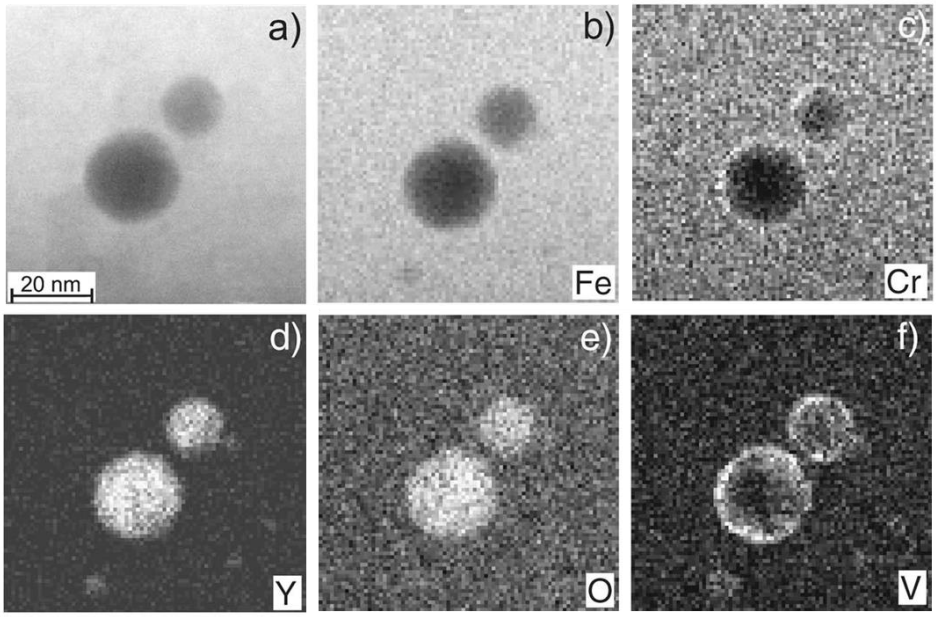

Figure 1.15 The EDX elemental composition mapping of two ODS particles. (a) HAADF image of the particles (b) to (f) elemental maps acquired using Fe-Kα, Cr-Kα, Y-Lα, O-K and V-Kα EDX lines, respectively [Klimenkov 2009].

1.2.5.6 Properties of ODS Steels after Irradiation

ODS steels for future nuclear power generations will be operated under extreme irradiation conditions. The stability of the oxides formed will therefore be tempted at such extreme conditions. Studies have thus investigated the stability of the ODS material under different irradiation conditions [Schaublin 2006, Klimenkov 2007, Pareige 2007, Yamashita 2007, Steckmeyer 2010, Tong 2010, Kuksenko 2011, Miller 2011, Swenson 2017]. Once such study is by Ribis *et al.* [Ribis 2011, 2014] where the stability of oxides in MA957 was investigated by neutron irradiation. Nanoparticles with the pyrochore-type structure were observed before the irradiation. After the irradiation up to 50 dpa at 412°C and up to 75 dpa at 430°C, they found that there was no significant difference between the nanoclusters observed before and after the irradiation. Only the density of the nanoclusters had decreased slightly. In a similar investigation of ODS steels under irradiation, ODS Eurofer, 13.5Cr ODS and 13.5Cr0.3Ti ODS irradiated with Fe (5.6 MeV) or Ti (4.8 MeV) at RT and 300°C have been studied by [Rogozhkin 2016]. The number density of the oxide particles in all the samples increased and the fraction of the small nanoparticles in the particle size distribution had also increased as shown in the *Figure 1.16* for the irradiation performed at RT. A similar feature was recorded for the irradiation performed at 300°C. Regarding the swelling, [Tanaka 2004] reported that

ODS ferritic alloy suppressed the swelling of the alloy to less than 0.01% under triple ion irradiation of Fe^{3+}, He^{+} and H^{+} at 510°C up to 50 dpa. A comprehensive review of the irradiation evolution of oxide nanoparticles dispersed in FeCr systems can be found in Wharry *et al.* [Wharry 2017].

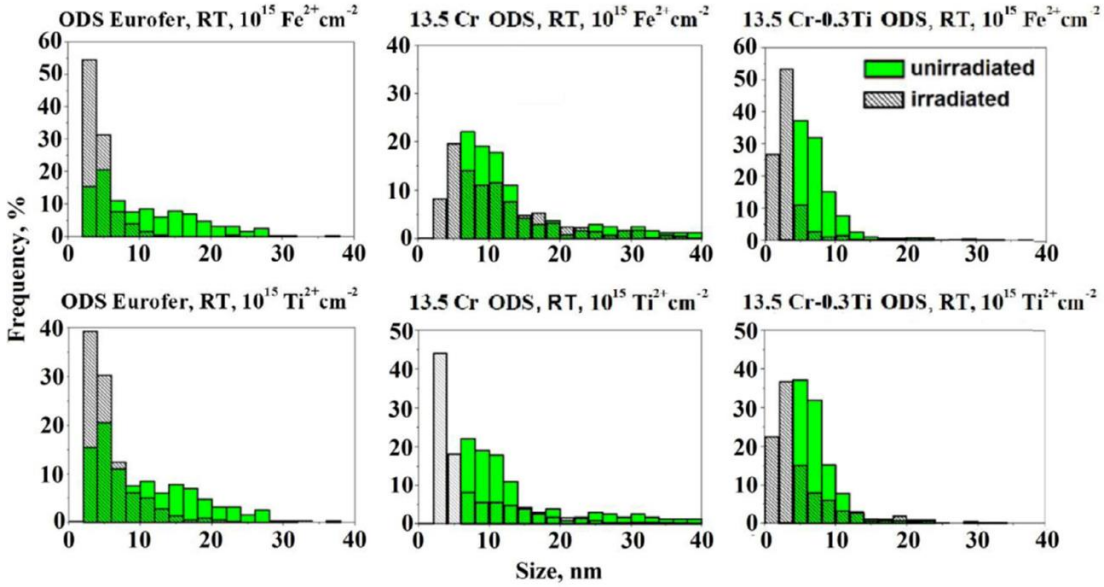

Figure 1.16 Comparison of size distributions of oxide particles in unirradiated ODS steels (ODS Eurofer and 13.5Cr-(0-0.3)Ti ODS) after irradiation at RT [Rogozhkin 2016].

For ODS steels dedicated to fusion applications, one very important issue that affects the properties of these steels is the synergistic effects of irradiation damages and helium. The nuclear reaction of 14 MeV fast neutrons produces helium in ferritic steels [Kishimoto 2006]. The helium is insoluble in steels and usually precipitates as gas bubbles, which are the formation sites for both growing voids and grain boundary creep cavities [Kishimoto 2006]. In the ODS steels, the high density of the nanoprecipitates/nanoclusters provide a high number of trapping sites for transmutation helium (He), avoiding the helium agglomerating to coarsen bubbles. The effect of this is to minimize the risk of helium embrittlement in the structural materials for fusion reactor application. Several investigations have indeed confirmed that the helium bubbles and the coarsening of the helium bubbles are suppressed in ODS steel [Kimura 2000, Kimura 2005, Lu 2014].

1.2.6 Propositions of mechanisms of formation of nanoparticles

1.2.6.1 The global formation steps

Based upon the observation of a core/shell structure of nanoparticles in ODS steels, Hsiung *et al.* [Hsiung 2010] proposed a possible mechanism for the elaboration of ODS steels in three stages after investigation of their 16Cr-4.5Al-0.3Ti-2W-0.3Y_2O_3 ODS ferritic steel. The steps are proposed to include:

i. Fragmentation of starting Y_2O_3 particles during early stages of ball milling
ii. Agglomeration and solid state amorphization of Y_2O_3 fragments mixing with matrix constituents during later stages of ball milling

iii. Crystallization of the amorphous agglomerates larger than 2 nm to form oxide nanoparticles with a core/shell structure during the consolidation at 1150°C. The agglomerates or clusters smaller than 2 nm remain amorphous (disordered). See *Figure 1.17*.

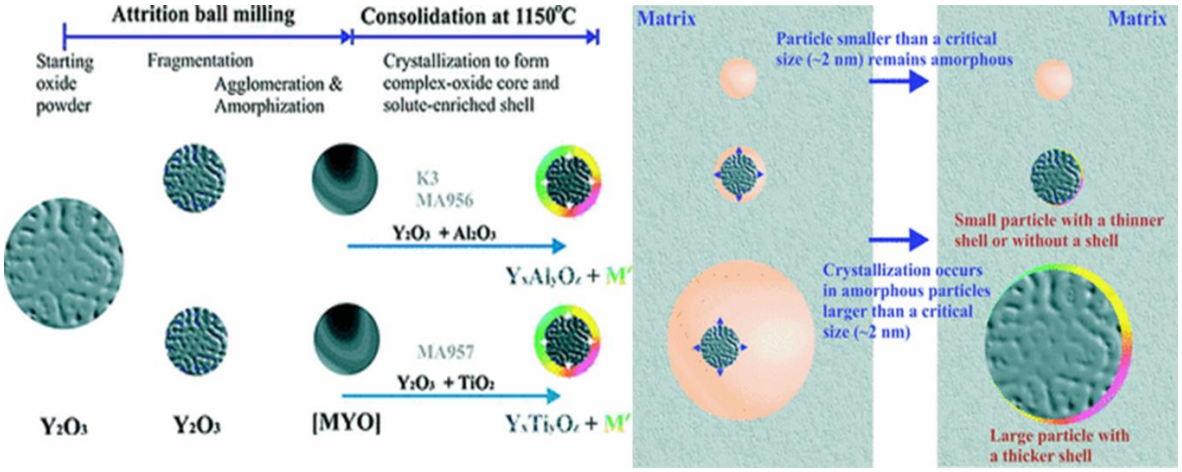

Figure 1.17 (a) The three-stage mechanism involved in the nano-oxide particle containing a core/shell structure during MA and consolidation for Al as well as for Ti-containing ODS steel. The size effect on the formation of a core/shell structure in ODS particle. A solute-enriched shell can form in particles larger than 2 nm when the solute depletion rate from the core is greater than solute diffusion rate from the oxide/matrix interface during the crystallization process; a particle smaller than 2 nm remains amorphous [Hsuing 2010].

Many other studies such as Alinger *et al.* [Alinger 2009], which do not demonstrate the core/shell structure, have similar formation steps. These involve the fragmentation and dissolution of the Y and O in the Fe alloy powder matrix in the mechanical alloying (MA) processes followed by precipitation during the consolidation stage and an eventual nucleation at high thermo-mechanical heat treatment temperatures.

1.2.6.2 Kinetic pathway of nanoparticle formation

The above investigations illustrate the global steps leading to the formation of the nanoparticles in ODS steels but do not demonstrate the early formation steps or kinetic pathway for the formation of these particles. Understanding the kinetic pathway for the precipitation of these oxides in ODS steels would help to optimize the processing methods and the performance of these steels at the required extreme environments.

With this in mind, Hin *et al.* [Hin 2009,2010,2011] have investigated the homogeneous precipitation of oxides in Fe-Y-O and Fe-Ti-O alloys during anisothermal heat treatments. Their investigations were performed using Kinetic Monte Carlo simulations based on parameters obtained with density-functional theory (DFT) in the local density approximation and experimental data. They used a rigid lattice model with a simple cubic symmetry and a lattice parameter of α-Fe. In this way, the Y and Ti as well as the Fe atoms are positioned at the substitutional lattice sites and the O atoms positioned at the octahedral sites. The interaction energies between a pair of the species are assigned up to the fourth nearest neighbour. The kinetics in this alloy is predicted using a model where, the diffusion of Fe and Y atoms occur by a mechanism in which atoms exchange position with a vacancy V located on the first nearest-neighbour, O atoms can diffuse directly onto any of the free nearest neighbour octahedral sites and the jump frequency is a thermally activated process. A stoichiometric Y_2O_3 phase coherent with the matrix can be constructed from the lattice. The

simulations predict different kinetic behaviours, including transient precipitation of metastable iron oxides followed by precipitation of Y_2O_3 or Ti_2O_3. In the case of Fe-Y-O ternary alloys, rapid diffusion of O with respect to Y could be the driving force for iron oxides precipitation. For the isothermal heat treatment, the formation of Fe_2O_3 is followed by the nucleation of Y_2O_3 precipitates, which occurs in the Fe_2O_3. A phase $Fe_xY_{2-x}O_3$ subsequently grows with an increase in Y content and a decrease in Fe content. The anisothermal heat treatment reveals the formation of a large number of very small Fe_2O_3 precipitates and Y-O dimers during the initial stages of heat treatment. The iron-oxides precipitates and the dimers dissolve. The nucleation of Y_2O_3 precipitates mainly occurs within the Fe_2O_3 precipitates and this is followed by the growth and coarsening type reaction of the $Fe_xY_{2-x}O_3$ precipitates, which are usually more enriched in Y. The kinetic path for the development of the stable Y_2O_3 phase therefore is:

$$Fe_2O_3 \rightarrow Fe_xY_{2-x}O_3 \rightarrow Y_2O_3$$

The Fe-Y-O system reaches the coarsening type reaction at 1125 K.

However, in the case of Fe-Ti-O ternary alloys, a similar model can be used to prescribe the formation of Ti_2O_3 precipitates. The significant difference however between the two is the fact that the precipitation kinetic may have already reached a plateau at 1125 K for the Fe-Ti-O alloys whilst the Fe-Y-O system may have only reached the coarsening type reaction. The difference was attributed to the fact that the Ti diffusion coefficient is much higher than the Y diffusion co-efficient by a factor of about 10^5 [Hin 2011].

In a similar study by DFT calculations, Jiang *et al.* [Jiang 2009] studied the atomic scale energies, structures and formation mechanisms of dissolved Y, Ti, and O solutes and small amount of Y-Ti-O nanoclusters in a bcc Fe lattice. They predicted that Y-Ti-O nanocluster formation could be achieved without the assistance or help of any pre-existing vacancies. This assertion was based on the fact that the excess vacancies are not a persistent thermodynamic-energetic constituent of the Fe-Y-Ti-O system and will thus quickly annihilate at dislocations during high temperature powder consolidation.

A stark contrast to this was the work performed by Fu *et al.* [Fu 2007] who predicted that the basic mechanism leading to the formation of nanoclusters in defect-containing Fe systems is by a vacancy mechanism for the nucleation of stable O-enriched nanoclusters. The O has a high formation energy showing very little solubility. The O presents a high affinity towards vacancies and which reduces the formation energy for the O-vacancy pair. The driving force therefore for the formation of nanoclusters is the O-vacancy cluster mechanism, which enables the nucleation of O-enriched nanoclusters. These nanoclusters will eventually attract the solutes (Y and Ti) with high affinities for O leading to the formation of Y-Ti-O nanoclusters.

Monte Carlo simulations by Claisse *et al.* [Claisse 2013] serves as a bridge between the two previous investigations where they reported that indeed a vacancy is not needed to attain stability, but can increase considerably the binding energy. Additionally, they stated that Y and O bind strongly to a vacancy in the 1NN position and this results in a low diffusion of Y in Fe. In more recent investigations, Bocquet *et al.* [Bocquet 2017] stated that due to this strong affinity and a high binding energy between the Y-V pair, the energy is so high that even though the size of Y is reasonably big, the pair formation is no longer stable. This pairwise interaction may relax spontaneously towards a new configuration where the atom of the Y may have to sit in the middle of two vacancies. This information is supported by work carried out by Mastrikov *et al.* [Mastrikov 2018] where they indicated by ab initio VASP calculations

that indeed the Y solute atoms could be stabilized by vacancies in the Fe matrix. Most investigations including experimental and simulation techniques appear to point out the fact that the strong interaction between Y and vacancies as well as O could be the driving force and the basis for the formation of any nano-oxide particles in ODS steels.

In addition, experimental investigations into the precipitation mechanisms of these nanoparticles by Ribis *et al.* [Ribis 2017] predicted that the nanoparticle formation evolves through a three steps formation process: (i) The formation of Y-, Ti-, Cr- non-stoichiometric oxide, (ii) annealing results in the formation of stoichiometric $Y_2Ti_2O_7$ with a Cr enriched shell and (iii) enhanced annealing at 1300°C results in the disappearance of the Cr enriched shell.

1.3 The use of Ion beam synthesis for understanding the first formation stages

Until now, it is quite evident that there is no consensus on the mechanisms leading to the formation of the nanoparticles. Ion beam synthesis is envisaged as an alternative method of fabrication of ODS steels. This approach involves ion implantation of desirable ions (i.e. Y, Ti, O) into a solid target (in this case a high purity FeCr sample) typically at room temperature followed by a subsequent high-temperature heat treatment. The ion beam synthesis has been widely used as a powerful technique in recent times mainly in the electronics industry for the modification of the subsurface of solids. This technique comes in handy due to the fact that the implantation concentrations, depth of implantation and many other implemented parameters can be effectively controlled making it possible to decorrelate the influence of the various factors employed. The formation of a new precipitation phase in the form of nanocluster arrays or subsurface layers are facilitated after the high-temperature heat treatment. Hence, a direction implantation of Y, Ti, O ions into a high purity FeCr alloy could be an ideal means of synthesizing Y,Ti oxides in ODS steels.

Even though such a technique may not be feasible on a large scale fabrication, this method is seen as one that could provide relevant information on the mechanisms of the nanoparticle formation as well as information useful to optimize the fabrication schemes. A first attempt of such a technique to synthesize ODS particles was by Sakuma *et al.* [Sakuma 2004] where Y and O co-implantation is used as a substitute for the MA technique. The Y and O ions directly implanted to the ferritic base matrix creates an oversaturated solid solution of the implanted ions. A subsequent annealing at high temperatures may induce the precipitation and nucleation of a dense distribution of homogeneous nano-oxide particles. More recently, Zheng *et al.* [Zheng 2014, 2015 and 2017] performed an implantation of Al and O ions into a high purity FeCr sample where nanoparticles were observed directly after implantation with an fcc crystal structure and a Al-Cr-O composition. Annealing at a high temperature of 500°C resulted in the growth in the size of the nanoparticles whilst maintaining a similar Al-Cr-O composition. These clusters were however predicted to possess a possible corundum hexagonal crystal structure. The cost of such a technique may be quite expensive depending on the availability of facilities and the cost of fabricating enough samples. However, the huge advantages of such a technique on understanding the physics behind the formation of these metallic nano-oxide cannot be discounted.

1.3.1 Ion implantation/irradiation process

Ion implantation process involves the acceleration of ions through an electric field and their impact into a solid target. During the process, as each ion passes through the target, a variety of interactions may occur due to ion-solid interactions. When the energetic ion goes through a target, its energy may be lost because of elastic or inelastic collisions. Elastic collision takes place when the incident ion interacts with the target atom such that the total kinetic energy remains constant. This causes the displacement of atoms from their equilibrium position in the solid target. Inelastic collision occurs between the incident ions and the bound electrons causing an excitation of the bound electrons. The energy of the incident ion is critical to determine whether or not atom will be displaced. Kinchin *et al.* [Kinchin 1995] put in brief the various interactions for the incident Energy of the ions E_o and the threshold energy of the target or displacement energy E_d, which is defined as the minimum energy to permanently displace an atom from its lattice site leaving behind a vacancy.

If $E_o<E_d$, the implanted ion cannot displace any atoms of the target. The ion loses its kinetic energy by the vibration of the matrix of the target and the ion is stopped inside the matrix and becomes an interstitial.

If $2E_d<E_o$, the kinetic energy transferred to the target atom is sufficient, it travels through the crystal, colliding with its neighbors and displacing them from their sites. In return, they may repeat such events, leading to a collision cascade.

If $2E_d<<E_o$, the energy loss is achieved by inelastic collision and there is no atomic displacement.

If $E_d<E_o<2E_d$, the knocked atom leaves its lattice site, leaving behind a vacant site or a vacancy. The knocked atom becomes an interstitial or is recombined with a vacancy created by other atoms.

The loss of energy by the incident ions has been mentioned and the process by which these ions lose energy can be classified as: (i) direct collision with the nucleus due to the electrostatic interaction, (ii) interactions with electrons in the target and the charge exchange processes between the ion and the atoms of the target. The different processes have different contributions and the rate at which the ions lose energy and finally settle in the target can be described as the total stopping power [Rautray 2011]. The total stopping power is defined by the relation:

$$\frac{dE}{dx} = \left(\frac{dE}{dx}\right)_{nucl.} + \left(\frac{dE}{dx}\right)_{elec.} + \left(\frac{dE}{dx}\right)_{exch.}$$

Where $\left(\frac{dE}{dx}\right)_{nucl.}$ is the nuclear stopping power which describes the interaction between ions and atoms of the target,

$\left(\frac{dE}{dx}\right)_{elec.}$ is the electron stopping power, which describes the interaction between the ions and the electrons of the solid and,

$\left(\frac{dE}{dx}\right)_{exch.}$ is related to the charge exchange between the ions and atoms of the target.

The ions travel a path by the various prescribed processes until it comes to rest. When the array of ions is incident on the target, the distance travelled between successive collisions and the energy transfer varies from one ion to another. As a consequence, all the incident ions of

a given type and energy do not travel the exact same distance within the target material. Hence, if the initial energy of the incident ion is E_o, the total path by which the ions travel before they are brought to a rest can be described the following relation:

$$R_{tot} = \int_0^{Eo} -\frac{dE}{(dE/dx)_{total}}$$

This equation is useful in calculating the depth of penetration of ions. Usually, for low doses, the distribution of the depth of ions is approximately a Gaussian profile and the peak represents the most probable range called the mean projected range R_p.

1.3.2 Irradiation Induced-defects

Different kinds of irradiation-induced defects are present in any crystalline lattice. These are described according to the order of dimension and include:

(i)Point defects (0D): vacancies and interstitials,

(ii) Line defects (1D): dislocation lines,

(iii) Planar defects (2D): dislocation loops and

(iv) volume defects (3D): voids, bubbles, stacking fault tetrahedra.

The most basic types of these defects are essentially point defects and these play a role in the effects of irradiation of materials. In the following sections, focus will be based on the point defects in materials.

Interstitials: Interstitial atoms are located in a position of a crystal that is not a regular lattice. Since our raw material is a *bcc* FeCr base matrix, we will only discuss interstitials in *bcc* crystal lattices. There are two main classifications of interstitials in *bcc* crystal lattices. These are the octahedral and tetrahedral interstitial sites. For the *bcc* lattice, the atoms reside at the corners of the unit cell with one in the centre of the cell giving a total of two atoms per unit cell *i.e.* 1 + 8 corner sites x 1/8 site/unit cell = 2 sites. The octahedral interstitial sites are located at the faces and the edges of the unit cell giving 6 faces x ½ site per face + 12 edges x ¼ sites per edge = 6 sites per unit cell. The tetrahedral interstitial sites are located on the faces and in the corners of the faces. There are 6 faces x 4 locations per face x ½ sites/face = 12 tetrahedral sites. The simplistic description of the interstitials does fully present the stable configuration of self-interstitial atoms (SIA) in metals. The stable configuration of self-interstitial atoms in metals is the dumbbell or split-interstitial configuration where two atoms are associated with or share a sinle lattice site [Was 2007]. The core of the atoms repels each other and the atoms arrange themselves in the lowest energy orientation which is the <100> direction for *bcc* lattice. In order to accommodate two atoms in one lattice site, the atoms adjacent to the dumbbell are displaced slightly off their lattice positions, which then disrupts the neighbouring atoms.

Vacancies: Vacancy describes the defect where an atom is missing from its lattice site. It is possible for vacancies to bind to an oversize impurity atom or an oversize solute atom to ensure that the overall free energy of the matrix is lowered. The solutes can serve as efficient trap sites for these vacancies in the lattice or vice versa.

The matrix atoms as well as the solute atoms can take random jumps via the defects in their vicinity. Such jumps for the matrix atoms describe the self-diffusion of the matrix and similar

jumps by the impurities or solute atoms are described as heterodiffusion. The diffusion of atoms is usually driven by forces such as temperature or stress.

1.3.3 The Macroscopic Description of Diffusion

The macroscopic description of diffusion is governed by two fundamental laws as derived by Fick. The first law defines the relationship between the flux, J and the concentration gradient of the diffusing species. This is given by the relation:

$$J = -D\nabla \mathrm{C}$$

Where D is the diffusion coefficient and $\boldsymbol{\nabla}$C is the composition gradient. Expressing this diffusion in one dimension gives the relation:

$$J = -D\frac{\partial C}{\partial x}$$

Where the negative sign shows that the diffusion takes place in the decreasing direction to the concentration of the diffusing species.

The second law by Fick expresses the relation between the concentration gradient and the rate of change of concentration as caused by the diffusion at a specific point within the system. The relation gives:

$$\frac{\partial C}{\partial t} = -\nabla . D\nabla \boldsymbol{C}$$

In one dimension, this expression can be simplified to:

$$\frac{\partial C}{\partial t} = -D\frac{\partial^2 C}{\partial x^2}$$

1.3.4 The Microscopic Description of Diffusion

The description of diffusion by Fick on the microscopic level works quite well. However, in our investigation, it could be ideal to understand diffusion at the microscopic level as well. The diffusion is driven by the nature of the diffusing species and the host lattice. The mechanism of diffusion which basically describes am elementary act of a jump of an atom from one stable position to another in the lattice can therefore be different. The mechanism may or may not require the presence of defects to occur. A quick description of the different diffusion mechanisms will now be presented.

The exchange and ring mechanism: This mechanism involves the exchange of two atoms from their lattice positions located in adjacent crystal sites. Such a mechanism does not require the presence of defects and may be highly unlikely in close packed crystals since this may require considerable deformation and a high activation energy.

Interstitial mechanism: The interstitial mechanism entails the movement of any atom from one interstitial position to another. Here, considerable energy is required in order to force its way through the barrier atoms, which are separating the interstitial sites in the crystal structure. In practice, this type of mechanism occurs in the presence of diffusing species which have a size smaller that the atoms of the host lattice. In a similar fashion, there is also a mechanism known as the interstitialcy mechanism (indirect interstitial mechanism) and this is quite similar to the interstitial mechanism in that a lattice atom is displaced to an interstitial

site by an interstitial atom (two jumps are required to move the atom from one interstitial site to another). The only difference is that the diameters of the atoms are comparable in this interstitialcy mechanism. Another interstitial mechanism is the Dumbbell interstitial mechanism. This mechanism involves the symmetrical placement of an interstitial atom and a lattice atom about a simple lattice site such that they share the lattice site [Was 2007].

Vacancy mechanism: The vacancy mechanism describes the simplest form of diffusion and this occurs in metals and alloys. The diffusion involves the jump of an atom from the lattice site to a vacant site. The presence of vacancies is required for such a movement of the atom to a neighbouring vacancy to occur. Vacancy movement is opposite that of the atom and hence, the vacancy-type diffusion is regarded as either a movement of the atom or a movement of the vacancy.

The diffusivity as described by the two main mechanisms are different in detail but can both be described similarly in the form of two factors : the first is a constant that is independent of temperature and the other is an exponential of the temperature containing an energy term. The readership is advised to revisit [Was 2007] for detailed description and elaboration of the two factors. The diffusivities can be written using an Arrhenius equation of the form:

$$D = D_o \exp\left(\frac{-Q}{kT}\right)$$

Where D is the diffusivity or diffusion coefficient, D_o is the temperature independent term, Q is the activation energy, k is the Boltzmann constant and T is the temperature.

The activation energy varies for the two mechanisms of diffusion. It should however be noted that the diffusion of an atom via a defect mechanism is different from the pure diffusion of the point defect. For example for a lattice atom diffusing by the vacancy mechanism, such a diffusion is different from the pure vacancy diffusion (which is also referred to as the vacancy self-diffusion). The activation energy for the diffusion of atoms in the crystal therefore depends on both the energy of the formation of the defects and the energy required for the migration of the defect in the lattice structure.

Hence for a vacancy diffusion,

$Q_v = E_m^v$ where E_m^v is the energy for vacancy migration. The pure vacancy diffusion coefficient is given by the relation: $D = D_o \exp(\frac{-E_m^v}{kT})$

And for the vacancy self-diffusion,

$Q_a^v = E_f^v + E_m^v$ where E_f^v is the vacancy formation energy. The vacancy self-diffusion coefficient is given by the relation:

$$D = D_o \exp(\frac{-(E_m^v + E_f^v)}{kT})$$

Similarly for an interstitial diffusion,

$Q_i = E_m^i$ where E_m^i is the energy for the interstitials migration. The pure interstitial diffusion coefficient is given by the relation: $D = D_o \exp(\frac{-E_m^i}{kT})$

And for the interstitial self-diffusion,

$Q_a^i = E_f^i + E_m^i$ where E_f^i is the interstitial formation energy. The interstitial self-diffusion coefficient is given by the relation: $D = D_o \exp(\frac{-(E_m^i + E_f^i)}{kT})$

1.3.5 Radiation-Enhanced Diffusion

Irradiation creates excess of point defects. These defects can however be lost either by the recombination of vacancies and interstitials or they can be lost to a defect sink (i.e. void, dislocation, dislocation loop, precipitate, grain boundary or a surface). The total concentration of the point defects in the lattice at any point in time is described as a balance between the production rate and the rate of loss of the point defects. These competing processes can be described by thermodynamics diffusion equations expressed as:

$$\frac{dC_v}{dt} = K_0 - K_{iv}C_iC_v - K_{vs}C_vC_s \quad (1)$$

$$\frac{dC_i}{dt} = K_0 - K_{iv}C_iC_v - K_{is}C_iC_s \quad (2)$$

Where C_v is the vacancy concentration, C_i is the interstitial concentration, K_0 is the defect production rate, K_{iv} is the vacancy-interstitial recombination rate coefficient, K_{vs} is the vacancy-sink recombination rate coefficient and K_{is} is the interstitial-sink recombination rate coefficient.

The solutions of the two equations have been developed analytically and described for different conditions [Was 2007]. The concentrations of the defects initially increase linearly with $C_v = C_i = K_0t$. Based on conditions such as the sink density and the temperature, the evolution of the defect concentration will experience different regimes including mutual recombination, vacancy annihilation contributed by sinks, and interstitial annihilation contributed by sinks. The steady-state vacancy and interstitial concentrations can be solved if it is assumed that the sink strength for both vacancies and interstitials are the same (i.e. no preferential absorption of any type of defect at the sink). The steady state equations for the vacancies and the interstitials can be given as:

$$0 = K_0 - K_{iv}C_iC_v - K'_{vs}D_vC_vC_s \quad (3)$$

$$0 = K_0 - K_{iv}C_iC_v - K'_{is}D_iC_iC_s \quad (4)$$

Where $K_{vs} \propto D_v$ and $K_{is} \propto D_i$ and these K terms can be written as $K = K'D$.

The equations (3) and (4) mean that the vacancies and interstitials contribute the same amount to the diffusion of the atom. If the $K'_{vs} \approx K'_{is}$, then:

$$D_vC_v = D_iC_i$$

The steady-state equation has shown that the contribution of the vacancies and interstitials to the atom mobility is equal even though the concentration of interstitials are much lower than the concentration of vacancies. This is due to the fact that the interstitials have a faster diffusion rate compared to the vacancies and therefore ensure equal contribution. When addressing real metals, the K_{vs} and the K_{is} are not the same. Different sinks (i.e. dislocations and precipitates) have a bias for certain types of point defects which then allow the sinks to grow.

For pure materials such as metals, the diffusivity under radiation is expressed by the relation:

$$D_{rad} = D_v C_v + D_i C_i$$

The concentration of vacancies and interstitials produced during irradiation conditions is much higher than the ones produced thermally [Sickafus 2007]. Hence, the radiation enhanced diffusion coefficients are much higher than the thermal diffusion coefficients.

1.3.6 Interaction between implanted elements (Ti, Y, O) and vacancies in *bcc* Fe

The diffusion and/or mobility of the solute atoms and point defects depend on the factors such as the temperature and concentration gradient as mentioned in section 1.3.4. The binding energy between the solute atoms and different species including vacancies may also affect the diffusivity of these atoms in the FeCr matrix. These binding energies may be useful to understand the first stages of clustering and give information on the stability of the clusters

For the impurity atoms in this investigation (i.e. Y, Ti O) atoms in an FeCr *bcc* lattice, theoretical calculations have suggested that the most stable configuration for an interstitial Y and Ti atom is the substitutional positions in the *bcc* Fe. Meanwhile, the stable configuration for an interstitial O atom is the octahedral position [Jiang 2009, Murali 2010, Murali 2013].

The solute atoms interact with themselves as well as with vacancies. Several studies have investigated the various pairwise interactions between solute atoms, vacancies and O. The *Table 1.4* shows the binding energies for various pairwise interactions between the solute atoms and vacancies and oxygen for the first nearest neighbour (1nn) and the second nearest neighbour (2nn) distances. The strongest binding energies are recorded for the O-V, Y-V (1nn) and Y-O (2nn) interactions. The Ti and Cr binding energies with vacancies and O is relatively low. Elsewhere, the binding energies between the pairwise metallic impurity atoms and Cr (i.e. Cr-Cr, Cr-Ti, Cr-Y, Ti-Ti and Ti-Y) are all negative showing repulsive interaction. The only pairwise attraction is recorded in the 2nn for the Y-Y interaction (not shown). From the various binding energies between various pairwise interactions, it is evident that strong O-V, Y-V and Y-O binding energies could contribute to the early stages of nano-oxide clustering keeping these clusters bonded in ODS steels.

Pairwise species	Binding energy (eV) (Murali 2010)	
	1nn	2nn
O-V	1.65	0.75
Y-V	1.45	0.26
Ti-V	0.26	0.16
Cr-V	0.05	0.02
Y-O	-0.35	1.01
Ti-O	0.26	0.55
Cr-O	0.25	-0.02

Cr-Cr	-0.21	-0.13
Cr-Ti	-0.15	-0.11
Cr-Y	-0.16	-0.15

Table 1.4 Binding energies between various pairwise species of the solute atoms and vacancies

Increasing the number of species in the clusters containing oxygen and vacancies increases significantly the binding energy of the species [Murali 2010]. The *Table 1.5* from Murali *et al.* shows the significant increase in binding of the species with more constituents. Such very high binding energies could make the clusters very stable while serving as nucleation sites for the potential growth and nucleation of the clusters.

Pairwise species	Binding energy (eV) [Murali 2010]
Ti-O-V	2.45
Y-V-O	3.35
Ti-Y-V-O	4.10
$Y_2O_4V_2$	8.70
$Y_2O_4V_2Ti_4$	12.50

Table 1.5 Binding energies between triple and quadriple species of the solute atoms and vacancies

1.4 Factors driving the nanoparticle formation

Until now, several factors appear to influence tremendously the formation of the nanoclusters in the FeCr alloys. These factors directly and indirectly affect the precipitation and/or nucleation of clusters in our typical FeCr samples. Some of the factors that are critical to the formation of clusters within the FeCr samples include the defect creation as well as the binding energies between the implanted elements, matrix components and the defects created, as developed in the previous section. The diffusivity and concentration of the implanted and alloy elements also affects the kinetics of the cluster formation. The material under irradiation is usually far from thermodynamic equilibrium and phases that are not stable or metastable under equilibrium may form. At elevated temperatures though, where atoms are significantly mobile, equilibrium phases are expected. The formation of a particle with an interface also requires the system to overcome an energy barrier for nucleation that includes the interfacial energy and the change in volume free energy associated with precipitation. Some of the factors that are or may be relevant to explain the nanoparticle formation, and which were not developed up to here, are detailed in this section.

1.4.1 Diffusivity of the alloy elements (unirradiated materials)

The sections 1.3.3-1.3.5 illustrate in detail the role of the diffusion of solute atoms in the base alloy. Several investigations have studied the diffusion of Cr [Braun 1985, Lee 1990, Ramunni

2015], Ti [Klugkist 1995, Marali 2011], O [Takada 1986, Hin 2009, Shang 2014] and Y [Hin 2009, Murali 2011, Mock 2017] in Fe as well as the Fe self-diffusion [Hin 2009, Murali 2011]. Even though there appear to be a disparity between experimental and calculated values, the pattern of the diffusivity of the species remains constant. Y is described as a relatively large sized solute atom (46% bigger) in host Fe [Murali 2011] and possesses a low solubility, (0.046 at%) in Fe at 800°C [Li 1993]. The high binding energy of Y to O and vacancies (as stated in section 1.3.6) coupled with the large size has been reported to induce its very low mobility in Fe [Bocquet 2017]. Ti on the other hand has lower binding energies with vacancies and O. This coupled with its relatively smaller size ensures that Ti may diffuse faster than Y. O is known as the fastest diffusion species among the various alloying elements. The *Table 1.6* gives the calculated diffusivities of Fe, Cr, Ti, Y and O in Fe.

	D(Cr) (m^2s^{-1}) [Lee 1990]	D(O) (m^2s^{-1}) [Takada 1986]	D(Ti) (m^2s^{-1}) [Plugkist 1995]	D(Y) (m^2s^{-1}) [Hin 2010]
800°C	6.5×10^{-16}	1.2×10^{-11}	1.1×10^{-15}	5.4×10^{-21}
1100°C	4.2×10^{-13}	1.1×10^{-10}	1.4×10^{-12}	1.1×10^{-17}

Table 1.6 Diffusion coefficients for elements within Fe base matrix

1.4.2 Enthalpy of formation: thermodynamically stable oxide phases and affinity for oxygen

The M-O reaction is an oxidation reaction with an associated free energy. For the solute elements considered in this thesis, various oxides can be formed from the oxidation of the metallic element. The standard heat of formation, or standard enthalpy of formation, of some of the most thermodynamically stable oxides of Fe, Cr, Ti and Y are presented in the *Table 1.7* per mole of oxides, per mole of O and per mole of M-O (where M=metal and the M-O is the bond between an atom of the metallic element and oxygen). The enthalpy values are calculated at 298 K. The table is presented in a descending order towards the oxides with the more negative enthalpy of formation per mole of O, which is sometimes used to compare oxygen affinities of particular elements. However, the enthalpy of formation of oxides per mole of M-O bond is probably a more pertinent parameter to estimate the relative oxygen affinities of these elements. From this, the elements, which are more likely to attract oxygen, are Y and Ti, which also form the more thermodynamically stable oxides, i. e., those with the more negative enthalpy of formation per mole oxide.

Oxide Phase	M:O ratio	-ΔHf (kJ/mol (Oxide)) [Gale 2004]	-ΔHf (kJ/mol O)	-ΔHf (kJ/mol of M-O bond)
Fe_2O_3	2:3	822	274	68
Fe_3O_4	3:4	1118	280	70
CrO_2	1:2	583	292	97
Cr_2O_3	2:3	1130	377	94

TiO_2	1:2	944	472	157
Ti_3O_5	1:1.67	2457	491	163
$YCrO_3$	2:3	1493	497	
Ti_2O_3	2:3	1522	507	127
TiO	1:1	543	543	181
$Y_2Ti_2O_7$	1:1.75	3874	553	
Y_2O_3	2:3	1907	636	159

Table 1.7 Standard enthalpy of formation at 298 K of selected pure binary and triple oxides.

1.4.3 Barrier of nucleation

The kinetics of the nanoparticle formation depends on the energy barrier for nucleation. This energy barrier for nucleation includes the change in volume free energy associated with the oxide precipitation and the energy associated with the formation of the metal-oxide interface. The cluster or precipitate formation may possess relations of orientation with the matrix. The orientation relations observed between most ODS nanoparticles and the matrix have been detailed in section 1.2.7.1: some particles were observed to be coherent, some partially coherent and others semi-coherent. The formation of coherent precipitates is usually favoured because of their lower interface energy as compared to incoherent precipitates, which lower the energy barrier and facilitate nucleation [Smallman 2007].

1.5 Objective and outline of the PhD thesis

The review of the literature up until now clearly shows that there is a tremendous amount of information available concerning ODS steels and the nanoparticles formation. There are disagreements and disparities in the various aspects relating to the nanoparticle formation. Even with the huge amount of information regarding the nanoparticle formation in ODS steels, the formation steps especially for the early stages is yet to be fully established. The nanoparticle formation in ODS steels has been achieved conventionally by the powder metallurgy method of mechanical alloying (MA). Most of the available literature are therefore based on this technique. A more recent approach by the use of another powder metallurgy technique known as Spark Plasma Sintering has been developed with initial results appearing quite similar to the MA conventional technique.

This thesis is aimed at implementation of the ion beam synthesis (described in section 1.3) to synthesize (Y,Ti) oxides in FeCr model high-purity steels and eventually get some relevant information that could help understand the mechanisms of the nanoparticle formation. The ion implantation technique is supposed to experimentally simulate the ball milling technique used in conventional ODS steels fabrication by introducing metallic elements and oxygen as well as point defects in an Fe10wt%Cr matrix. Similarly to the high-temperature consolidation techniques that follow ball milling in conventional ODS steels fabrication, thermal annealing

are performed after ion implantation. In this approach, we will follow two different modes as sketched in *Figure 1.18*.

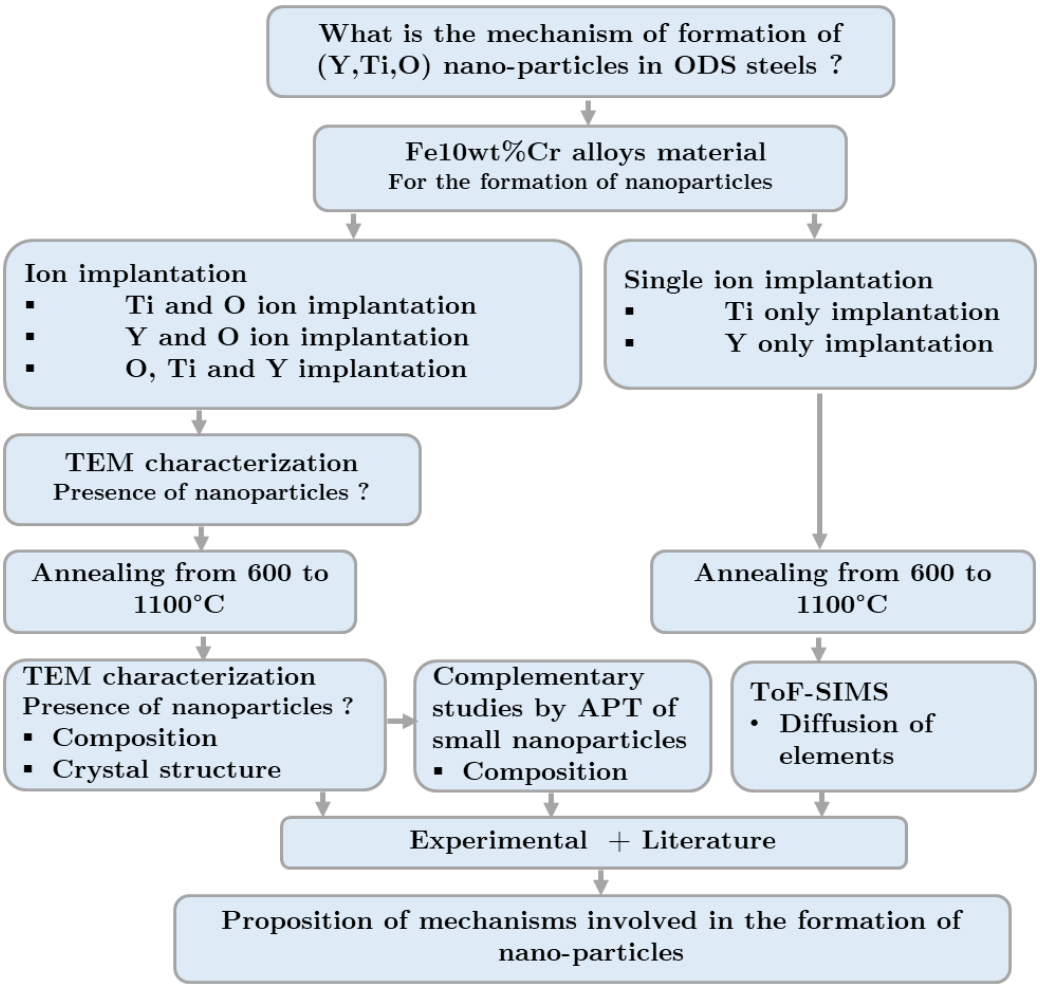

Figure 1.18 Schematic representation of the experimental approach implemented in this study.

The first mode is to understand how the various solutes elements (i.e. Y and Ti) diffuse in the FeCr high purity based matrix. Here, we directly implant Y and Ti ions into the matrix at room temperature followed by high temperature annealing (in the range 600°C-1100°C). The diffusion of the implanted elements in the specimens is obtained by performing Time-of-Flight Secondary Ion Mass Spectroscopy (ToF-SIMS) experiments.

The second mode involves the main work of this PhD with the synthesis of oxide nanoparticles by ion implantation and thermal annealing. We will begin with the sequential implantation of dual elements (i.e. Ti and O, and Y and O) at room temperature followed by high temperature annealing. A final step involves the sequential implantation of all three elements (i.e. Y, Ti, O) at room temperature followed by high-temperature annealing. Characterization of the possible oxide formation in these conditions is achieved by various Transmission Electron Microscopy (TEM) techniques as well as Atomic Probe Tomography (APT).

The main principles of experimental techniques used during this study are developed in the following chapter.

Chapter 2 Experimental Approach

2. Experimental Approach

2.1 The as received material

Nanoparticle formation in ODS steels is based on ferritic-martensitic steels with 9-12%Cr (see section 1.1.3.2). These steels have adequate corrosion resistance at elevated temperatures and makes them ideal structural materials for advanced nuclear applications. These steels may contain several different alloying elements and the effects of some of the alloying elements can be found in section 1.2.2. The minor alloying elements have been identified to contribute to the formation of varied nanoparticles. To eliminate any contribution of these minor alloying elements, a high purity FeCr alloy with approximately 10wt%Cr has been obtained for use. The as-received bulk material was provided by École Nationale Supérieure des Mines, Saint Etienne, France. The nominal compositions of the as-received bulk material are given in the *Table 2.1* with composition of 90.14wt% (89.46 at%) for Fe and 9.86wt% (10.54 at%) for Cr, which represent the major elements. The minor elements or impurities are expected to have a composition of next to zero wt%.

Elements	Fe	Cr	C	N	O	S	Others
wt%	90.14	9.86	≤0.001	≤0.001	≤0.001	≤0.001	<0.001

Table 2.1 Nominal compositions of the high purity FeCr alloy as provided by the supplier

The goal in ODS steel fabrication is to produce a homogenous distribution of nanoparticles and as fine as possible the size of the nanoparticles. Among the various characterization techniques used in ODS nanoparticle studies (as given in section 1.2.5.2), Transmission Electron Microscopy (TEM) gives not only information about the composition of the nanoparticles, but also precise information about the nature and structure of the nanoparticles. TEM has therefore been adopted and used to obtain information relating to the chemical composition and crystallographic structure of the nanoparticles if any are formed in the high purity Fe10wt%Cr alloy samples. In addition, two techniques, namely; Time-of Flight Secondary Ion Mass Spectroscopy (ToF-SIMS) and Atom Probe Tomography (APT), have been implemented to obtain complementary information relating to the nanoparticle formation. The ToF-SIMS has been used to gain information relating to the diffusion and mobility of the implanted elements within the material at different conditions. The APT technique has also been adopted to investigate the composition of minute nanoparticles which remain quite difficult to characterize by TEM.

2.2 Transmission electron microscopy

Characterization by the use of Transmission Electron Microscope (TEM) has been performed on the as-received material, the as-implanted samples as well as the implanted and annealed samples to investigate the nanoparticle formation. Four different TEMs have been employed in this study (the two main TEMs are pictured in *Figure 2.1*):

• *FEI Tecnai G² 20 twin* LaB6 filament operating at 200 kV, equipped with an EDX spectrometer and a Gatan Image Filter (GIF) located at CSNSM/JANNuS-Orsay, France [CSNSM/TEM, Website]. The Tecnai G^2 20 twin microscope was used to perform both conventional and analytical characterization (mostly EFTEM).

• *JEOL 2010F* field emission gun (FEG) operating at 200 kV, equipped with an EDX spectrometer and an EEL spectrometry at CEA-SRMA, Saclay, France. HRTEM structural characterizations were performed with this TEM.

Two additional microscopes, an *FEI Titan 80-300 X-FEG* with Cs aberration correction, equipped with a SuperX EDX and a *Talos FX200* also equipped with a SuperX EDX located at the Mat. Sci. Dept. of North Carolina State University, Raleigh, USA, were used for STEM-EDX elemental mapping in ChemiSTEM mode.

The main principles of the different techniques used related to TEM are explained in the following paragraphs.

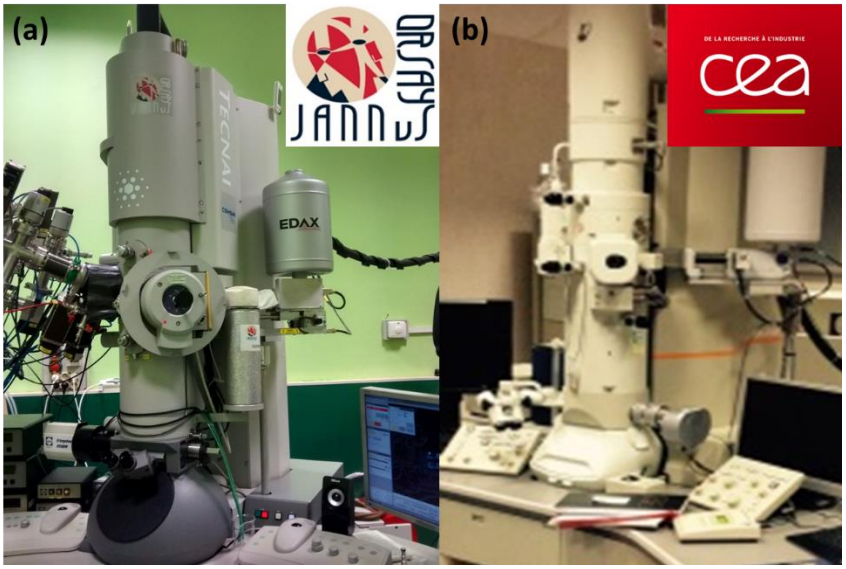

Figure 2.1 Images of the two main TEMs used in the investigation of samples in this study.

2.2.1 Interaction of Electrons with matter and the General TEM Operating Principle

In a TEM, an electron beam is accelerated and impinges on sample that is typically a few tens of nm thick, allowing the electron beam to go through and be investigated. The collision between the electron beam and the sample produces various interaction mechanisms. The versatility of electron microscopy and associated analysis techniques is derived in large measure from these different interactions that the beam undergoes in the specimen.

The components of a TEM can basically be summarised as: the emission source or illumination source, the objective lens/stage and a viewing screen or Imaging system. In an extremely brief description, the illumination source comprises the electron gun and the condenser lenses. Here, electrons are generated from a source (usually W or LaB_6) and accelerated to an energy usually ranging between 100 and 300 kV in the gun. The electron beam by the aide of magnetic coils, is aided to pass through a set of condenser lenses in order to have a beam of a desired diameter. This is then directed to the objective lens and specimen holder system. The specimen holder system is where all the various interactions take place and details relating to the nature of the specimen can be obtained. These details are then magnified for viewing in the viewing screen. In the imaging screen, various types of lenses are used for magnifying the image according to

the image mode. A phosphorous viewing screen connected to a detector and a computer is then used for viewing, capturing and recording the images.

2.2.2 Conventional TEM Methods : SAED, BF, DF, WBDF

2.2.2.1 Selected Area Electron Diffraction (SAED)

In electron microscopy, the energy of the electron beam is high enough to easily traverse the thin foil. The periodic structure of crystalline materials acts as a diffraction grating, thus diffracting the beam at particular angles. These angles are defined by the Bragg's Law:

$$\lambda = 2_{dhkl} \sin \vartheta$$

Where λ is the wavelength of the electron beam, d_{hkl} is the spacing between the hkl planes in the atomic lattice and ϑ is the scattering angle. The diffraction pattern on the imaging screen is a series of spots, each spot corresponding to a specific atomic spacing d_{hkl} (family of planes (hkl)) apart from the central intense spot corresponding to the electrons that have not been deflected (direct beam). This pattern can yield information about the orientation, atomic arrangements and the phases present in the sample under investigation. In order to view a diffraction pattern, the objective stage of the microscope with the lenses are adjusted in such a way that the back focal plane of the objective lens acts as the object plane for the intermediate lens. Hence, the observed pattern is projected onto the phosphorous or viewing screen. A selected area aperture is inserted to acquire a selected area electron diffraction (SAED) pattern of a region of interest. The smallest SAED aperture of the microscope at CSNSM (Tecnai JANNuS-Orsay) can select a region of approximately 300 nm. From the Bragg's equation (given above), at low scattering angles, it is possible to deduce an equation, which enables to obtain interplanar distances:

$$\lambda \text{ x } L = D_{hkl} \text{ x } d_{hkl}$$

Where λ x L is the camera constant or camera length which is dependent on the TEM microscope and D_{hkl} is the distance measured between the direct spot and the (hkl) diffraction spot in the diffraction pattern.

2.2.2.2 Bright Field (BF) and Dark Field (DF) Imaging

In BF TEM imaging, an objective aperture is inserted to select only the direct beam (usually centred). In this case, diffracted beams are blocked by the aperture (as illustrated in *Figure 2.2(a)*). Regions of the specimen of high scattering appear dark indicating regions of high mass, thickness or strong diffraction effects. On the other hand, in dark field imaging, the image is formed with the electrons scattered in a specific direction usually as a result of diffraction from a particular atomic plane or planes. The direct and most intense beam is blocked and only one diffracted beam is allowed to pass through the objective aperture (as in *Figure 2.2(b)*). The image can easily be distorted by aberrations and hence, the objective aperture remains centred whilst the incident beam and the optical axis is tilted to ensure that the scattering angle between the incident beam and the diffracted beam is not changed. The regions of high intensity represent strong scattering. The diffracted beams have strongly interacted with the specimen and hence DF images provide valuable information about nanoparticle formation or other defects creation.

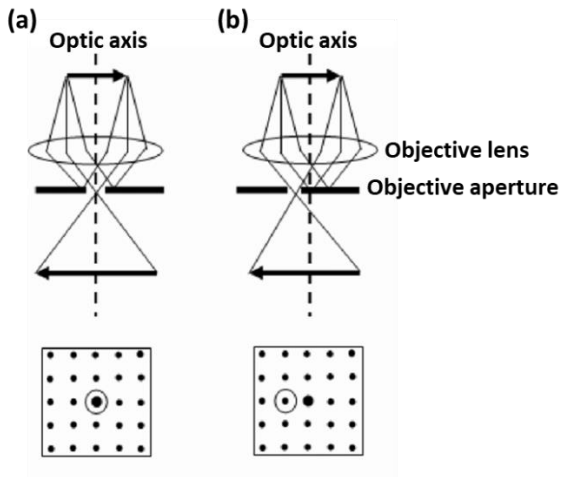

Figure 2.2 Schematic illustration of conventional TEM (a) Bright Field (BF) and (b) Dark Field (DF) imaging [Goo 2007].

Images formed in these conditions are usually taken close to focus. There is however useful information that can be acquired and certain technical advantages obtained in operating out of focus. The defocus value is dependent on the strength given to the objective lens:

- If the strength of the lens is increased such that the image is formed above (i.e. before the rays get to) the image plane, then the image will be out of focus and the lens is described as *overfocused*.
- On the contrary, if the lens is weakened and the image is formed below (i.e. after) the image plane, the image is described as being out of focus and the lens *underfocused*.

It is well known that cavities are invisible when the image is in focus, but can be observed out of focus. The oxide precipitates formed by ion implantation in the present study can be imaged in a similar way and present similar contrast to cavities.

2.2.2.3 Weak Beam Dark Field (WBDF) imaging

This imaging technique is used notably for marking sharp images of dislocation lines and resolving pairs of dislocations or loops. The first and most important aspect of this imaging technique is to orient the specimen in a good two-beam condition. Two-beam condition occurs when the specimen is tilted so that only one diffracted beam (reflection g), is strong and the other strong spot in the diffraction pattern is the direct beam. In order to make a WBDF image, the crystal is tilted to a large, positive value of excitation error s ($s>>0$) where the diffraction is weak (the exact Bragg condition corresponds to $s = 0$). The procedure for obtaining a WBDF image in (g, 3g) condition is summarized as follows : orientating the specimen in a two-beam condition and exciting the appropriate diffraction spot of reflection g, then tilting the incident beam until the position of the diffraction spot moves to the position of the direct beam. The diffraction spot becomes weak ($s>>0$) and the strong diffraction spot is now the 3g spot (Bragg condition exactly satisfied). The image is formed by selecting the diffraction spot of the reflection g with the objective aperture. With the increasing value of the excitation error, the defects observed in the DF image may be much sharper whilst the contrast of the DF image is much weaker. This imaging method allows dislocation and dislocation loops to be observed as sharp bright lines and bright rings/loops, respectively.

2.2.3 Analytical Chemical Composition Characterization techniques

2.2.3.1 Energy Dispersive X-ray spectroscopy (EDX)

Energy-dispersive X-ray spectroscopy (EDX, EDS, EDXS or XEDS) is a quantitative and qualitative X-ray microanalytical technique which provides information on the chemical composition of a sample for elements with an atomic number Z >3. In EDX, the electron beam of the TEM is focused on the sample and the electrons from the primary beam penetrate the sample and interact with the atoms of the sample. Two types of X-rays result from these interactions: Bremsstrahlung X-rays, which means 'braking radiation' and are also referred to as continuum or background X-rays, and characteristic X-rays:

- Bremsstrahlung X-rays are produced by slowing down of the primary beam electrons by the electric field surrounding the nuclei of the atoms in the sample. The primary-beam electrons lose energy and change direction due to inelastic scattering in the sample. Some of the lost energy is converted to X-rays which have a range of energies. A primary beam electron may lose all of its energy in a single interaction event in which case it will produce one X-ray with energy E_o, but it is much more likely that the energy will be lost in a number of interactions in which small proportions of the initial energy are lost and an equivalent number of low-energy X-rays is produced. Although a large number of low-energy Bremsstrahlung X-rays is generated, most are absorbed within the sample or the detector and the Bremsstrahlung X-ray intensity observed in the spectrum decreases at low energy (see *Figure 2.3*).

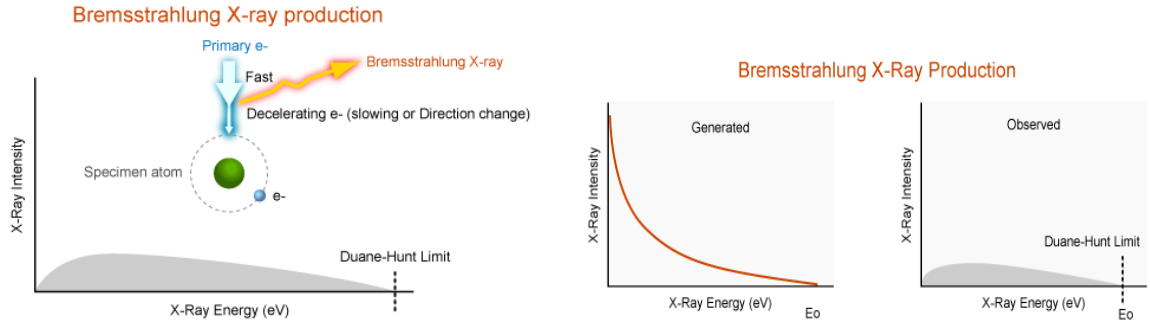

Figure 2.3 Representation of the electron beam interaction with the electric field around the atom where electrons lose part of the energy to produce Bremsstrahlung X-rays and (b) X-ray spectrum showing many X-rays are produced at lower energies but the detector may not be so sensitive [ammrf, *website*].

- Characteristic X-rays are produced by electron transitions between the electron shells. The electrons in each shell and subshell have specific ionization energies, and these are different for every element. The production of characteristic X-rays is a two-stage process: ionization followed by relaxation. Firstly, an electron is removed from one of the inner shells of the atom by an electron from the primary beam so that the atom is ionized and in an unstable state. Secondly, the atom regains stability when an electron from an outer shell fills the inner shell vacancy and an X-ray photon is emitted. The energy of the emitted X-ray is equal to the difference between the ionization energies of the electrons involved in the transition. In spectroscopy, the most commonly used naming convention for characteristic

X-ray lines is the Siegbahn notation. An illustration of this process is given in *Figure 2.4(a)*. The first component of the name is the element involved, e.g. Si. The second component is the electron shell that was ionized to produce the X-ray, e.g. K, L or M. The third component reflects the relative intensity of the line within each shell, e.g. α is the most intense line, followed by β and γ. The lines within each shell make up a family, or series, of lines for that shell, e.g., the K family comprises the Kα and Kβ X-ray lines. The spectrum seen in the output from the Energy Dispersive Spectrometer (EDS) shows the characteristic X-ray lines superimposed on the Bremsstrahlung X-rays (see *Figure 2.4(b)*).

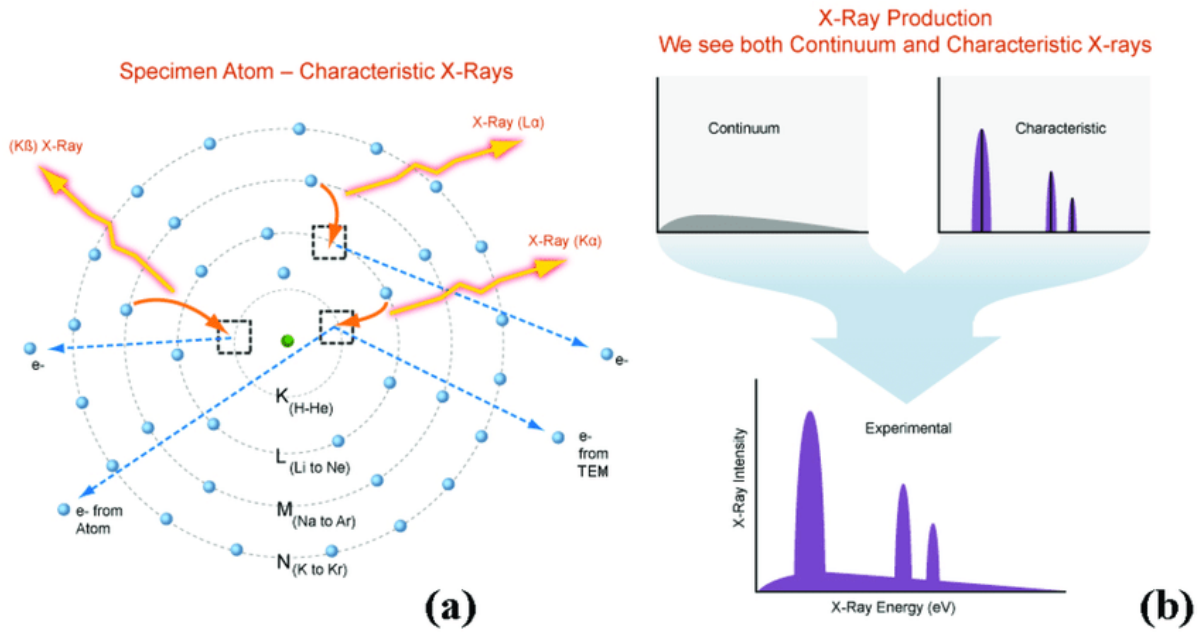

Figure 2.4 (a) The electron transitions involved in generating the Kα, Kβ, and X-ray photons from electron-atom interaction (b) The X-ray spectrum displayed by the Energy Dispersive system which comprises characteristic X-ray peaks superimposed on the continuum (Bremsstrahlung X-rays) [ammrf, *website*].

The intensity of the X-rays is proportional to the number of atoms generating the X-rays. The EDX detector measures the relative abundance of the emitted X-rays versus the energy. Detectors used are usually Si(Li) or Si drift (SDD) EDX detector. When the incident X-ray strikes the detector, it creates a charge pulse that is proportional to the energy of the X-ray. The charge pulse is converted to a voltage pulse by a charge-sensitive preamplifier. The signal is then sent to a multichannel analyser where the pulses are sorted by voltage. The energy, as determined from the voltage measurement, for each incident X-ray gives final output. The spectrum of X-ray energy versus counts is evaluated to determine the elemental composition of the specified volume. Some peaks of different elements may overlap in the spectrum. It is particularly observed for energy levels below 2.5 keV, where the main peaks are not well resolved. The identification of minor peaks of higher energy may help to confirm the presence of an element using automatic-peak identification software. In our samples, as will be again stated in the following chapter 3, the O K_α and Cr $L_{\alpha,\beta}$ peaks overlap. It is thus difficult to identify the presence of oxygen by EDX in our specimens and quantitative analysis is also compromised.

2.2.3.2 Electron Energy Loss Spectroscopy (EELS)

Electron Energy Loss Spectroscopy (EELS) is an analytical technique, which involves the measurement of the energy distribution of electrons that have passed through and interacted with the specimen and lost energy by way of inelastic scattering. EELS in most modern microscopes is quite effective and capable of giving compositional and chemical information about the sample.

TEM-EELS instrumentation is based on the magnetic prism, in which a uniform magnetic field B (of the order of 0.01 T) is generated by an electromagnet with carefully shaped polepieces, according to Egerton [Egerton 2009]. The electrons follow circular paths R within this field and are deflected through an angle of typically 90° due to Lorentz force. The sideways force of an electron is given by:

$$\mathrm{F} = \mathrm{B}ev = \mathrm{m}v^2/\mathrm{R}$$

Where e, v and m are the electron charge, speed, and relativistic mass, respectively, giving a bend radius that depends on speed and therefore on electron energy:

$$\mathrm{R} = (m/e)(1/\mathrm{B})\ v$$

The spectrometer entrance aperture size is crucial for the electrons entering the prism. The electron beam arriving through the entrance aperture originates from a point known as the spectrometer object point. The electrons of a particular energy are then returned to a single image point. All electrons that have lost no energy are collected at a single point. The bold lines in the *Figure 2.5* illustrate this. Subsequently, electrons that have lost same amount of energies are also collected at a single point. From this, a spectrum can be obtained for the various energy losses as a function of counts, which is described as the electron energy loss spectrum (EELS spectrum). The EELS spectrum is analyzed according to various scattering process. The spectrum is described according to three main energy loss regimes; zero-loss, low-loss and high-loss regions.

Zero-loss peak: The first peak, the most intense for a very thin specimen, occurs at 0 eV and is therefore called the zero-loss peak. These are basically electrons that still have the original beam energy E_0, i.e., they have only interacted elastically or not at all with the specimen. Since the zero-loss beam contains not much useful information, it is often omitted during spectrum collection. However, this enables to determine the specimen thickness. The thickness has been assessed in this experiment using the Log-ratio method. With this and following Poisson Statistics, the ratio of zero-loss electrons to the total transmitted intensity gives a relative measure of the specimen thickness [Joy 1979, Leapman 1984]. This is measured in terms of the total inelastic mean free path λ from the relation:

$$\frac{t}{\lambda} = \ln\left(\frac{I_t}{I_o}\right)$$

Where $\boldsymbol{t/\lambda}$ is the mean number of scattering events per incident electron with t the thickness and λ the mean free path of inelastic electrons while $\boldsymbol{I_o}$ and $\boldsymbol{I_t}$ are the zero-loss intensity and total intensity respectively. It is imperative to determine if the region of interest is thin enough for EELS. Typically, $t/\lambda < 1$ is a suitable region for EELS.

Low loss region (< 50eV): This region contains the electrons that have interacted with the weakly bound electrons of atoms (outer shells). In particular, it contains the electrons that have induced plasmon oscillations. Owing to the fact that the plasmon generation is the most frequent inelastic interaction of the electrons within the specimen, the intensity recorded in

this region is relatively high. The specimen thickness affects both the intensity and number of plasmon peaks in that the number of plasmon peaks and intensity increases as the specimen thickness increases.

High-Loss region (> 50 eV): For the ionization of atoms, a specific minimum energy, the critical ionization energy E_C or ionization threshold, must be transferred from the incident electron to the expelled inner-shell electron, which leads to ionization edges in the spectrum at energy losses that are characteristic of an element. Thus, EELS is complementary to X-ray spectroscopy, and it can be utilized for qualitative and quantitative element analysis as well. In particular, the possibility to detect light elements is an advantage of EELS. Compared to the plasmon generation, the inner-shell ionization is a much less probable process, leading to a low intensity of the peaks. In the high-loss region, the amount of inelastically scattered electrons drastically decreases with increasing energy loss, thus small peaks are superimposed on a strongly decreasing background. Therefore, the background to a particular ionization edge needs to be extrapolated and subtracted before EELS quantification. After this subtraction, the remaining intensity of ionization edges give a quantitative estimate of the concentration of the corresponding element.

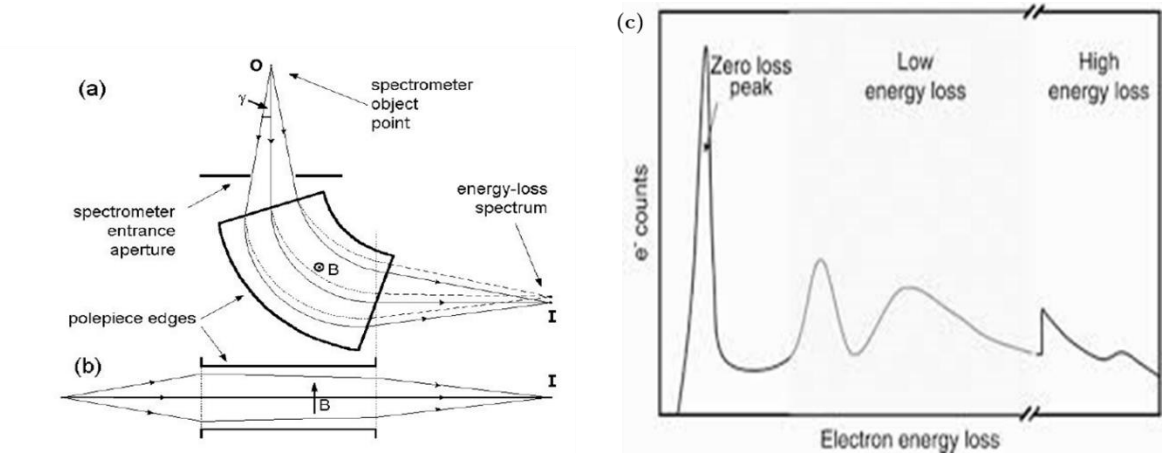

Figure 2.5 The dispersive and focusing properties of a magnetic prism (a) in a plane perpendicular to the magnetic field and (b) parallel to the field. Solid lines represent zero-loss electrons (E = 0); dashed lines represent those that have lost energy during transmission through the specimen [Egerton 2009] (c) EELS spectrum indicating the Zero-loss, Low-energy loss and high-energy loss regions.

2.2.3.3 Comparison between EDX and EELS techniques

Analytical characterization by EDX and EELS are very powerful tools in achieving detailed elemental composition of samples. No one single technique can be comprehensively complete in usage and hence both techniques can be used to complement each other. Even though both techniques are relatively easy to analyse qualitatively and their quantification could range from easy to complicated depending on how accurate results are expected, there are significant differences that enables the choice of use of a particular technique.

EDX technique is usually the easier to use and does not contaminate the specimen as much as EELS. However, the recorded energy peaks could quite easily overlap and is the worse of the two techniques regarding spatial resolution. Most importantly, during the beam interaction with the specimen, the X-rays, which provide the elemental information, travel in all directions. Only the X-ray detector ensuring a low signal collection efficiency collects a fraction of these

emitted X-rays. The EELS technique on the other hand faces no such issues. It makes use of the electrons that have passed through the sample and with the spectrometer located beneath the sample and viewing screen, most of these electrons are able to traverse and eventually arrive at the spectrometer entrance. This ensures that the EEL spectrometer possesses a better signal collection efficiency even though only a limited region of the sample of interest is under consideration. The energy peaks of the elements are usually quite well separated preventing any overlap of peaks and has a quite good spatial resolution. One drawback however is the fact that the sample could eventually be contaminated since a limited region of the sample is under investigation.

2.2.3.4 Energy Filtered TEM (EFTEM)

Energy Filtered TEM (EFTEM) technique makes it possible to obtain images with electrons that have lost a given energy. This imaging is achieved using a post column Gatan Imaging Filter (GIF) (as shown in *Figure 2.6*). The electrons arriving in the magnetic prism are dispersed according to their energy losses where two pre-slits magnify the energy dispersion and the resulting spectrum is projected onto an energy-selecting slit. It is at this point that the electrons are energy filtered. The user is able to select the exact width and position of the energy-selecting slit to be used for imaging. There is an arrangement of a series of quadrupole and sextupole lenses (see *Figure 2.6*), which compensates for the energy dispersion of the spectrometer and projects the achromatic energy-filtered image onto the detector. The images are then recorded using a slow-scan charge coupled device (CCD) allowing signal integrating times ranging from a few seconds up to a couple of minutes.

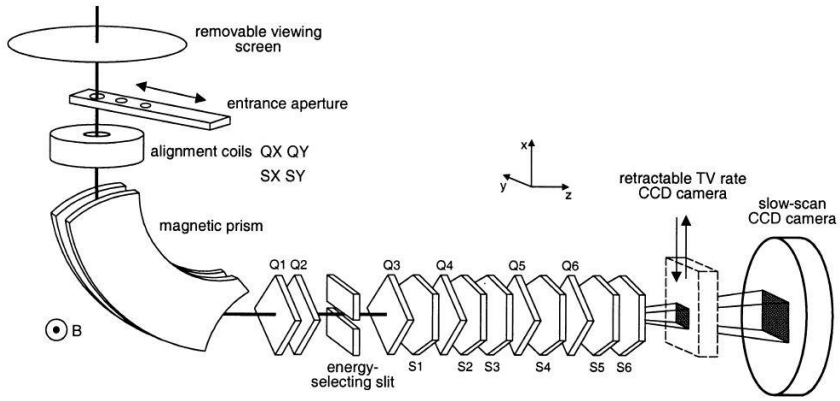

Figure 2.6 Schematic diagram of the Gatan Imaging Filter (GIF). This post-column design disperses the electrons according to energy loss using a magnetic prism, after which an energy-selecting slit allows the electrons to be filtered before the image is restored by a series of quadrupole and sextupole lenses. The final image is recorded on a slow-scan CCD camera [Thomas 2002].

Electron spectroscopic images could be taken exactly at or beyond the ionisation edge corresponding to a specific elemental species. The post edge images recorded in such cases contain information relating to the spatial distribution and concentration of the specified element, as well as an additional underlying contribution from the background corresponding to a variety of inelastic interactions at lower energy losses. As a result, the spectral background contribution must be taken into account when acquiring elemental distribution maps from a core-loss image. Thick samples may produce a significant background contribution, which may over-ride any signal and any eventual useful information. Consequently, it is imperative to verify the specimen thickness and ensure specimens investigated are thin enough for EFTEM

investigation. The measurement of the thickness of specimens is based on the log-ratio method (briefly mentioned in section 2.3.2 EELS). The threshold for elemental mapping is given as $t/\lambda < 0.4$. Among the number of measures proposed to remove the influence of background contribution, two main methods appear to have satisfactory results and have been implemented in this thesis. These are the two-window jump ratio method and the three-window method.

Two-window jump ratio method:

This method involves recording two images by selecting an energy window before (pre-edge image) and after (post-edge image) the characterisation edge of the element of interest. The post-edge image is divided by the pre-edge image to give a jump-ratio image. This procedure yields maps with enhanced contrast that are sensitive to low concentrations with minimum additional noise [Johnson 1979]. The jump-ratio images are particularly susceptible to artefacts as a result of their sensitivity to changes in the preceding background arising from thickness change of the specimen or from preceding core loss edges [Ahn 2006]. However, in cases where background is difficult to model, for example in the case of overlapping edges, jump-ratio method compared to three-window method is quite ideal for obtaining qualitative elemental distribution maps [Hofer 1995]. The signal/noise ratio is also better in this case.

Three-window method:

In the three-window elemental mapping technique, two energy windows are selected (pre-edge images) before the ionisation edge of the element of interest and a third energy window after (post-edge) the edge. The pre-edge images are taken at slightly different energies for the purpose of evaluating the background contribution. With this, the background is extrapolated from the two pre-edge images of equal width. Subtraction of this background contribution from the post-edge image is then performed to obtain the desired elemental map. The choice of the position of the pre-edges should be optimized as possible to reduce the signal-to-noise ratio.

Both the jump-ratio and three-window methods were performed for each investigation to exclude artefacts. The energy thresholds for the considered ionisation edges were found as 456 eV, 532 eV, 575 eV, and 708 eV for Ti-$L_{2,3}$, O-K, Cr-$L_{2,3}$ and Fe-$L_{2,3}$, respectively. The width of the windows for each element was chosen considering possible nearby elements and background contribution. Acquisition times ranged between 6 and 10s for each acquisition. The *Table 2.2* and 2.*3* summarizes the ionization edges, slit widths, pre and post initial position of the edges used for imaging Ti, O, Cr, Fe and Y employing the use of both the Jump-ratio (two-window) and the three-window methods. The given positions correspond to the beginning of the windows.

Element	Ionization edge	Pre-edge	Post-edge	Width
Ti	456	412	458	40
O	532	497	534	30
Cr	575	556	580	20
Fe	708	666	710	40
Y	157	140	159	15

Table 2.2 Jump-ratio method energy windows for elements of interest

Element	Ionization edge	Pre-edge 1	Pre-edge 2	Post-edge	Width
Ti	456	391	421	461	30
O	532	469	499	532	30
Cr	575	522	547	577	16
Fe	708	625	665	720	30
Y	157	122	140	158	15

Table 2.3 Three-window method energy window for elements of interest

Before EFTEM investigations, the samples were verified to be adequately thin for observations. The imaging was performed using a large objective aperture (100 µm). Hence, the contrast of images taken with the GIF camera with no energy filtering are very low and the particles are not easily visible. The acquired EFTEM maps have a dark and white contrast. These images were given colour coding to easily identify and facilitate observations.

2.2.4 Scanning Transmission Electron Microscopy (STEM)

The Scanning Transmission Electron Microscopy technique was developed alongside the conventional TEM but received much attention in recent decades. STEM combines the principles of transmission electron microscopy and scanning electron microscopy and requires the use of thin samples similar to the case of CTEM. In STEM, a very finely focused beam of electrons scans across the specimen in a raster pattern (as shown in *Figure 2.7(a)*). The electrons passing through the sample can be collected to produce a number of transmission images and as with TEM, backscattered electrons and X-rays are also produced. Typically, STEMs are conventional transmission electron microscopes equipped with additional scanning coils, required circuitry and detectors that enable a user to switch between operating as a CTEM or a STEM, which is what, has been implemented in this study. Nonetheless, dedicated STEM instruments are also available.

2.2.4.1 Bright Field (BF) imaging in STEM

Details relating to BF imaging in CTEM have been detailed earlier. The electrons which have been transmitted and collected on axis in the STEM give the BF image. These collected electrons may have been elastically or inelastically scattered. The BF imaging mode under certain conditions in STEM is identical to the CTEM mode. Even though the STEM does give a small spot size, the detector angle is small compared to the beam convergence so collection efficiency is very low. Hence, under TEM conditions, the STEM images are noisier even though similar images are acquired using the two instruments. Therefore, there is very little benefit in operating the STEM in such a non-optimum mode. On the other hand, by using a much larger detector, the detector angle becomes relatively large and improves the efficiency.

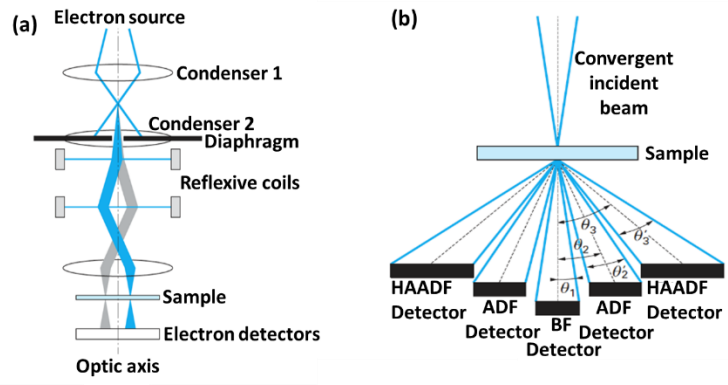

Figure 2.7 (a) Principle of Scanning Electron Microscope (STEM) (b) Scheme of the different electron detectors in a STEM [Jouffrey 2012].

2.3.6.2 High Angle Annular Dark Field

In contrast to the BF imaging mode, the STEM dark field mode of operation provides significant benefits. The inner detector angle of the annular dark field is so large so that no Bragg diffracted electrons could be collected (see *Figure 2.7(b)*). The imaging therefore results from the electrons that have been scattered elastically which pass very close to the atomic nuclei in the sample. High resolution can be achieved since there is no unwanted diffraction contrast which can mask the structural information. The signal produced in HAADF imaging is directly proportional to the density and thickness of the sample as well as also being proportional to $Z^{3/2}$ (Z is the atomic number). It is therefore possible to produce images which show a contrast due to mass-thickness or Z contrast images (where the signal is proportional to the atomic number of the sample.

2.2.4.2 STEM Energy Dispersive X-Ray Spectroscopy (STEM-EDX)

Even though EDX analysis is available in conventional TEM imaging, the spatial resolution is limited by the inability of the imaging system to focus the electron beam. In the case of EDX in the STEM mode, the EDX analysis can be performed at the nanometer scale using quite thin samples. The STEM-EDX mode of operation therefore do not only improve the spatial resolution but also offers improved sensitivity in comparison with the TEM imaging. The reasoning is attributed to the fact that the solid angle of X-ray collection subtended at the EDX detector in the STEM mode is about 2.5 times larger than in TEM mode, resulting in a similar increase in the sensitivity. Thin specimens are ultimately used in which a high spatial resolution can be achieved but with a low X-ray count rates from these specimens, it is usually necessary to perform the data collection over long and extended periods of time. This is essentially accompanied by a specimen drift, where the spatial resolution could be limited. Recent TEMs have adjustments to rectify this issue where the microscopes are equipped with a dynamic drift compensation system, in which the images of the sample from the phase contrast are compared to the original image and feedback adjustments are made to the position of the electron beam to eliminate any effects associated with the drift.

2.2.4.3 STEM-EDX Imaging using the ChemiSTEM Technology

Just as it has been detailed earlier concerning EDX imaging technique in the conventional mode, the challenges associated with this include limited spatial resolution and low signal

collection efficiency. STEM-EDX ensures that the small nanoprobe for investigation greatly improves the spatial resolution. However, the low signal collection angle, as well as the fact that thin specimens usually produce very limited counts means that the investigations should be conducted over long periods.

ChemiSTEM technology has therefore been developed at FEI over the last few years with the express purpose of removing any old barriers in performance, bringing orders-of-magnitude improvement in many key metrics, such as the sensitivity and speed. This technology reduces the analysis times from hours to minutes, and sample features and elements that previously were hidden can now be easily detected.

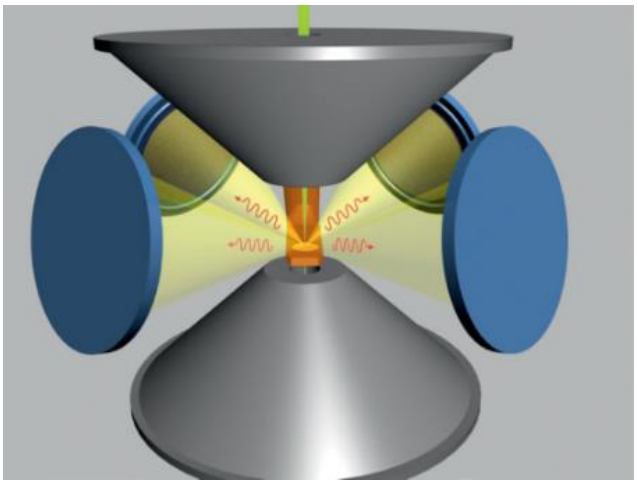

Figure 2.8 A schematic representation of the ChemiSTEM design, showing the X-FEG high brightness, Schottky electron source, and the Super-X geometry including 4 SDD detectors arranged symmetrically around the sample and the objective lens pole pieces [ChemiSTEM 2010].

The main advantage of this technology in the Super-X design comes from a large solid angle for X-ray collection provided by four SDD detectors symmetrically arranged around the specimen, as shown in *Figure 2.8*. These detectors are windowless to improve the collection efficiency and the detection of light elements. The Super-X system together with significant improvements in the design ensures that the detectors are more than 4 times better than the usual STEM-EDX. The vast improvement does not just facilitate the speed of acquisition, but also ensures the detection of hidden features and elements that may not have been previously detected. Very low concentrations of elements (below 1 wt%) can be detected. This makes this technique such a powerful tool in elemental composition characterization.

2.2.5 Analytical crystallographic structure characterization by HRTEM

High resolution TEM is an imaging technique, which enables imaging directly the atomic structure of a specimen. The term that quickly pops up when we talk of HRTEM is Phase-contrast imaging. Indeed HRTEM and Phase-contrast imaging are thought to be synonymous even though in principle phase contrast could appear in some TEM images even at relatively low magnifications. Interference effects (phase effects) form the basis of the formation of images in atomic resolution. Imaging requires the use of a large objective aperture to select several beams from a specimen oriented in a zone axis, as shown in *Figure 2.9*, and the image results from the interference.

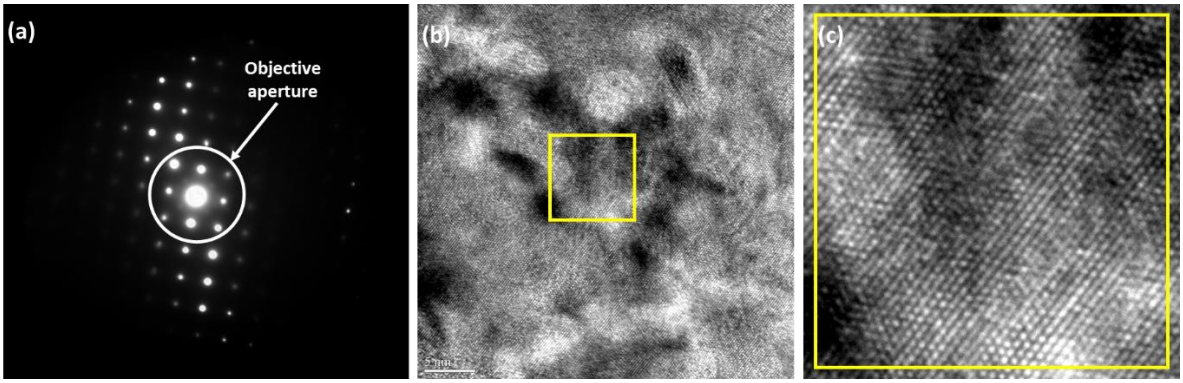

Figure 2.9 (a) Diffraction pattern of FeCr matrix in a zone axis B = 100 indicating a large objective aperture for high-resolution TEM imaging (b) Resulting high-resolution TEM image for the FeCr matrix and (c) magnified region of the sample.

Specimens investigated by HRTEM are usually very thin (10 – 30 nm) and therefore the amplitude of the incoming electrons is unchanged ensuring that there is no amplitude contrast. The phases of the diffracted electrons however are out of phase in relation to the incident electrons and these phase changes appear as differences in the phase contrast. It is however possible to defocus (subfocusing or focusing above the specimen) by introducing into the diffracted beams an additional phase shift with respect to the transmitted beam, which will compensate for the phase shift due to spherical aberration. It is this defocus, which is known as the Scherzer defocus that makes the periodicity of the crystal lattice appears in the contrast of the image. The image formation in HRTEM is achieved in two steps; interaction of the electron waves with the crystal and the transfer of the wave to the output of the crystal by the microscope, which introduces the parameter called the Contrast Transfer Function (CTF). The contrast transfer function describes the various imperfections within a TEM lens system which ensures the modification of the amplitudes and the phases of the electron beam (wave) as it goes through the lenses onto the imaging plane. The function can be expressed as:

$$T(k) = -\sin[\frac{\pi}{2} C_s \lambda k^4 + \pi \Delta f \lambda k^2]$$

Where C_s is the spherical aberration coefficient which depends on the quality of the objective lens, λ is the wavelength defined by the accelerating voltage, k is the spatial frequency (nm^{-1}) and Δf is the defocus value. Very important features of the function CTF are shown in the *Figure 2.10*.

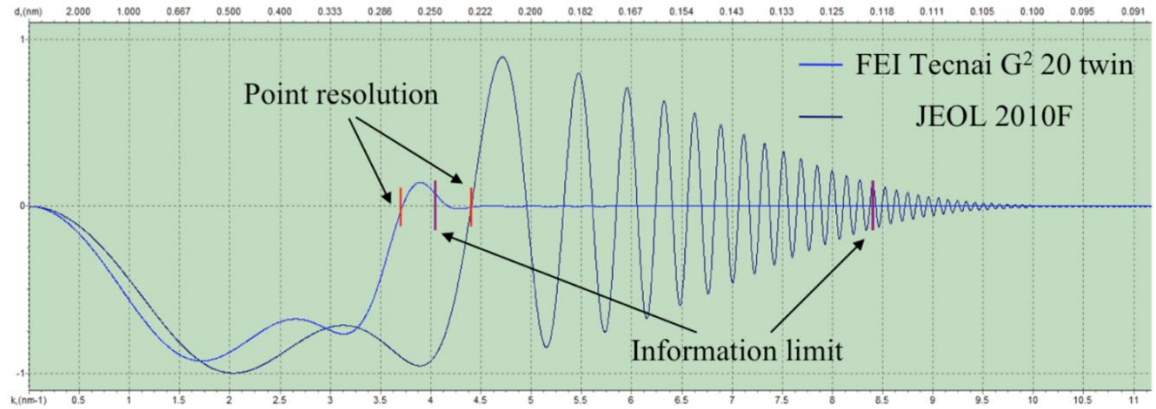

Figure 2.10 Capabilities of high resolution TEM imaging of two different TEM microscopes: Two curves of the contrast transfer function (CTF) were drawn by the simulation software Contrast Transfer Function Explorer using Scherzer defocus (Δf = -86.7 nm and -61.3 nm for FEI and JEOL

microscopes, respectively) and the same magnification. Both curves are modified by envelope functions: the temporal coherency envelope and the spatial coherency envelope [Zheng 2015b].

The CTF generally starts at 0, decreases up to close to -1 and stays almost constant before increasing and crossing the k-axis. It then repeatedly crosses the spatial frequency k-axis as k increases. This function as shown in *Figure 10* could continue, but this is actually modified by envelope functions and eventually dies off. The exact mathematical form of such envelope functions is complex and the result is described by multiplying the function by both the temporal coherency envelope E_c and the spatial coherency envelope E_a to yield the effective transfer function $T_{eff}(k)$:

$$T_{eff}(k) = T(k)E_cE_a = -\sin[\frac{\pi}{2} C_s\lambda^3k^4 + \pi\Delta f\lambda k^2] E_cE_a$$

Where the temporal coherency envelope E_c is caused by chromatic aberrations, focal and energy spread, instabilities in the high tension and objective lens current; the spatial coherence E_a is caused by the finite incident beam convergence.

The point resolution δ of a TEM depends on the wavelength of the electrons λ (i.e. the given kinetic energy to the electrons by the accelerating voltage) and the quality of the objective lens (spherical aberration coefficient C_s in particular) and is defined as the spatial frequency where the CTF crosses the k-axis for the first time (see *Figure 2.10*). The best performance is obtained at a particular defocus value called Scherzer defocus and the point resolution at this defocus is given by:

$$\delta \approx \lambda^{3/4} Cs^{1/4}$$

The resolution of the microscope can therefore be enhanced in two ways; by either using a small wavelength λ (very high accelerating voltage) or a very low spherical aberration coefficient C_s. Microscopes operating at very high voltages could be ideal for achieving a very high point resolution but these microscopes have an associated high risk of damage to the samples. There is then the option of C_s correction. C_s values for high voltage microscopes (200 – 300 kV) are given in the order of 0.5 mm. Recent developments have introduced C_s corrected microscopes. This consists of a system of multipolar lenses (two hexapoles and four additional lenses) and lenses rotationally symmetrical. The aberration of the objective can be compensated and it is this set of optical elements that reduce the C_s to a few microns. The resolution of a microscope with a C_s corrector is then controlled by the chromatic aberration which, in corrected systems, is a little more important than in magnetic lenses.

The choice of the use of a TEM for HRTEM is essential in obtaining the right amount of information. One important property is the brightness of the electron source. Two common emission sources are the thermionic sources (LaB_6) and the field emission sources (FEG). TEMs equipped with Field Emission Gun (FEG) are preferable and better than those equipped with an LaB_6 source due to the fact that the FEG is much brighter than an LaB_6 source [Williams 2009]. The choice of microscope of use also depends on the inter-planar distances of the structure of interest.

The *Figure 2.10* illustrates the Contrast Transfer Functions of *JEOL2010F* equipped with a FEG and FEI Tecnai G^2 20 twin equipped with an LaB_6 filament. The CTF of each were drawn using Scherzer defocus and the same magnification. Both microscopes are noted to be operated at 200 kV and the comparison shows the convergence angles obtained are 1 mrad for the FEI and 0.1 mrad for the JEOL. The smaller convergence angle of the JEOL shows it has

not only a smaller information limit, but also a better spatial coherency than the FEI. The FEG is able to measure much smaller interplaner distances as compared to the LaB_6. The given details explain the choice of the JEOL2010F use for HRTEM imaging.

Resulting images from HRTEM imaging present maxima and minima intensity that may correspond to the probability of passing of electrons given by the product of wave function associated with the electron. This maxima and minima are present in the form of a periodicity of the crystals. The issue then is to verify if this periodicity corresponds to any structure of interest. In the present study, the interpretation of the HRTEM images was performed using the Fast Fourier Transform (FFT). This presents a spot pattern that represents the periodicities observed on HRTEM images. Such obtained pattern is compared to the simulated diffraction pattern of compounds of interest obtained using CrystalMaker and SingleCrystal softwares. The parameters are also compared to data from Pearson Crystallographic and Electron Diffraction data [Villars 1985].

2.2.6 Sample Preparation for TEM

In order to obtain very good specimens and ultimately good results, special attention has been paid to the preparation of samples for TEM investigations. There are two main requirements for sample investigation: the sample should be small enough to fit inside the TEM sample holder (TEM sample holders usually require specimens in the form of 3 mm disks) and the specimens should be 'transparent' to electrons ($<$ 150 nm).

The raw material used in this study is a high-purity material of FeCr (9.86 wt%Cr) alloy provided by École Nationale Supérieure des Mines, Saint Etienne, France. The material is obtained in the form of cylindrical rods of about 2 cm in height and about 1.5 cm in diameter (see *Figure 2.11(a)*). These are then cut into much slender pieces of about 1mm in thickness (*Figure 2.11(b)*). At this stage, the pieces are mechanically polished using Silicon Carbide (SiC) abrasive papers. SiC abrasive papers with finer grains are used as the thickness of the material decreases. The material is polished up until a thickness of about 100 microns (*Figure 2.11(c)*). The final step mechanical polishing is achieved by polishing both sides of the material with abrasive papers with grain size of less than 1 micron, which eventually produces mirror polished surfaces. The required 3mm disks (*Figure 2.11(f)*) are then punched out of the sample using a puncher (*Figure 2.11(d)* and *(e)*).

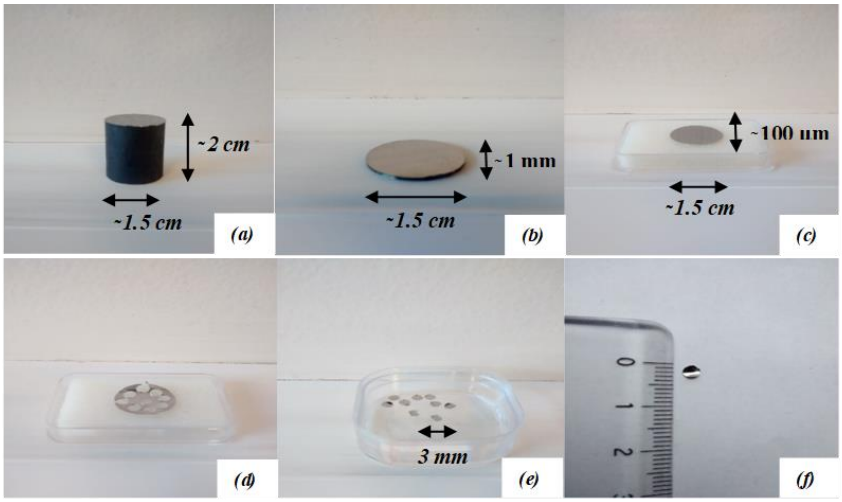

Figure 2.11 Sequential stages of TEM sample preparation.

The polished specimens are then electro-polished using a twin-jet electropolisher (Struers Tenupol-5) with a 10% perchloric acid and 90% ethanol solution at a temperature of -20°C. The thin foils are electropolished on both sides until a hole is created at the centre of the specimen. The region closest to this hole is quite thin (ideally <100 nm) and thus ready for direct TEM observation as in *Figure 2.12(a)*. This view in direct TEM observation will be referred to as the 'Plane View'. The specimens obtained after this stage are ready for ion implantations. Prior to implantations, the specimens are referred to as the as-received (or virgin) thin specimens or as-received thin foils. Other samples are also only electro-polished on side to remove any mechanical stresses on the surface of the sample and these are referred to as the bulk samples.

In the present study, some as-received thin foils were ion implanted and annealed. However, the investigation of the formation of nanoparticles in these TEM thin foils was not without challenges, in particular due the formation of an oxide layer on the surface of the sample (this will be detailed in subsequent chapters). This oxide layer makes the characterization and observation of other details below the surface of the sample quite difficult to achieve. Hence, a vertical blade (window) of a few microns in length and breadth was extracted from the surface of implanted and annealed specimens by focused ion beam (FIB) to enable TEM characterization in transverse view (see *Figure 2.12(b)*). This FIB sample preparation was conducted at the Institut d'électronique, de Microélectronique et de nanotechnologie, Lille, France. The prepared FIB lamella had a final thickness of < 50 nm. This made them quite ideal for the TEM investigations such as EFTEM and HRTEM. The FIB lamellae were extracted to a depth of about 400 nm to ensure that the entire implanted region (≈ 100 nm) is captured. The length of the window was approximately 4 microns. This gives the dimensions of a typical FIB lamella as 4 x 0.4 µm. These samples hereafter will be referred to as FIB lamella.

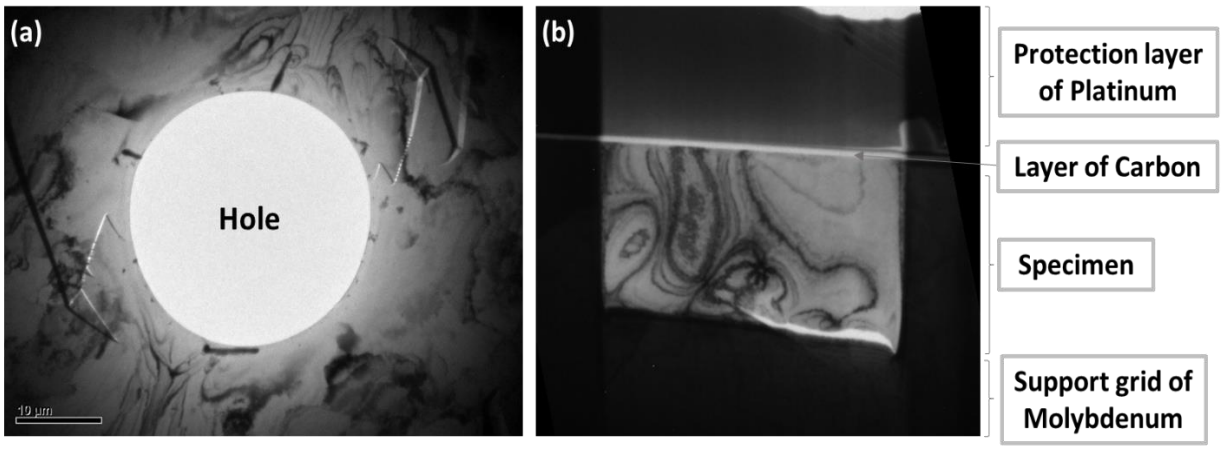

Figure 2.12 (a) TEM bright field (BF) image of thin foil displaying a hole at the centre and surrounded by regions thin enough for electrons to pass through (b) TEM bright field (BF) image of a window from the FIB extracted lamella showing the sample, a layer of carbon and a protection layer of platinum mounted on a Molybdenum grid.

2.3 Ion implantation

The ion implantations have been conducted on the as-received thin foils after TEM observations to verify the thickness and adequacy of these samples, as well as on bulk prepared

samples. Prior to implantation, the material has been checked to correspond to a *bcc* FeCr with a lattice parameter of 0.287 nm, close to the theoretical value. The ion implantation experiments have been performed at the Centre de Sciences Nucléaires et de Sciences de la Matière (CSNSM, Orsay, France), a joint research centre between the University of Paris-Sud and CNRS/IN2P3, using the JANNuS-Orsay/SCALP platform. This JANNuS-Orsay/SCALP platform (see *Figure 2.13*) encompasses a 2 MV ARAMIS accelerator and a 190 kV IRMA ion implanter which can be both coupled directly with a 200 kV FEI TECNAI G^2 20 TWIN transmission electron microscope (TEM) to provide simultaneous irradiations and *in situ* TEM observations.

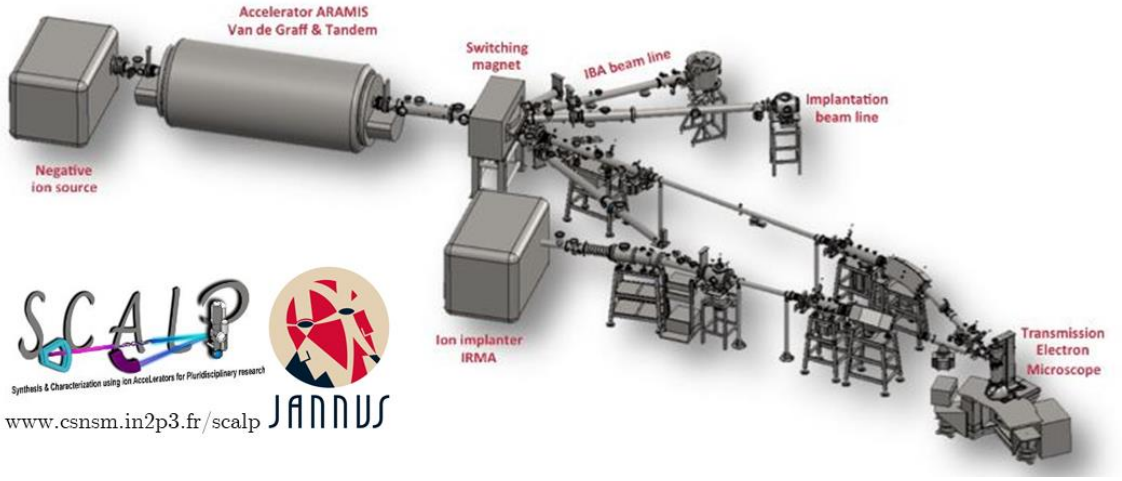

Figure 2.13 Schematic representation of the JANNuS-Orsay/SCALP platform located at CSNSM/JANNuS-Orsay which comprises a 2 MV accelerator (ARAMIS) and a 200 kV ion implanter (IRMA) both coupled to a TEM. Other adjoining equipment include a 50 kV isotope separator (SIDONIE). Only the ion implanter IRMA and the TEM have been employed in this study.

2.3.1 The Instrument and Principle

The *ex situ* ion implantations were carried out with the 190 kV IRMA implanter on both thin and bulk samples. The samples obtained directly after implantations are referred to as as-implanted samples in this study.

IRMA is an ion implanter which is capable of introducing ions into a material below a depth of 500 nm. It accelerates virtually all elements using the Bernas-Nier ion source with which it is equipped. The basic parts include the ion source, ion extraction, ion separation magnet or analysing magnet, the ion acceleration with the electrostatic deflection and finally the target. The ions are generated in a plasma vacuum system. The ions are produced by stripping electrons from the source ions in the plasma. The extracted ions are then passed through the ion separation magnet where only the ions of the required properties are selected. They are booted up to speed to be implanted in the target. Finally, the ions are refocused, scanned and implanted into the target. An image of the IRMA ion implanter is given in *Figure 2.14*.

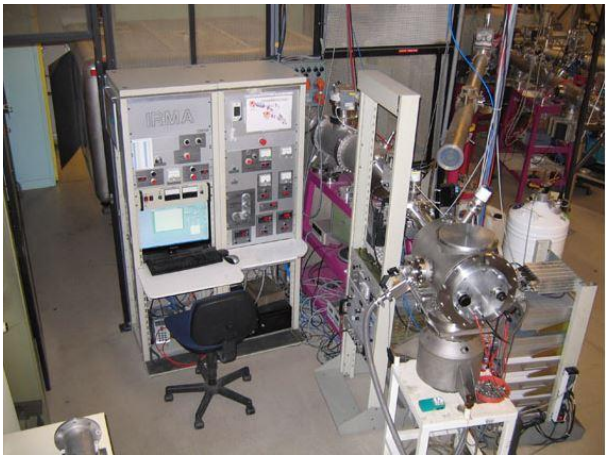

Figure 2.14 An image of the 190 kV ion implanter (IRMA) located at CSNSM, JANNuS-Orsay/SCALP platform.

2.3.2 Ion implantation and parameters

It has been stressed that typical nanoparticles formed in ODS steels are (Y, Ti) oxides. Y is introduced into the conventionally fabricated ODS alloys in the form of Y_2O_3 and Ti is added in other cases of Ti containing ODS steels. The goal of this study is to simulate experimentally the formation of oxides of Ti and Y. Y^+ and Ti^+ ions are therefore chosen together with O^+ ions to be implanted into the as-received samples. The industrial alloys have a typical concentration of close to 0.3%wt of Y_2O_3 whilst that of Ti is of the order 0.3 – 0.8%wt of Ti. To facilitate the formation of these oxides, we chose to implant close to 4%wt Y and Ti, which is approximately ten times the composition of the conventional alloys. Such increased concentration provides a favourable condition for precipitation and formation of nanoparticles. Keeping in mind that for direct observation of TEM thin foils the ions should be implanted to thicknesses between 0 and 100 nm, we chose the energy of ions such that the ion distribution has a maximum implantation peak or a mean projected range of close to 40 – 50 nm.

A Monte Carlo simulation code known as the Stopping and Range of Ions in Matter (SRIM) is used to estimate the energies of the elements to obtain a mean projected range close to 40 nm. The energies were determined as 100, 170 and 37 keV for Ti^+, Y^+ and O^+, respectively. A fluence of $2x10^{16}$ cm^{-2} was chosen for the metallic ions (Ti, Y) and twice this fluence was chosen for the O ions ($4x10^{16}$ cm^{-2}). The ion flux was 6.8×10^{12} $cm^{-2}s^{-1}$ for all ion implantations. The as-received samples were mounted on a molybdenum sample holder. This sample holder can take up to a maximum of 45 different samples. The sample holder was mounted in the IRMA chamber exactly perpendicular to the ion beam. Sequential ion implantations beginning with the metallic element (Y or Ti) were performed followed by oxygen implantations. Between these implantations, a change of source was required. This takes up to an hour or two whilst maintaining the samples in the vacuum chamber. The duration of the implantation of each element varied between close to an hour and three hours. No deliberate heating of the specimens was performed during the course of the implantations. A summary of the implanted parameters is summarized in the *Table 2.4*.

Element	Energy (keV)	Fluence	Max conc (at%)	Max dpa
Oxygen	37	$4x10^{16}$ cm^{-2}	8.9	25.1
Titanium	100	$2x10^{16}$ cm^{-2}	4.9	44.4
Yttrium	180	$2x10^{16}$ cm^{-2}	5.8	89.8

Table 2.4 Summary of the parameters used for ion implantation

The concentration profiles of the implanted ions were simulated using the SRIM code [Ziegler 1996]. The mean projected range in all the three cases appear to occur around 40 nm. The maximum concentration was recorded as 8.9, 4.9 and 5.8 at% for O, Ti and Y, respectively (from the plot in *Figure 2.15(a)*). Similarly, the *Figure 2.15(b)* presents the concentration profile of the vacancies created by the ion implantation for Ti, Y and O ions. The peak of the profile of vacancies occurs at 25-30 nm. Peak concentrations of the vacancies are recorded as 0.7, 2.7 and 5.1 vacancies per ion per Angström ($ion^{-1}Å^{-1}$) for O, Ti and Y, respectively. These calculations were performed in Fe using full damage cascades mode with a displacement energy (E_d) for Fe of 40 eV [Juslin 2007].

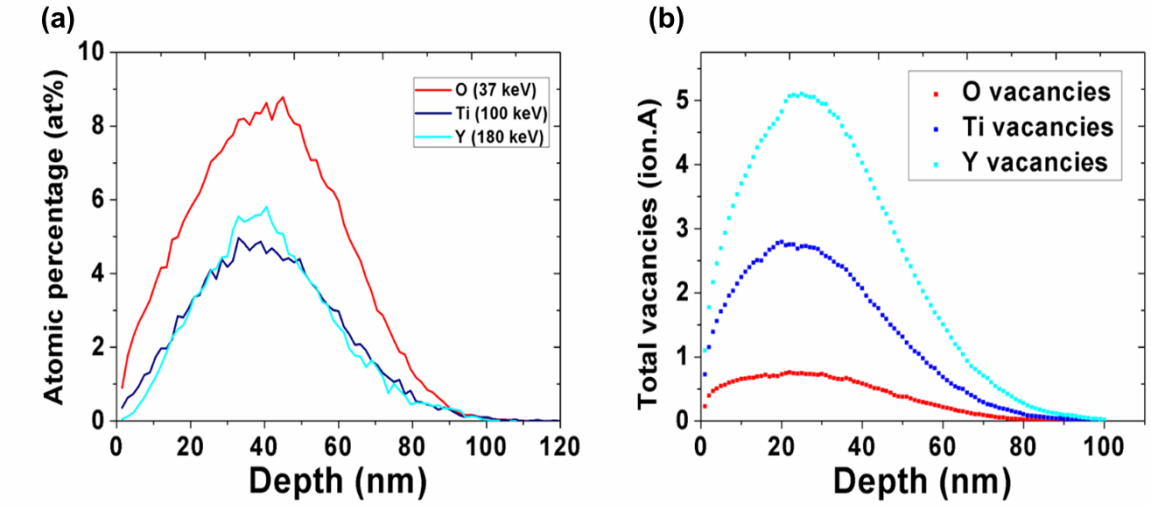

Figure 2.15 Predicted concentration profiles by SRIM using a displacement energy of 40 eV for Fe. (a) Concentration profile of implanted Ti, Y and O ions with a projected range of 40-50 nm (b) Concentration profile of vacancies created by the ion implantation for Ti, Y and O ions.

An estimation of the damage profile expressed in displacement per atom (dpa) was also determined from the concentration of the vacancies. The expression for the rate of displacements per atom is given as:

$$dpa/s = \frac{n\,x\,1x10^{8}\,x\,\phi}{\rho}$$

Where n is the number of vacancies created ($ion^{-1}Å^{-1}$), ϕ is the ion flux ($ions.cm^{-2}s^{-1}$) and $\boldsymbol{\rho}$ is the atomic density ($at.cm^{-3}$). The number of dpa at the peak of damage is reported in *Table 2.4* for the three different implantations. The profiles of damage production rates for these implantations are plotted in *Figure 2.16*.

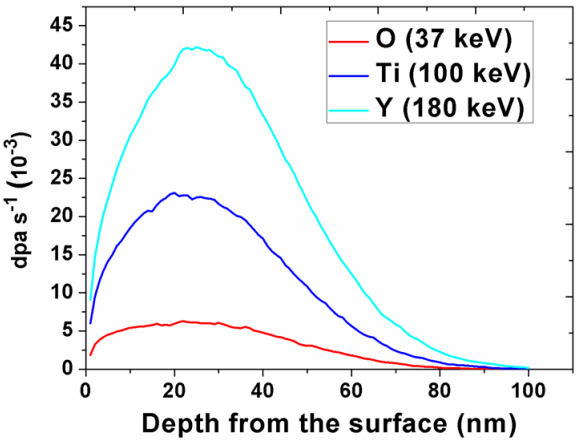

Figure 16. Profiles of damage production rate for 37 keV O, 100 keV Ti and 180 keV Y as predicted by SRIM using a displacement energy of 40 eV Fe and the ion flux of $7x10^{12}$ $cm^{-2}s^{-1}$.

2.4. Thermal Annealing

2.4.1 *In situ* TEM annealing

In situ TEM annealing of TEM thin foils and annealing of bulk samples were both performed. The *in situ* TEM annealing was performed with the FEI Tecnai G^2 20 twin microscope using a Gatan TEM heating specimen holder with a maximum allowed temperature of 800°C. Hence, only *in situ* TEM annealing at 500 and 600°C have been performed using this sample holder. The duration of *in situ* annealing at both these temperatures was 90 minutes. In each of these annealing conditions, one as-implanted sample (sample implanted at room temperature with no deliberate heating) was mounted onto the sample and then inserted into the microscope. The vacuum inside the column of the TEM was $1.2x10^{-5}$ Pa. The sample holder is connected to a controller as well as a water tube for cooling. The controller allows inputting a current and as the current density increases, the temperature increases and can be checked on a viewing screen. The water tube ensures that water keep passing both during and after annealing until the temperature of the sample holder returns to room temperature. The heating of the sample to the required temperature was achieved within 15 minutes (this does not include the annealing duration) and maintained for the duration of annealing (90 minutes). The sample holder whilst still in the TEM was cooled after the experiment with the help of the running water in steps of 100°C to about room temperature.

2.4.2 *Ex situ* Annealing

Ex situ annealing was performed for mainly bulk samples and some thin foils. Annealing temperatures varied from 600 up to a maximum of 1100°C. This annealing was carried out in the IRMA implanter chamber, which has a similar pressure to that of the TEM (1.2×10^{-5} Pa). The samples are mounted on a Molybdenum sample holder, which was also used for implantations. The sample holder is capable of taking up to a maximum of 45 (5 rows x 9 columns) samples. The sample holder is then mounted on a stage inside the vacuum, which is attached to a tungsten filament. Voltage is applied to the tungsten filament in steps until the required temperature is reached. The principle is quite rightly similar to that used in the in-situ annealing as a rise in the current density due to the applied voltage ensures an increase

in the temperature., It is possible to view the steady rise in the temperature and eventual stabilization at the maximum temperature. The time required to ramp the temperature to the desired temperature varies between 30 minutes and an hour depending on the chosen temperature. In almost all cases in which the *ex situ* TEM annealing was used, the annealing duration was 2 hours after reaching the desired temperature. After the annealing process, the samples are left to gradual cool back to room temperature which could take a couple of hours. The temperature evolution during the annealing process is given in *Figure 2.17* for the different annealing temperatures. The FIB lamellae were extracted only after the annealing process.

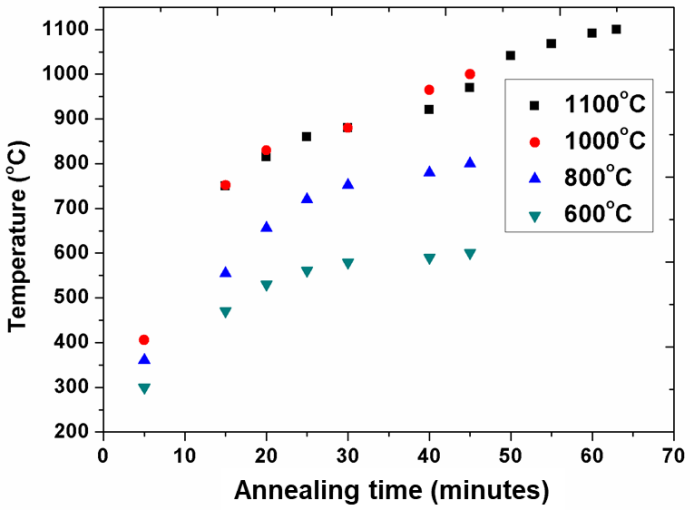

Figure 2.17 A plot of the annealing temperature evolution as a function of time used for annealing at different temperatures.

2.5 Atom Probe Tomography

The APT investigations have been conducted at the Institut Matériaux Microélectronique Nanosciences de Provence (IM2NP) in Marseille in collaboration with Dr Marion Descoins and Dr Dominique Mangelinck through the METSA demand 2019. The sample investigated in this study was a sample implanted with Y, Ti and O sequentially at RT. This sample was annealed *ex situ* at 800°C. The idea of investigating this sample by APT will be revisited in section 3.3.2.2.

2.5.1 APT sample preparation

The samples under investigation were prepared by mechanical polishing and electro-polishing using an electrolyte of 10% perchloric acid and 90% ethanol just as used in the case of conventional TEM sample preparation (see TEM sample preparation). The samples were then implanted using the same implanted conditions as described in section 2.3.2. The sample was then annealed under vacuum at 800°C for 2 hours. All these stages of the sample preparation, ion implantations and annealing were conducted at CSNSM-Orsay. The sample was then sent to IM2NP for final APT sample preparation. A FIB lift-out method was chosen and used to produce the APT sample tips using an FEI SEM of the type Helios 600 Nano-Lab focused ion beam. The needle-shaped tips with apex radius of about 50 nm are required for APT in order to field evaporate the atoms.

The surface of the sample to be investigated was deposited with carbon to protect the sample surface from any damage created by the ion beam. The samples together with a support system were mounted on a sample holder. This sample holder was mounted inside the SEM and a pump used to create vacuum. A platinum layer of 25 um by 2-3 um with a thickness of approximately 100 nm was used to protect the region of interest (selected zone) and in addition highlight this zone (as shown in *Figure 2.18(a)*). Rectangular blade (typically referred to as a wedge) was extracted by digging trenches around this highlighted zone of interest. A first horizontal trench was made using Ga ions as the cutting tool at an angle of 22° normal to the sample surface (as shown in the position 1 in *Figure 2.18(b)* along the elongated direction. A second trench in a similar fashion is made at the opposite end of the region of interest by rotating the sample 180° (as shown by the position 2 in *Figure 2.18(b)*. The dug trenches are made quite deep such that both trenches do meet and that the trenches encapsulate the implanted region. A third vertical trench is dug on one end of the highlighted region to meet the trenches 1 and 2 (as illustrated by the position 3 in *Figure 2.18(b)*. At this stage, the wedge is hanging by just the end opposite to the third trench. A micro-manipulator is then attached to the end of the wedge on the end of the trench 3 using a platinum deposition (illustrated in the *Figure 2.18(c)*. A final trench is made using the Ga ions on the other edge to detach the dug trenches from the sample and the wedge held in place only by the micro-manipulator. At this stage, the original sample is lowered from its position.

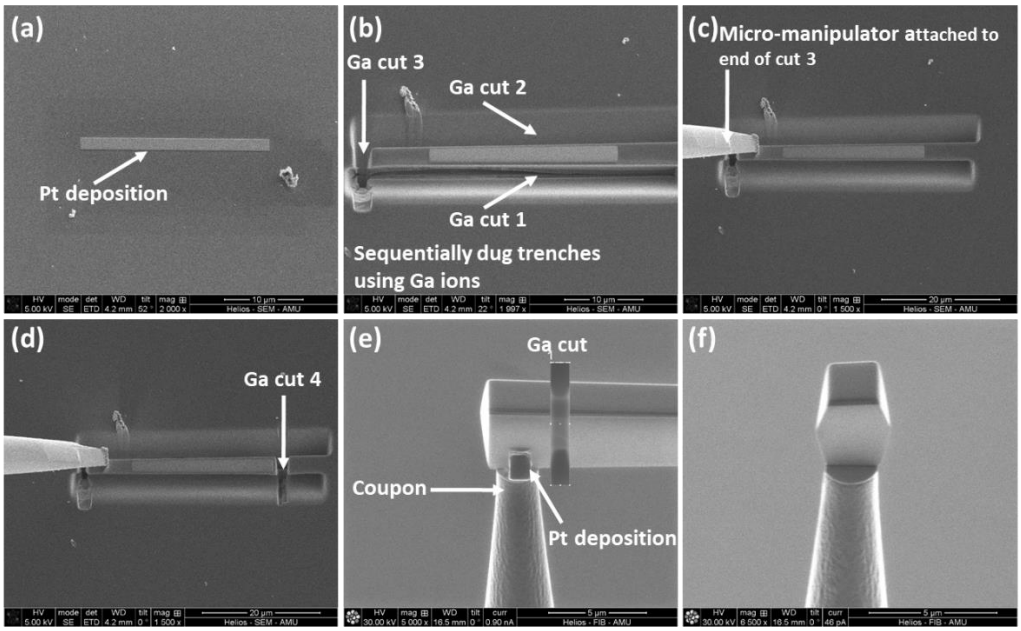

Figure 2.18 Images of the sequential stages involved in the in-situ lift-out process by FIB indicating; (a) Pt deposition on the region of interest. (b) Sequentially dug trenches using Ga ions. (c) Attachment of the micro-manipulator to the wedge. (d) Final Ga cut (e) Attachment of the trench to a microtip. (f) Final cut wedge attached to a microtip for final stage APT preparation.

The micro-manipulator which now holds the horizontal wedge is used to transport the wedge onto a stage (support system) holding a network of 6 by 6 micro-tips which is usually referred to as coupon. The high number of microtips present makes it possible to prepare a number of tips for APT as required in a short period of time in a similar fashion. A part of the wedge is then attached on the microtip. This is achieved by attaching the free end of the rectangular trench onto the flat part of a microtip using a Pt deposition and cutting the opposite end of

the rectangular trench with Ga ions to create more smaller wedges with a dimension of approximately 2 by 2 um. Usually six tips are prepared by sample. The final stage of the sample preparation involves the conversion of these smaller trenches into the required conical tips as shown in *Figure 2.19*. This is performed by using annular milling with decreasing diameter rings. To finish up, the final shape is polished using low energy of 2-5 keV as well as carefully chosen current and time to produce finely polished needle shape tips. In doing so, we try to as much as possible remove any remaining Pt deposition, C deposition and oxide layer on the surface of the sample. It is crucial to finish this stage as fine as possible to avoid removing the implanted layer (100 nm from the surface) which falls just beneath the oxide layer without implanting too much of Ga ions used for the polishing.

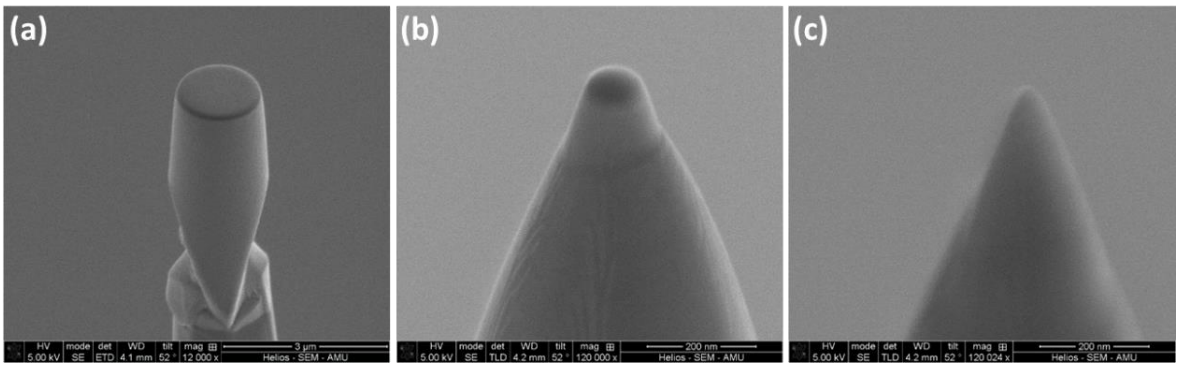

Figure 2.19 Images of the annular milling pattern for APT tips using FIB. (a) Initially milled trench. (b) Milled tip for final stage polishing. (c) Final APT prepared tip.

2.5.2 The Atom Probe Tomography Principle and Mode of Operation

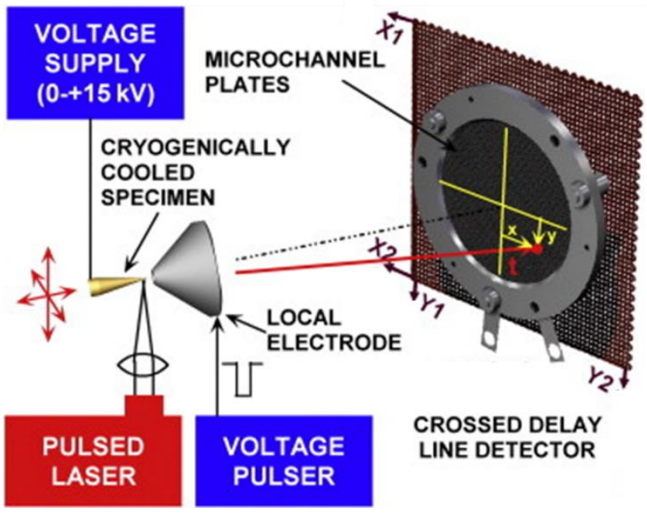

Figure 2.20 Schematic diagram of a local electrode atom probe (LEAP) with a crossed delay line single atom detector at the end of the time-of-flight spectrometer indicating voltage and laser pulsing modes of field evaporation [Miller 2009].

The principle of APT is based on field evaporation of atoms from the previously prepared needle-shaped sample. This instrument may be described as a field ion microscope which is equipped with a time-of-flight mass spectrometer and a position sensitive detector. In a brief description, the prepared specimen is placed in an ultrahigh vacuum where it is cryogenically cooled. Voltage ranging between 5 and 20 kV is applied to the sharp tip as in the *Figure 2.19(c)* where atoms on the surface of the sample tips are ionized in the presence of the high

electric field. Ions produced are accelerated and directed towards the detector in the presence of an electric field. As shown in the *Figure 2.20*, each ion detected is associated with a particular time of flight. The measured time of flight for each species enables the mass to charge ratio (m/n) to be determined and thus the chemical nature of the species. The relation is derived from energy conversation given by;

$$neV = \frac{1}{2} mv^2$$

Where n is the charge state, e is the charge of the electron, V is the potential applied to the specimen and m is the mass of the ion in a.m.u.

The ion velocity v can be determined by the ion flight time t and the length of the flight L (i.e. distance from the sample to the detector) by the expression $v = \frac{t}{L}$.

The mass to charge ratio can therefore be expressed by the relation;

$$\frac{m}{n} = 2e \times (V_o + V_p) \times (\frac{t}{L})^2$$

Where Vo and Vp are the standing electric and pulse voltages which give the total voltage.

The detector obtains data presented in the form of a histogram called the mass spectrum for each mass to charge ratio. The peaks appearing in the mass spectrum can then be identified corresponding to an element, isotope or molecular ions. The *Figure 2.21* is a typical mass spectrum for the Y,Ti,O implanted sample annealed at 800°C. The Fe, Cr, Y, Ga, TiN and TiO peaks are clearly observed from the mass-to-charge ratio from 25 to 35. The unique feature of each mass spectrum corresponding to each species makes this technique quite useful for elemental characterization.

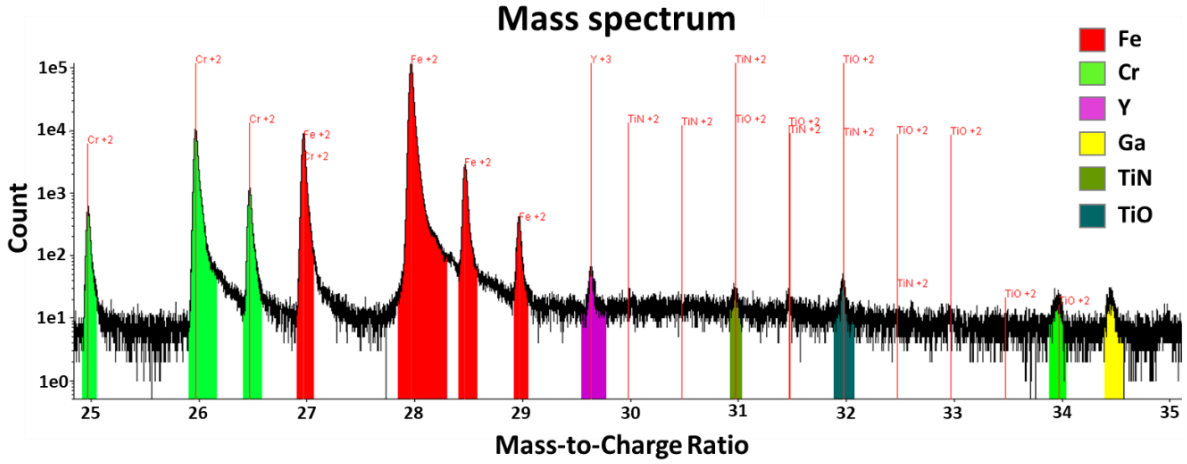

Figure 2.21 The mass spectrum for the Y,Ti,O sample implanted at RT and annealed at 800°C from the run R30_10306.

2.5.3 Experimental conditions

The APT experiments were performed at IM2NP in Marseille, France using an atom probe (LEAP 3000TM XHR, Imago Scientific Instruments) equipped with a pulse laser (Pulse Width = 10 ps, wavelength = 532 nm). The LEAP instrument comprises a mass reflectron that

improves the mass resolution. The specimens were kept at a temperature of approximately 80 K in an ultrahigh vacuum (<1.7 x 10^{-11} Torr). The laser was operated in the laser-pulsing mode where the energy varied from 0.5 to 1.2 nJ. Three different runs were performed on three prepared tips and a summary of each run is presented in the *Table 2.5*. In laser-pulsing mode, the threshold of good hits is 50-60% and the runs from this experiment produced good hits of about 90% illustrating good quality APT measurements.

Run No.	Coupon No.	Temperature (K)	Good Hits (%)	Target evaporation (%)	Total time
R30_10306	M18	80	88.9	0.20	5:24:08
R30_10307	M17	80	95.1	0.20	9:25:32
R30_10308	M16	80	91.8	0.20	7:27:00

Table 2.5 Summary of APT experimental investigation conditions

2.5.4 The 3D reconstruction

The 3D reconstruction involves the conversion of the measurement into an actual 3D image of the specimen. The mass to charge ratio gives the nature of the ions but we need to determine its position in the sample. During the APT measurements, the position sensitive detectors record useful information relating to the (X,Y) positioning of the atoms. These X,Y coordinates of the atoms ensures that the positions of the atoms can be determined using inverse stereographic projection. This projection assumes that all the atoms are emanating from a fixed projected point P. The magnification is derived from the specimen shape by the relation:

$$G = \frac{L}{(m\ +1)R}$$

Where L is the length of the ion flight, m is the compression factor (m+1 can be empirically taken as 1.45 [Bhattacharya 2016]), and R is the specimen end radius. This radius is related to the electric field and the voltage by the relation, $R = \frac{V}{E\beta}$, where E is the evaporation field and β is the specimen shape related factor.

The magnifications once known could be used to determine the exact position of the atoms from the specimen tips from the given expressions:

$$x = \frac{X}{G}$$

And

$$y = \frac{Y}{G}$$

The final parameter is the dimension z. This parameter corresponds to the depth and this can be determined from the total number of evaporated atoms and their atomic volume. From the various atoms that are detected, the depth is incremented by

$$\Delta z = \frac{G^2 V_{at}}{QS}$$

Where V_{at} is the atomic volume, Q is the detection efficiency of an atom probe and S is the surface area of the detector. The 2D projection of the atoms on the detector can be obtained as the experiment progresses where the final 3D image of the investigated specimen is obtained after the whole duration of the run.

2.5.5 The APT Data Treatment

The 3D reconstruction of the sharp tip was performed in this study using a commercial software known as IVAS™. This software was also used for a further analysis. After reconstructing the 3D peak, the aim is to obtain information about the possible segregation, clustering or compositional changes which may have occurred in the sample. Any nanocluster formation is analysed using clustering algorithm which is based on the principle that nanoclusters are regions enriched in solute atoms. The algorithm used for the analysis of the clusters is known as the maximum separation method [Vaumousse 2003]. This method is based on the selection of solute-rich regions by connecting solute rich atoms which lie within a fixed distance and taking clusters above a certain minimum number of solute atoms. From the description it is essential that a few parameters are defined.

The parameter d_{max} (nm): This distance corresponds to the maximum distance where atoms within this distance are grouped into a cluster [Vaumousse 2003]. This is based on the nearest neighbour distance between atoms in a possible cluster. Hence, if two solute atoms have a distance less or equal to this distance, they are considered part of the same cluster.

The parameter N_{min}: This parameter involves the elimination of any clusters containing a number of solute atoms less than this value. It is needed in order to differentiate between random and non-random distributions as occasional density fluctuations may easily cause misinterpretation. All clusters below this Nmin threshold are discounted. In the extreme and unlikely case where a large d is selected, all the atoms would be connected to one very large cluster.

The parameter L (nm): For any atoms surrounding the cluster, this parameter is constructed to add the atoms within a distance L greater than dmax which may be part of the core of the cluster.

The parameter D_{erode} (nm): This parameter described as the method of erosion helps to eliminate any artificial layer created after the previously introduced L parameter.

The main parameters are mostly the d_{max} and the N_{min} and this is determined for any possible clusters formed. The same determined parameters are used for the analysis of all the three APT specimens. Once this algorithm helps to identify any clusters within the specimen, they are further characterized and analysed in terms of the composition of the cluster, the size of the cluster and the density of the cluster.

The composition of the cluster: If the concentration of an element is given by i in the analysed volume, the concentration can be expressed as:

$$C_i(at\%) = \frac{N_i}{N_t} \times 100$$

Where C_i is the concentration of the element, N_i is the number of atoms corresponding to the element i and N_t is the total number of atoms in the given volume.

The precision of the compositional measurement considering only statistical variation is given by the expression:

$$\sigma_i = \sqrt{\frac{C_i\,(1 - C_i)}{N_i}}$$

Where σi is the statistical error.

The cluster size: The determination of the size of clusters is made from the Radius of gyration (Rg) which defines the average distance between each atom present in the cluster and the centre of mass of the cluster [Zheng 2015b]. The radius of gyration Rg from 3D APT experiments is given by the relation:

$$R_g = \sqrt{\frac{\sum_{i-1}^{n}[\,(x_i - \bar{x})^2 + (y_i - \bar{y})^2 + (z_i - \bar{z})^2}{n}}$$

It is believed that the radius of gyration gives a value of the size of the cluster usually smaller than the actual size of the cluster [Zheng 2015b]. Hence, the radius of gyration can be commonly converted to an alternative parameter known as the Guinier radius. The relation between the two parameters is given by the equation:

$$R_G = \sqrt{\frac{5}{3}\,R_g}$$

The cluster number density: The number density of clusters can be reasonably ascertained by the determination of the number clusters within a given volume. The volume is estimated from the products of the x, y directions of the analysed volume but an accurate estimation of this value is difficult to estimate due to the fact that during the APT experiment, there is a blunting of the peak during the experiment and hence the extent of the x and y directions may thus increase. However, estimation of this number density is given by the expression:

$$\rho = \frac{N_p \zeta}{N_{vol}\Omega}$$

Where **ρ** is the number density, Np is the number of observed clusters, ζ is the detection efficiency of the single-ion detector, Nvol is the total number of atoms in the given volume and Ω is the average atomic volume.

2.6 Secondary Ion Mass Spectroscopy(SIMS)

Secondary Ion Mass Spectroscopy (SIMS) has been used to investigate the diffusion of the implanted metallic ions in FeCr. With the ability to detect almost all elements with a high spatial resolution, this makes this technique quite useful. In SIMS, the composition of the surface of the specimen could be analyzed by bombarding the specimen with a focused primary ion beam which leads to the emission of particles. The ejected particles could be neutral or ionised. The ejected ions (secondary ions) are collected and analyzed by a mass spectrometer which enables the determination of the elemental, isotopic and molecular composition.
The instrumentation of a secondary ion mass spectrometer involves (i) a primary ion source responsible for the generation of primary ion beam as well as acceleration of the beam to be focused on the sample, (ii) a high vacuum system for holding the sample, (iii) an ion extraction system, (iv) a mass spectrometer or mass analyzer for the separation of the ions and (v) an ion detection system for the detection of the ions and onward imaging as a mass spectrum, depth profile or a 2D/3D image.

Primary ion source: A high energy primary beam is focused and bombards the surface of the sample. The types of primary beams often used are O^{2+}, O^-, Cs^+, Ar^+ or Ga^+. As in most surface interactions, a transfer of the kinetic energy of the primary beam to particles on the surface results in the ejection of various particles from the surface. Some of the ejected particles get ionised upon leaving the surface. The type of secondary ions ejected depends on the properties of the primary beam such as the beam energy, the current density and the composition of the sample to be analysed. Oxygen primary beam is used for the investigation of electropositive elements as it favours the probability of generation of positive secondary ions whilst Caesium primary beam is used for the investigation of electronegative elements as it favours the probability of generation of negative secondary ions.

High Vacuum system: This contains the sample for investigation. It is essential that the instrument is kept at ultra high vacuum during investigation and analysis. The vacuum of the analysis chamber can go down to about $10x10^{-10}$ Torr [Benningghoven 1973]. Under these vacuum conditions, the probability of secondary ion interaction with a gas molecule is almost zero.

Ion extractor: Upon interaction of the primary beam with the sample surface in the vacuum chamber, secondary ions formed by the bombardment of the sample are immediately extracted by an extractor or immersion lens. The purpose of this extraction lens is to focus the secondary ion beam onto the entrance slit of the mass spectrometer or analyzer.

Mass analyzer/ mass spectrometer: The mass spectrometer separates the various secondary ions produced and isolates the ions of interest. Three types of mass analyzers are commonly used ; magnetic sector, quadrupole mass filter and time-of-flight mass analyzer. Magnetic sector analyzer are commonly used due to their high mass resolution. This analyzer uses a combination of an electrostatic analyzer and a magnetic analyzer to separate the secondary ions based on the mass to charge ratio. In the quadruple mass analyzer, based on resonant electric fields, only masses of interest are selected and analyzed. Time-of-flight mass analyzer is based on the principle that ions with the same energy but different masses travel with different velocities. Secondary ions are accelerated to a common energy and travel over a drift path. The flight time for these ions is then recorded and enables the determination of its mass.

Ion detector: The ion detection system enables recording of the magnitude of the secondary ion signal. The ion beam passes through the detector slit and strikes a metal cup. A Faraday cup is then used to measure the ion current hitting the metal cup. The detection system is usually coupled to a fluorescence screen or a CCD-camera. A micro-channel plate can also be used coupled to phosphor screen.

SIMS is usually described according to two operating modes : Dynamic and Static Secondary Ion Mass Spectroscopy. Dynamic SIMS utilises a continuous, focused beam of primary ions to sputter and remove particles from the surface of the material. The fraction of sputtered material that is ionized is extracted into a double-focusing mass spectrometer, which uses electrostatic and magnetic fields to separate the ions according to their mass-to-charge ratio. By adjusting the strength of the magnetic field, ions of different mass to charge ratio are selected. Static SIMS on the contrary utilises a pulsed ion beam to sputter and remove material from the surface of the sample. Secondary ions are collected and focused onto a time-of-flight (ToF) mass analyzer. The combination of the primary ion density which ensures low surface damage and high sensitivity of ToF analyzer makes the technique useful in studying top surface of a sample. The ToF analyzer also covers a wide mass range of detection and is useful for the detection of trace levels of contaminants on the surface of the sample.
Two terms are quite important for SIMS investigation : the yield and the detection area.
Two types of yield are considered, the sputter yield and the ion yield. The sputter yield represents the fraction of atoms that are sputtered by the primary beam whilst the more important or useful term is the ion yield or the ionization efficiency and this defines the fraction of sputtered atoms that become ionized.

Detection area :
In SIMS investigation, not all the surface of the material is used. A raster scan is performed on the region chosen for sputtering the atoms. The detection area falls within the total rastered area, as in *Figure 2.22*. In depth profiling, the total rastered area cannot be used for detection of secondary ions because of contributions from the crater walls. Usually, a large raster-to-crater area ratio is required for analyzing. This is to ensure that secondary ions from the sidewalls are excluded and only secondary ions from the detection area at the bottom of the crater is measured.

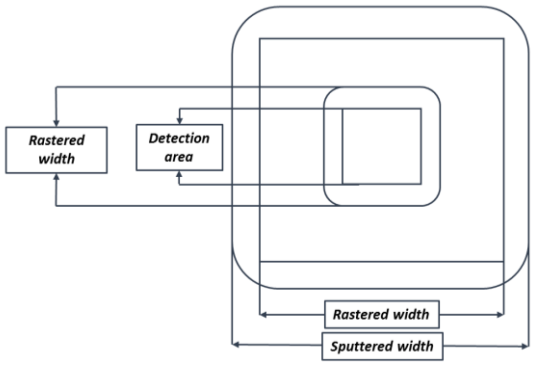

Figure 2.22 Illustration of the sputtered and detection region for SIMS investigation

In this study, the particular mass spectroscopy technique utilised is the ToF-SIMS. This has been performed at the Regional Platform of Surface Analysis, part of the Unité de Catalyse et Chimie du Solide (UCCS-UMR 8181) of the Université Lille 1. This platform encompasses a Kratos X-Ray Photoelectron Spectrometer (XPS-AXIS ULTRA DLD), a Low Ion Energy Ion

Scattering (LEIS) instrument (Qtac 100) and a Time-of-Flight Ion Mass Spectroscopy (ToF SIMS5) from IONTOF, all coupled to a ultra high vacuum. A picture of the facility is shown in the *Figure 2.23.*

Figure 2.23 Surface analysis platform of Unité de Catalyse et Chimie du Solide (UCCS) located at Université de Lille 1. This platform encompasses a Kratos X-Ray Photoelectron Spectrometer (XPS-AXIS ULTRA DLD), a Low Ion Energy Ion Scattering (LEIS) instrument (Qtac 100) and a Time-of-Flight Ion Mass Spectroscopy (Tof SIMS5)

The LEIS provides elemental and structural characterisation of the top atomic layer. The XPS technique measures elemental composition, chemical state and electronic state of the elements present in the surface layer (about 1 – 12 nm) and the ToF-SIMS is used to probe deeper depth to analyse the composition of these solid surfaces. The coupling of these techniques makes this platform quite a unique centre for surface analysis. The ToF-SIMS has been utilized to study the depth profile of implanted ions in implanted and annealed samples.

2.6.1 Time-of-Flight Secondary Ion Mass Spectroscopy (ToF-SIMS)

This technique is suitable for a wide range of materials including metals, ceramics and polymers. ToF-SIMS is based on the fact that ions with the same energy but different masses travel with different velocities. The principle is illustrated in *Figure 2.24.* An electrostatic field accelerates the generated ions to a common energy. These accelerated ions then travel over a drift path to the detector. The lighter ions fly with a higher velocity and arrive at the detector before the heavier ions. The flight time is measured and allows the determination of the ion mass. This technique requires a pulsed secondary ion generation using either a pulsed primary ion gun or a pulsed secondary ion extraction. The analysis by the detector then produces an imaging in the form of surface spectrometry, surface imaging, depth profiling or a 3D analysis. The imaging mode implemented in this study was the depth profiling. In this mode, two ion beams operate in the dual beam mode. While the first beam is sputtering a crater from the surface of the sample, the second beam is progressively analysing the detection area in the crater bottom.

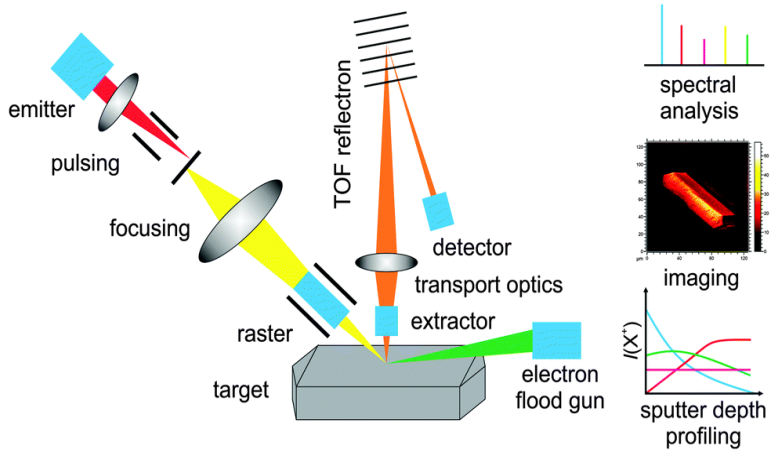

Figure 2.24 Illustration of TOF-SIMS Operation principle [Hofmann 2014].

2.6.2 Experimental Conditions

The IONTOF 5 ToF -IMS has been used in the depth-profiling mode to investigate the mobility of implanted elements in Fe10wt%Cr samples. A picture of the equipment used is reported in *Figure 2.25*. The samples used in this study are bulk samples that were prepared by mechanical polishing without any electropolishing. Feasibility of the use of thin samples (electropolished with the creation of a hole at the centre of the sample) was also investigated. The prepared samples have been implanted with either Ti or Y at either room temperature or 500°C. Some of the samples implanted at RT were then subsequently annealed at 500, 800, 1000 and 1100°C for each element.

The IONTOF 5 employs the use of Cs and O primary beam for sputtering but only the O beam has been used at an energy of 1 keV (an O beam is favourable for the study of Y and Ti ions). A second beam of Bismuth at 25 keV is used for the analysis of the ejected secondary ions in the depth profiling. The angle between the primary beam for sputtering and the mass spectrometer is 45°C and the angle between the Bi beam for analysing and the spectrometer is also 45°C. For sputtering, a region of 300µm x 300µm and an analysis region of 50µm x 50µm is then chosen close to the centre of the sputtering region. It is important that both the sputtering beam (O) and the analysing beam (Bi) are located at the same position to ensure that maximum number of secondary ions are analysed. Different regions of the specimens from the centre to the edges, were considered. A maximum concentration of metallic elements appeared to be present at the centre of the sample and the concentration was observed to decrease continuously towards the edges of the sample. Hence, the region of investigation was chosen as closest to the centre as possible for each sample.

The Faraday cup of the detector measures the current reaching the detector. It is this current reaching the detector which is converted to the intensity by the formula:

$$I_t = I_p Y[C_t]\gamma_t T$$

Where I_t is the intensity to be calculated, I_p is the primary ion current from the detector, Y is the secondary ion yield, C_t is the correction of the species, γ_t is the secondary ion formation and survival probability and T is the instrument transmission factor.

In simple elaboration of the process, the samples are placed on a copper grid, which is then placed on a sample holder. The sample holder is inserted inside the chamber and the vacuum is created. A software known as *Navigator* enables to view inside the chamber. The beams are then focused on the sample to be studied at the centre of the chosen region with the help of a

joystick. The duration of measurement is then set and the profiling begins. In this experiment, a chosen sputter time of 2500 seconds was set and the profiling completed in about 90 minutes. At the end of the profiling, the raw data of all possible isotopes of element present in the sample is saved.

Figure 2.25 IONTOF 5 instrument located at Unité de Catalyse et Chimie du Solide (UCCS), Université de Lille 1.

The data is then treated using a software known as *SurfaceLab* from IONTOF to perform analysis. All the spectroscopy modes including Surface spectroscopy (mass spectrum), surface imaging, depth profiling and even 2D/3D imaging are all possible. In this study only depth profiling and image depth profiling have been used. The isotopes of interest are selected and reconstructed in the *SurfaceLab* software to give both their depth profiles and depth profile images. The depth profiles are given in intensity against sputter time.

2.6.3 Calibration of depth profiles

Due to the fact that the depth profiles from the ToF-SIMS experiment are given in intensity as a function of the sputter time, calibration and quantification is essential for providing the depth profile in a much appreciated form.
In this purpose, Ti and Y as-implanted specimens were used as calibration references with respect to annealing conditions. A conversion factor between the intensity counts and the atomic concentration of metallic element was obtained assuming that all implanted atoms remains in the as-implanted specimens, i.e., the integral of the intensity profile as a function of depth for the as-implanted specimen corresponds to the implanted fluence. A reference as-implanted sample and annealed samples with the same implanted ion were thus analysed on the same day to get a valid conversion factor. This conversion factor may indeed vary in time. Finally, to convert the abscissa given in sputter time into depth, the maximum depth for each created crater on the sample was measured at the Institut de Physique Nucléaire d'Orsay (IPNO) using a confocal microscope at the PANAMA facility.

2.6.4 Comparison of SIMS with SRIM

The *Figure 2.26* shows the depth profiles of the as-implanted samples for Ti and Y implantations as well as the depth profiles predicted by SRIM. Compared to the SRIM concentration profiles, the SIMS profiles are shifted towards the surface of the sample with a peak concentration located for each element of interest close to 25-30 nm instead of the 40 nm as predicted by SRIM.

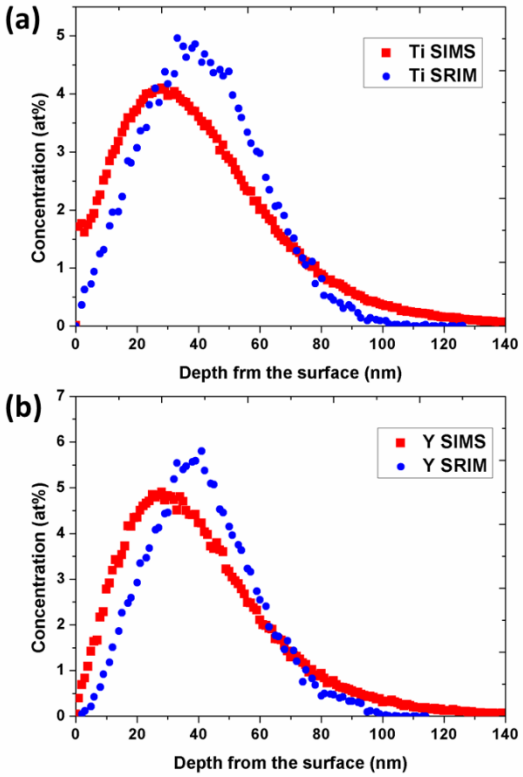

Figure 2.26 Comparison of the SIMS concentration profile with the SRIM concentration profile for (a) Ti and (b) Y implantations.

Chapter 3: Results

3. Synthesis of oxide nanoparticle in Fe10wt%Cr alloys using ion implantation

As detailed in the objective of the thesis (section 1.5), ion beam synthesis has been deployed as an experimental simulation technique of the milling processes used in the conventional fabrication of ODS steels to produce nano-oxide particles in FeCr alloys. Having in mind the fact that nanoparticles found in ODS steels are typically yttrium oxides or yttrium-titanium oxides and the idea of simulating the conventional scheme of fabrication, we focused on elaborating the formation of such yttrium oxides or yttrium-titanium oxides. Hence, we have implanted Y, Ti and O ions directly into FeCr samples using the implantation parameters as detailed in section 2.3.2. Thermal annealing was then performed to force the formation of nanoparticles in various samples (detailed conditions described in section 2.4). Characterizations have been performed using various conventional and analytical transmission electron microscopy (TEM) techniques. Conventional imaging techniques including bright Field (BF), dark field (DF) and diffraction patterns (DP) have been utilized. Analytical characterization techniques such as Energy Dispersive X-ray (EDX), Energy Filtered TEM (EFTEM) and Electron Energy Loss Spectroscopy (EELS) were also used for the determination of the elemental composition and the crystallographic structure of nanoparticles was determined using high resolution TEM (HRTEM).

This study has been conducted following three different modes of nanoparticle synthesis. In a first step, Ti and O ions have been implanted sequentially into FeCr samples at room temperature. The second set of experiments involved the implantation of Y and O ions into the FeCr sample. Finally, implantations of all three ions, Y, Ti and O, were performed in two different sequential orders. Investigations were then conducted on room temperature as-implanted samples and annealed samples as well as high temperature implanted samples in a few cases.

3.1 The case of Ti and O ion implantations into high purity FeCr

In the first scenario, Ti and O have been implanted into the FeCr matrix at room temperature. Firstly, both as-implanted and annealed thin foils were investigated by various TEM techniques, but oxidation effects possibly resulting from the formation of corrosion oxides (which will be elaborated in the following sections) made such samples quite difficult to study. Hence, bulk specimens were also implanted and annealed at high temperatures. The thin foils were annealed up to 800°C and the bulk specimens annealed up to 1100°C.

3.1.1 The as-implanted samples

Initially, thin foils implanted with Ti and O at room temperature were investigated by Energy Dispersive X-ray Spectroscopy (EDX) to confirm the presence of the implanted ions. The *Figure 3.1* shows an EDX spectrum of the as-implanted sample taken from a region with a thickness of approximately 80 nm, as measured by EELS. The spectrum indicates a peak of Ti not observed before implantation. A peak of O is observed at lower energy but this appears

overlapped with the Cr peak. Quantification by EDX gives a Ti concentration of about 2.8 at%, which is in good agreement with the implanted Ti concentration (i.e. 2.5 at.% as calculated by SRIM, see section 2.3.2). Due to the overlap of the peaks of O and Cr, an accurate quantification of the elemental composition is excluded.

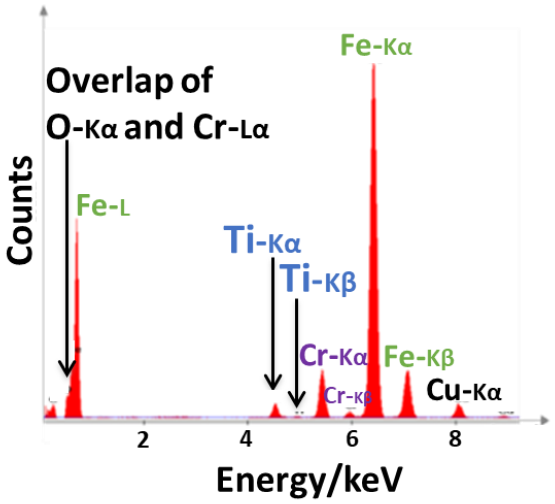

Figure 3.1 Energy Dispersive X-ray Spectroscopy (EDX) spectrum for the as-implanted (Ti,O) thin foil indicating the presence of Ti and O.

Conventional TEM bright field (BF) and dark field (DF) imaging conducted on the as-implanted thin foil sample showed a significant amount of defects including dislocation loops but no visible particles (as in *Figure 3.2(a)*). Diffraction patterns (DP) were also acquired on different regions of the thin foil. The diffraction pattern in the *Figure 3.2(b)* is the DP of the region imaged in *Figure 3.2(a)*. The dark region observed in *Figure 3.2(a)* is oriented close to a zone axis B = [-111]. The strong change of contrasts in the picture show a distortion of the specimen frequently observed in irradiated thin foils. In this region as well as for other regions of the thin foil and orientations of the matrix, only the spots corresponding to the matrix are visible in the diffraction patterns.

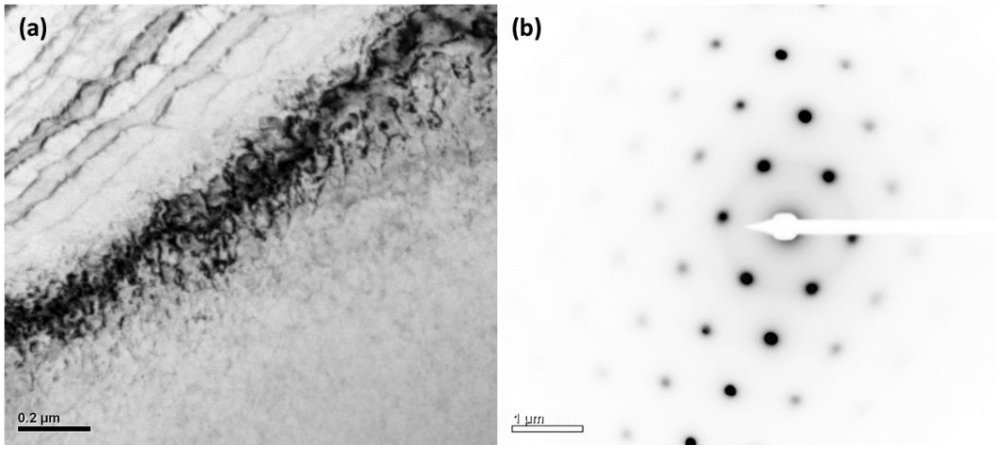

Figure 3.2 (a) Bright Field image of as-implanted Ti and O thin foil for a region with a (b) Diffraction Pattern orientated with B= [-1,1,1].

Finally, elemental characterization by the use of Energy Filtered TEM (EFTEM) was performed to highlight potential nanoparticles, which would not be observed in the conventional TEM characterization techniques. EFTEM images were acquired using both the

jump ratio (two-window) and three-window methods for the as-implanted sample (see section 2.2.3.4). The maps for all the investigated elements (Fe, Cr, Ti and O) - not shown here - appeared quite homogeneous indicating no enhancement of elemental presence within any clusters.

All the investigation techniques (both conventional and analytical characterization techniques) on the as-implanted thin foil thus suggest no nanoparticle formation after room temperature implantation.

With no nanoparticles evidently formed after room temperature implantation, annealing was performed to eventually enable the formation of nanoparticles. The aim was geared towards migration of the implanted atoms within the crystal structure, leading to precipitation of nanoparticles. Hence, both *in situ* TEM annealing of thin foils and *ex situ* annealing of bulk samples were performed to facilitate the formation of nanoparticles.

3.1.2 *In situ* annealing of TEM thin foils

3.1.2.1 Annealing at 500°C

In situ TEM annealing was carried out on the as-implanted sample using the FEI Tecnai G^2 20 twin microscope. The sample was mounted on a specific Gatan heating sample holder which possesses a maximum temperature of 800°C. The sample was heated to a desired temperature of 500°C within a period of 15 minutes for a duration of 90 minutes under vacuum. Observations were carried out during and after the annealing process. Diffraction patterns obtained after annealing immediately revealed additional reflections not observed before the annealing process. An example is reported in the *Figure 3.3*.

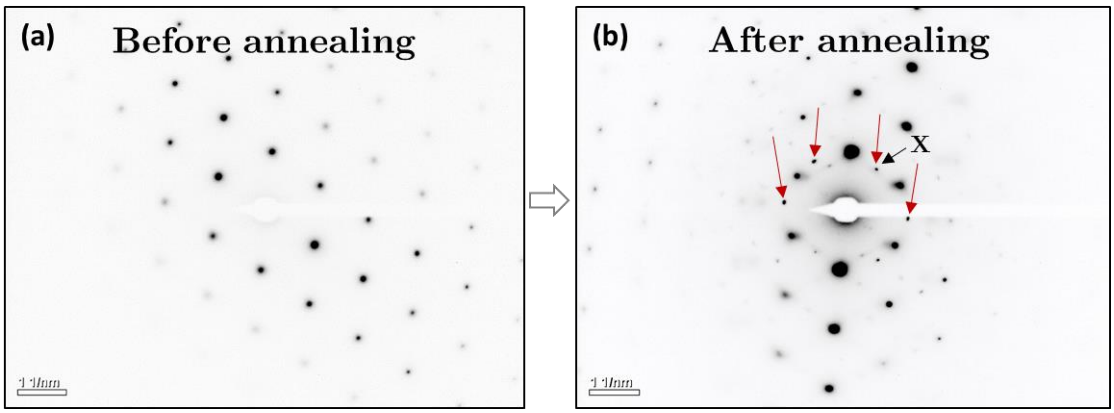

Figure 3.3 (a) Diffraction pattern of as-implanted Ti and O ions thin foil close to a zone axis B = [-111] (b) the DP of the same thin foil after annealing at 500°C for 90 minutes in the same orientation indicating additional reflections not observed before annealing. These additional reflections are highlighted with arrows.

Subsequent DF images corresponding to these reflections were taken. Many white spots were observed in the DF images obtained. These spots indicate precipitation of a crystalline phase. The same DF imaging was carried out in different zones within the sample and using other additional reflections, which produced similar results. The *Figure 3.4(a)* is the bright field image of the zone having the diffraction pattern shown in the *Figure 3.3(b)*. The corresponding dark field image using one of the additional reflections (labelled X) in the *Figure 3.3(b)* is shown in the *Figure 3.4(b)*. Analysis of the white spots observed in the *Figure 3.4(b)* was

performed using ImageJ software. Each precipitate (white dot) size was estimated using the equivalent diameter, which is defined as:

$$d_{eq} = 2 \times \sqrt{\frac{S}{\pi}}$$

Where d_{eq} is the equivalent diameter and S is the surface of the precipitate (white dot) observed in the dark field TEM image.

A total of 226 precipitates sampled produced an average d_{eq} of 5.8 nm. The size distribution of the precipitates in the *Figure 3.4(b)* is shown in the *Figure 3.4(c)*. The size of the precipitates range between 2 and 26 nm with most precipitates found between 3 and 12 nm.

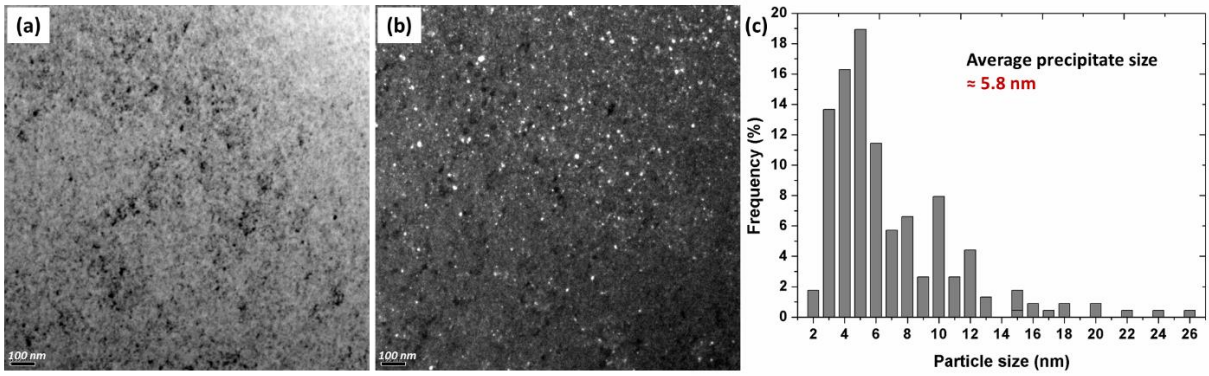

Figure 3.4 (a) Bright Field and (b) corresponding Dark Field image using one additional reflection of Figure 3.3(b) of the Ti and O ion-implanted thin foil and annealed at 500°C. The white spots indicate the formation of precipitates (c) size distribution of the nanoprecipitates formed in the Figure 3.4(b).

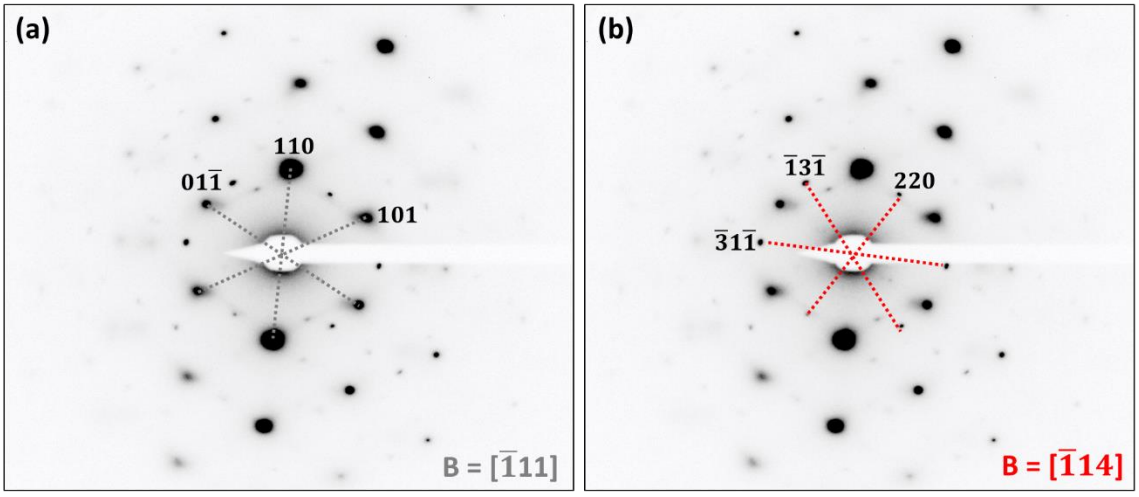

Figure 3.5 (a) Diffraction Pattern (DP) of thin foil implanted with Ti and O ions at room temperature and annealed at 500°C for 90 minutes with a B = [-1,1,1] orientation (b) indicating highlighted spots matching that of an *fcc* crystal structure of $FeCr_2O_4$ with an orientation B = [114].

The *Figure 3.5(a)* is the diffraction pattern for a selected zone after annealing. This is the same zone and diffraction as displayed in the *Figure 3.3(b)*. There are observed additional reflections in the diffraction pattern as compared to that before annealing (see *Figure 3.3(a)*). The highlighted reflections in grey in the *Figure 3.3(a)* correspond to the as-received FeCr matrix with an orientation B = [-111] (see detailed characterisation in section 2.2.6). A closer look at that diffraction pattern shows that the additional reflections with lower contrast (highlighted with red in *Figure 3.3(b)*) form a hexagon. The ratio of the lengths measured and

the angles formed seem to correspond to an *fcc* crystal structure with the orientation B = [-114]. The lattice parameter for this structure was determined as 0.85 nm from the measured interplanar distances. This quite closely matches the lattice parameter of Fe_3O_4 and $FeCr_2O_4$ of 0.8344 nm and 0.845 nm respectively. With Cr enrichment or presence confirmed by EFTEM within these precipitates (see below), the formation of $FeCr_2O_4$ appears most likely.

Elemental characterization was performed using Energy-Filtered TEM (EFTEM) to verify the composition of the identified clusters. The acquisition was done using Fe-L, Cr-L and Ti-L characteristic edges. The parameters used for each EFTEM investigation is given in section 2.2.3.4. The resulting jump ratio images are reported in *Figure 3.6*. Before EFTEM investigations, the samples were verified to be adequately thin for observations. The thickness of the zone from which the EFTEM elemental maps were acquired is estimated to be approximately 30 nm from the thickness map with an inelastic electron mean free path $\lambda \approx 110$ nm. The Ti map is smooth and homogenous with very little that can be inferred from. On the other hand, for the Cr, there appear enhanced coloured patches through most regions across the surface, although not very obvious. These enhanced coloured patches represent an enrichment in Cr. For the Fe, jump-ratio images on the contrary exhibited dark spots across most regions characteristic of a depletion of Fe. The presence of Fe in these spots cannot be excluded: the depletion in Fe only implies a lower Fe concentration compared to the matrix. The spots, which exhibit a depletion of Fe, coincide with the enrichment of Cr. Hence, there is Fe depletion in regions of Cr enrichment. Thus observed nanoprecipitates in conventional TEM should be of Cr rich composition.

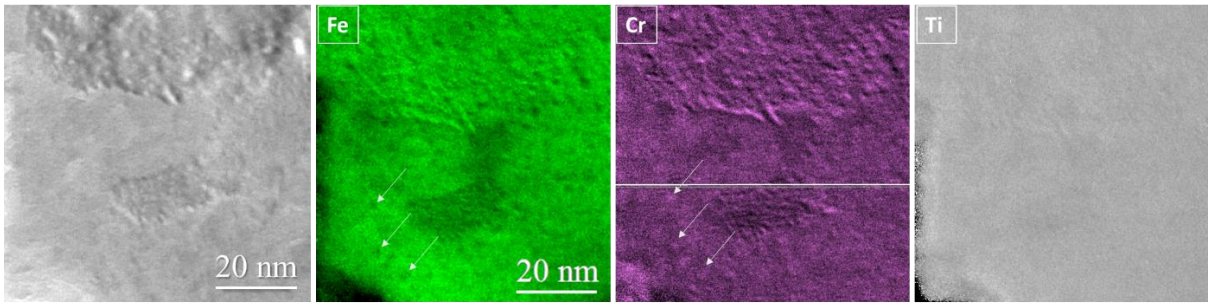

Figure 3.6 Bright Field (BF) image of chosen region together with EFTEM elemental maps acquired using the jump-ratio method for the thin foil implanted with Ti and O ions at room temperature and annealed at 500°C for 90 minutes in the vicinity of Fe-$L_{2,3}$ edge, Cr-$L_{2,3}$ and Ti-$L_{2,3}$ edges.

3.1.2.2 Annealing at 600°C

A further *in situ* TEM annealing was performed at a temperature of 600°C using the same microscope and conditions for 2 hours on as-implanted thin foils to further enhance the possibility of the formation of oxides of Ti. A unique observation made during the course of the *in situ* annealing was the fact that all the thin areas around the hole began to appear with white contrast. These regions with this white contrast evolved in time to form rectangular patches that grew to cover thicker regions away from the hole as is displayed in *Figure 3.7*.

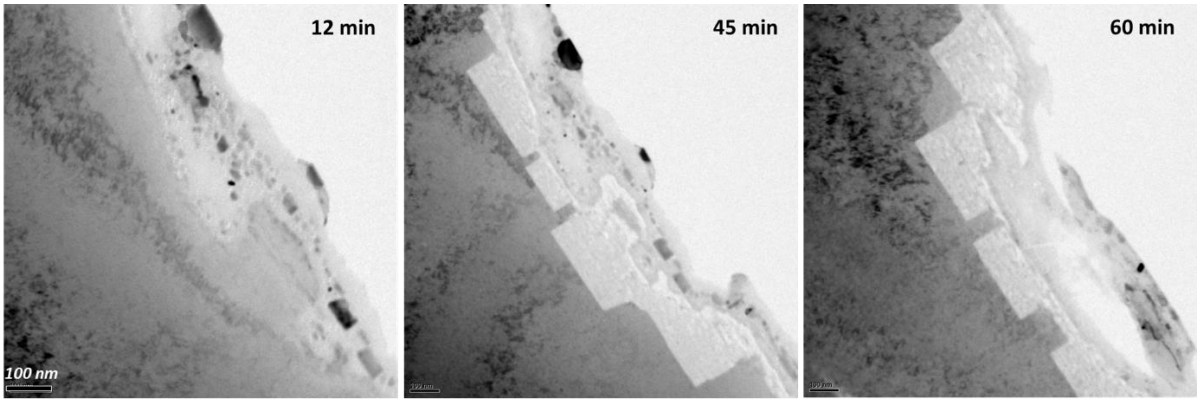

Figure 3.7 Bright Field (BF) TEM images of the as-implanted (Ti,O) thin foil during the *in situ* TEM annealing at 600°C showing the evolution as a function of time of the thinnest regions close to the hole.

A closer look at the regions further away from these large rectangular patches revealed the formation of many other small spots, some of which displaying a square shape. The *Figure 3.8(a)* is a bright field (BF) image of relatively small rectangular patches. Farther away from them, much smaller spots can be observed with a white contrast in underfocus condition. The contrast of these observed spots change in the overfocus condition as shown in *Figure 3.8(b)* and *(c)*. It is therefore these small clusters that grow in time to form the large rectangular patches.

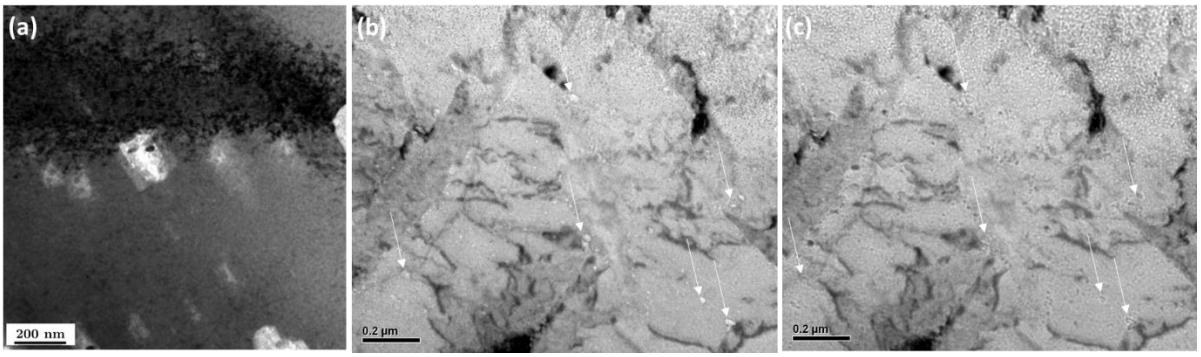

Figure 3.8 (a) Bright field image of small rectangular patches away from the edge of the thin foil as well as many small precipitates observed much further away from the hole in the (Ti,O) ion-implanted thin foil and annealed at 600°C observed in (b) underfocus and (c) overfocus conditions.

An elemental analysis was performed using EFTEM to characterize both the small spots and the big patches close to the hole. The *Figure 3.9(a)* shows an overview of the hole of thin foil and *Figure 3.9(b)* is a magnified view of a zone close to the hole including white contrast patches and a darker contrast region away from the hole. In the following, as annotated on *Figure 3.9(b)*, region A will refer to the white patches whilst region B will refer to a thicker region with dark contrast. The region chosen for EFTEM investigation is highlighted in *Figure 3.9(b)* with a square.

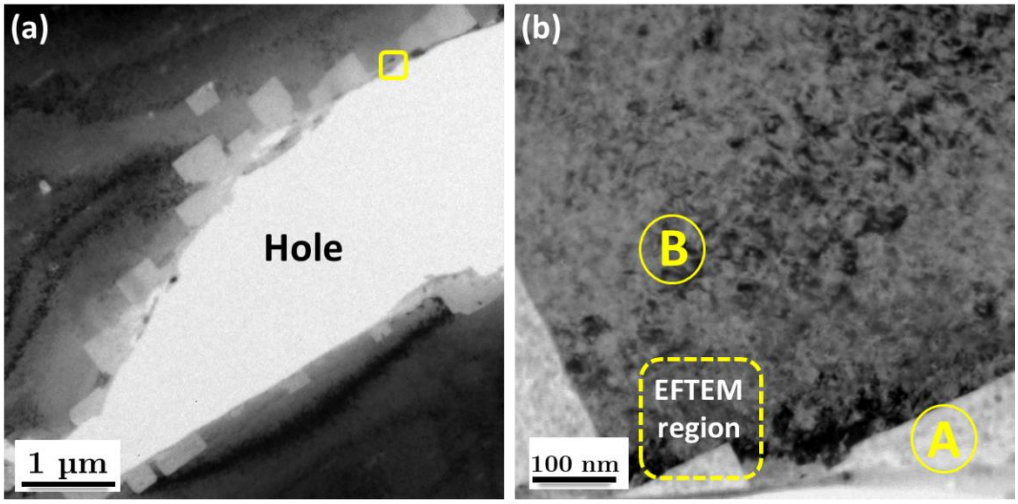

Figure 3.9 (a) Bright Field (BF) image of the hole of the thin foil implanted at room temperature and annealed at 600°C for 2 hours indicating the white contrast regions close to the hole and (b) Magnified image showing two distinct regions [A] closest to the hole and [B] further away from the hole as well as the region chosen for EFTEM.

The EFTEM elemental maps are reported in *Figure 3.10*. In region B, dark spots, which represent an elemental depletion, are observed in the Fe elemental map. These spots with Fe depletion correspond to white spots in Cr and O maps, highlighting an enrichment of Cr and O. Ti elemental maps again appear quite homogeneous in the region B. In region A, similar contrasts are observed showing a depletion of Fe and enrichment in both Cr and O. The Ti map also shows a slightly enhanced white contrast in region A which could be an artefact resulting from a varying thickness. The elemental characterization therefore appears to suggest the formation of Cr (and possibly Fe) oxide formation with no obvious indication of Ti presence.

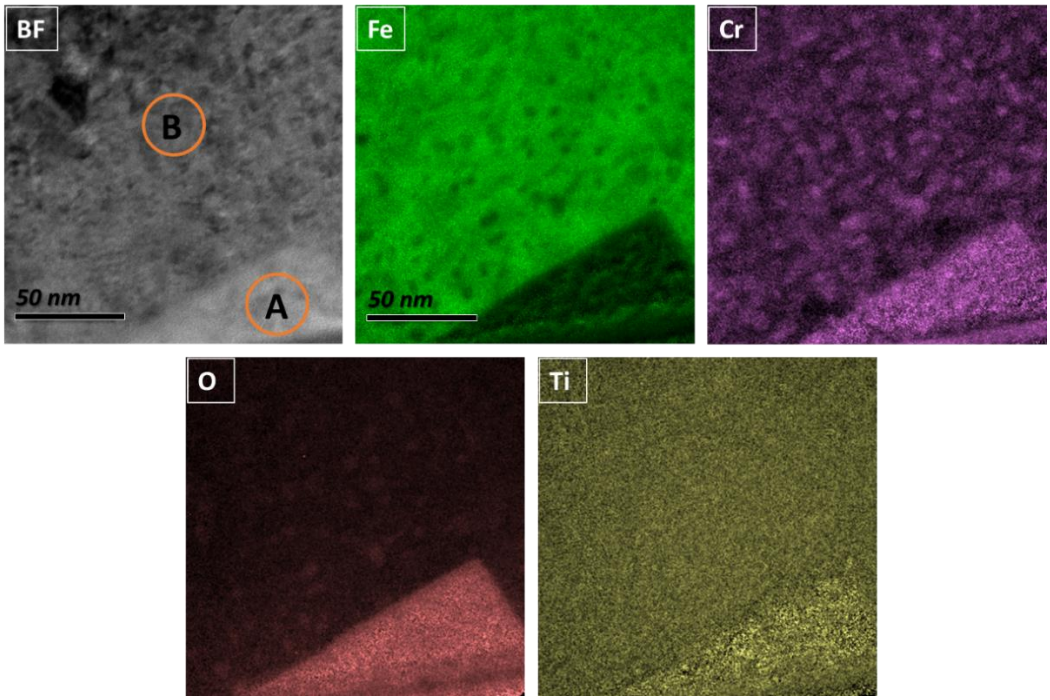

Figure 3.10 Energy-Filtered TEM elemental characterization of the thin foil implanted with Ti and O ions at room temperature and *in situ* annealed at 600°C for 2 hours. Bright Field (BF) image of the region chosen for EFTEM together with elemental maps acquired using the three-window method in the vicinity of Fe-$L_{2,3}$ edge, Cr-$L_{2,3}$, O-K and Ti-$L_{2,3}$ core loss edges.

The detailed crystallographic structure and elemental quantification characterisation of zones A and B were performed and showed the presence of $FeCr_2O_4$ oxide (see annex 1).

The presence of $FeCr_2O_4$ on the thin edges of the specimen implies that the *in situ* annealing performed at 600°C resulted in the loss of Fe from the FeCr matrix into the vacuum chamber. This Fe is probably attracted and attached to the magnetic pole-pieces of the TEM. *In situ* annealing was thus discarded in the following in favour of *ex situ* annealing under vacuum in the chamber of IRMA ion implanter.

Choice of annealing temperature

The next issue to address was to determine at which higher temperature to conduct the annealing to force the formation of oxides of Ti. As explained in section 2.6, Time-of-Flight Secondary Ion Mass Spectroscopy (Tof-SIMS) was performed to observe the diffusion of Ti atoms in the FeCr base alloy and chose an appropriate annealing temperature to ensure the formation of oxides of Ti.

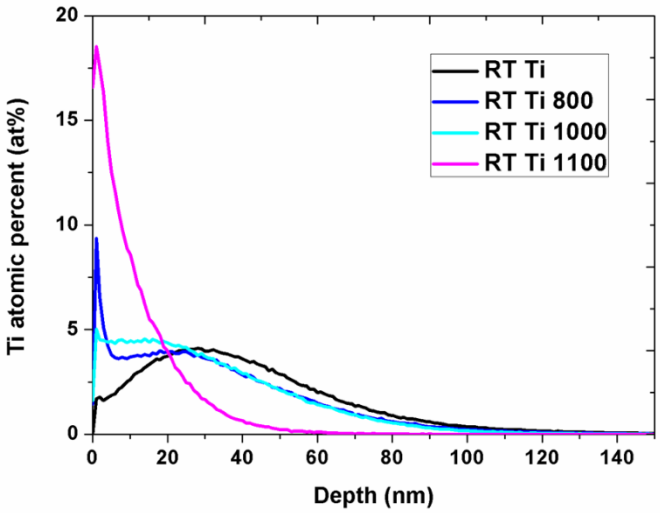

Figure 3.11 Depth profiles obtained using Time-of-Flight Secondary Ion Mass Spectroscopy (ToF-SIMS) for Ti ions implanted in Fe10Cr at room temperature and subsequent annealing at 800, 1000 and 1100°C.

In the *Figure 3.11* are the distributions of ion profiles as a function of depth for a Ti implanted sample as well as samples Ti-implanted and annealed from 800 to 1100°C. As compared to the profile for the as-implanted sample, the profile for the sample annealed at 800°C tends to drift towards the surface of the sample. The ions appear to diffuse more towards the surface of the sample at 1000°C and even more at 1100°C, thereby showing an enhanced diffusion of Ti atoms towards the surface with increasing annealing temperature. Since a diffusion of Ti ions seems to already occur at 800°C, the subsequent annealing was conducted at this temperature.

3.1.2.3 Annealing at 800°C

A further *ex situ* annealing was thus conducted on thin foils at 800°C for 2 hours in a chamber with a similar pressure as the one in the column of the TEM (*i.e.* 1.2 x 10^{-5} Pa). The annealing temperature of 800°C was reached within 45 minutes and was maintained for 2 hours. These annealed thin foils immediately revealed two distinct types of particles. Smaller

types of particles of the order of a few nanometres and much larger types of particles of the order of a hundred nanometres were observed. The *Figure 3.12* is an image illustrating the particles in focus, over-focus and under-focus conditions.

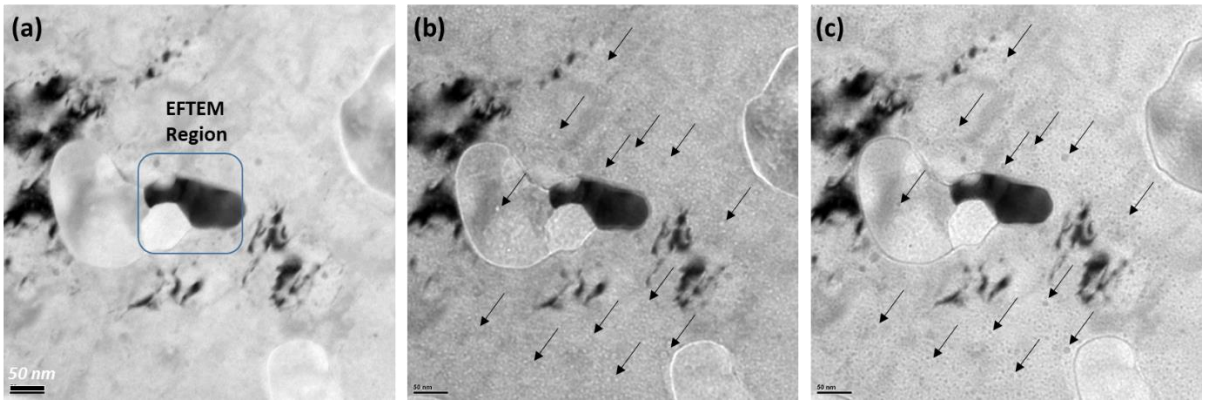

Figure 3.12 Bright Field (BF) TEM imaging of the (Ti,O) as-implanted sample annealed at 800°C for 2 hours indicating the formation of large and smaller clusters within the sample as well as the chosen region for EFTEM investigation (a) close to focus condition (b) in the underfocus condition and (c) overfocus condition.

To verify the chemical composition of these particles, Energy-Filtered TEM (EFTEM) investigations were conducted. The EFTEM investigation targeted the composition of both types of particles (small and large particles). A region as indicated in the bright field (BF) image in *Figure 3.13* was chosen (the average thickness of this region was determined as approximately 24 nm by EELS investigation). The EFTEM elemental maps are reported in *Figure 3.13* along with a BF image of the zone. The elemental map for Fe indicates that both large and small clusters are depleted in Fe. They are however enriched in Cr and O as was evident in the previous annealing conditions. Unlike the previous annealing conditions, these zones are also clearly enriched in Ti. The small and large precipitates formed after Ti and O ion implantation and annealing at 800°C thus contain Cr, O and Ti elements.

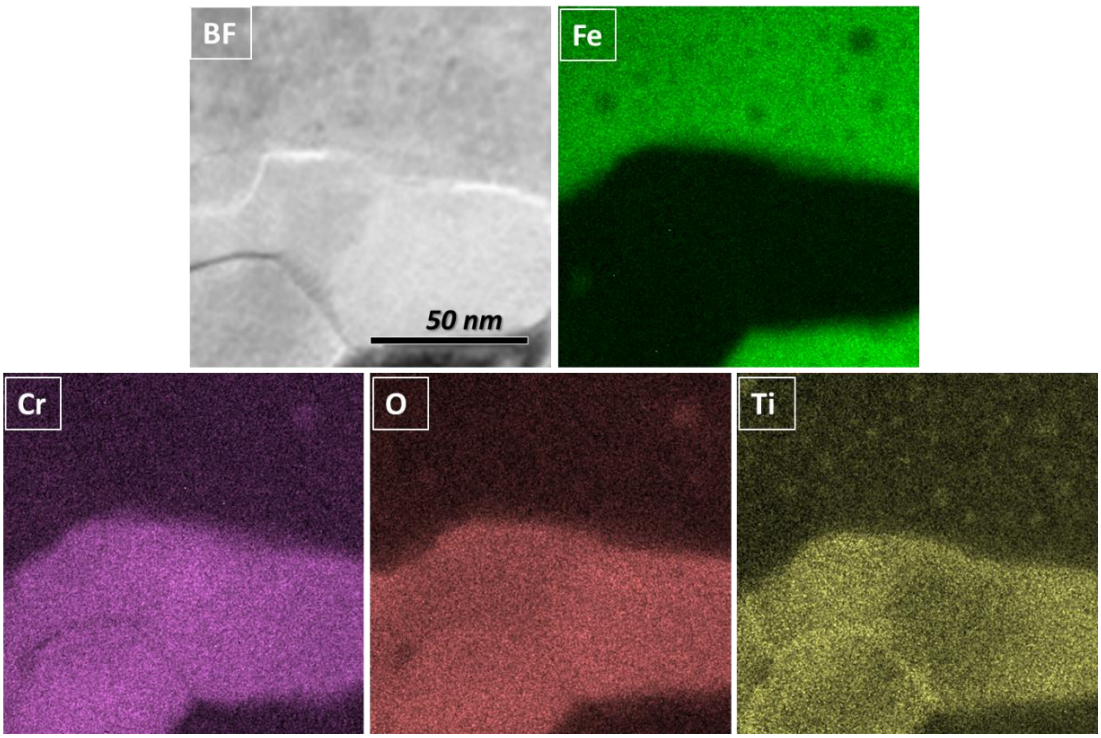

Figure 3.13 Energy-Filtered TEM (EFTEM) elemental characterization of the thin foil implanted with Ti and O ions at room temperature and annealed at 800°C for 2 hours. Bright Field (BF) image of the region chosen for EFTEM together with elemental maps acquired using the two-window jump ratio method in the vicinity of Fe-$L_{2,3}$ edge, Cr-$L_{2,3}$, O-K and Ti-$L_{2,3}$ core loss edges.

To confirm this result, a STEM-EDX investigation was carried out on one of the large particles. The *Figure 3.14* shows one selected particle with a size of approximately 100 nm, which is surrounded by a white contrast region. EDX spectrum imaging in a horizontal line was conducted running through the particle as indicated in *Figure 3.14*. Four distinct zones have been highlighted. The zone 1 is a zone outside the particle, the zone 2 represents the zone within the particle, the zone 3 represents the white contrast zone around the particle and the zone 4 is the other zone outside the particle. The spectra obtained corresponding to zones 1 and 4, which effectively represents the matrix, shows in *Figure 3.15* high peaks for Fe, weaker Cr peaks and much weaker peaks for Ti. The O-K peak (roughly 0.52 eV) overlaps with the Fe-L peak (roughly 0.70 eV) as well as Cr-L peak (roughly 0.57 eV) at low energy and hence oxygen is not easily identifiable. The overlapping of the peaks also makes an accurate quantification quite complicated to achieve. In the zone 2, which represents the particle, the Cr, Ti and presumably O peaks increase significantly whilst the Fe peak decreases significantly. This confirms EFTEM results with particles containing Cr, Ti and O, or Fe, Cr, Ti and O with lesser amounts of Fe compared to the matrix. The zone 3 with the white contrast regions as indicated in the *Figure 3.15* had much less counts compared to other zones suggesting a very thin region. The relative intensity of peaks is roughly equivalent to what is observed in zone 2 (Spectrum 2). The white contrast of zone 3 thus results from a thinning of the zone associated with the precipitation of the oxide.

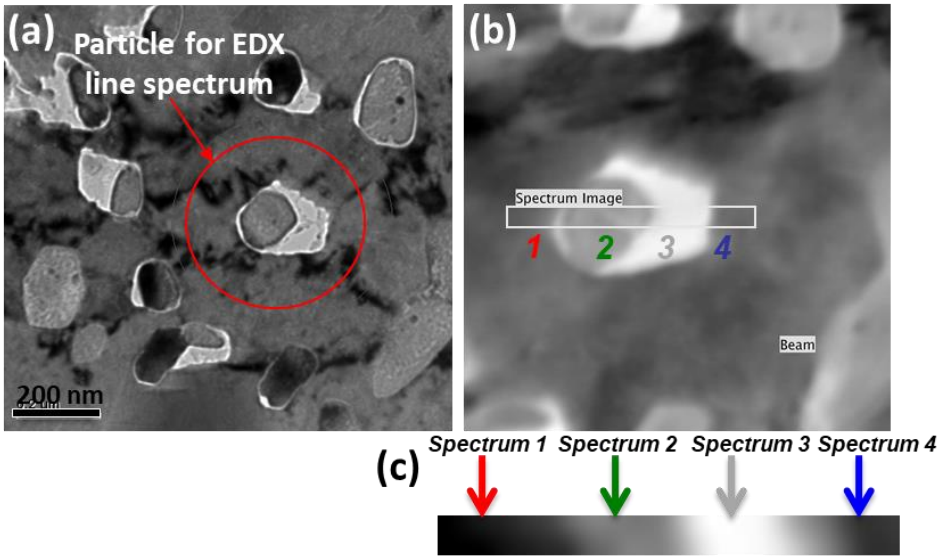

Figure 3.14 (a) Bright Field (BF) image of the region showing the particle of interest (b) Bright Field image of the particle of interest indicating the line spectrum imaging and 4 distinct zones highlighted (c) Image showing the pixels from which EDX spectra shown in Figure 3.15 are extracted are also indicated.

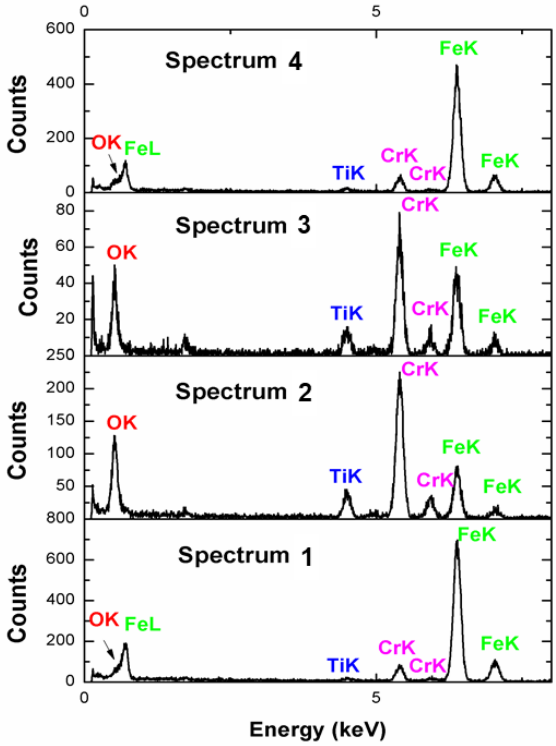

Figure 3.15 Scanning Transmission Electron Microscopy-Energy Dispersive X-ray Spectroscopy (STEM-EDX) spectra of the highlighted particle in Figure 3.14 from the (Ti,O) ion-implanted and annealed thin foil at 800°C for the four distinct chosen regions highlighted in Figure 3.14 (c) where spectrum i represents the spectrum from the chosen region i and so on.

Crystallographic structure of the particles observed with Cr,O and Ti was investigated using the High Resolution TEM (HRTEM) technique. HRTEM imaging was performed on several regions and particles of the thin foil. The *Figure 3.16(a)* is a HRTEM image of a selected region of the sample showing a typical observed particle with a diameter of approximatively 12 nm and surrounded by the base matrix. The *Figure 3.16(b)* is a fast fourier transform (*fft*) image of a zone outside the particle. The ratio of the lengths and interplanar distances were determined and checked to match the FeCr matrix. The *fft* corresponds to a zone axis B = [111] of the FeCr *bcc* structure.

The *fft* of the highlighted particle is also displayed in the *Figure 3.16(c)*. It shows a presumable orientation of a *bcc* structure with B= [111]. This could also correspond to an *fcc* structure with B = [111] or a hexagonal closed pack (*hcp)* structure with B = [0001] orientation. Knowing the composition of the matrix and the implanted elements as well as results from the chemical characterization techniques described, the possible oxides formed were considered for these structures (see list of considered oxides in annex VII). The interplanar distances seem to only match those of $FeCr_2O_4$ among the large variety of different oxide compounds. Details relating to the angles and ratio of the lengths between the spots appeared to correspond to an *fcc* crystal structure with a lattice parameter of 0.863 nm, which quite matches the lattice parameter of $FeCr_2O_4$. The formation of an oxide having a $FeCr_2O_4$ structure is quite reasonable as this crystallographic structure is already observed for lower annealing temperatures.

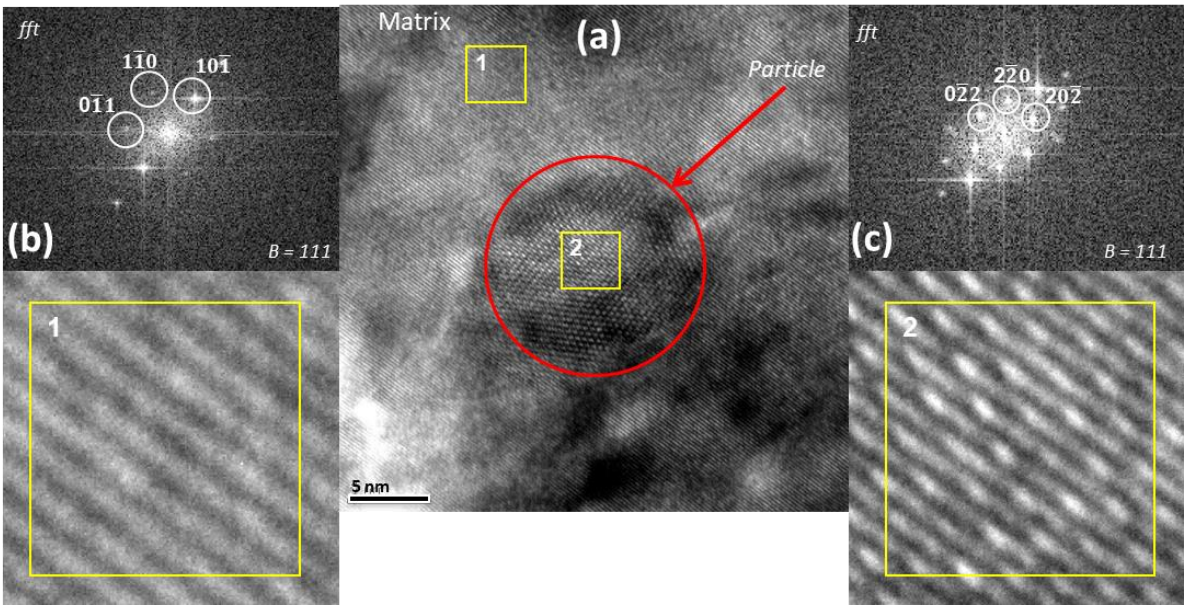

Figure 3.16 High Resolution TEM (HRTEM) image of a selected particle observed in the thin foil implanted with Ti and O ions annealed at 800°C for 2 hours. In the middle is the selected particle surrounded by the matrix indicating two specified regions 1 and 2. The highlighted zone 1 is the matrix and on the left is a magnified image of this region and a corresponding Fast Fourier transform with an orientation B = [-1,1,1] matching the *bcc* crystal structure of the FeCr matrix. On the right is a magnified zone of the particle and a corresponding Fast Fourier transform with an orientation B = [-111] matching an *fcc* crystal structure of $FeCr_2O_4$.

3.1.2.4. Conclusions on *in situ* annealing of TEM thin foils implanted with Ti and O ions

Room temperature implantation of Ti and O ions into TEM thin foils does not result in the formation of visible nanoprecipitates. Annealing at high temperatures of 500 and 600°C results in the formation of large $FeCr_2O_4$ patches on the thin edges of the thin foil as well as smaller patches further away from the hole. During the annealing, the large patches grow in time to cover thicker regions, therefore highlighting a surface process. The diffusion of Ti atoms triggered at the annealing temperature of 800°C results in the Ti enrichment of the $FeCr_2O_4$ precipitates on the surface of the thin foil.

It has been established that chromium-containing steels can be degraded at elevated temperatures by carburization, sulfidation or active oxidation. In most publications dealing with corrosion of FeCr under water [Bischoff 2012, Hu 2013, Isselin 2010, Chen 2007, Cho 2007] or in air [Hoelzer 2000, Kaito 2004], the formation of a dual or triple oxide layer is observed and explained due to differences in atomic diffusion rates. Under thermal annealing, the O diffuses inwards forming Cr-rich oxides with the slow diffusing Cr. The Fe diffuses outwards towards the surface forming an Fe-rich oxide on the surface. An interface between these oxide layers forms an Fe-Cr rich oxide. The protection layer is thus normally a triple oxide layer: an outer layer usually formed of Fe_3O_4 (magnetite), an inner layer formed of a mixed iron-chromium spinel and a diffusion layer containing Cr rich precipitates [Bischoff 2012, Kaito 2004, Hoelzer 2008]. In more recent investigations [Martinelli 2015], the formation of the mixed iron-chromium oxide has been reported to be that of the Fe_2CrO_4. As in many corrosion experiments reported in literature, the present results on thin foils show that $FeCr_2O_4$ is formed on the surface of the annealed samples. The amorphous oxide layer formed on the thin foils is predicted to be resulting from the oxygen and other gases (i.e. CO_2) from the vacuum chamber

within the TEM after pumping as well as a probable oxide layer formed directly after thinning in the Tenupol during the TEM thin foils preparation (see section 2.2.5). Both factors are proposed to provide enough O atoms for the corrosion processes under annealing. No Fe_3O_4 particles are detected which is probably due to the fact that these experiments are performed under vacuum contrary to the corrosion experiments in the literature. In our experiments, the out-diffusing Fe atoms are very likely to be attracted by the magnetic pole-pieces of the TEM. In addition to this contamination, the surface oxide inhibits the observation and possibly formation of potential nanoprecipitates beneath the surface of the sample. This prompted the investigation of bulk specimens instead of TEM thin foils. Hence, in the subsequent sections, lamellas which have been extracted to give a transverse view or a cross section after ion implantation and annealing of bulk specimens, are considered.

3.1.3 Bulk sample annealing

Focused Ion Beam (FIB) lamellas in cross-sections have been extracted from bulk samples implanted with Ti and O ions at room temperature followed by subsequent annealing under vacuum at high temperatures. The bulk samples after ion implantation at RT were annealed inside a vacuum chamber with similar pressure as that in the operating TEM (i.e. approximately 2 x 10^{-5} Pa). The FIB lamellas were extracted only after annealing. The prepared FIB lamellas have a final thickness of < 50 nm. This made them quite ideal for the TEM investigations such as EFTEM and HRTEM. These samples extracted using the FIB thin foil preparation will be described hereafter as FIB lamella of annealed bulk specimen.

3.1.3.1 Annealing at 600°C

As-implanted bulk samples with Ti and O ions were annealed within the vacuum chamber for 2 hours at 600°C. The *Figure 3.17* is a typical region of a FIB lamella annealed at 600°C. The protection layers used in the FIB milling process can be observed. Conventional TEM Bright Field (BF) imaging reveals a distinct white contrast layer formed on the surface of the sample with a thickness of close to 10 nm and even thicker at certain regions. This layer is very likely to be a surface oxide layer of $FeCr_2O_4$ as observed in the previous section, and as suggested by the EFTEM results reported below. Additional particles with a size ranging between 2 and 20 nm are observed beneath the surface within the bulk of the specimen. These particles are quite difficult to visualize in the BF imaging close to focus. They are however clearly seen in underfocus and overfocus conditions as in the *Figure 3.17 (b)* and *(c)*, respectively.

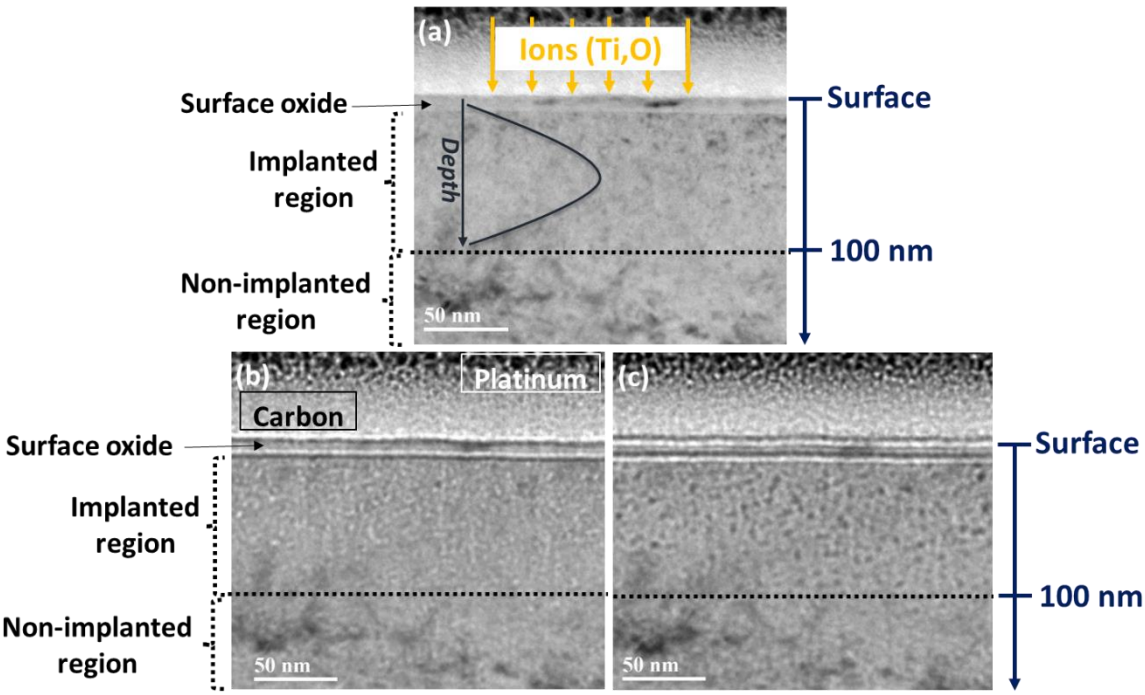

Figure 3.17 Bright Field (BF) imaging of FIB lamella from bulk specimen implanted with Ti and O ions and annealed at 600°C indicating the formation of nanoparticles within the bulk of the sample (a) close to the focus condition, (b) in underfocus and (c) overfocus conditions. The profile observed in (a) is an illustration of the distribution of ions as estimated by SRIM. See section 2.3.2 for details on SRIM profile ion distribution.

Some of the particles appear to be slightly elongated. The use of Feret's diameter F or Caliper diameter is therefore preferable to the use of equivalent diameter. The Feret's diameter measures the size of the object of interest along a specified direction and in this case, along the largest dimension or the elongated direction. The averaged Feret's diameter is expressed simply as: $< F > = P/\pi$ where P is the perimeter of the surface [Walton 1948].

The average length (Feret's diameter) of these observed particles was determined for a region pictured in the *Figure 3.18*. The chosen region covered an area of 110 nm by 450 nm (as shown in *Figure 3.18(a)* highlighted region with dashed lines) and the average length of the particles was determined using the ImageJ software to be approximately 6 nm. These particles have been observed from the surface of the sample to a depth of about 80 nm – 100 nm. Taking into account an implanted region of close to 100 nm, these particles are formed precisely within the implanted region, as expected (see SRIM Ti ions profile superimposed in *Figure 3.17(a)*). The particle size density was determined to be approximately 10^{23} m^{-3} for the region, which was measured to be approximately 38 nm thick.

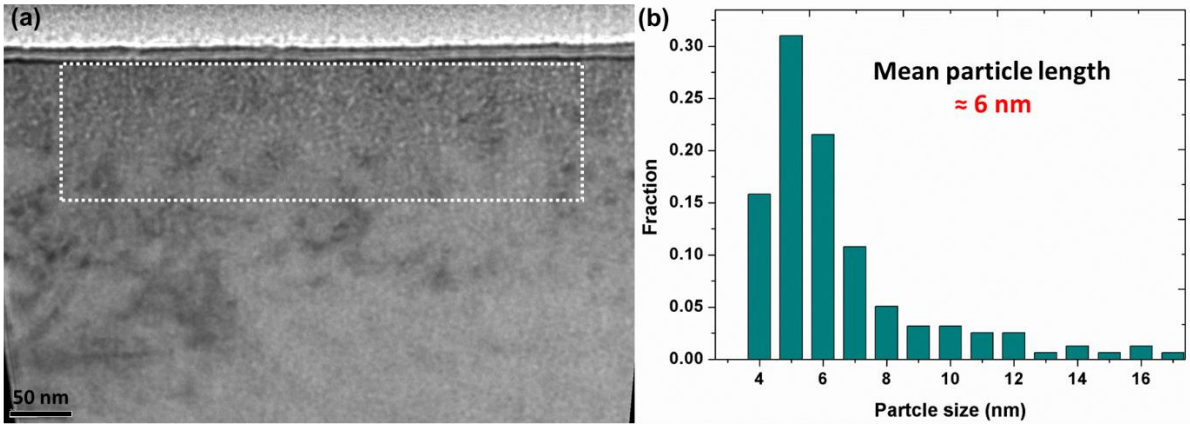

Figure 3.18 Bright Field (BF) image of the region chosen from bulk specimen implanted with Ti and O ions and annealed at 600°C for particle analysis and (b) Particle size (using the Feret's diameter) distribution of particles observed in the Figure 19 (a) highlighted region.

Chemical characterization by the use of EFTEM technique was performed on the sample to determine the chemical composition of these observed particles. EFTEM elemental maps presented in the *Figure 3.19* reveal a surface layer as observed in the BF image with enrichment in Cr and O and depletion in Fe. Ti elemental maps appeared quite homogeneous. Additionally, several spots corresponding to the particles were observed in the sub surface layer. These spots are enriched in Cr and O and depleted in Fe, as can be seen for the surface layer. The chemical composition results by EFTEM is similar to the previous annealing temperature of 500°C and 600°C for the thin foil and hence a similar assertion can be made with a precipitation and formation of nanoparticles composed of Cr and O and possibly Fe. The surface layer is very likely to be made up of $FeCr_2O_4$ as observed in thin foils.

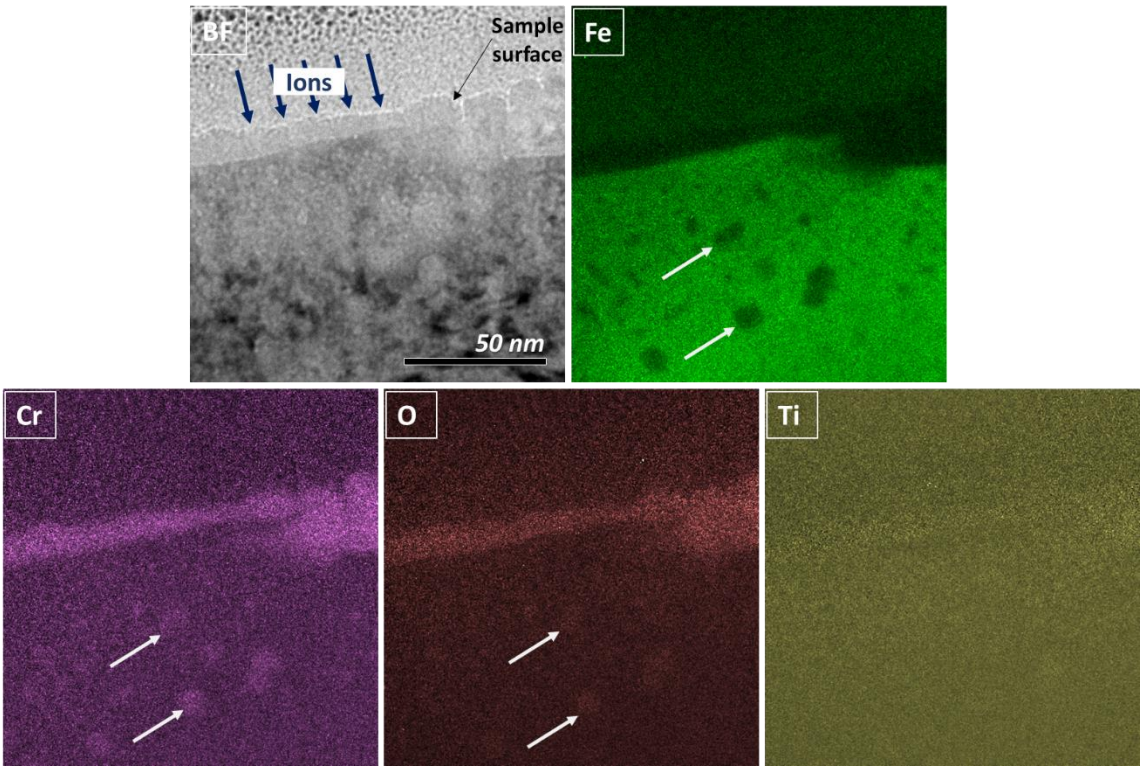

Figure 3.19 Energy-Filtered TEM (EFTEM) elemental characterization of the FIB lamella extracted after ion implantation at room temperature and annealing at 600°C for 2 hours. Bright Field (BF) image of the region chosen for EFTEM together with elemental maps acquired using the two-window

jump ratio method in the vicinity of Fe-$L_{2,3}$ edge, Cr-$L_{2,3}$, O-K and Ti-$L_{2,3}$ core loss edges. The thickness of the FIB lamella in the chosen region was determined by EELS as approximately 30 nm.

As a complimentary investigation and to verify the composition of the particles observed in the FIB lamella, STEM-EDX imaging using the ChemiSTEM technology has been performed. The design and principle of the ChemiSTEM is detailed in section 2.2.3. In the *Figure 3.20(b)* is a BF image of the mapped region with a lower magnification image highlighting this region in the *Figure 3.20(a)*. The Fe elemental map displays dark patches representing a depletion in Fe, which correspond to observed nanoparticles in the conventional imaging. Cr maps indicate that these particles are enriched in Cr. The Ti map does not appear homogeneous but the nanoparticles do not seem to be enriched in Ti. The O map appears quite homogeneous even though it is clear that such nanoparticles are oxides. This may result from a strong absorption in the specimen of the low energy O-K X-rays, or alternatively from an oxide layer covering the whole surface of the FIB lamella.

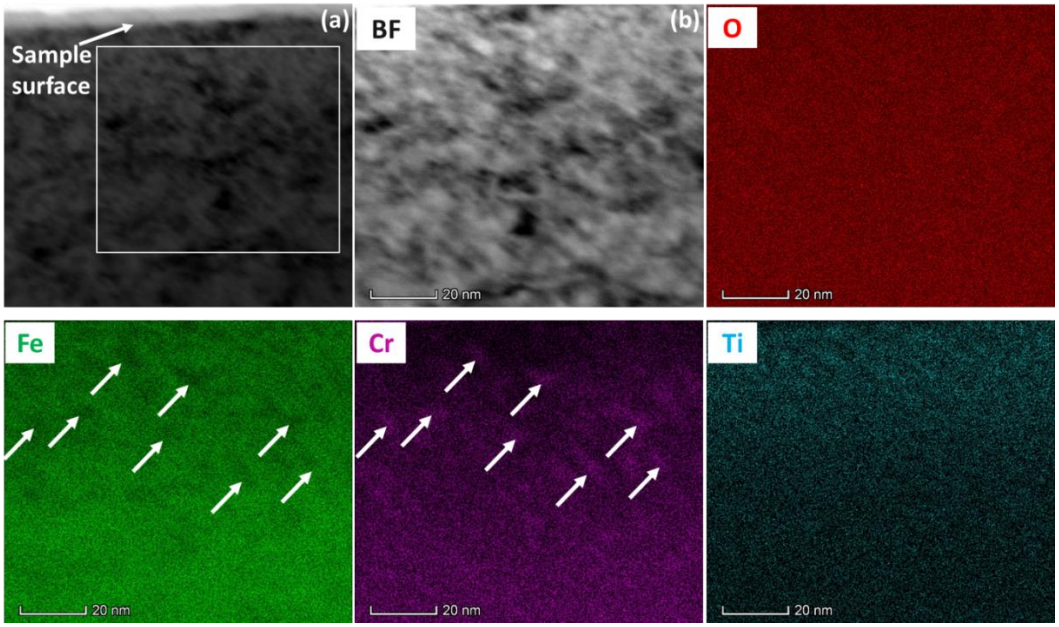

Figure 3.20 STEM-EDX elemental mapping of FIB lamella of Ti and O ion-implanted bulk specimen annealed at 600°C using ChemiSTEM technology. (a) Bright Field (BF) image indicating the selected region, (b) a zoom of the Bright Field (BF) image showing the mapped region, together with elemental maps for Fe, Cr, Ti and O as indicated. The mapping has been performed for 40 minutes at a count rate of 40k counts/second.

A line scan was then performed for one of these particles imaged as highlighted in the *Figure 3.21(a)*. Fe depletion is clearly observed for this particle together with the Cr enrichment. No Ti is detected in the particle.

It can therefore be confirmed from the EFTEM and STEM-EDX results that the particles observed in the FIB lamella after annealing at 600°C are chromium-oxide nanoparticles with apparently no Ti in their composition.

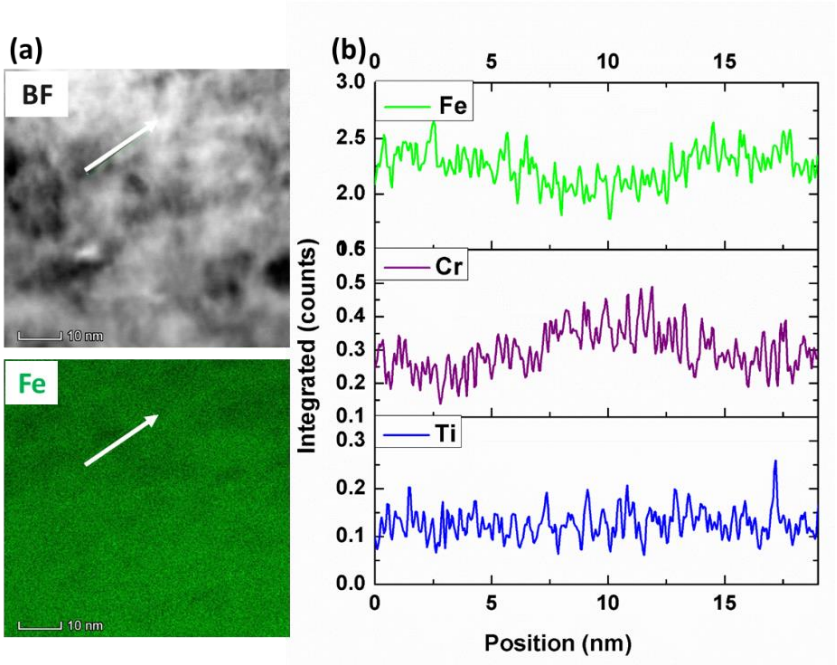

Figure 3.21. STEM-EDX 1-D line scan of particle within the FIB lamella of Ti and O implanted bulk specimen annealed at 600°C using ChemiSTEM technology. (a) BF image and Fe elemental map indicating the position of the line scan for a particle (b) Line scans for Fe, Cr, Ti.

To identify the crystallographic structure of particles observed, HRTEM imaging of these particles were performed. Several particles from many different regions within the implanted region were investigated. Out of all the particles identified and characterized, the *Figure 3.22* shows HRTEM images taken for four different observed particles, which have been labelled *(a)* to *(d)*. For each of these particles, the image labelled *(i)* is the HRTEM image of the particle embedded in the matrix, the image labelled *(ii)* is the high magnification image of the particle and the image *(iii)* illustrates the fast Fourier transform (*fft*) of the particle. The sizes of these particles were determined to be less than 10 nm.

The *Figure 3.22(a)* and *(b)* illustrates two particles, which appear to be elongated and identical in the magnified TEM images in *(ii)*. The orientations of these two particles are also exactly similar regarding the *fft* images. In the *fft* images, the measured angles and interplanar distances closely match those of the zone axis B= [2-21] of the corundum hexagonal crystal structure of the type Cr_2O_3 : the measured interplanar distances for the (110), (012) and (114) atomic planes are 0.24, 0.37 and 0.28 nm, respectively, whilst the theoretical interplanar distances of the corundum hexagonal crystal structure of the type Cr_2O_3 are d_{110} = 0.24, d_{012} = 0.36 and d_{114} = 0.26 nm, and the measured angles between (110) and (102) atomic planes, and between (102) and (114) atomic planes, were determined as 41° and 49°, respectively, with theoretical values of 43° and 47°. From the *fft* image, it appears that the (110) planes of the FeCr matrix are parallel to the (110) planes of the Cr_2O_3 structure type particle ((110)FeCr//(110)Cr_2O_3).

In the *Figure 3.22(c)* and *(d)* are two additional investigated particles where a similar orientation for both of the particles is illustrated in the *fft* images albeit with an angle of rotation. The interplanar distances and angles from the *fft* images match those of a zone axis B = 511 of the corundum hexagonal structure of the type Cr_2O_3 (the interplanar distances of (011), (210) and ((201) or (221)) atomic planes were measured as 0.40, 0.24 and 0.20, respectively, whilst the theoretical values are d_{011} = 0.40, d_{210} = 0.24 and d_{201} or d_{221} = 0.21

nm). Elsewhere, the measured angles between (011) and (210) atomic planes were determined as 88 and 92° which are closely related to the angles of the corundum hexagonal structure of the type Cr_2O_3 at 90°. Orientation relationships between the lattices of the particles and the matrix are highlighted on the *fft* images. In both *(c)* and *(d)*, the zone axis B = -111 of the matrix is parallel to the zone axis B = [122] of the particle ((-111)FeCr//(122)Cr_2O_3) and in the image plane, all the spots of the matrix coincides with the spots of the particle with (110)FeCr//(0-22)Cr_2O_3, (01-1)FeCr//(-201)Cr_2O_3, (101)FeCr//(2-21)Cr_2O_3 and (-112FeCr//-2-12)Cr_2O_3.

The HRTEM imaging therefore demonstrates that particles with different orientations as shown correspond to the formation of the corundum hexagonal crystal structure of the type Cr_2O_3. A noticeable point for all the particles observed by HRTEM is that they all appear to be elongated in parallel to {110} planes of the FeCr matrix (planes of highest atomic density).

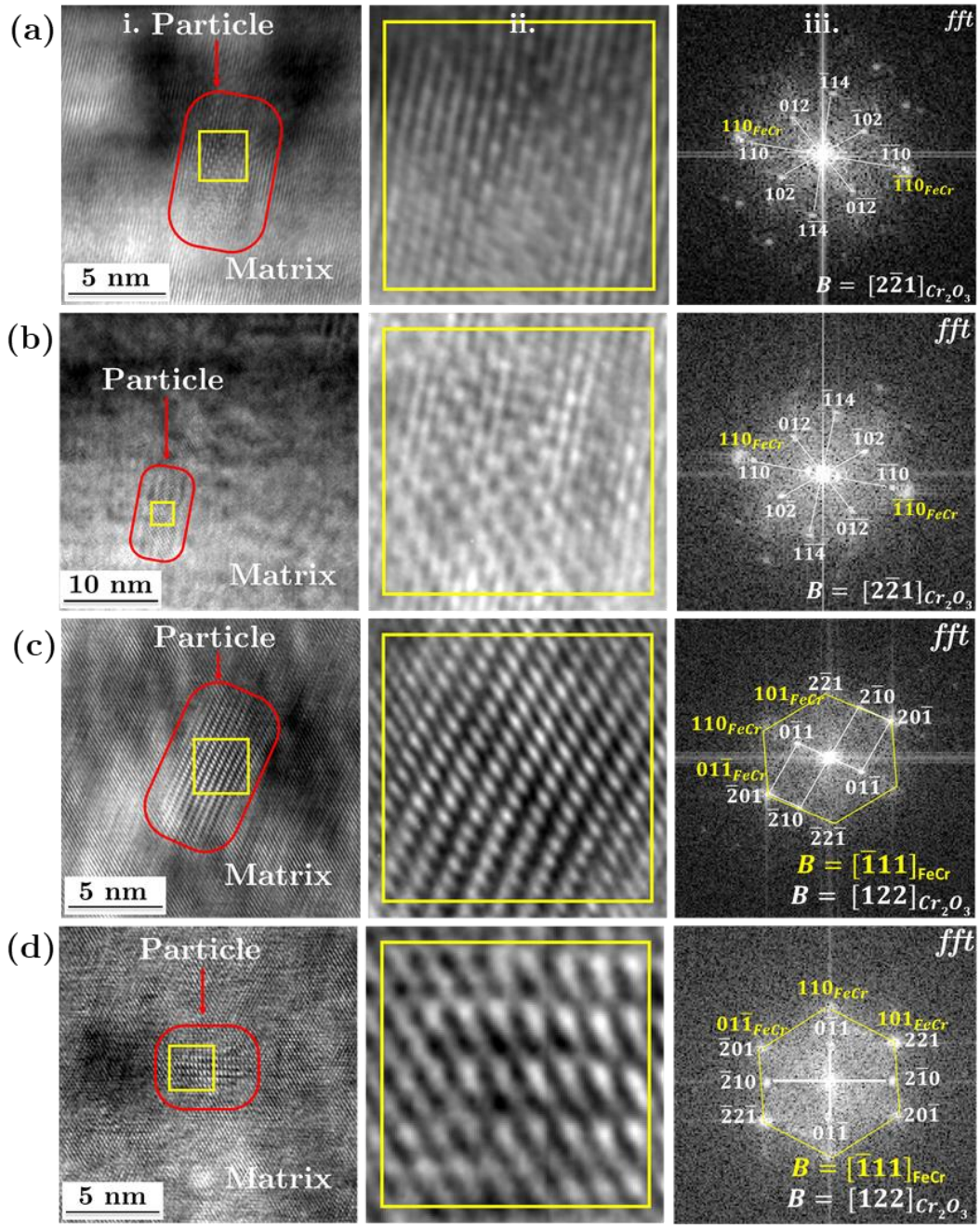

Figure 3.22 (i) High Resolution TEM (HRTEM) image of selected particles embedded in the matrix from the FIB lamella extracted after implantation of Ti and O ions at room temperature in bulk FeCr and annealing at 600°C for 2 hours. The red contour associated with red arrow on each picture highlights the elongated shape of the particle. (ii) Magnified image of the selected region of the particle and the (iii) corresponding Fast Fourier Transform (*fft*) of the particle. The particles correspond to the corundum hexagonal crystal structure of the type Cr_2O_3 with orientations B = [2-21] for (a) and (b), and B = [511] for (c) and (d).

Based on EFTEM elemental characterization indicating the depletion of Fe in precipitates but an enrichment in Cr and O of these same precipitates, HRTEM results appear to confirm the formation of Cr_2O_3 (Chromia) with the corundum hexagonal structure.

3.1.3.2 Annealing at 800°C

A surface layer is again observed on the FIB lamella of the bulk sample annealed at 800°C, even though this surface layer appears quite thinner than the one on the specimen annealed at 600°C. The thickness of this layer appears to be <10 nm and varies slightly from one region to the other. Investigation of the lamella in different defocus conditions revealed the presence of nanoparticles formed within the sample (below the surface layer), as shown in *Figure 3.23*. The particles once again show a changing contrast with the defocus: they are white in underfocus and black in overfocus conditions.

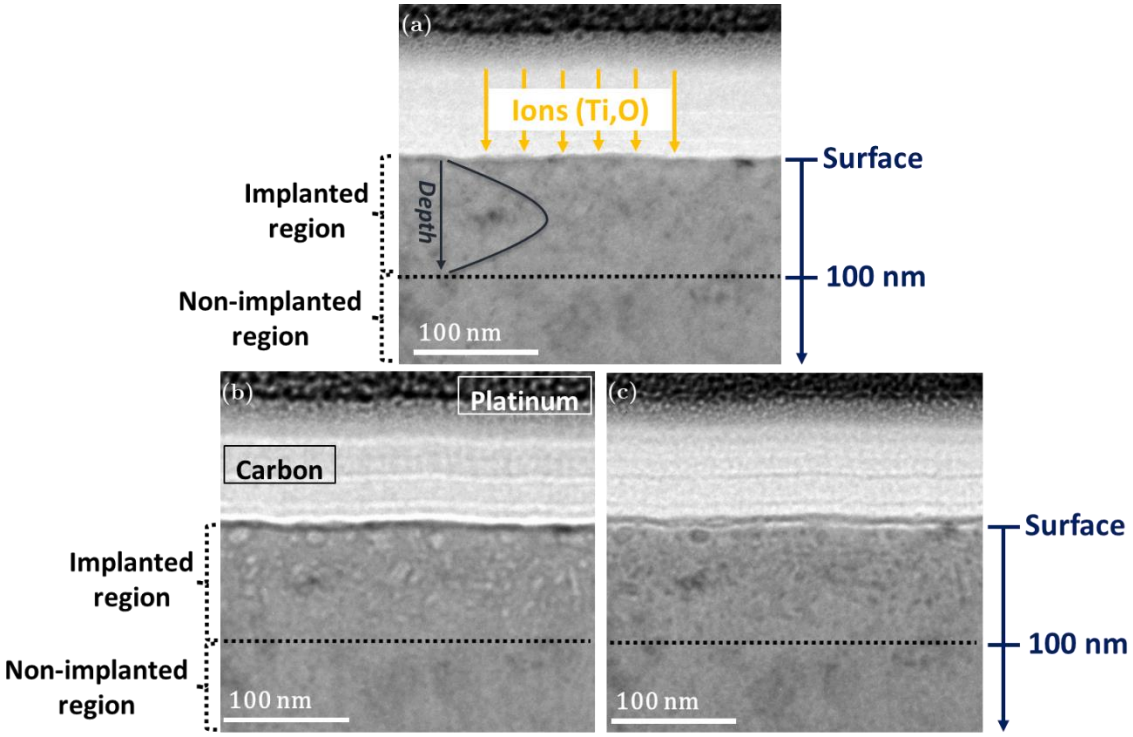

Figure 3.23 Bright Field imaging of the FIB lamella of the bulk specimen implanted with Ti and O ions and annealed at 800°C indicating the formation of nanoparticles within the implanted region (a) close to the focus condition (b) in underfocus and (c) overfocus conditions.

A region of the sample was chosen with the surface area of approximately 100 by 450 nm for particle size analysis (see *Figure 3.24(a)*). Sampling of the observed particles in the *Figure 3.24(b)* showed particles ranging between 4 and 39 nm in length. The average length (using the Feret's diameter) was determined as 11 nm. The particles were observed within the sample from the surface to about a 70 nm depth from the surface. This again falls within the implanted region of about 100 nm.

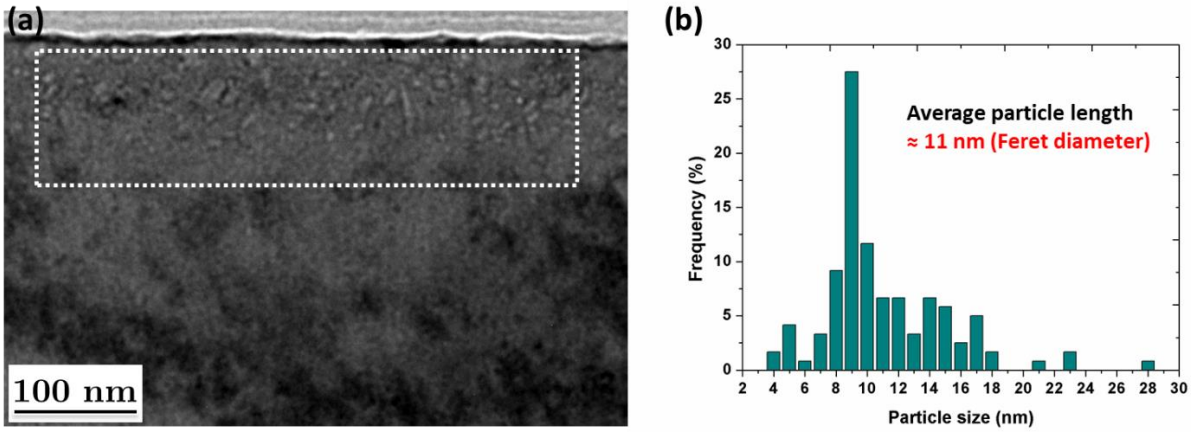

Figure 3.24 (a) Bright Field (BF) image of FIB lamella extracted after room temperature implantation of Ti and O ions and annealing at 800°C and (b) Particle size (using the Feret's diameter) distribution of particles observed in the Figure 3.23(a).

EFTEM elemental mapping was carried out on the sample as shown in *Figure 3.25* and revealed a surface layer depleted in Fe and enriched in Cr and O. However, contrary to previous lower annealing temperatures but in agreement with experiments performed on the thin foil annealed at 800°C, Ti is also observed to enrich certain regions of the surface layer. Beneath the surface layer, several particles are observed with a depletion in Fe, and an enrichment in Cr and O. Again, contrary to the previous annealing condition, Ti is clearly observed to enrich the particles. Ti diffusion has already been reported by ToF-SIMS experiment in the thin foils annealed at 800°C and hence the Ti presence in these particles is expected. The nanoparticles formed after annealing at 800°C thus contain Ti and O as well as Cr and possibly Fe.

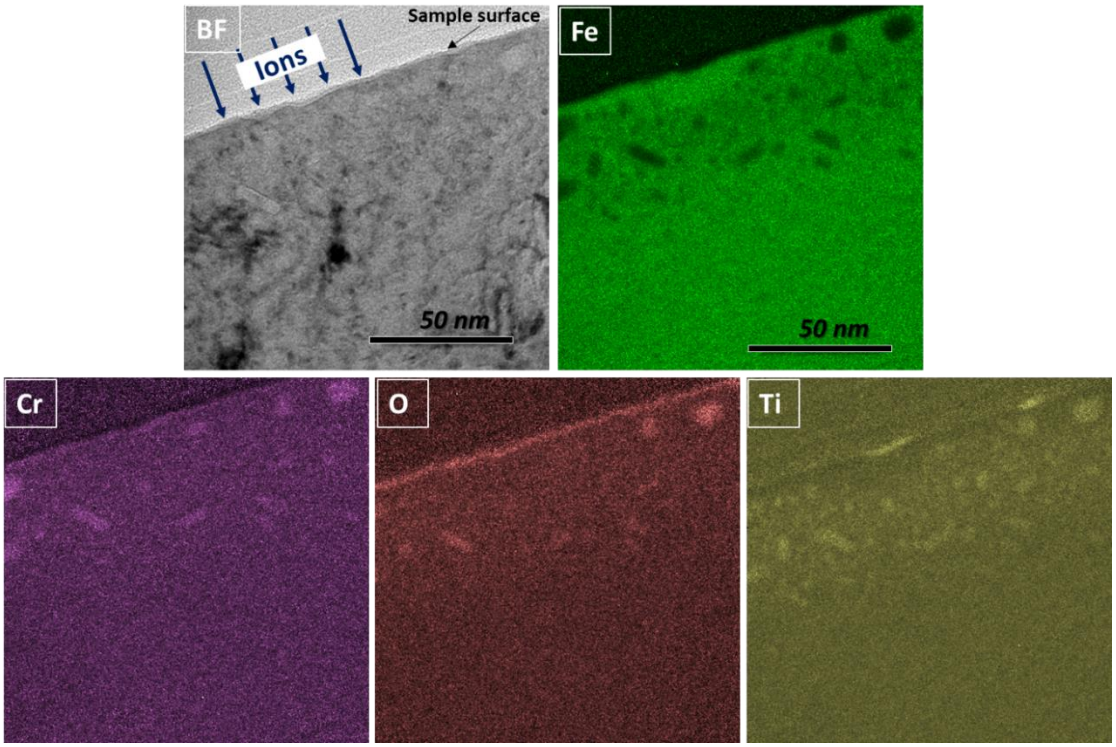

Figure 3.25 Energy-Filtered TEM (EFTEM) elemental characterization of the FIB lamella extracted after Ti and O ion implantation at room temperature and annealing at 800°C for 2 hours. Bright Field (BF) image of the region chosen for EFTEM together with elemental maps acquired using the two-window jump ratio method in the vicinity of Fe-$L_{2,3}$ edge, Cr-$L_{2,3}$, O-K and Ti-$L_{2,3}$ core loss edges.

HRTEM imaging was conducted for different particles from various regions of the FIB extracted lamella to verify the crystallographic structure of these particles. In the *Figure 26* are HRTEM images acquired for five different analysed particles. The sizes of these particles range between 5 and 15 nm, which is typical of the particles observed in the conventional and elemental characterizations.

In the *Figure 3.26(a)* and *(b)* are two elongated particles with similar orientation as illustrated by the *fft* images. The measured interplanar distances and angles on the *fft* correspond to those of a zone axis B = [122] of the corundum hexagonal crystal structure of the type Cr_2O_3 (the interplanar distances for the (011), (210) and ((201) or (221)) atomic planes as 0.40, 0.24 and 0.21 nm, respectively. The measured angles between (011) and (210) atomic planes were determined as 91 and 89° (theoretical values of 90°). The same orientation, with same orientation correlation between the lattices of the matrix and the particle, has been observed for selected particles after annealing at 600°C in the *Figure 3.22(c*) and *(d)*. The matching spots between the matrix and particles suggest a possible coherency between the particle and the matrix.

Another particle found in the *Figure 3.26(c)* appears to be similar to the particles observed in the *Figure 3.26(a)* and *(b)* albeit with a tilt of the orientation. Similar interplanar distances, orientation as well as the correlation between the particle and the matrix are applicable.

Finally, in the *Figure 3.26(d)* and *(e)* are two particles with a similar orientation that seems to correspond to a zone axis B = [-111] of the corundum hexagonal crystal structure of the type Cr_2O_3. The interplanar distances for the (011) and (112) atomic planes were determined as 0.37-0.40 and 0.34 nm, closely matching the theoretical values d_{011} = 0.40 and d_{112} = 0.36 nm, and the measured angles between the two (011) atomic planes and between the (011) and (112) were determined as approximately 62° and 57-61° whilst theoretical values amounts to 68.6° and as 55.7°. The particles displays orientation relationships with the matrix structure : [-111] zone axes coincide for both lattices, and the main spots of the FeCr matrix almost coincide with spots of the Cr_2O_3 particle with (101)FeCr//(-12-3)Cr_2O_3, (110)FeCr//(11-2)Cr_2O_3 and (01-1)FeCr//(2-11)Cr_2O_3.

From all the observed particles, it is evident that annealing at 800°C appears to maintain the corundum hexagonal structure of the type Cr_2O_3 previously observed after annealing at 600°C even though these particles demonstrated an enrichment in Ti by the elemental characterization. The shape of the particles is also maintained with an elongation parallel to {110} planes of the FeCr matrix.

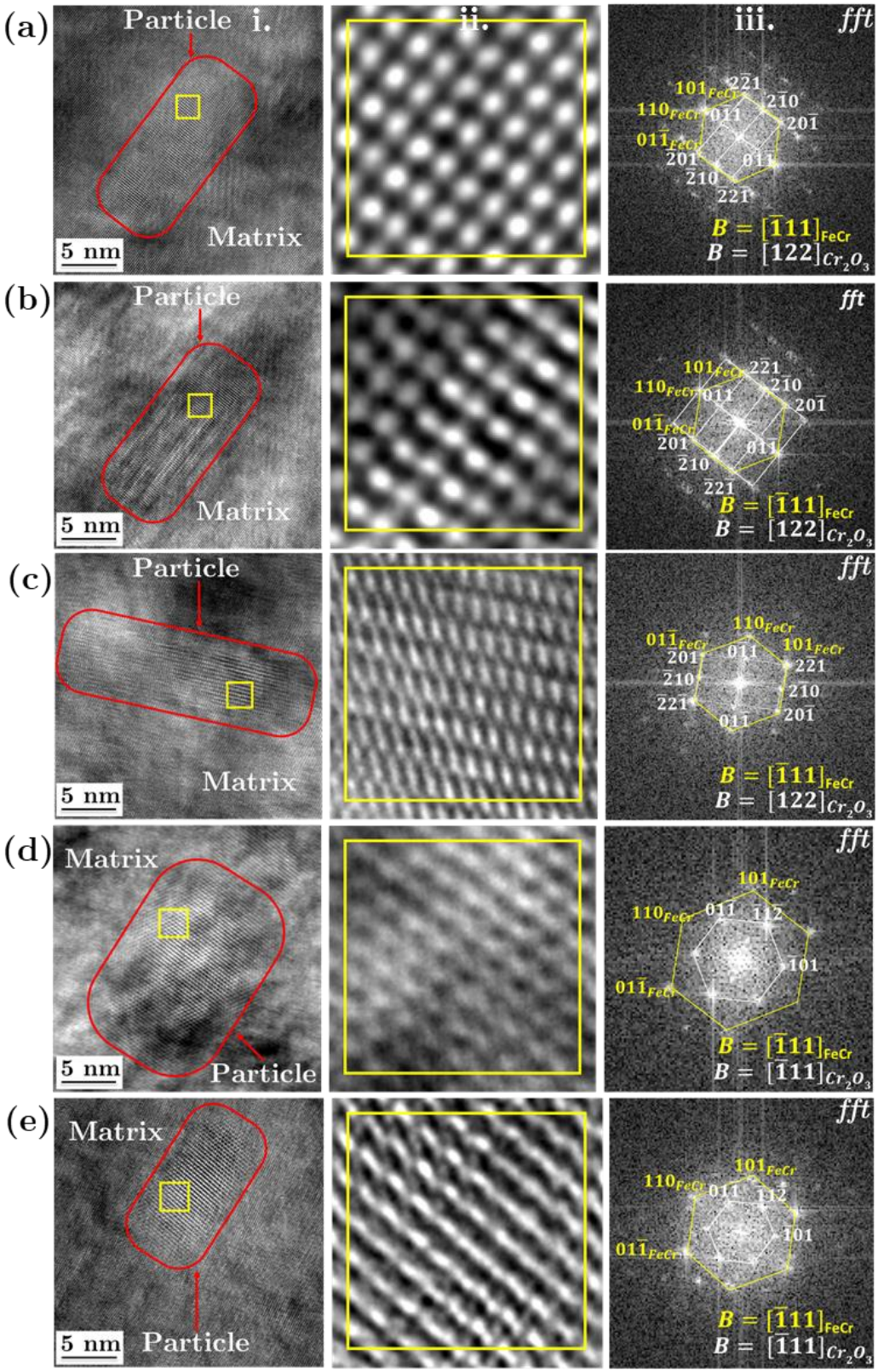

Figure 3.26 (i) High Resolution TEM (HRTEM) image of selected particles embedded in the matrix from the FIB lamella extracted after implantation of Ti and O ions at room temperature in bulk FeCr and annealing at 800°C for 2 hours. The red contour associated with red arrow on each picture highlights the elongated shape of the particle. (ii) Magnified image of the selected region of the particle and the (iii) corresponding Fast Fourier Transform (*fft*) of the particle. The particles correspond to the corundum hexagonal crystal structure of the type Cr2O3 with orientations B = [511] for (a), (b) and (c) as well as B = [-111] for (d) and (e).

The chemical and crystallographic structure information obtained therefore confirms the formation of a titanium enriched chromium oxide with the corundum hexagonal structure of the type Cr_2O_3.

3.1.3.3 Annealing at 1000°C

Higher temperature annealing has been performed at 1000°C. As seen in section 1.2.2 in the FeCr phase diagram, there is a phase transformation from the α-Fe phase with a *bcc* structure to a γ-Fe phase with an *fcc* structure at a temperature of close to 880°C. The structure of the FeCr matrix was therefore checked by HRTEM and found to match the original *bcc* structure. This will be revisited in the following section.

As seen in *Figure 3.27*, a surface layer is again formed which is predicted to correspond to the surface oxide $FeCr_2O_4$. The thickness of this layer varies from zone to zone between 20 and 40 nm. Observations quickly reveal the formation of nanoparticles below this surface layer. These particles are again not evident in the BF image in *Figure 3.27* close to focus due to the weak imaging contrast. These are however clearly observed with a changing contrast in underfocus and overfocus conditions.

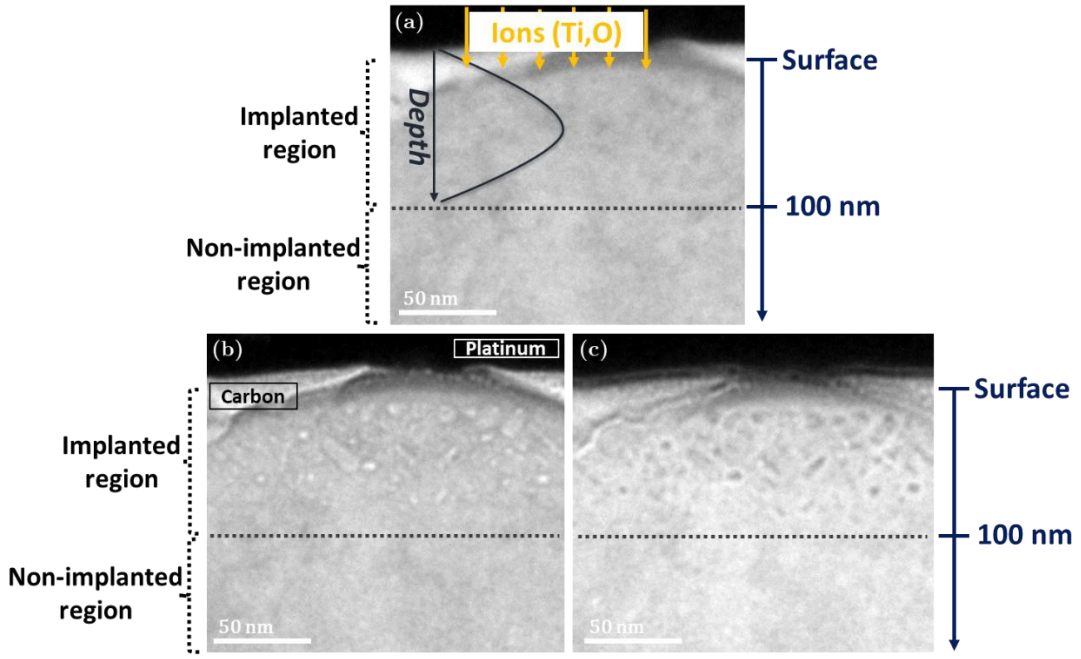

Figure 3.27 Bright Field (BF) imaging of the FIB lamella of the bulk specimen implanted with Ti and O ions and annealed at 1000°C indicating the formation of nanoparticles within the implanted region (a) close to the focus condition (b) in underfocus and (c) overfocus conditions.

A region of this sample with an area of approximately 100 by 450 nm was again selected (see *Figure 3.28*) for the sampling of the nanoparticles formed. The distribution of the particles was analysed and determined to range between 4 and 30 nm. The average length (using the Feret's diameter) of these particles was determined as 12 nm. This represents only a slight increase in the size of the particles as compared to the particles observed at 800°C. These particles are again observed predominantly from the surface of the sample to a depth of about 80 nm, which precisely represents the implanted region, as calculated by SRIM (see section 2.3).

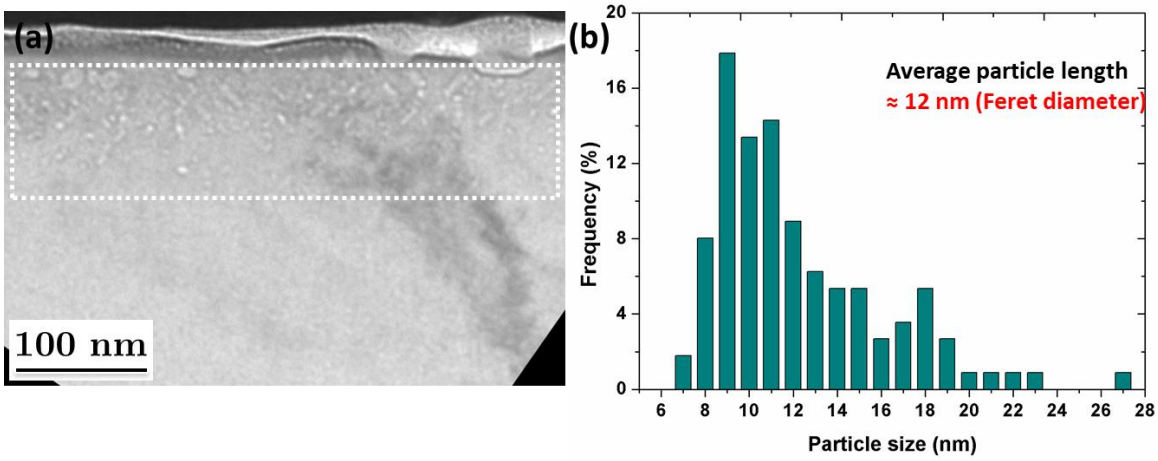

Figure 3.28 (a) Bright Field (BF) image of FIB lamella extracted after room temperature implantation of Ti and O ions and annealing at 1000°C showing the region chosen for particle analysis and (b) Particle size (using the Feret's diameter) distribution of particles observed in the Figure 3.28 (a).

The elemental compositions of the observed particles were investigated by EFTEM. The *Figure 3.29* illustrates the EFTEM elemental map observed for Fe with a depletion of Fe in these particles. On the other hand, the elemental maps indicate that these spots are enriched in Cr and O as well as Ti. This is exactly similar to what is observed for the specimen annealed at 800°C.

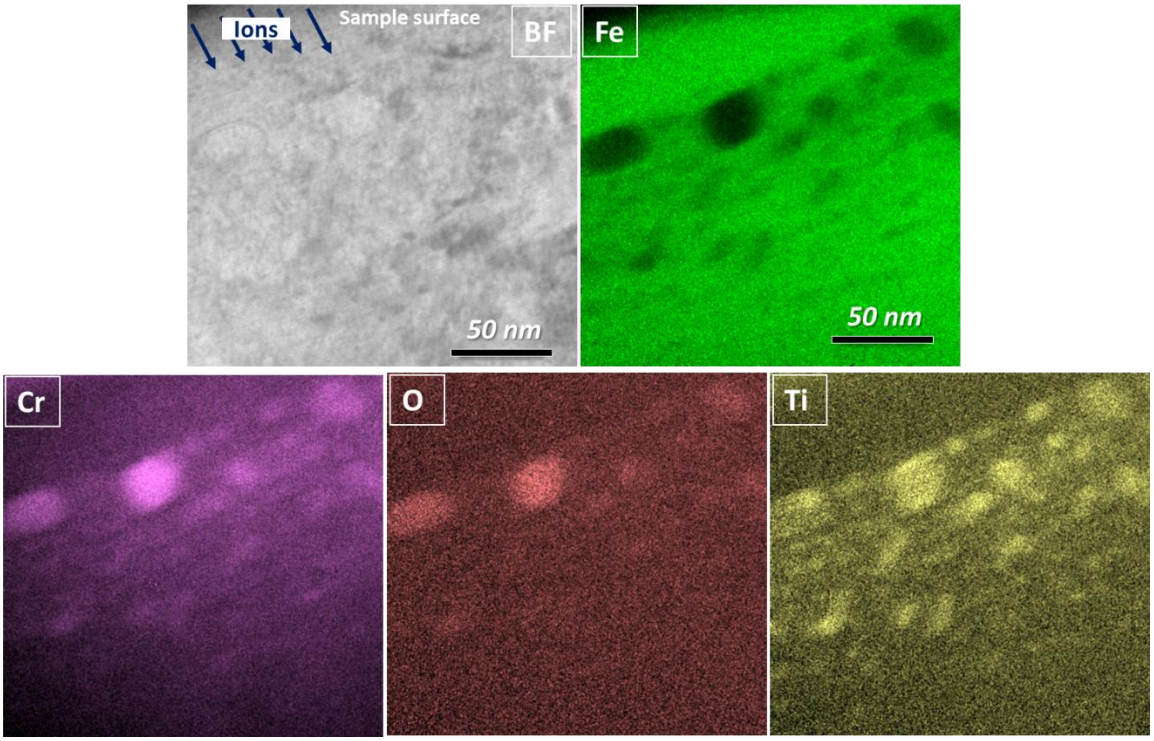

Figure 3.29 Energy-Filtered TEM (EFTEM) elemental characterization of the FIB lamella extracted after implantation of Ti and O ions at room temperature and annealing at 1000°C for 2 hours. Bright Field (BF) image of the region chosen for EFTEM together with elemental maps acquired using the two-window jump ratio method in the vicinity of Fe-$L_{2,3}$ edge, Cr-$L_{2,3}$, O-K and Ti-$L_{2,3}$ core loss edges.

Phase transformation of the Fe10wt%Cr base alloy occurs from the *bcc* α-Fe to the *fcc* γ-Fe crystal structure at a temperature of approximately 880°C as stated in section 1.2.2. The crystallographic structure of the matrix of the sample annealed at 1000°C was therefore verified by HRTEM. One would practically expect the formation of the *fcc* γ-Fe crystal structure. However, the HRTEM imaging revealed that the matrix structure corresponds to the bcc crystal structure of Fe. The annealing at 1000°C definitely transformed the *bcc* Fe to an fcc typed Fe: the transformation back to the bcc crystal structure very likely results from the very slow cooling implemented. A detailed characterization of the matrix structure after annealing at 1000°C is given in Annex II. The same bcc structure of the FeCr matrix was observed after all annealings performed at 1000 and 1100°C and will not be commented in the following sections.

As performed for the previous annealing conditions of 600 and 800°C, HRTEM investigations have been performed to determine the crystallographic structures of the particles. In the *Figure 3.30* are the images of some of the analysed particles with similar sizes. The *Figure 3.30(a)* and *(b)* illustrates two particles displaying same zone axis. All the interplanar distances and angles indicate a B = [001] orientation of the corundum hexagonal structure of the type Cr_2O_3 (where the (110) and (120) atomic planes were roughly equal and measured to be 0.24 nm, in accordance with theoretical values). The orientation correlation between the lattices of the particle and the matrix observed in the *fft* of *Figure 30(a)* is [-113]FeCr//[001]Cr_2O_3, (21-1)FeCr//(220)Cr_2O_3 and (-12-1)FeCr//(300)Cr_2O_3 with matching spots, suggesting partial coherency between the particle and the matrix.

In addition, two particles are shown in *Figure 3.30(c)* and *(d)* with a similar orientation. The interplanar distances and angles correspond to a zone axis B = [111] of the corundum hexagonal structure Cr_2O_3 : the interplanar distances for the (01-1) and (321) atomic planes were measured as 0.38 and 0.15 nm respectively, closely matching the theoretical distances ($d_{01\text{-}1}$ = 0.40 nm and d_{321} = 0.16 nm), and the two angles between {011} and {321} planes were determined as 84 and 96° whilst theoretical values are 81.8 and 98.2°, respectively.

Also, another particle is shown in the *Figure 3.30(e)* which has been identified to correspond to the corundum hexagonal crystal structure of the type Cr_2O_3 with the orientation B = 1-11. The interplanar distances of the (110) and (123) atomic planes were determined as 0.25 and 0.21 nm, respectively and the angle between the (-123) and (-213) atomic planes was determined as 50° whilst the angle between the (110) and (-123) atomic planes was determined as 65°, whilst theoretical values are 52 and 64°, respectively. An obvious orientation correlation between the particle and the matrix is [-113]FeCr//[1-11]Cr_2O_3 and (110)FeCr//(-213)Cr_2O_3 with matching spots, suggesting, at least, partial coherence between the particle and the matrix. In addition, the spots of the (220) planes of the particle are found close to the spots of (1-21) planes of the FeCr matrix, as is the case for the (033) spots of the particle and (2-11) spots of the matrix.

All the analysed particles were therefore found to correspond to the corundum hexagonal crystal structure of the type Cr_2O_3 and seem to display at least a partial coherency with the matrix, as observed for the previous annealing conditions. As for lower annealing temperatures, some particles appear to be elongated in parallel to {110}FeCr planes. Others appear elongated along another direction (undefined), which could be due to projection effects.

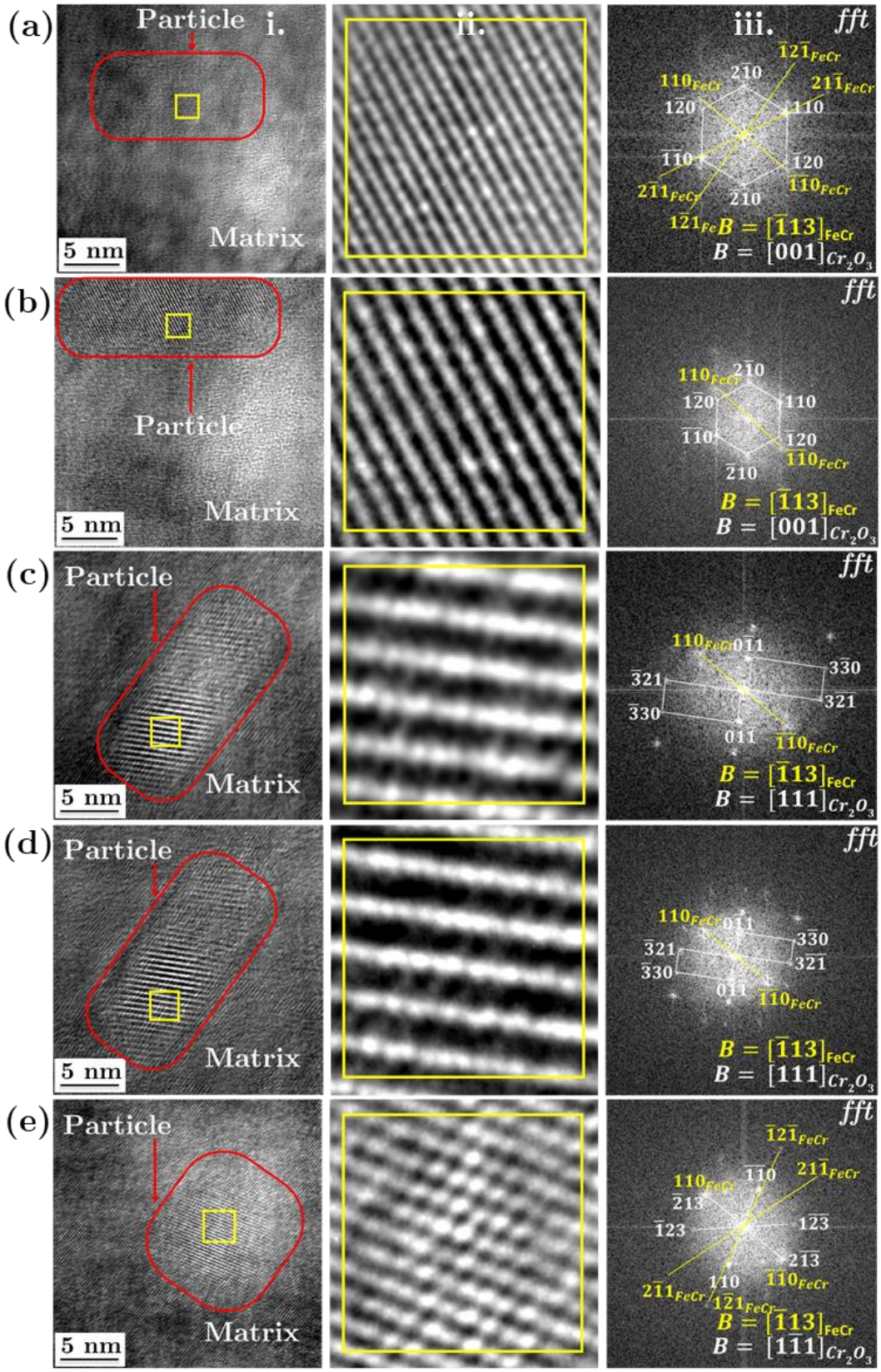

Figure 3.30 (i) High Resolution TEM (HRTEM) image of selected particles embedded in the matrix from the FIB lamella extracted after implantation of Ti and O ions at room temperature in bulk FeCr and annealing at 1000°C for 2 hours. The red contour associated with red arrow on each picture highlights the elongated shape of the particle. (ii) Magnified image of the selected region of the particle and the (iii) corresponding Fast Fourier Transform (*fft*) of the particle. In (b), (c) and (d), the zone axis of the matrix was determined slightly further from the particle.

3.1.3.4 Annealing at 1100°C

Keeping in mind the fact that ODS steels produced by the conventional ball milling method are consolidated at close to 1100 or 1150°C, one final attempt was made to go close to these conditions. Hence, bulk samples implanted with Ti and O were annealed at a temperature of 1100°C. An oxide layer was again observed on the surface of the sample as in previous annealing conditions with a thickness of <10 nm, which was varying from region to region. Direct TEM investigations again showed the formation of nanoparticles evident in underfocus and overfocus conditions (*Figure 3.31(b)* and *(c)*).

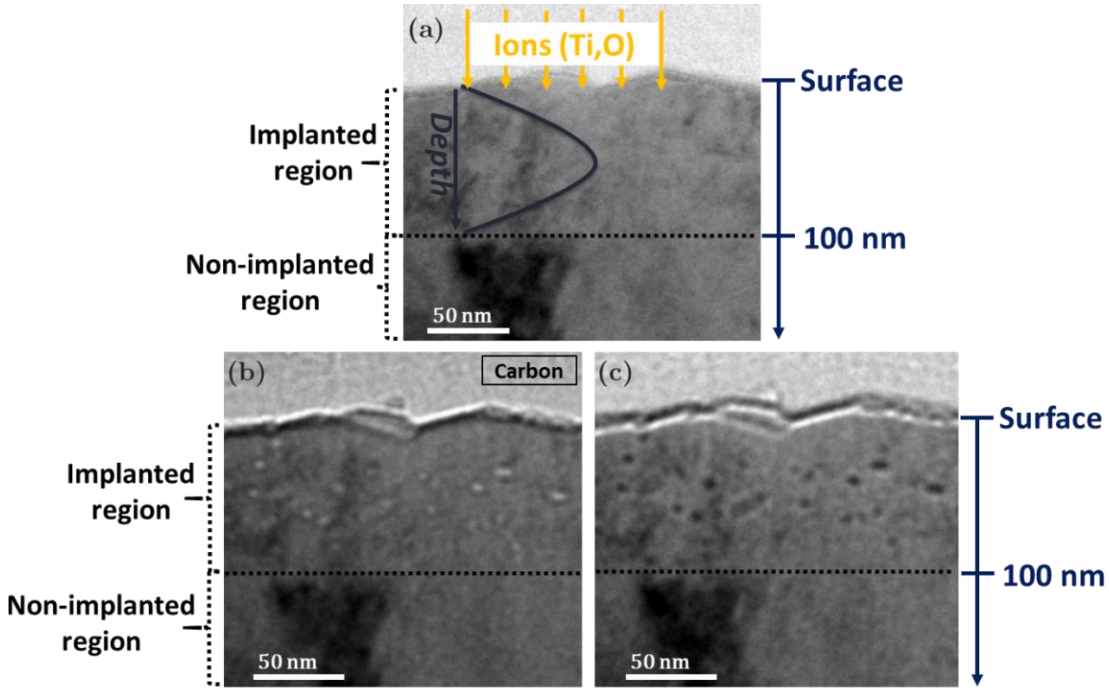

Figure 3.31 Bright Field (BF) imaging of the FIB lamella of the bulk specimen implanted with Ti and O ions and annealed at 1100°C indicating the formation of nanoparticles within the implanted region (a) close to the focus condition, (b) in underfocus and (c) overfocus conditions.

The particles are also highlighted in DF as in *Figure 3.32(c)*. The *Figure 3.32(a)* is a diffraction pattern (DP) obtained in the implanted region of the sample close to an orientation B = [-111] of the FeCr matrix. Additional reflections with weak contrasts are observed in the DP. One of the additional reflections highlighted in the *Figure 3.32(a)* was used to obtain the corresponding dark field (DF) image in the *Figure 3.32(c)*. Many small white spots are evidently visible. These spots represent the nanoparticles formed in the sample and are observed exactly within the implanted region. The corresponding Bright Field (BF) image for this region is also reported in the *Figure 3.34(b)* but does not show any contrast for the particles since taken close to focus.

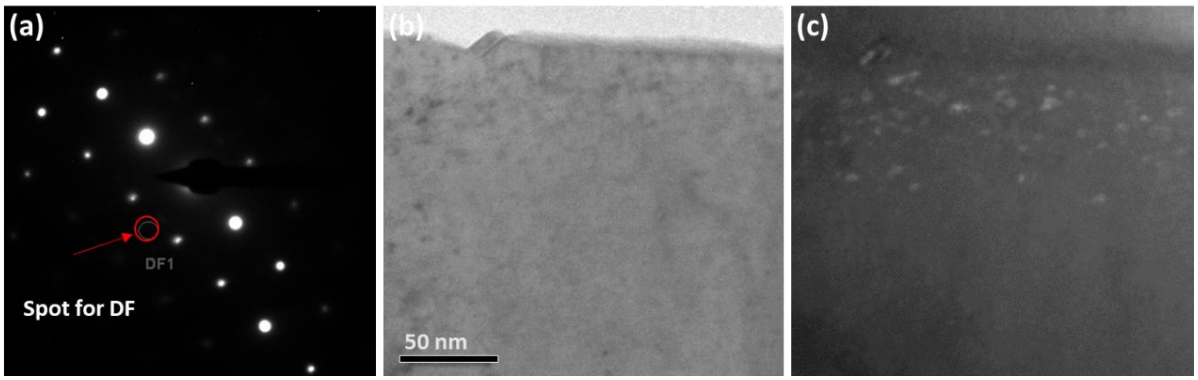

Figure 3.32 (a) Diffraction pattern (DP) for FIB lamella extracted after room temperature implantation of Ti and O ions and annealing at 1100°C for 2 hours (b) Bright Field (BF) image of zone from which the DP was taken and (c) corresponding Dark Field (DF) image.

The sampling of the particles was again performed by selecting a region of 100 by 450 nm on a BF image as in the *Figure 3.33(a)* and *(b)*. The size of the observed particles was determined to range between 3 and 25 nm. The average size of the particles (using the Feret's diameter) was determined to be approximatively 10 nm. This is closely related to the size of the particles observed after annealing at 800 and 1000°C. These particles were again observed from the surface of the sample to a depth of about 80 nm, i.e., exactly in the implanted region.

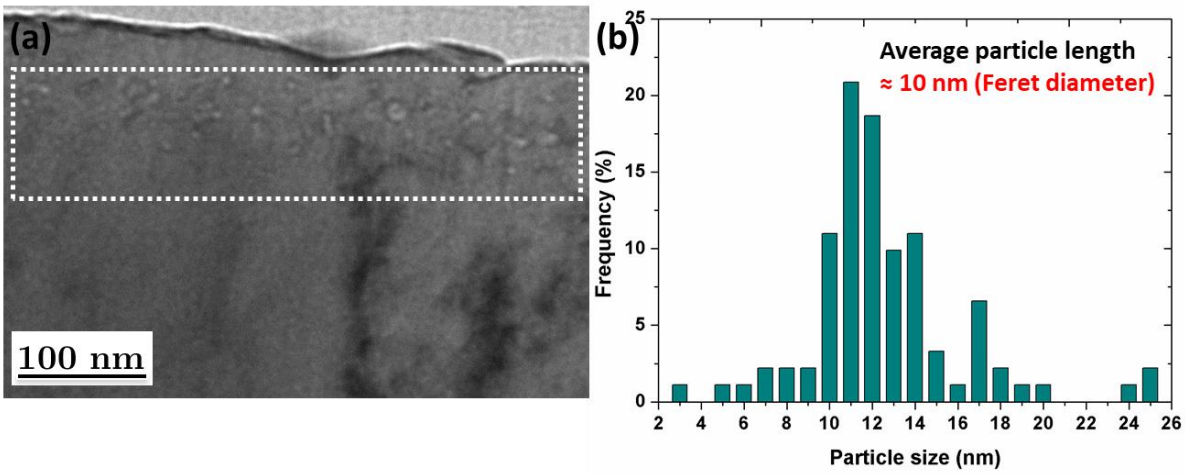

Figure 3.33 (a) Bright Field (BF) image of the chosen region for particle size analysis from the FIB lamella extracted after room temperature implantation of Ti and O ions and annealing at 1100°C (b) Size (using the Feret's diameter) distribution of the particles observed in the Figure 3.33(a).

EFTEM characterization was performed for different regions. In the *Figure 3.34* is a bright field (BF) image of a region chosen for EFTEM imaging and the elemental maps obtained. Darker spots representing a depletion are observed in the Fe elemental map. Elemental maps for Cr and Ti appeared to have enhanced coloured patches for the regions with a depletion in Fe. The O map however appeared quite homogeneous. This is not exactly a reflection of the O elemental map as technical challenges experienced using the jump ratio method for imaging the O surfaced. The nanoparticles just as experienced in the previous annealing conditions are expected to be composed of O. Hence, the nanoparticles contain Cr, Ti as well as very probably O.

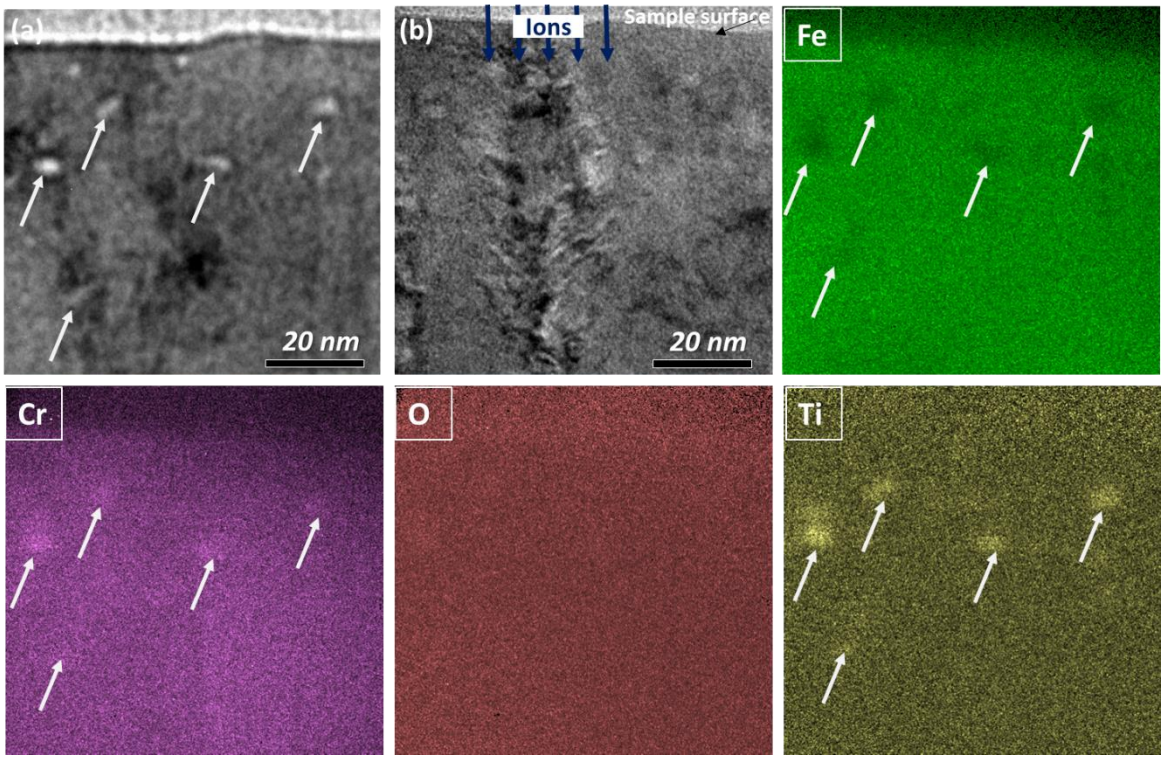

Figure 3.34 Energy-Filtered TEM (EFTEM) elemental characterization of the FIB lamella extracted after implantation of Ti and O ions at room temperature and annealing at 1100°C for 2 hours. (a)Bright Field (BF) image of the region chosen for EFTEM and (b) Bright Field image acquired with the GIF camera where particles are not easily visible together with elemental maps acquired using the two-window jump ratio method in the vicinity of Fe-$L_{2,3}$ edge, Cr-$L_{2,3,}$ O-K and Ti-$L_{2,3}$ core loss edges. Arrows show some nanoprecipitates.

Just as was performed for the annealing condition of 600°C, complementary elemental characterization was performed using ChemiSTEM EDX. In the *Figure 3.35(a)* is a low magnification image highlighting the mapped region. BF and corresponding HAADF for this mapped region are presented in the *Figure 3.35(b)* and *(c)*. Two distinguished types of particles are observed in the elemental mapping. The first type of particles with an example labelled 1 in the Fe elemental map displays a depletion in Fe. The depletion in Fe corresponds to enrichment in Cr and Ti as well as probably O. This is similar to what was previously observed after annealing at 800 and 1000°C. In addition to these particles, another set of particles are observed with an example labelled 2 in the Fe elemental map. These types of particles display a depletion in Fe corresponding to an enrichment in Ti and O. In addition, there appear to be a depletion of Cr in these particles probably suggesting the formation of Ti oxide particles. The particles displaying a depletion in Cr also show irregular patches of Cr enrichment around the particle leading to the conclusion that the Ti oxide particles possess a probable Cr enriched shell.

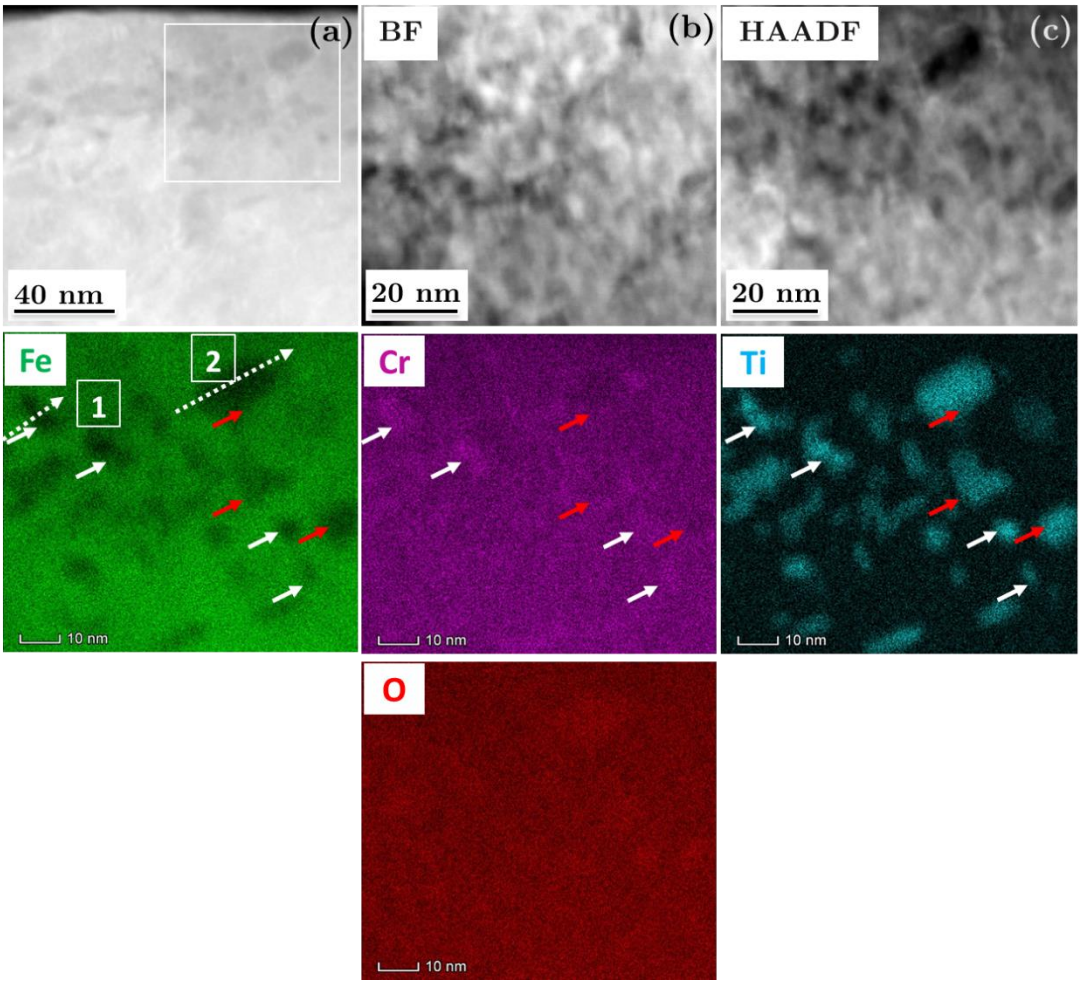

Figure 3.35. STEM-EDX elemental mapping of FIB lamella of Ti and O ion-implanted bulk specimen annealed at 1100°C using ChemiSTEM technology. (a) Bright Field (BF) image indicating the selected region (b) the corresponding Bright Field (BF) and (c) High Angle Angular Dark Field (HAADF) image together with elemental maps for Fe, Cr, Ti and O. The duration of the scan was 45 minutes with a count rate of 50k counts/second.

To highlight these results, line scans extracted from the ChemiSTEM analysis are reported for the two different types of particles observed. The line spectra in *Figure 3.36(a)* and *(b)* are for the particle labelled 1 and 2 respectively in Fe elemental map in *Figure 3.35*. The Fe depletion together with Cr and Ti enrichment are clearly observed for the particle 1. In the particle 2, the Fe and Cr depletions are clearly observed in coincidence with a Ti enrichment and probable O enrichment. There is a strong Cr enrichment at the edges of the particle confirming the core/shell structure of the Ti oxide particles.

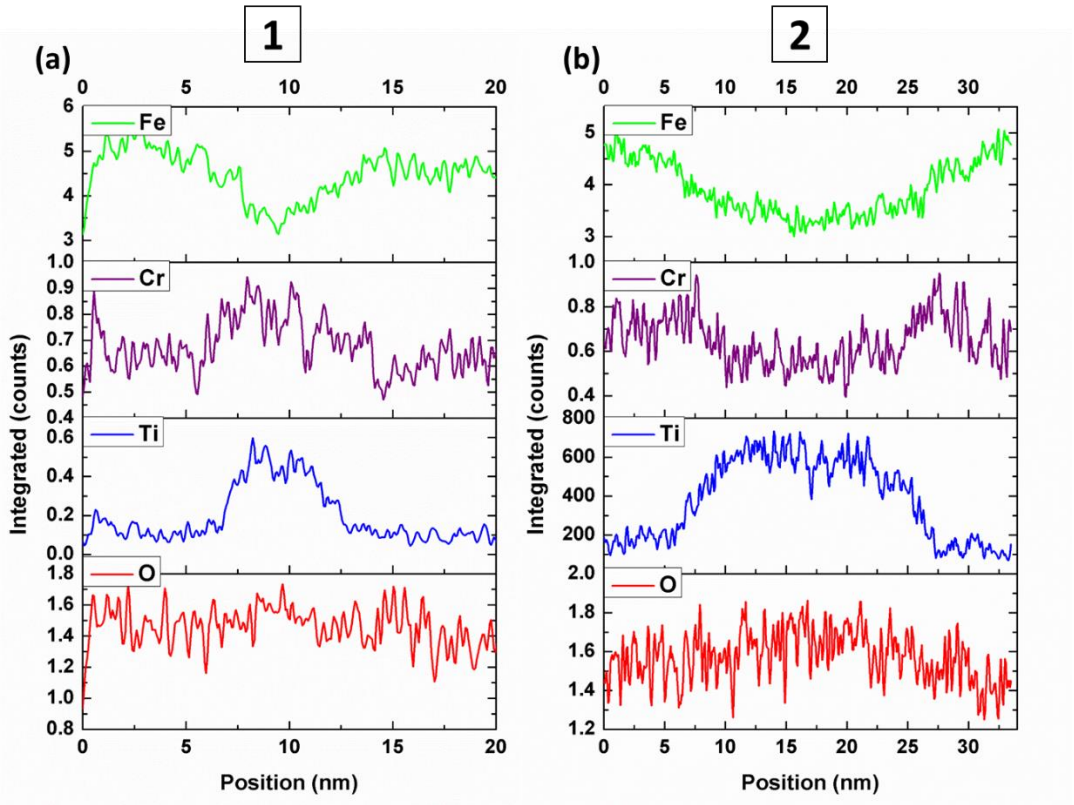

Figure 3.36 STEM-EDX 1-D line scan using ChemiSTEM technology of particles 1 and 2 as labelled in Figure 3.35 within the FIB lamella extracted from Ti and O ion-implanted bulk specimen and annealed at 1100°C. The direction of the line scan is given by the dotted lines in figure 3.35.

The crystallographic structure of the particles, similar to previous annealing conditions, was performed by HRTEM imaging. Two of the analysed particles are shown in the *Figure 3.37*: their length is of approximately 10 nm. The orientation of these particles is similar, as shown in the *fft* image. The interplanar spacings and angles indicate a zone axis B = [-441] of the corundum hexagonal structure of the type Cr_2O_3 : the interplanar distances for the (110) and 104) atomic planes were determined as 0.249 and 0.27 nm, respectively, with theoretical values of 0.248 and 0.267 nm, and the measured angle between the (104) and (0-14) atomic planes was determined as 65° whilst the angle between the (110) and the (104) atomic planes was determined as 57.5° (theoretical values of 65.02 and 57.49°). No visible orientation relationships can be deduced between the particles and the matrix since matrix spots are not obviously identified on the *fft* images.

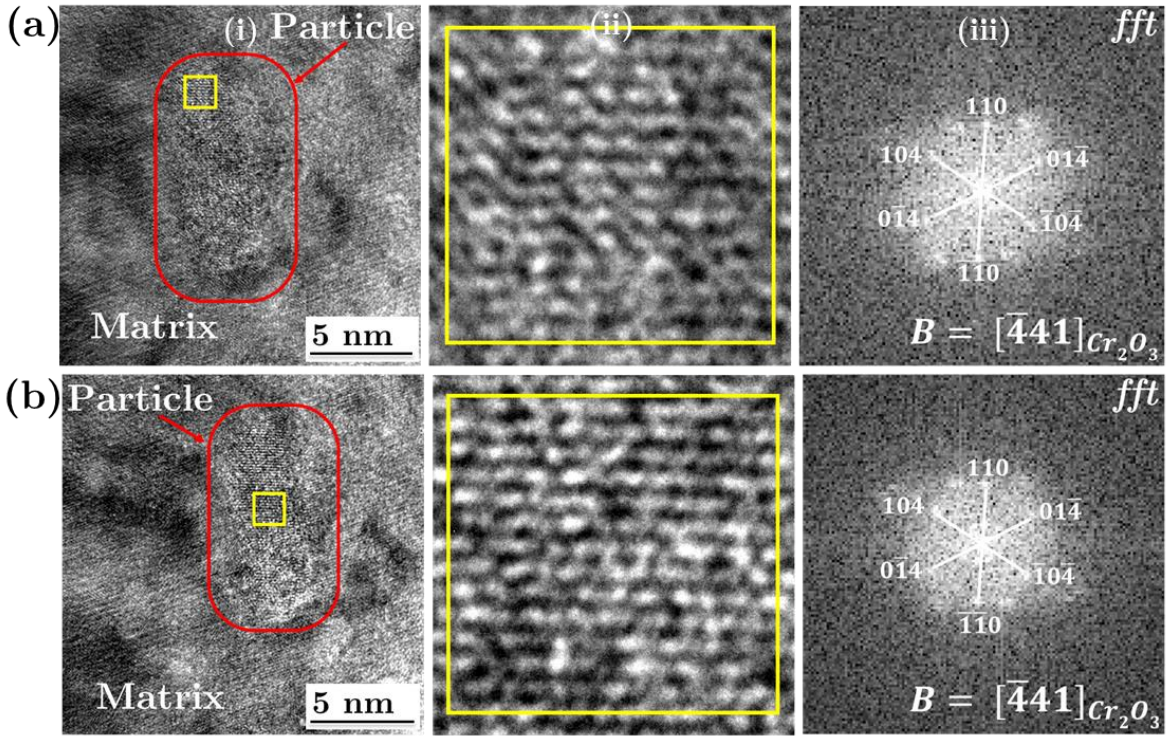

Figure 3.37 (i) High Resolution TEM (HRTEM) image of selected particles embedded in the matrix from the FIB lamella extracted after implantation of Ti and O ions at room temperature in bulk FeCr and annealing at 1100°C for 2 hours. (ii) Magnified image of the selected region of the particle and the (iii) corresponding Fast Fourier Transform (*fft*) of the particle.

The elemental composition characterization displayed two types of particles formed. The conventional chromium-titanium and oxygen enriched particles, as well as particles with a titanium and probably oxygen enriched core and a chromium enriched irregular shell. These Cr_2O_3 structure typed particles observed by HRTEM presumably corresponds to the chromium-titanium oxide particles as elaborated for the previous annealing conditions. No particles were identified to correspond to the core titanium enriched particles with a Cr enriched shell. However, there were several other particles observed by HRTEM imaging which did not appear to correspond to corundum Cr_2O_3 or to some other tentatively selected structure of typical oxides of Cr, Ti, Fe (i.e. $FeCr_2O_4$, Fe_3O_4, TiO_2-rutile, brookite, anatase, Cr_6O_{15}). See detailed crystallographic structures of these oxides in annex VII. These unidentified particles could thus correspond to the Ti enriched oxides but with a non-equilibrium structure.

3.1.4 Summary of the synthesis of oxide nanoparticles after Ti and O ion implantation

Ti and O room temperature implantations have been conducted at room temperature in both thin foils and bulk samples. The thin foils were annealed up to 800°C, at which temperature the Ti is observed to diffuse and enrich an $FeCr_2O_4$ oxide that begins to form at lower temperature. The formation of $FeCr_2O_4$ results from corrosion processes taking place on the surface of the thin foils and impedes the study of the formation of nanoparticles inside the bulk of the specimen. The annealing on thin foils was thus abandoned in favour of experiments on bulk specimens, which were *ex situ* annealed up to 1100°C. FIB lamellae were then extracted after annealing, allowing also an observation as a function of the depth.

Nanoparticles were observed in the implanted region after annealing at 600, 800, 1000 and 1100°C. The *Figure 3.38* gives the distribution of the size of particles observed at different annealing temperatures. A similar region size of 100 by 450 nm was chosen for each condition and the analysis was performed using ImageJ software. The Feret's diameter was used to estimate the average particle size in each case. At 600°C, the particle size was determined as ≈ 6 nm. These particles appeared to match the corundum hexagonal Cr_2O_3. After annealing at 800°C, the average size of the measured particles increased significantly from 6 nm to 11 nm. The particles are identified as Cr_2O_3 enriched in Ti. Annealing further at much higher temperatures of 1000 and 1100°C presents no significant change in the size with the average particle size determined as ≈ 12 and ≈ 10 nm for the annealing condition of 1000 and 1100°C, respectively. The particle size thus appears to reach a saturation after 800°C. At 1100°C, the results of elemental analysis show two type of particles : i) one type of particles enriched in Cr, O and Ti and having a Cr_2O_3 structure, as for annealing at lower temperatures, and ii) one type of particles enriched in Ti and O, depleted in Cr and surrounded with irregular Cr patches whose structure could not be identified. These particles are likely to be Ti oxide particles with a Cr shell.

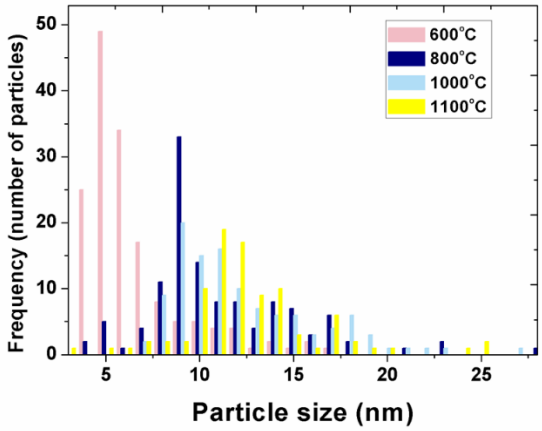

Figure 3.38 Size distribution of particles in FIB lamellae extracted from bulk samples after room temperature implantation of Ti and O ions and subsequent annealing at 600, 800, 1000 and 1100°C. The size refers to the Feret's diameter taken as the largest dimension in our case.

The *Table 3.1* represents a resume of the bulk specimens for observations made in each condition relating to chemical composition of any nanoparticles observed and the possible crystallographic structure where possible.

Many different orientation relationships (ORs) have been observed to exist between the matrix and the Cr_2O_3 nanoparticles formed. It suggests that most of the particles display at least a partial coherency with the matrix. The particles appear to be elongated in specific directions. For the lower annealing temperatures, some particles appear to be elongated in parallel to {110}FeCr planes. Others appear elongated along another direction (undefined), which could be due to projection effects.

Bulk FeCr sample implanted with Ti and O ions, and	Nanoparticle formaton	Composition		Structure		
		Observation technique	Chemical composition	Observation technique	Crystallographic structure	Identification
Annealed at 600°C	Nanoparticle ≈ 6 nm	EFTEM, ChemiSTEM	Fe depletion Cr, O enrichment Ti homogeneous	HRTEM	Corundum hexagonal Cr_2O_3-type structure	Chromium oxide with the Cr_2O_3 structure
Annealed at 800°C	Nanoparticle ≈ 10 nm	EFTEM	Fe depletion Cr, O, Ti enrichment	HRTEM	Corundum hexagonal Cr_2O_3-type structure	Chromium-titanium oxide with the Cr_2O_3-type structure
Annealed at 1000°C	Nanoparticle ≈ 12 nm	EFTEM	Fe depletion Cr, O, Ti enrichment	HRTEM	Corundum hexagonal Cr_2O_3-type structure	Chromium-titanium oxide with the Cr_2O_3-type structure
Annealed at 1100°C	Nanoparticle ≈ 11 nm	EFTEM, ChemiSTEM	Two types of particles Particle 1 : Fe depletion Cr, O, Ti enrichment Particle 2 : Fe depletion Ti, O enrichment Cr enriched shell	HRTEM	Unidentified structure	Two types of particles: Particle 1: Chromium-titanium oxide with Cr_2O_3 structure Particle 2: Titanium oxide with a chromium enriched shell and an unidentified structure

Table 3.1 Summary of composition and structure of nanoparticles observed in Ti and O implanted and annealed bulk samples

3.1.5 The effect of Cr: implantation of Ti and O ions in pure Fe

Obviously, the Cr has a leading role in the precipitation in most of the conditions reported above for Ti and O ion implantations in high purity Fe10wt%Cr alloy. Before arriving at this conclusion and in parallel to the above reported experiments, the same implantations were performed in pure Fe to observe any effect of the Cr in the precipitation or eventually force the formation of a pure Ti oxide. To this aim, a high-purity Fe sample was obtained from Goodfellow, France. The nominal compositions of the sample are given in the *Table 3.2*. Samples have been prepared similar to the high purity FeCr alloy bulk samples.

Element	Fe	Si	C	P	Co	Cr	Ni	Al	B	Cu	Others
Conc (ppm)	Matrix	69	20	7.9	6.7	2.4	1.5	1.5	1.1	0.9	<1

Table 3.2 Compositions of high purity Fe samples as reported by the supplier

The supplied high-purity Fe bulk materials were obtained as rectangular specimens of 2 cm x 2 cm and a thickness of <500 μm. To facilitate the mechanical polishing, these materials were cut into smaller specimens of 1 cm x 1 cm and a thickness of <500 μm. These samples were polished mechanically using SiC abrasive papers to obtain a thickness of about 100 μm. 3 mm TEM thin foils were then prepared using the method reported in section 2.2.5 using a 5% perchloric acid and 95% methanol solution at -40°C. FIB lamellae were also extracted by the *in situ* lift out technique.

A sample was investigated after implantation of Ti and O ions at RT. No additional reflections are visible in any of the diffraction pattern taken close to a zone axis. The bright field images did not also reveal visible nanoparticles.

There appear therefore to be no nanoparticles formed within the as-implanted Fe sample similar to the as-implanted FeCr sample. Hence, bulk samples implanted with Ti and O ions at room temperature were annealed at 800°C. A FIB lamella was then extracted. In the *Figure 3.39* are corresponding bright field images. Defects created as a result of the ion implantation can be easily observed in the implanted region. No nanoparticles are visible within the implanted region contrary to the case where Ti and O were implanted into the high purity FeCr sample and after annealing at 800°C. However, a surface layer with a contrast similar to the contrast of the sample is observed on the deposited carbon layer. This surface layer appears significantly thick with a thickness of approximately 40 nm and is strongly irregular in shape.

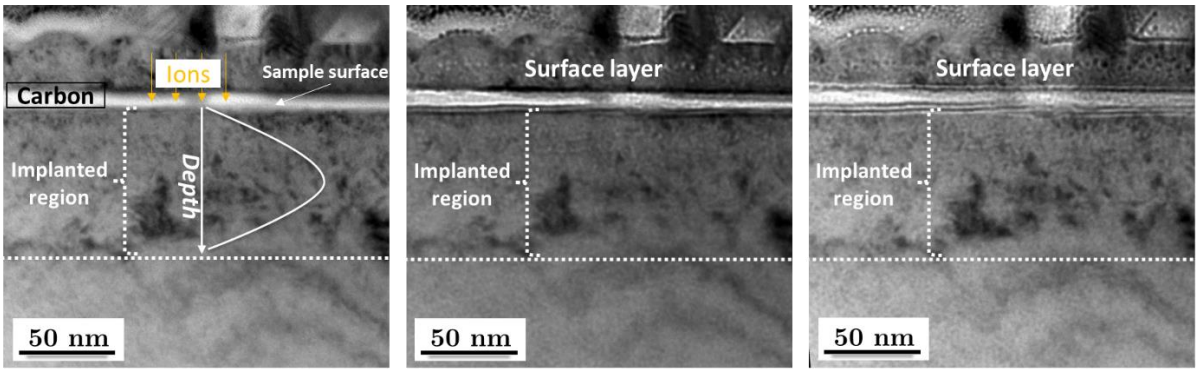

Figure 3.39. Bright Field (BF) imaging of the FIB lamella of the high purity Fe bulk specimen implanted with Ti and O ions and annealed at 800°C (a) close to the focus condition (b) in underfocus and (c) overfocus conditions. No nanoparticle is visible.

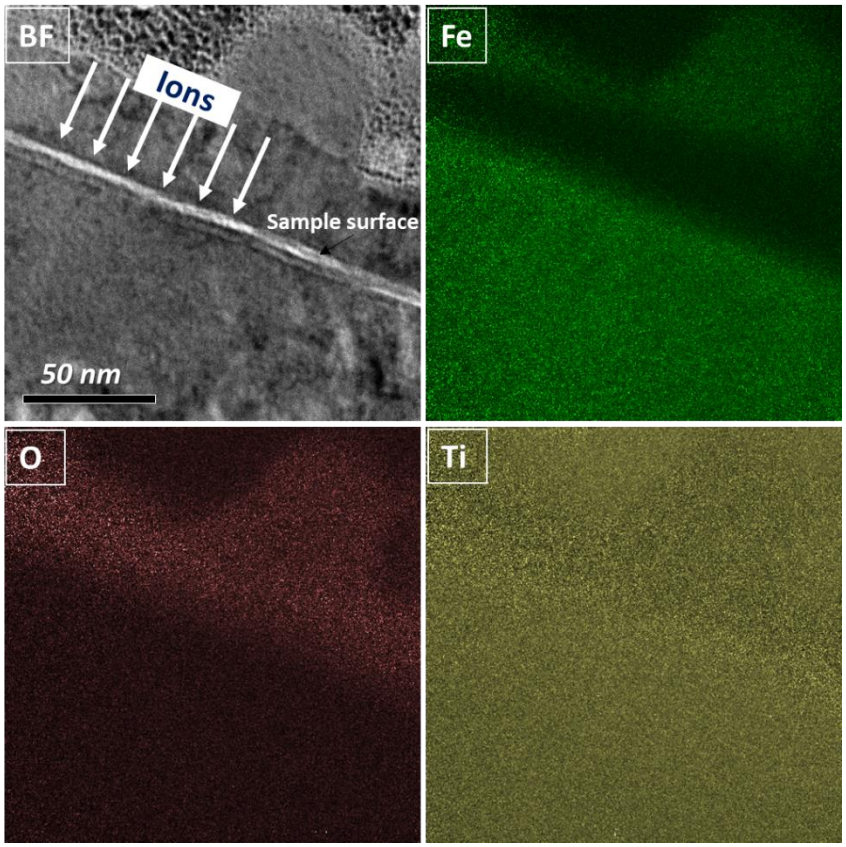

Figure 3.40. Energy-Filtered TEM (EFTEM) elemental characterization of the FIB lamella extracted from Fe bulk specimen after implantation of Ti and O ions at room temperature and annealing at 800°C for 2 hours. Bright Field (BF) image of the region chosen for EFTEM together with elemental maps acquired using the two-window jump ratio method in the vicinity of Fe-$L_{2,3}$ edge, Cr-$L_{2,3,}$ O-K and Ti-$L_{2,3}$ core loss edges.

EFTEM investigations were carried out to verify the composition of the surface layer and any potential nanoparticles. Within the bulk sample, elemental maps acquired for the Fe matrix as well as the O and Ti appeared quite homogeneous (see *Figure 3.40*). Interestingly however, the surface layer appeared to have an enrichment in Fe as well as O. The Ti elemental map however appeared quite homogeneous. This therefore suggests an iron oxide surface layer formed on top of the carbon protection layer.

To determine the structure of this surface layer, HRTEM imaging was performed for a region within the surface layer as indicated in the *Figure 3.41(a)*. A magnified image of the region from which the *fft* is shown in the *Figure 3.41(b)* and the corresponding *fft* is as given in *Figure 3.41(c)*. The results from the interplanar distances and angles confirm the formation of *fcc* iron oxide (Fe_3O_4) on the surface of the specimen. This probably means that Fe escaped the specimen but this out-diffusion does not seem to be associated with the formation of oxide particles in the bulk.

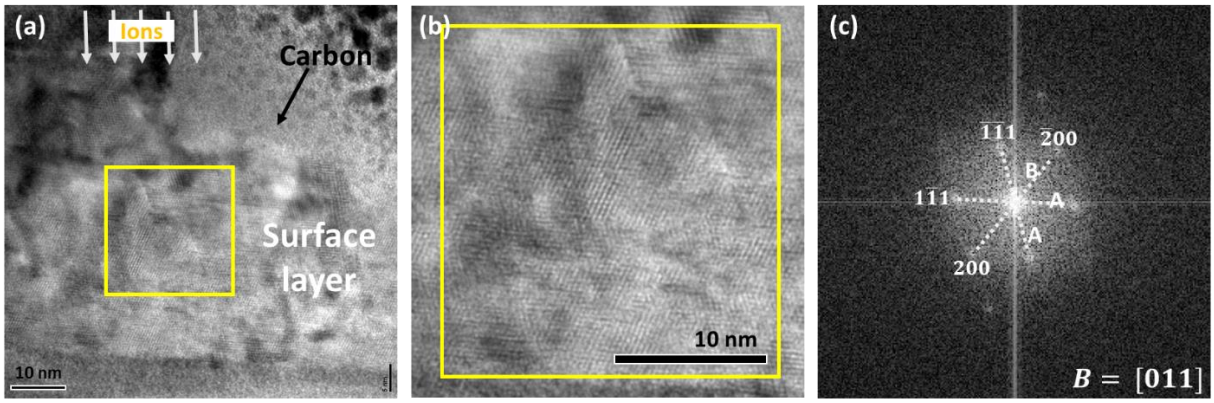

Figure 3.41 (a) High Resolution TEM (HRTEM) image of a selected particle from the FIB lamella extracted from high purity Fe sample after Ti and O ion implantation at room temperature and annealing at 800°C for 2 hours. (b) Magnified image of the selected region of the particle and the (c) corresponding Fast Fourier Transform (*fft*) of the particle.

Although the formation of very small clusters is not excluded, this experiment in pure Fe seems to confirm the leading role of Cr in the precipitation of particles in high purity Fe10Cr after implantation of Ti and O ions and subsequent annealing at 800°C.

3.1.6 The effect of O: single implantation of Ti ions in Fe10wt%Cr

In the absence of O, there is usually the possible formation of intermetallic clusters in FeCr alloys [Zheng 2014, 2015]. In order to evaluate the possible formation of Ti or Cr clusters in the high purity FeCr alloys, only Ti has been implanted into the high purity FeCr sample at room temperature using the Ti ion implantation parameters as was used in the Ti and O implanted samples.

The FIB lamella was extracted after annealing of the sample at 800°C for 2 hours. The *Figure 3.42* displays corresponding bright field images at a low magnification as well as at a much higher magnification. Many small grains, most of them with a dark contrast, are observed along the surface in the implanted region. Smaller white contrast regions are also observed.

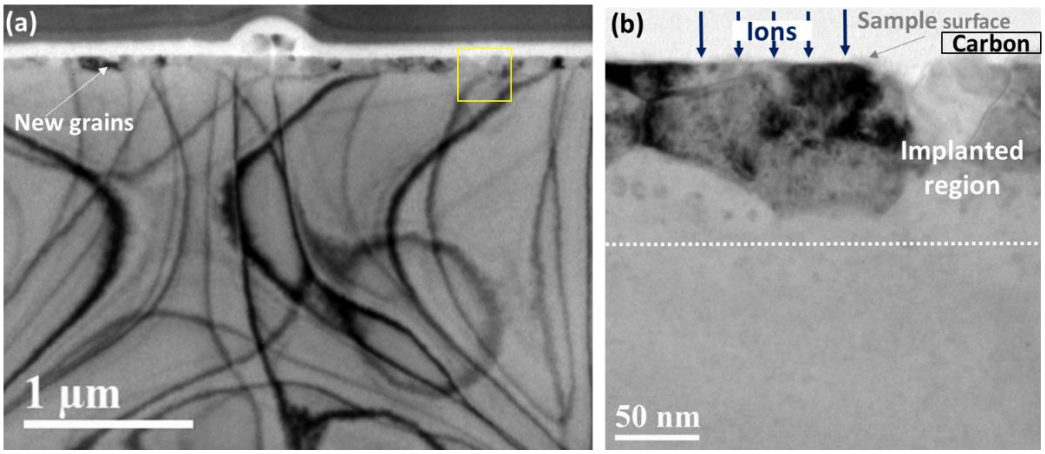

Figure 3.42 Bright Field (BF) imaging of the FIB lamella of the bulk Fe10Cr specimen implanted with Ti ions only and annealed at 800°C (a) at low magnification indicating the formation of many small grains along the surface in the implanted region as well as (b) high magnification BF for a selected region.

To establish the composition of these small grains and possible oxide or Ti-enriched regions formed close to the surface, EFTEM investigations were conducted on a selected region as

indicated in the *Figure 3.42*. Four regions namely 1, 2, 3 and 4 have been highlighted in the *Figure 3.43(a)*. The region 1 is a white contrast region which is likely an oxide formed on the surface of the sample, the regions 2 and 3 represent the many small grains formed within the implanted region and the region 4 is the matrix further from the implanted region. The regions 2 and 3 appears to have the same elemental information as the region 4 with all these regions appearing with a homogeneous contrast. It can therefore be supposed that these regions are also part of the FeCr matrix with no or few difference in composition. The region 1 however shows a depletion in Fe in the elemental map. This region shows an enrichment in O and Cr as well as Ti thereby suggesting a formation of chromium-titanium oxide on the surface of the sample.

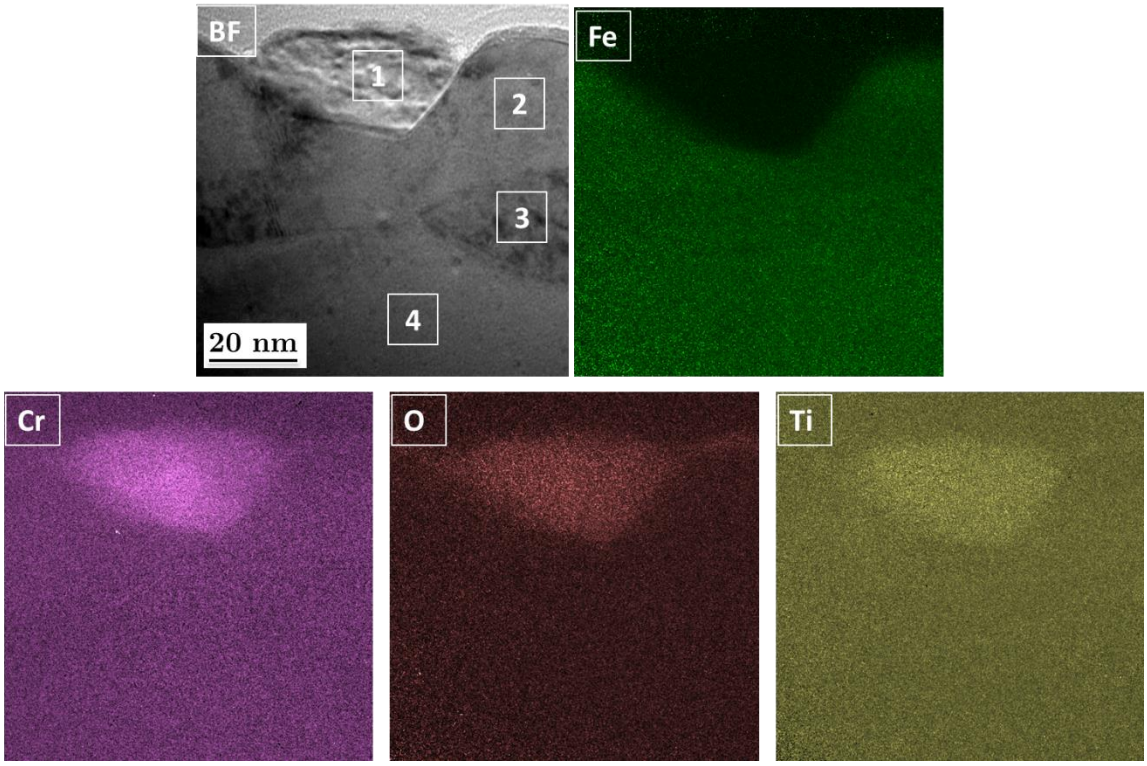

Figure 3.43 Energy-Filtered TEM (EFTEM) elemental characterization of the FIB lamella extracted from Fe10Cr bulk specimen after implantation of Ti only at room temperature and annealing at 800°C for 2 hours. Bright Field (BF) image of the region chosen for EFTEM together with elemental maps acquired using the two-window jump ratio method in the vicinity of Fe-$L_{2,3}$ edge, Cr-$L_{2,3}$, O-K and Ti-$L_{2,3}$ core loss edges.

STEM-EDX was further carried out at JANNuS-Orsay to verify the information within this sample. The *Figure 3.44* shows the Bright Field (BF) and High Angle Annular Dark Field Image (HAADF) within the implanted sample. Five regions have been selected namely A, B, C, D and E. The region A is a region outside the implanted region. The region B is the region within the small grains. The region C is another region within the small grains. The regions D and E are closer the surface of the sample in a white contrast region. In the region D, the contrast is whiter than in the region E.

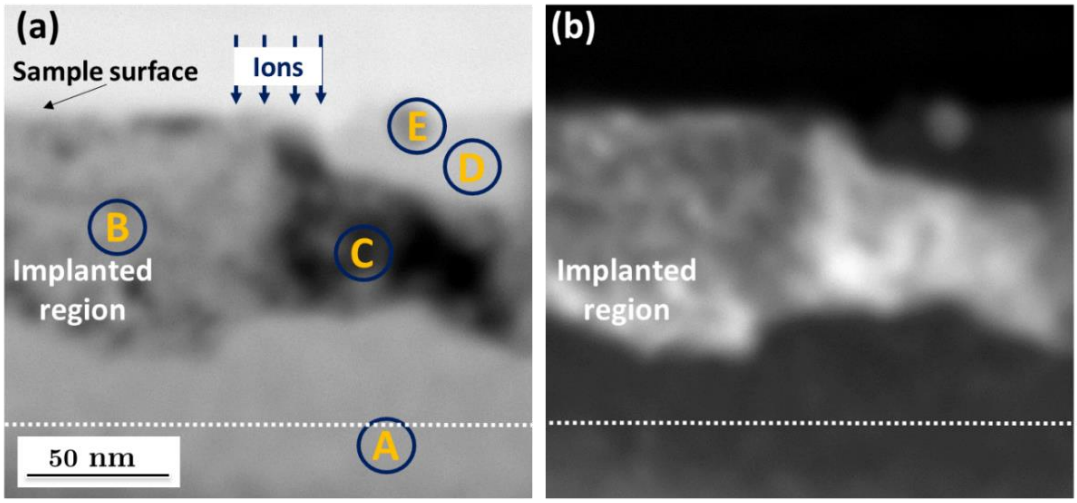

Figure 3.44 (a) BF image and (b) HAADF image of a chosen region for the FIB lamella extracted after implantation of Ti only at room temperature and annealing at 800°C for 2 hours.

The *Figure 3.45* gives the spectra obtained from the STEM-EDX image in the different regions highlighted in the *Figure 3.43*. The zones A, B and C have quite similar spectra with very intense Fe-K peaks and less intense Cr-K peaks, indicating that the small grains have a composition that is similar to the composition of the matrix (A) except for the presence of Ti. Ti is indeed observed in the implanted region but only in the zones B, D and E. The Ti presence in not obvious in region C. The spectra from the regions D and E on the other hand show very negligible Fe peaks. The Cr peaks are contrarily very high confirming the Cr presence in these regions. Because of the overlap of O-K and Cr-L peaks, it is difficult to conclude on the oxygen presence. The copper in all the peaks is also due to the copper grid upon which the FIB lamella has been mounted. However, given that the oxidation of the surface of the specimen is very likely and in light of the previous results of Ti and O implantations, these results suggest the formation of a chromium-oxide enriched in Ti in the regions D and E, close to the surface.

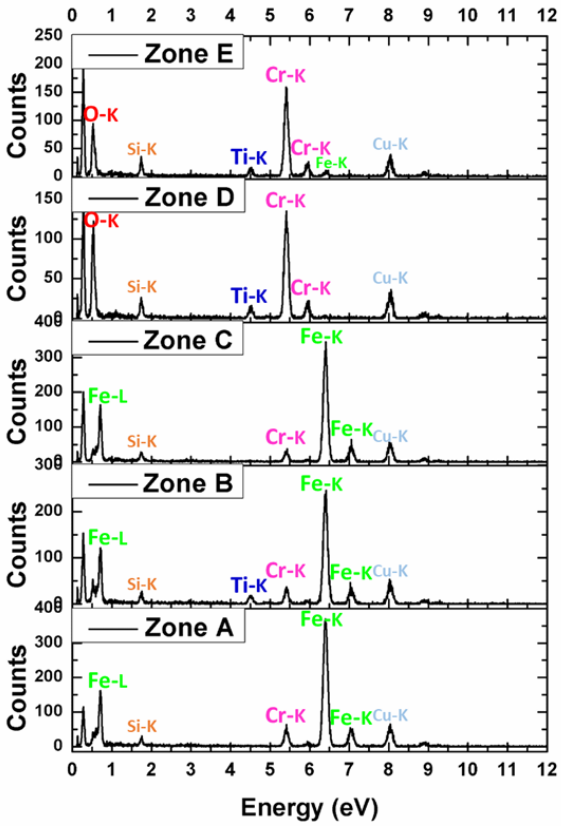

Figure 3.45 Scanning Transmission Electron Microscopy-Energy Dispersive X-ray Spectroscopy (STEM-EDX) spectra measured in the Ti as-implanted and annealed Fe10Cr thin foil at 800°C for the five distinct chosen regions highlighted in Figure 3.43 where spectrum A represents the spectrum from the chosen region A, spectra B, C, D and E also correspond to the spectra from the regions B, C, D and E respectively.

The formation of small matrix grains at the surface of the specimen as labelled region C in the *Figure 3.43* has been observed only in this occurrence and is not understood up to this point. This experiment should be repeated in the future to check the reproducibility of their formation before it can be firmly related to the absence of oxygen.

3.2 The case of Y and O ion implantations into high purity FeCr

In parallel to the Ti and O implantations, Y and O have also been implanted into the high purity FeCr alloy at a projected range of 40-50 nm at room temperature. Both thin foils and bulk samples were implanted.

3.2.1 As-implanted sample

Thin foils implanted with Y and O at room temperature were investigated to check for the potential formation of nanoparticles. In the *Figure 3.46* is reported a bright field image of a selected region together with its corresponding diffraction pattern. The BF image shows defects created within the sample but no visible nanoparticle. The diffraction pattern does not show any additional reflection to the diffraction of the FeCr matrix. The TEM characterizations therefore indicate no formation of nanoparticles after room temperature implantation of Y and O.

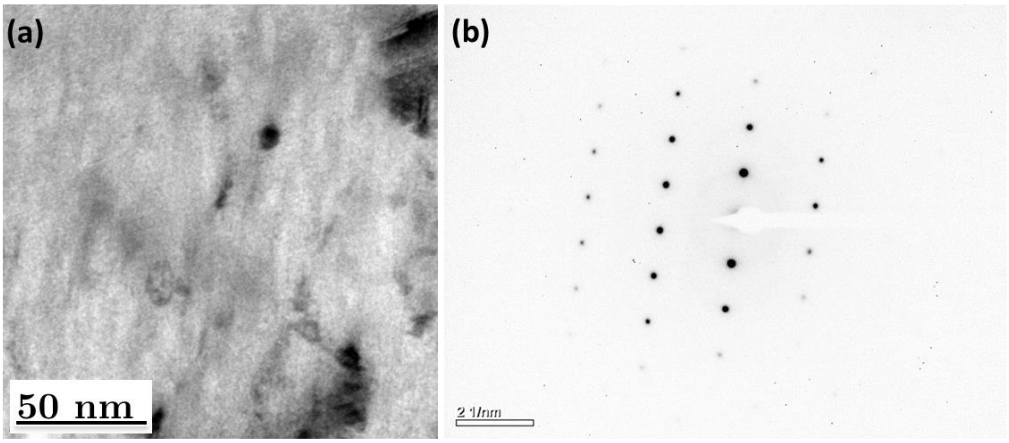

Figure 3.46 (a) Bright Field (BF) image of a selected zone in the as-implanted Y and O thin foil and (b) the corresponding diffraction pattern (DP) for this selected zone with the orientation B = [-113].

Samples implanted at RT were therefore annealed at high temperatures to force the formation of nanoparticles. Only bulk samples were considered for annealing due to the formation of surface oxide, which makes the thin foil characterization unsuitable for the investigation of nanoparticle formation as elaborated in detail in section 1.2.

3.2.2 Bulk sample annealing at 800°C

A FIB lamella was extracted after room temperature sequential implantation of Y and O and annealing at 800°C. The *Figure 3.47* illustrates bright field images of the extracted FIB lamella. A non-uniform surface oxide is formed on the surface of the sample with a thickness of approximately 10 nm. This surface oxide has not been investigated into details but similar to the case of Ti and O samples, proposed to correspond to $FeCr_2O_4$.

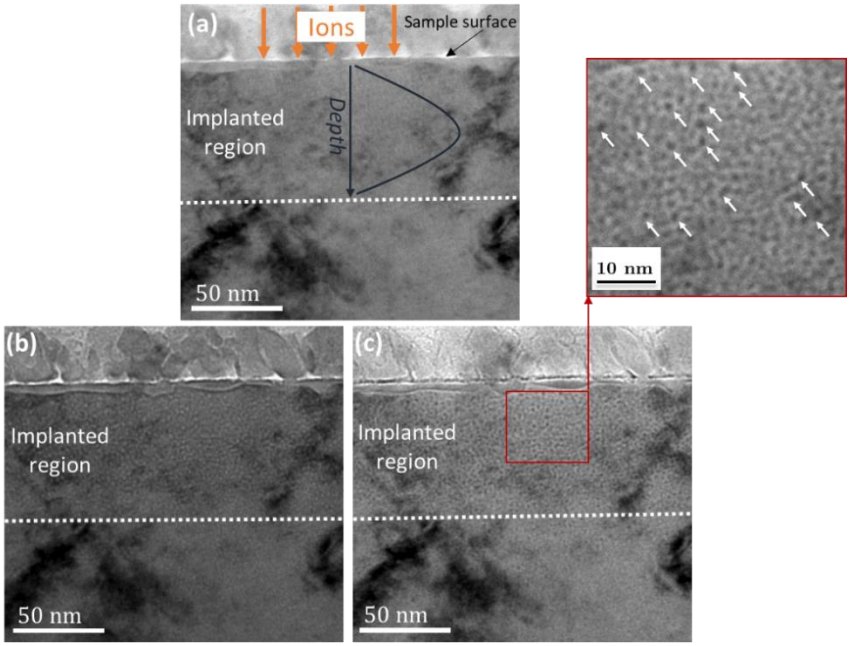

Figure 3.47 Bright Field (BF) imaging of the FIB lamella extracted from the Y and O as-implanted bulk FeCr alloy annealed at 800°C indicating the formation of very small nanoparticles within the implanted region of the bulk sample (a) close to the focus condition (b) in underfocus and (c) overfocus conditions (inset: high magnification of the very small nanoprecipitates).

In addition, many very small nanoparticles appear to be observed in the *Figure 3.47* in overfocus and underfocus conditions within the implanted region. As shown in *Figure 3.48*, the equivalent diameter of the particles ranges from 1 to 5 nm and their average size is ≈ 2 nm. Such small particles are too small to be resolved using the available analytical characterization techniques (EFTEM, EDX in ChemiSTEM). They are also difficult to observe in HRTEM and consequently, their crystallographic structure could not be determined.

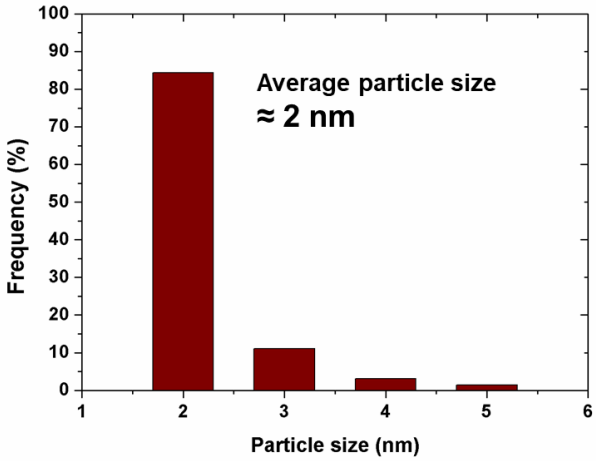

Figure 3.48 Size distribution of nanoparticles observed within the extracted FIB lamella after Y and O room temperature ion implantation and annealing at 800°C.

An enhanced annealing was therefore performed with the purpose of making these nanoparticles grow.

Similar to the case of Ti and O investigation, ToF-SIMS was implemented to investigate the diffusion of Y in Y ion-implanted FeCr specimen. The profiles in the *Figure 3.49* represent the distribution of atoms in Y implanted samples. The profiles for the samples annealed at 500 and 800°C appear to have a similar shape to the as-implanted sample. Hence, contrary to the Ti sample annealed at 800°C where the ions appear to diffuse towards the surface, there appear to be no significant Y diffusion at 800°C. As shown, the diffusion of Y ions towards the surface is triggered by an annealing at 1000°C. An enhanced Y diffusion is observed for the sample annealed at 1100°C.

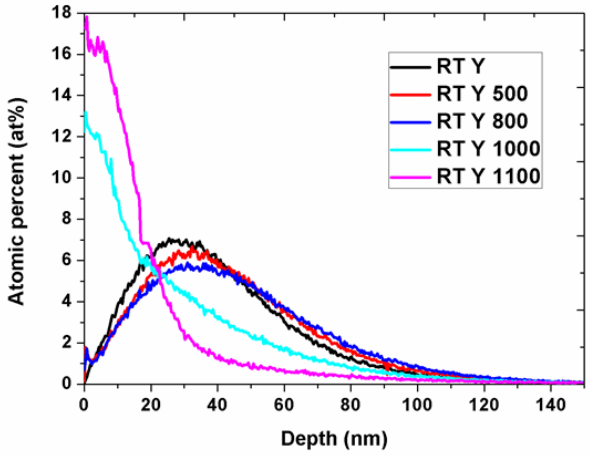

Figure 3.49 Depth profiles using Time-of-Flight Secondary Ion Mass Spectroscopy (ToF-SIMS) measured for Y ions implanted at room temperature in high purity Fe10Cr and annealing at 500, 800, 1000 and 1100°C.

3.2.3 Bulk sample annealing at 1100°C

Annealing of a bulk specimen was therefore performed at the temperature of 1100°C after which a FIB lamella was extracted. The *Figure 3.50* shows corresponding BF images. A surface oxide is observed on the surface of the sample with a thickness of approximately 10 nm. Beneath the surface layer are observed many nanoparticles up to a depth of 100 nm, which corresponds to the implanted region.

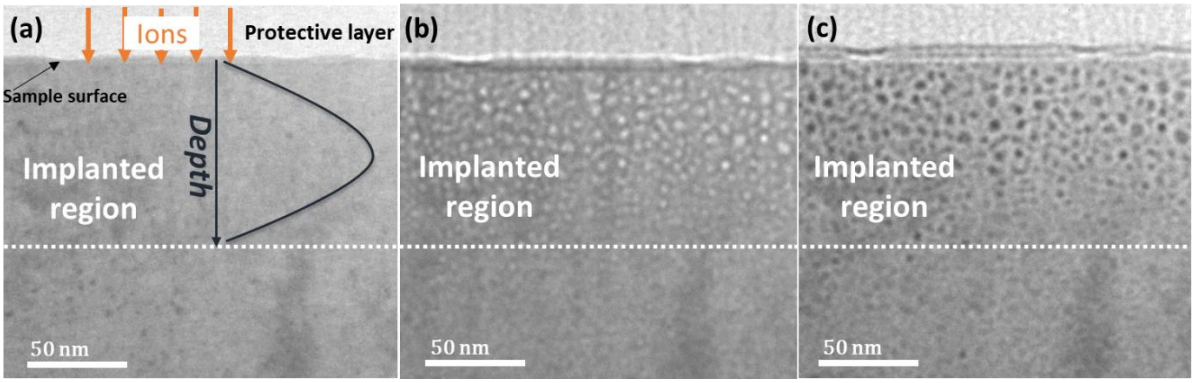

Figure 3.50 Bright Field (BF) imaging of the FIB lamella extracted from the Y and O as-implanted bulk Fe10Cr annealed at 1100°C indicating the formation of nanoparticles within the implanted region of the bulk sample (a) close to the focus condition (b) in the underfocus and (c) overfocus condition. Add sentence about SRIM profile in (a)

The nanoparticles observed within the implanted region range from a size of 3 to 12 nm. The average size of these particles was determined as ≈ 5 nm. The *Figure 3.51* shows the evolution of the nanoparticle size from the annealing condition of 800°C (approx. 2 nm diameter) to the annealing condition of 1100°C (average size 5 nm).

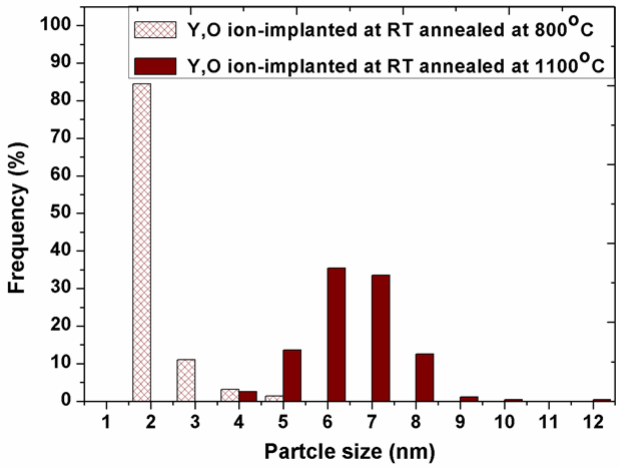

Figure 3.51 Size distribution of the nanoparticles within the extracted FIB lamella from Y and O room temperature ion implantation in bulk Fe10Cr and annealing at 800 and 1100°C.

The *Figure 3.52(a)* shows these nanoparticles observed in HRTEM at low magnification. The Fringes can already be observed indicating crystallinity. At higher magnifation as shown in the *Figure 3.52(b),* small and rounded nanoparticles are observed as highlighted by the yellow circles. In addition, slightly larger nanoparticles highlighted by the white cube or cuboid display some facets not easily observed in the small rounded particles. Also, other nanoparticles are observed with facets but more in the shape of a hexagon. There is a last set of nanoparticles also showing facets in the form of an elongated hexagon. From the evolution of the particle sizes, it is assumed that the small nanoparticles appear to be more rounded and without facets. The possibility of these small nanoclusters possessing facets cannot be discounted however. But this is not easily observable due to their very small size. The growth of the clusters appears with the development of facets as shown in the white cubes in *Figure 3.52(b)*. The formation of nanoparticles with facets in the form of a hexagon is then eventually formed. This shape could correspond to a cube with an orientation B = -111 or a dodecahedron. The more elongated faceted particles could be two neighboring particles coherent with each other and which overlap making the nanoparticle appear elongated.

The facets of most of the nanoparticles seem to be parallel to the {100} and {110} planes of the FeCr matrix.

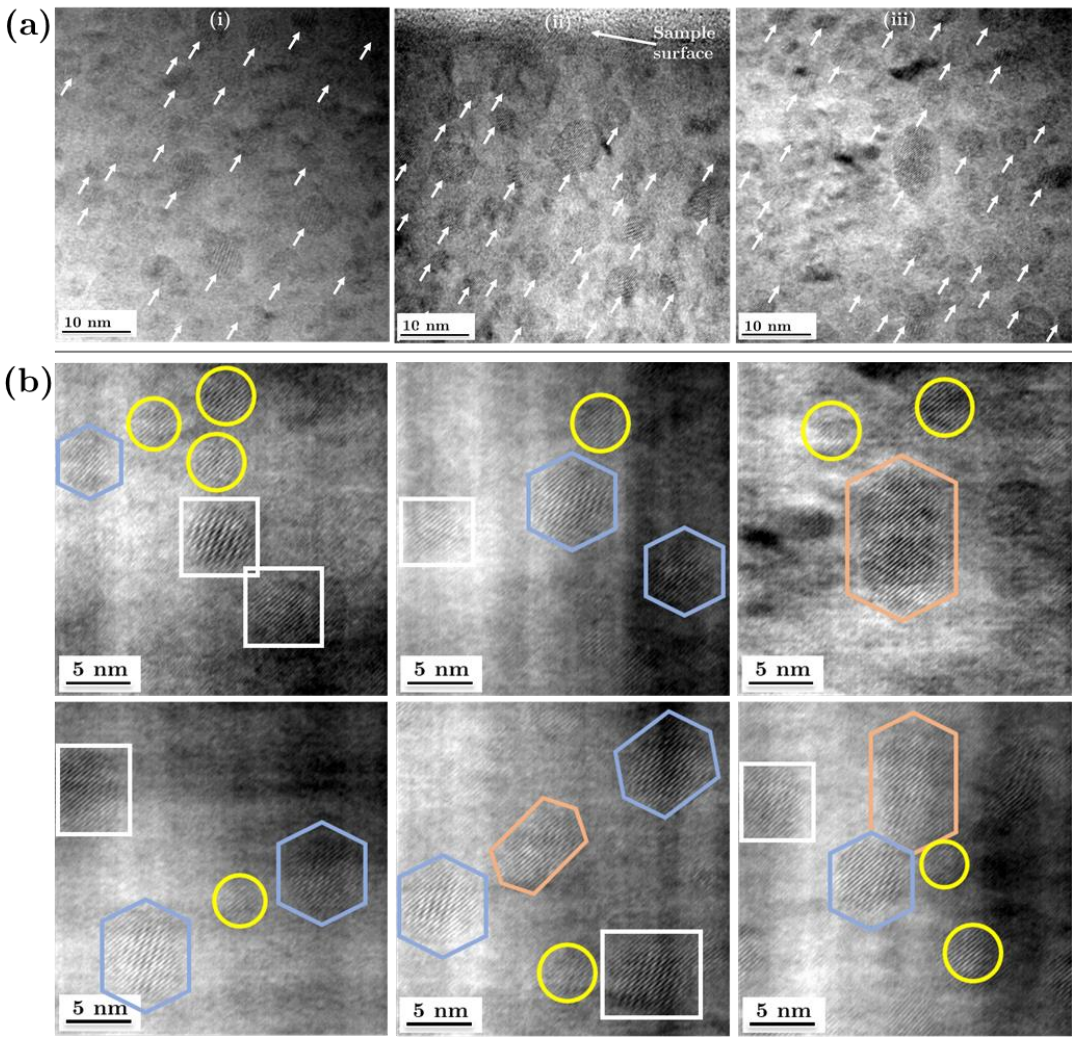

Figure 3.52. High-resolution images taken at low magnification in the FIB lamella extracted from Y and O ion-implanted annealed at 1100°C showing a dense distribution of crystalline nanoparticles within the implanted region.

The crystallographic structure of the observed particles has been investigated by HRTEM. Investigations were conducted on many different regions for various particles. In the *Figure 3.53* are HRTEM images for five different particles labelled *(a)* to *(e)*. For each particle, the image labelled *(i)* is the HRTEM image of the particle embedded in the matrix, the image labelled *(ii)* is the high magnification image of the particle and the image *(iii)* illustrates the fast Fourier transform (*fft*) of the particle. The sizes of these chosen particles range between 5 and 10 nm. The *fft* of the particles in *(a)* and *(b)* show four distinct spots labelled (222). The interplanar distance of these diffraction spots were measured as 0.305 nm and the angle between these spots was determined as 66°. These features match those of the diffraction of the *bcc* Y_2O_3 of lattice parameter a = 1.06 nm with an orientation B = [011]. It can therefore be concluded that these particles are Y_2O_3 structure type nanoparticles.

For the particle found in *Figure 3.53(c)*, the *fft* shows a hexagon labelled (111) and (200). The interplanar distances of these diffraction spots were measured as 0.305 and 0.256 nm for the (111) and (200), respectively. These distances were found to closely match the interplanar distances of (111) and (200) planes for the *fcc* Y_2O_3 with the lattice parameter a = 0.52 nm (d_{111} = 0.305 and d_{200} = 0.265 nm). Similarly, the measured angles between the two (111) was measured as 56° while the distance between the (111) and (200) was measured as 68°. These details of the measured distances and angles match the *fcc* Y_2O_3 structure-type with an orientation B = [011]. This therefore confirms the formation of Y_2O_3 nanoparticles within the sample. In addition, the (111) atomic planes of the Y_2O_3 particle is found to be parallel to the (011) atomic plane of the FeCr matrix ((011)FeCr//(111)Y_2O_3). A partial coherency could therefore be assumed to exist between the particles and the FeCr matrix. This orientation relationship between the particles and the matrix has been observed by Klimiankou *et al.* [Klimiankou 2003, 2004] in conventional RAFM-ODS steels.

For the two particles found in *Figure 3.53(d)* and *(e)*, the *fft* look quite similar. Three distinct interplanar distances are highlighted. The interplanar distances for the diffraction spots d_1, d_2 and d_3 are measured to be close to 0.54, 0.29 and 0.20 nm respectively. These distances are close to the (200), (222) and (521) theoretical interplanar distances at 0.53, 0.30 and 0.19 nm, respectively, for the *bcc* Y_2O_3 structure-type. The angles however do not correspond to a zone axis that would include these planes. A possible superposition of spots from *bcc* Y_2O_3 particles in different orientations could presumably explain this.

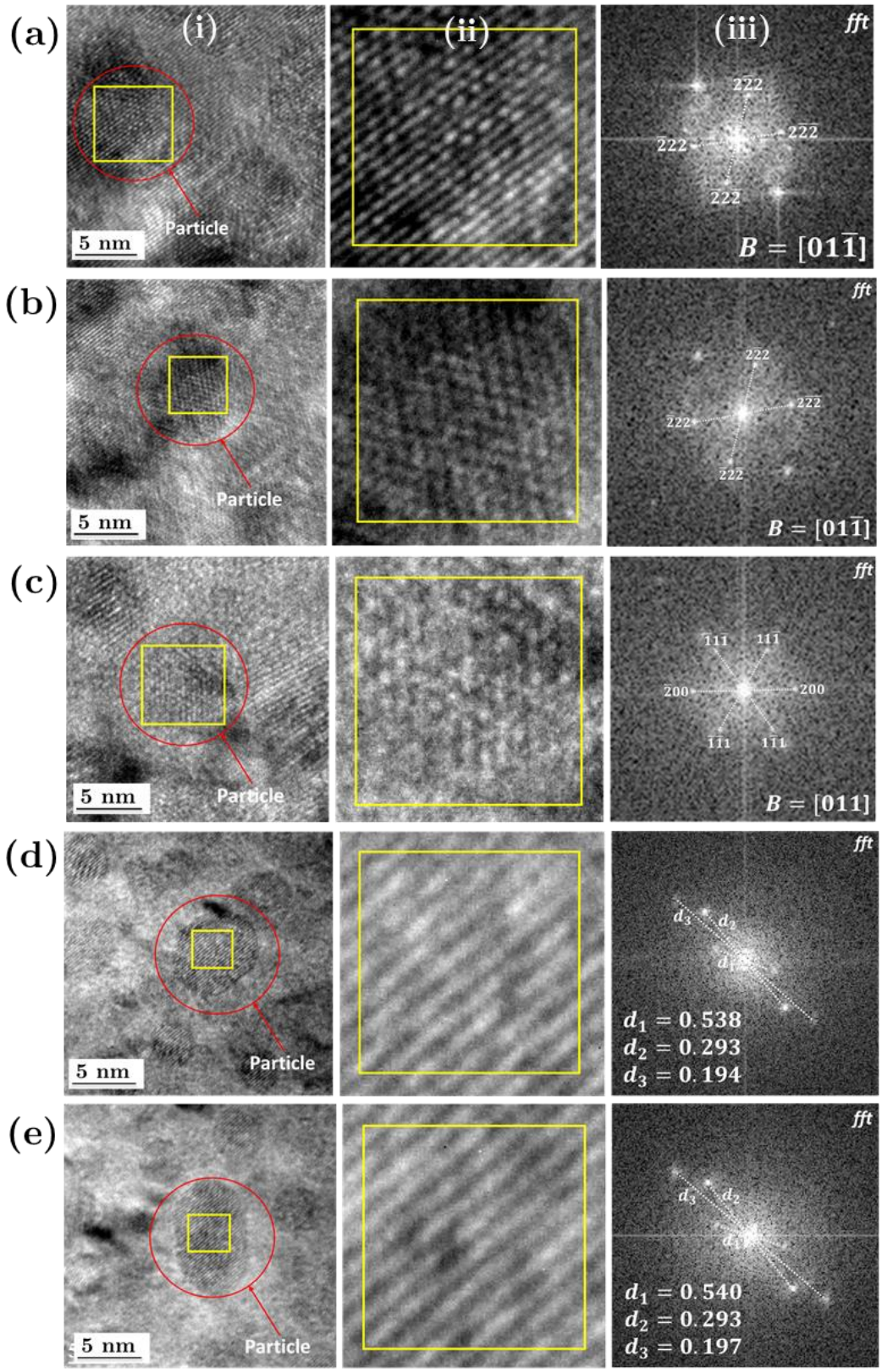

Figure 3.53. (i) High Resolution TEM (HRTEM) image of selected particle embedded in the matrix from the FIB lamella extracted after implantation of Y and O ions at room temperature in bulk FeCr and annealing at 1100°C for 2 hours. (ii) Magnified image of the selected region of the particle and the (iii) corresponding Fast Fourier Transform (*fft*) of the particle.

The chemical composition characterization was performed by STEM-EDX operating under the ChemiSTEM technology. Mappings conducted at both low and high magnifications produce a

similar result. Here, we will only show the mapping performed at high magnification. The *Figure 3.54(a)* is a low magnification bright field image indicating the zone from which the EDX mapping was performed. The corresponding BF and HAADF images for this region are given in the *Figure 3.53(b)* and *(c)*, respectively. Fe elemental maps appear with a depletion in patches which correspond to the 5 nm sized nanoparticles observed in conventional BF and high resolution imaging. These particles are visibly enriched in Y. The Cr elemental map however only shows a slight depletion of Cr in these particles. An enrichment of Cr is also observed in patches around the nanoparticles. This therefore suggests a possible Cr shell formation around the particle. The O elemental map surprisingly appears quite homogenous, which has already been commented above as an artefact (see section 2.2.3.1). The O presence is however obvious considering the previous results of the crystallographic structre.

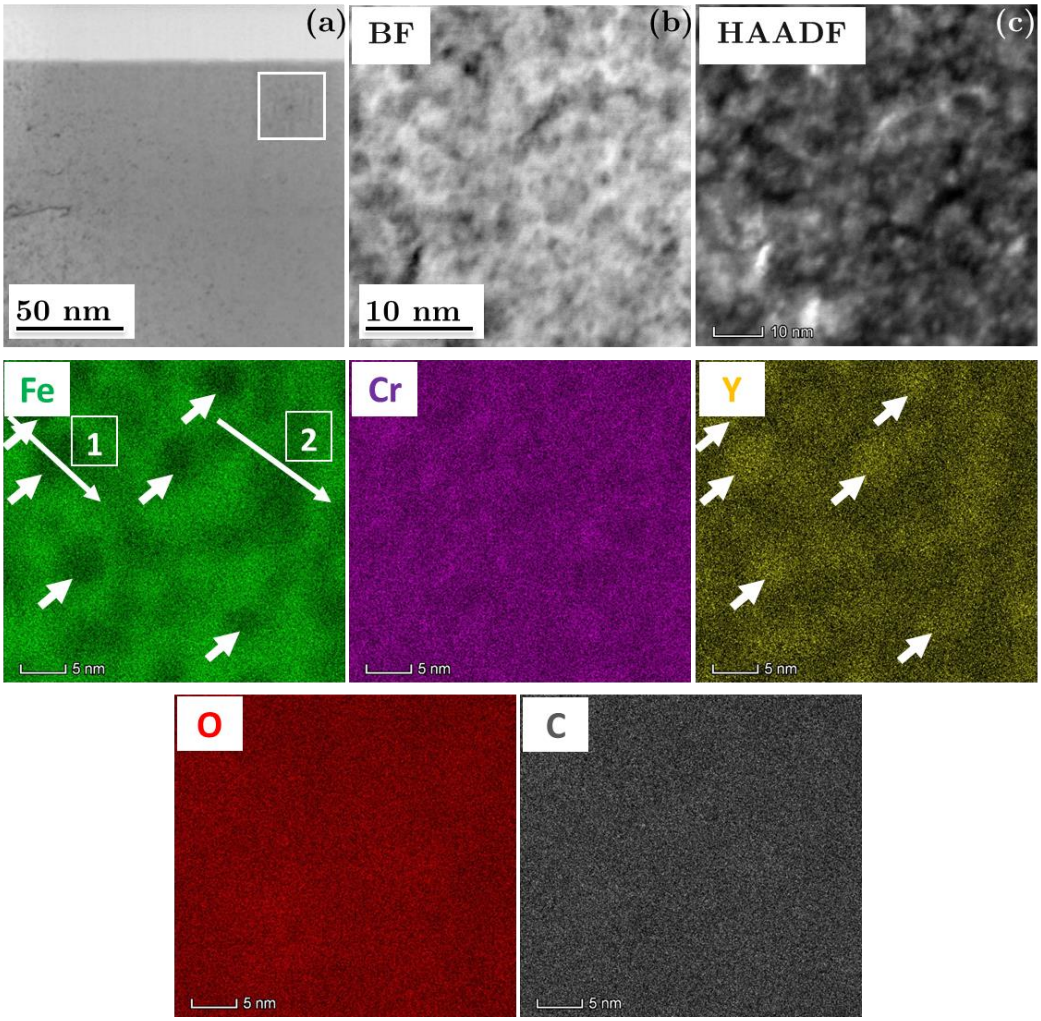

Figure 3.54 STEM-EDX elemental mapping using ChemiSTEM technology of FIB lamella extracted from Y and O implanted bulk FeCr specimen and annealed at 1100°C. (a) Bright Field (BF) image indicating the selected region (b) the corresponding Bright Field (BF) and (c) High Angle Angular Dark Field (HAADF) image together with elemental maps for Fe, Cr, Y, O and Cr. This scan was performed for a duration of 45 minutes with an EDX count rate of 40k counts/second. Two particles 1 and 2 are highlighted in the Fe elemental map and used for the line scans shown in Figure 54.

Line scans extracted from this analysis are reported in *Figure 3.55* for two different particles highlighted in the Fe elemental map in the *Figure 3.54*. The results of the two particles are exactly the same. The particles display a depletion in Fe and Cr. These particles are however enriched in Y. The Cr line scans for the two particles interestingly display an enrichment

around the particles as observed in the elemental maps. The elemental characterization therefore suggests the yttrium oxide formation with a Cr shell. This core/shell structure was previously observed in the Ti and O samples annealed at the same temperature, i. e., 1100°C.

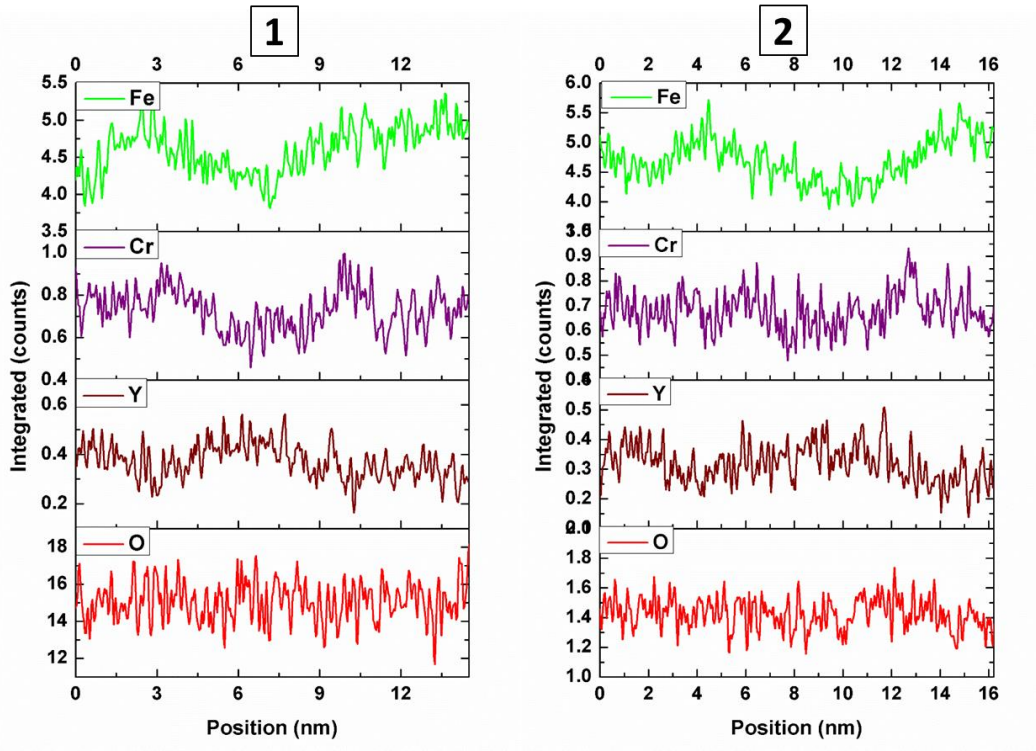

Figure 3.55. STEM-EDX 1-D line scan using ChemiSTEM technology of two particles within the FIB lamella extracted from FeCr bulk specimen implanted at RT with Y and O ions and annealed at 1100°C showing line scans for Fe, Cr, Y and O for two different particles labelled 1 and 2, highlighted in Figure 3.54.

The results of the elemental characterizations as well as the HRTEM thus show the formation of *bcc* and *fcc* yttrium oxide Y_2O_3 after room temperature Y and O ion implantation and annealing at 1100°C. These nanoparticles display a core/shell structure with an Y-enriched core and Cr-enriched shell.

3.2.4 Ion implantation at 500°C

Up to this stage, the investigations only concerned samples implanted with ions at room temperature and subsequently annealed at high temperatures. However, it is known that irradiation at high temperatures enhances dynamic annealing processes involving the migration and interaction of created point defects leading to the recombination of a fraction of Frenkel pairs as well as the clustering of point defects. The result is often that larger extended defects are observed when the temperature of ion implantation is increased. These processes could also favour the nucleation and growth of nanoparticles or even nucleate particles with a structure or composition that differs from what is observed after RT ion implantations and subsequent annealing. For this reason, a sequential ion implantation of Y and O has been performed at 500°C with the same parameters used for the RT implantation (see section 2.3).

The *Figure 3.56* shows BF images of the FIB lamella extracted from the bulk FeCr sample implanted with Y and O at 500°C. A very thin surface oxide <10 nm is observed on the surface

of the sample. Nanoparticles are observed within the sample from the surface to a depth of approximately 80 nm, which precisely represents the implanted region.

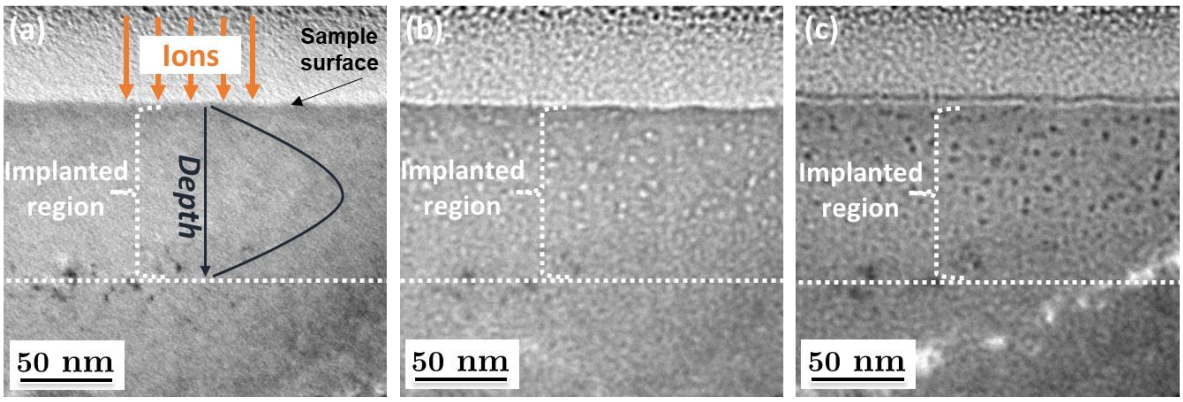

Figure 3.56 Bright Field (BF) imaging of FIB lamella extracted from FeCr specimen implanted with Y and O ions at 500°C, indicating the formation of nanoparticles within the implanted region of the bulk sample (a) close to the focus condition (b) in the underfocus and (c) overfocus condition

The size of the particles ranges between 3 and 12 nm with an average size of ≈6 nm, which is similar to the size of the nanoparticles found for the Fe10wt%Cr specimen implanted with Y and O ions at room temperature and subsequently annealed at 1100°C (see *Figure 3.57*). This similarity might be a coincidence, but it may also suggest a saturation of the mean size of the particles of Y_2O_3 structure that can be obtained by both room temperature ion implantation followed by annealing at high temperature as well as the high temperature ion implantation.

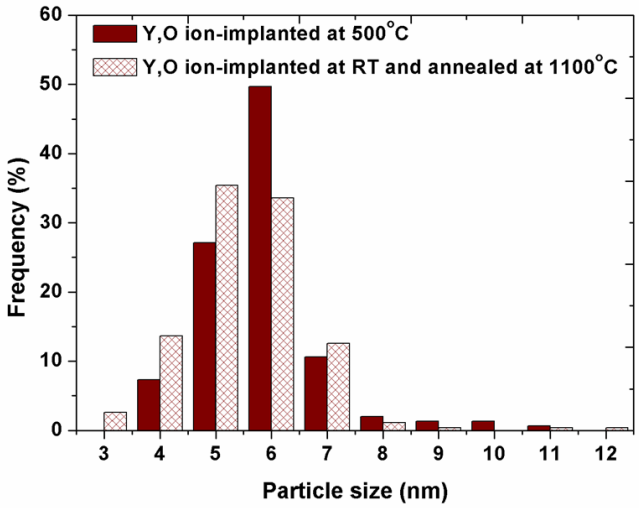

Figure 3.57 Size distribution of the nanoparticles within the extracted FIB lamella in bulk Fe10Cr after Y and O ion implantations at 500°C as a comparison to the specimen implanted with Y and O at RT and subsequently annealed at 1100°C

The *Figure 3.58* displays the HRTEM images for some of the particles observed within the sample implanted with Y and O ions at 500°C. Three different particles are shown, marked *(a)* to *(c)*. The particles in the *Figure 3.58(a)* and *(b)* have a size of approximately 5 nm. The *fft* of these particles show a hexagon for the spots which are labelled (111) and (200). The interplanar distances for these spots were determined to be 0.25 and 0.29 for the (111) and (200) respectively. These distances closely match the interplanar distances of (111) and (200) diffraction spots at 0.305 and 0.265 nm, respectively, for the *fcc* Y_2O_3. The angle between the

two (111) was measured as 56° while the angle between the (111) and (200) was measured as 68°. These are close to the angles found in the *fcc* Y_2O_3 with an orientation B = [011] (55° and 70°).

Another analysed particle is shown in *Figure 3.58(c)*. The *fft* of this particle illustrates a hexagon for spots of equal interplanar spacings labelled (220). The interplanar spacing for these diffraction spots was measured as 0.19 nm and the angle between two (220) was checked to be 60°. These measurements are closely matching the (220) of *fcc* Y_2O_3 with an interplanar spacing of 0.187 nm in a zone axis B = [111].

Thus, both ion implantation at RT followed by a subsequent annealing at 1100°C, and ion implantation at 500°C lead to the formation of nanoparticles of Y_2O_3 structure.

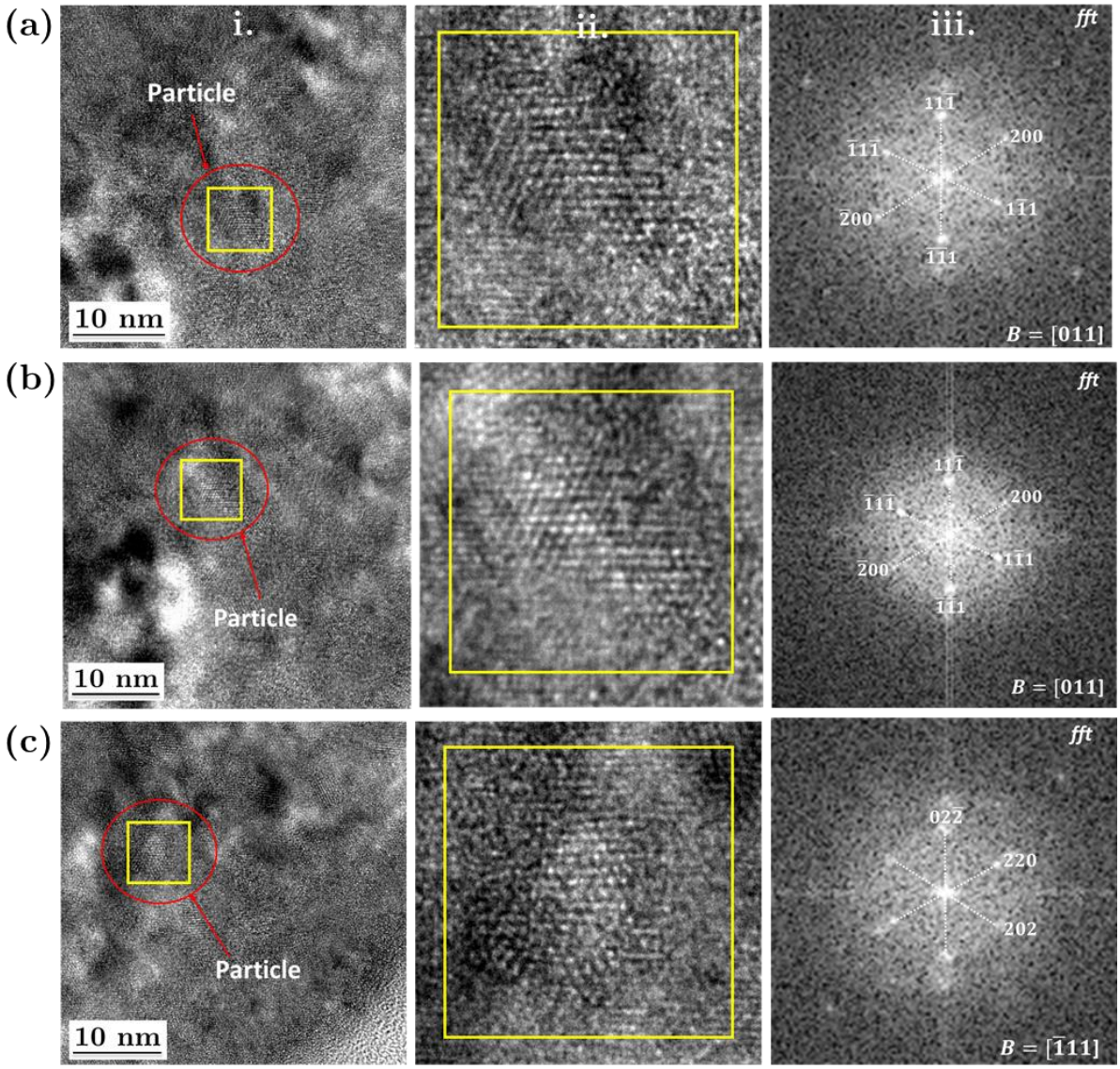

Figure 3.58 (i) High Resolution TEM (HRTEM) image of a selected particle embedded in the matrix from the FIB lamella extracted from bulk FeCr after implantation of Y and O ions at 500°C. (ii) Magnified image of the selected region of the particle and the (iii) corresponding Fast Fourier Transform (*fft*) of the particle.

The elemental characterization was again performed using ChemiSTEM EDX. Mappings were performed for relatively low and high magnifications but we only show the high magnification

mapping. In the *Figure 3.59(a)* is a BF image highlighting the zone from which the EDX mapping was performed. The BF and corresponding HAADF images are given in *Figure 3.59(b)* and *(c)*. Again, the elemental map for O appears surprisingly homogeneous, which is explained in previous sections. The Fe elemental map displays patches of Fe depletion corresponding to nanoparticles. These particles appear with an enrichment in Y as well as Cr. This is highlighted in *Figure 3.60* in line scans extracted for two particles marked in *Figure 3.59*. In certain particles in *Figure 3.59*, the Cr signal appears to be less intense at the center of the particle, which could suggest a possible beginning of formation of Cr shell similar to the previous condition where Y and O were implanted at RT and annealed at 1100°C. This is however unclear and has yet to be confirmed.

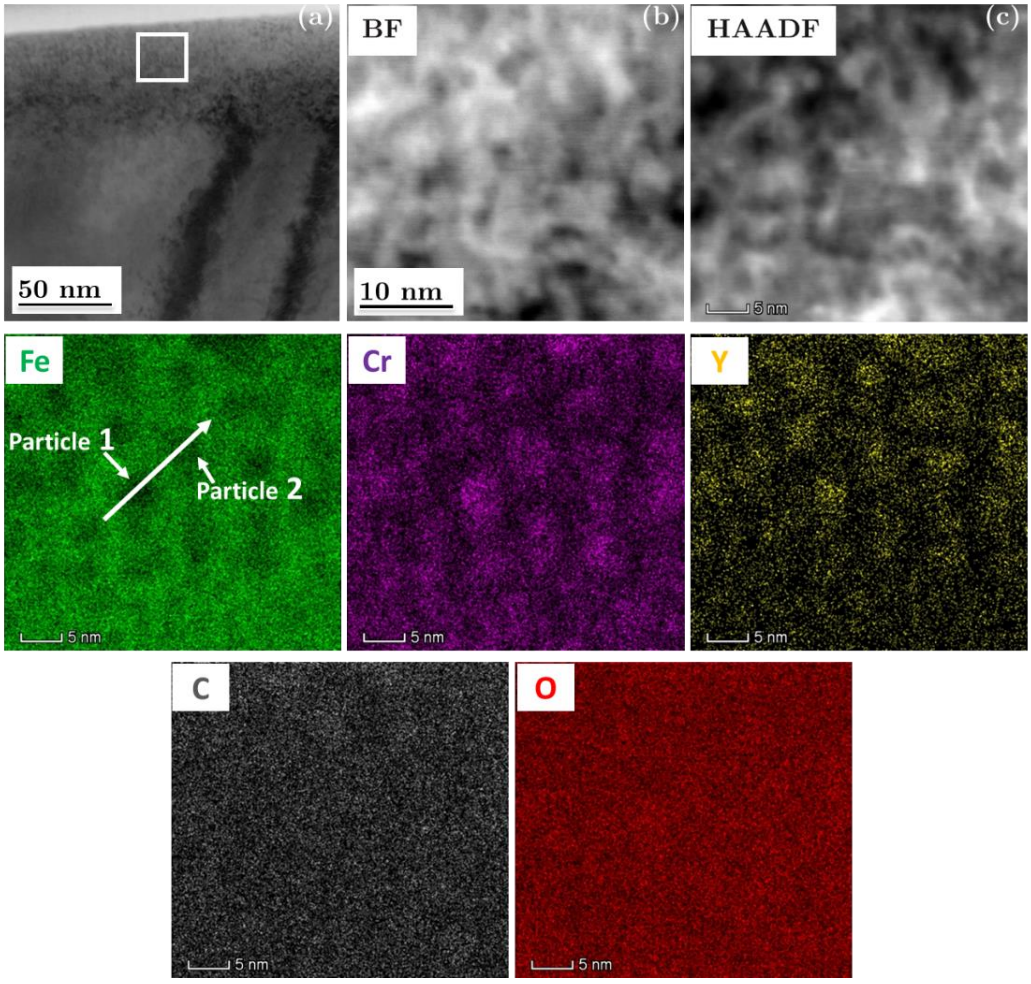

Figure 3.59 STEM-EDX elemental mapping using ChemiSTEM technology of FIB lamella extracted from FeCr bulk specimen implanted with Y and O ions at 500°C. (a) Bright Field (BF) image indicating the selected region (b) the corresponding Bright Field (BF) and (c) High Angle Angular Dark Field (HAADF) image together with elemental maps for Fe, Cr, Y, O and Cr. The scan was performed for a total of 45 minutes at a count rate of 35k counts/second. Two particles used for line scans shown in Figure 3.59 are highlighted in the Fe elemental map.

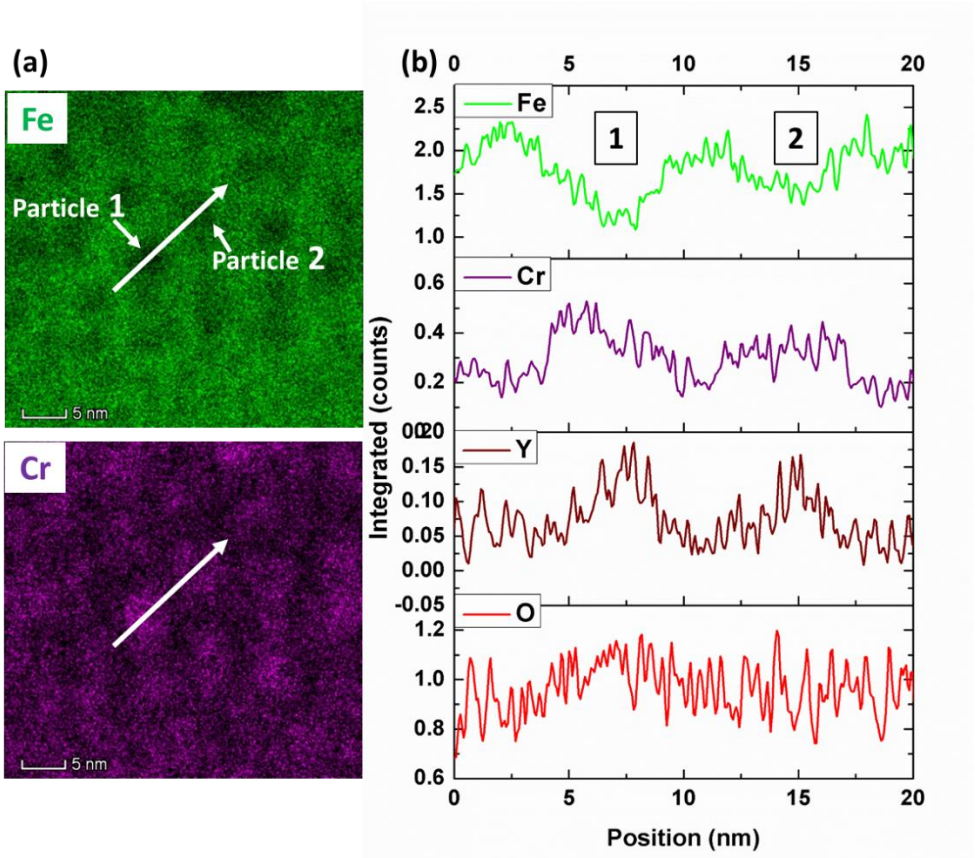

Figure 3.60 STEM-EDX 1-D line scan using ChemiSTEM of two particles within the FIB lamella of FeCr bulk specimen implanted with Y and O ions at 500°C. (a) Fe and Cr elemental maps indicating the trace of the line scan and (b) line scans for Fe, Cr, Y and O through the two particles.

3.2.5 Summary of Y and O ion-implanted samples

Y and O ions have been directly implanted into a high purity FeCr alloy in an attempt to produce Y oxides by ion beam synthesis. Neither the diffusion of Y nor the formation of nano-oxides of Y is recorded directly after room temperature ion implantation. Annealing has therefore been required to force the formation of nano-oxide particles. No significant diffusion of Y at 800°C is observed by SIMS but minute nanoclusters of the order of 2-3 nm are found. The size of these clusters does not enable the determination of their structure and chemical composition with the available equipments. Annealing at enhanced temperatures of 1000 and 1100°C ensures the diffusion of Y and O towards the surface of the specimens. After a 1100°C annealing, nano-oxide particles are observed with a size of approximately 5 nm. These nanoparticles are expected to be similar to those observed at the annealing condition of 800°C. They are identified as having *bcc* and *fcc* structure of Y_2O_3 nano-oxide particles with a shell rich in Cr. In addition to room temperature ion implantation followed by high temperature annealing, Y and O ions have been implanted into the FeCr matrix at a high temperature of 500°C. The sizes of these particles closely match the sizes of the nanoparticles observed after RT ion implantation and subsequent annealing at 1100°C. They are also identified as having an *fcc* Y_2O_3-type crystallographic structure but with an enrichment of Cr. The beginning of formation of a Cr shell surrounding a core depleted in Cr is not excluded. A resume of the sizes, chemical composition, crystallographic structure and the characterization techniques for each of these conditions is displayed in the *Table 3.3.*

Sample	Nanoparticle	Composition		Structure		Identification
		Observation technique	Chemical composition	Observation technique	Crystallographic structure	
Y+O RT As-implanted	No visible nanoclusters	BF		Diffraction pattern (DP)		
Y+O RT implanted and Annealed at 800°C	Nanoclusters ≈ 2-3 nm	ChemiSTEM	Unidentifiable	HRTEM	Unidentifiable	Probable yttrium-chromium oxides
Y+O RT implanted and Annealed at 1100°C	Nanoparticles ≈ 5 nm	ChemiSTEM	Y, Cr and O enriched core Cr enriched shell	HRTEM	Particle 1: *bcc* Y_2O_3-type structure Particle 2: *fcc* Y_2O_3-type structure	Particle 1: *bcc* Y_2O_3 nanoparticles with a Cr enriched shell Particle 2: *fcc* Y_2O_3 nanoparticles with a Cr enriched shell
Y+O ion Implantation at 500°C	Nanoparticles ≈ 6 nm	ChemiSTEM	Y, Cr and O enriched core Cr enriched shell	HRTEM	*fcc* Y_2O_3-type structure	*fcc* Y_2O_3 nanoparticles with a Cr enriched shell

Table 3.3 Summary of chemical composition and crystallographic structure of nanoparticles observed in Y and O ion-implanted samples.

3.3 The case of O, Ti and Y ion-implanted samples

The sections 1 and 2 focused on (Ti,O) as well as (Y,O) ion-implanted samples. In this section, we will look at the final step which involves all three elements (i.e. Y, Ti, O) similar to the conditions in conventional fabrication when Ti is introduced as well as the Y_2O_3 powder in the mechanical alloying process. A point that can be noted from the two previous ion implantation conditions is that, the metallic ions are implanted first followed by the O. This is to hinder any diffusion of O already at room temperature once it is implanted. During mechanical alloying, all the alloying powders are introduced at the same time and alloyed. Hence, in our case where only one element can be introduced at a time, the main question that pops is related to the sequential order of ion implantations, i.e., which metallic element is to be implanted first. To observe any effect of this sequential order, we performed both kind of experiments: i) ion implantation of Ti followed by Y and finally O (labelled Ti -> Y -> O), as well as ii) Y ion implantation followed by Ti and O (labelled Y -> Ti -> O). A comparison of the results from these two sets of experiments follows. Only bulk specimens were considered after subsequent annealing.

3.3.1 The as-implanted samples

Thin and bulk samples were implanted with all three elements at room temperature following the two sequences of ion implantations (Ti -> Y -> O and Y -> Ti -> O). Thin foils were readily observed by direct TEM observations after implantations. Conventional TEM imaging showed no visible nanoparticle formation. EFTEM elemental maps also displayed no evidence of nanoparticle formation after RT implantation of Ti -> Y -> O and Y -> Ti -> O. This is quite coherent and similar to the previous RT implantation of Ti and O as well as Y and O. Annealing therefore was again eventually required to enable the formation of particles. Thin foils were annealed at 800°C and displayed the formation of a surface oxide $FeCr_2O_4$. This can be found in Annex V. Here only the results of the bulk sample will be addressed in the next paragraphs.

3.3.2 Bulk sample annealing at 800°C : quick comparison between Ti -> Y -> O and Y -> Ti -> O

Bulk samples implanted with all three elements (Ti -> Y -> O and Y -> Ti -> O) were annealed at the temperature of 800°C under vacuum during 2 hours. Conventional TEM BF imaging was performed on both samples. *The Figure 3.61(a)* displays BF images of the FIB lamella extracted from the bulk FeCr sample implanted with Ti -> Y -> O ions at RT and subsequently annealed at 800°C. Two distinct types of particles are visible in underfocus and overfocus conditions: more elongated particles with a Feret's diameter of ≈ 35 nm and much smaller and rounded particles with a size of approximatively 5 nm. The rounded particles could however be particles that are elongated in the direction normal to the plane of the specimen. Both types of particles are formed precisely within the implanted region. The *Figure 3.61(b)* displays BF images for the Y -> Ti -> O samples. In this case, there is what appears to be a high density of very small particles. These particles look very different from the particles in the case of the Ti -> Y -> O sample: there are no elongated particles and the size of these particles is approximately 2-3 nm. These features are more pronounced within the first 50 nm from the surface of the sample.

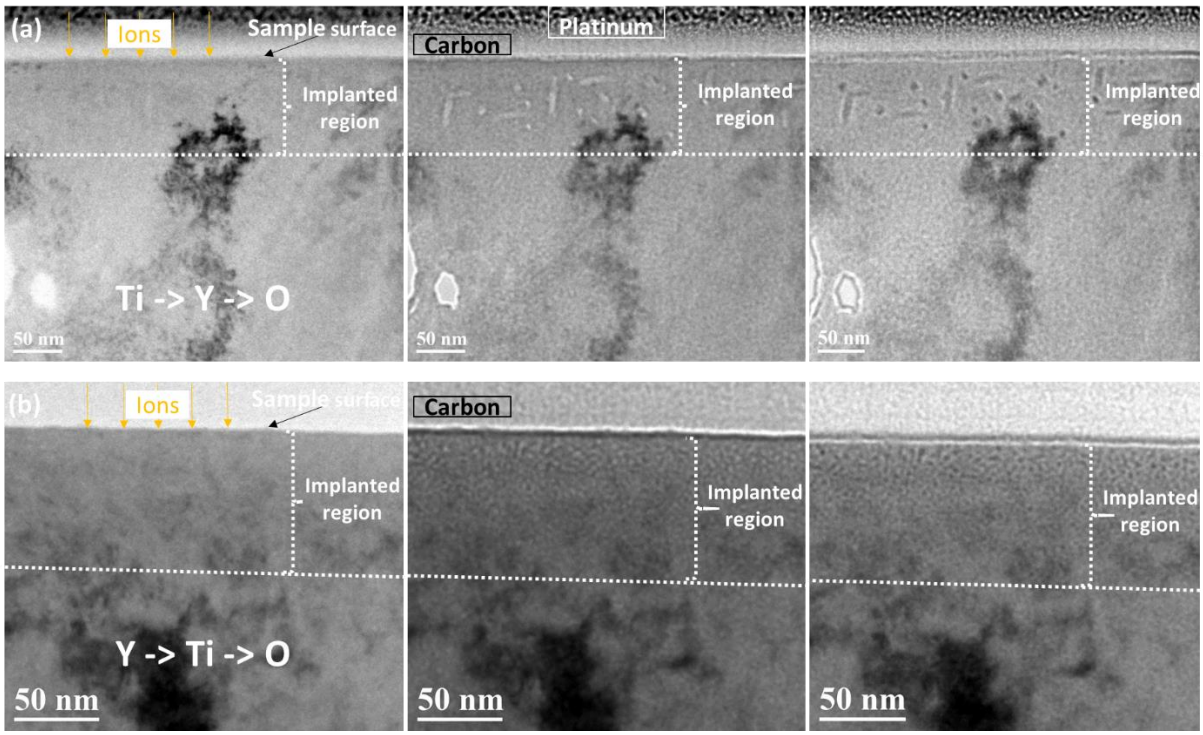

Figure 3.61 Bright Field (BF) imaging of the FIB lamella extracted after the implantation of (a) Ti -> Y -> O, or (b) Y -> Ti -> O ions, and annealing at 800°C indicating the formation of nanoparticles within the implanted region, with, from left to right, a close to focus condition, an underfocus and overfocus conditions.

The differences observed in shape and size of particles in the two sets of experiments (Ti -> Y -> O and Y -> Ti -> O) probably suggest different kind of particles in crystallographic structure and chemical composition. A further investigation of the structure and chemical composition of the particles obtained in the two cases was carried out.

3.3.2.1 Ti -> Y -> O annealed at 800°C

Conventional TEM imaging was performed on different regions. The *Figure 3.62(b)* shows a BF image of a selected region imaged close to the focus condition and hence the nanoparticles are not easily observed. A diffraction pattern was obtained for this selected region as given in the *Figure 3.62(a)*. Many small diffraction spots are observed in addition to the more intense spots, which correspond to the FeCr matrix. Two of these less intense spots were selected and the corresponding dark field images are reported in *Figure 3.62(c)* and *(d)*. Depending on which diffraction spots are selected, different particles are highlighted. On these pictures, and in contrast with the *Figure 3.61(a)*, all particles show an elongation, even slight, i.e., there is no rounded particles. This could suggest that there is no spherical particles but that all are similarly elongated in different directions.

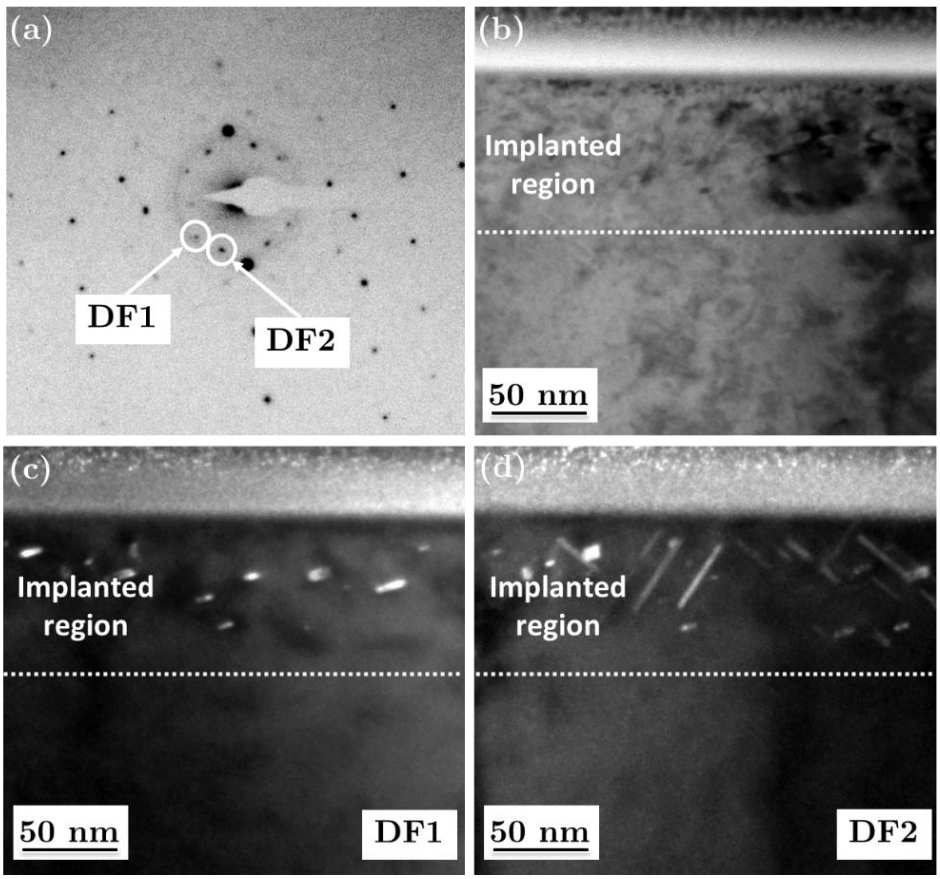

Figure 3.62 (a) Diffraction pattern (DP) of a selected region from the FeCr sample implanted with Ti -> Y -> O ions and annealed at 800°C for 2 hours with an orientation B = [012]. (b) Bright Field (BF) image of the region from which the diffraction pattern was taken. (c) corresponding Dark Field (DF) image acquired using the spot labelled as DF1 in (a), and (d) corresponding Dark Field (DF) image acquired using the spot labelled as DF2.

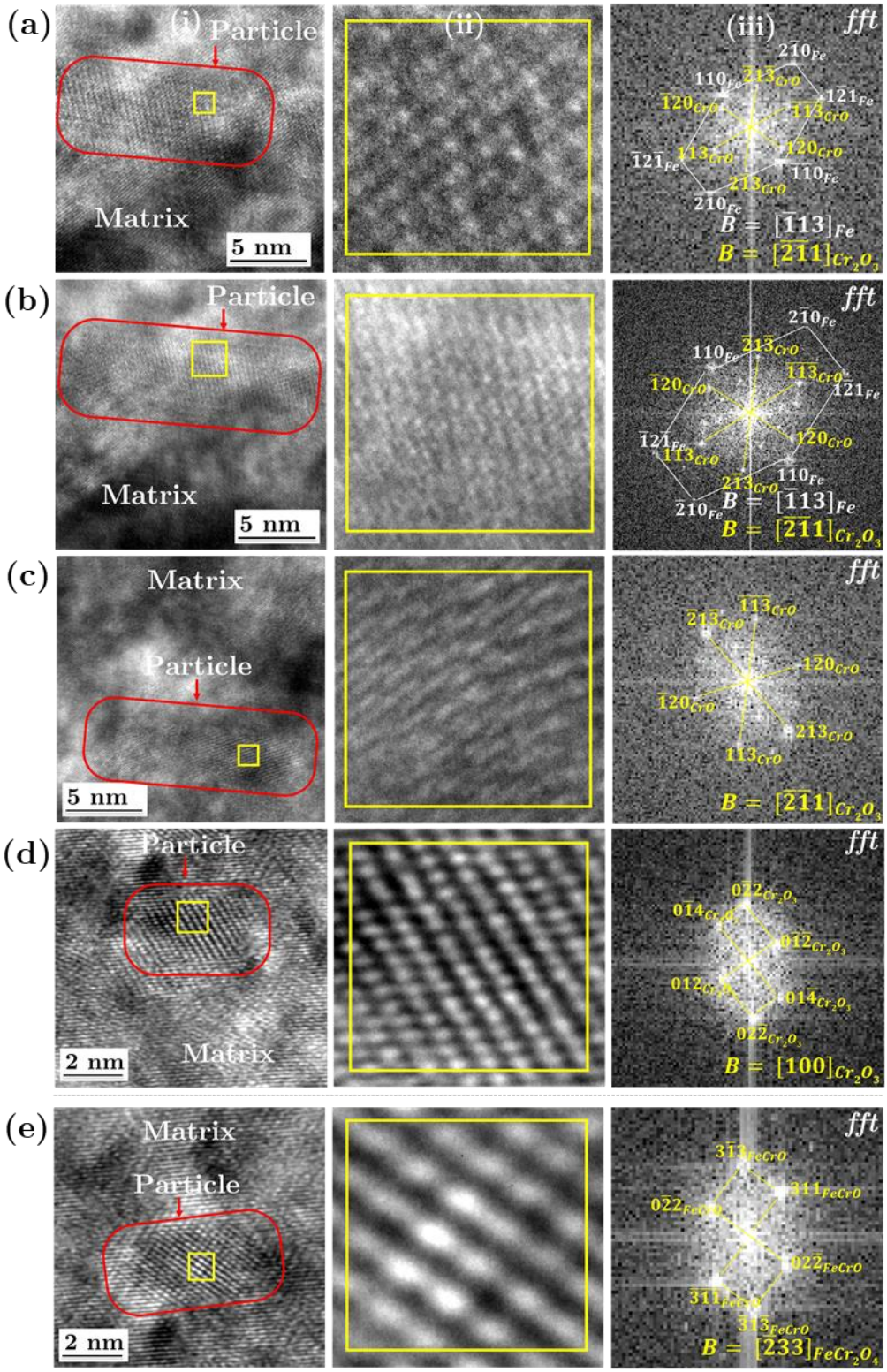

Figure 3.63 (a) High Resolution TEM (HRTEM) image of selected particles from the FIB lamella extracted from FeCr specimen after Ti, Y, O ion implantation at room temperature and subsequent annealing at 800°C for 2 hours indicating two particles. (b) Magnified image of the particle 1 and the corresponding Fast Fourier Transform (*fft*) (c) Magnified image of the particle 2 and the corresponding Fast Fourier Transform (*fft*).

The crystallographic structure identification of nanoparticles from different regions of the sample was performed by HRTEM. The imaging of five different particles are illustrated in the *Figure 3.63* where the sizes of these particles range between 5 and 15 nm.

In the *Figure 3.63 (a)* and *(b)* displays two identical particles with a very similar orientation. These particles were found to correspond to the corundum hexagonal crystal structure of the type Cr_2O_3 with the orientation B = [-2-11]. The measured interplanar distances for the (120) and (213) atomic plane was determined as 0.250 nm whilst the interplanar distances for the (213) and (113) atomic planes were exactly the same and determined as 0.214 nm. These values corresponding to the interplanar distances of the corundum hexagonal crystal structure of the type (Cr_2O_3) where (d_{120} = 0.248 nm and d_{113} or d_{213} = 0.217 nm). Elsewhere, the distance between the (113) and (213) atomic planes was determined as 52° whilst the angle between the (120) and (113) atomic planes was determined as 64° same as the Cr_2O_3. The (121) atomic planes of the FeCr matrix are parallel to the (113) atomic planes of the Cr_2O_3 crystal structure albeit with a tilt of less than 5° (121)Fe//(113)Cr_2O_3).

The *Figure 3.63(c)* and *(d)* show two additional particles. Both of these particles were identified to correspond to the corundum hexagonal crystal structure of the type Cr_2O_3. For the particle in *Figure 3.63(c)* this is quite similar to particles in the *Figure 3.63(a)* and *(b)* albeit with some degree of tilt. Also for the particle in the *Figure 3.63(d)*, this was identified to possess an orientation of B=[100]. The interplanar distances for the (012) and (014) atomic planes were determined as 0.36 and 0.26 nm respectively. All the above nanoparticles correspond to the corundum hexagonal structure of the type Cr_2O_3.

The *Figure 3.63(e)* did not appear to correspond to the corundum hexagonal crystal structure of the type Cr_2O_3 as observed for the previous four particles. The interplanar distances for the (022) and (311) atomic planes were determined as 0.30 and 0.24 nm respectively. The angle between the (311) and (022) atomic planes was also determined as 90°. These values are coherent with the *fcc* crystal structure of the type Fe_3O_4 or $FeCr_2O_4$ (where d_{022} = 0.296 and d_{311} = 0.253, the angle between the two atomic planes is also given as 90°).

Hence, in addition to the corundum hexagonal Cr_2O_3 nanoparticles formed within the FIB lamella, other particles are observed which are likely to correspond to $FeCr_2O_4$ nanoparticles as observed on the surface of the annealed thin foils. It is important however to note that these nanoparticles of the type $FeCr_2O_4$ were observed more closer to the surface than the Cr_2O_3 nanoparticles and thus could thus be considered as being part of the dominant surface oxides.

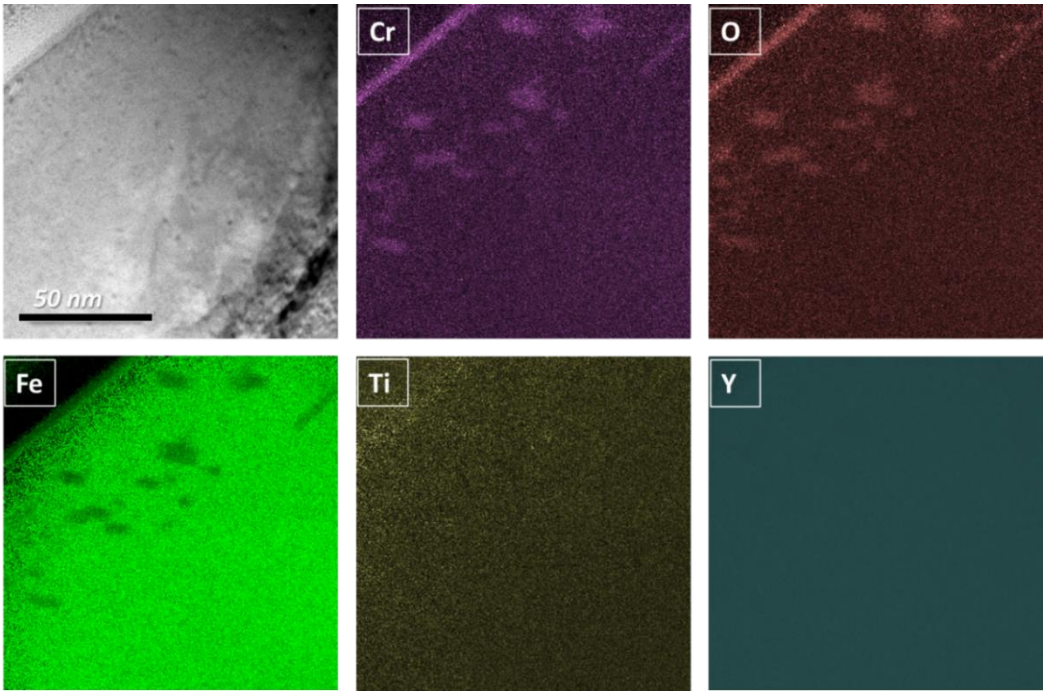

Figure 3.64 Energy-Filtered TEM (EFTEM) elemental characterization of the FIB lamella extracted from FeCr sample after implantation at room temperature of Ti -> Y -> O ions and annealing at 800°C for 2 hours. Bright Field (BF) image of the region chosen for EFTEM together with elemental maps acquired using the two-window jump ratio method in the vicinity of Fe-$L_{2,3}$ edge, Y-$M_{4,5}$, Cr-$L_{2,3,}$ O-K and Ti-$L_{2,3}$ core loss edges, as indicated.

An elemental characterization was performed by EFTEM. The image of the chosen region is given in *Figure 3.64*. As usual, the Fe elemental map shows a depletion. In the case of the Y elemental map, it appears completely homogeneous. However, the Y edges are not visible in the EELS spectra of our Y implanted specimens and EFTEM is therefore probably not sensitive to the presence of Y in our case. Enrichment in Cr and O is recorded for the spots depleted in Fe. The Ti map appears to have some patches but it is difficult to ascertain if these correspond to any nanoparticles.

The presence of Ti in the nanoparticles therefore appears quite inconclusive using Energy-Filtered TEM. To provide complementary information, ChemiSTEM EDX has been conducted on the Ti -> Y -> O sample annealed at 800°C. This investigation was conducted using an FEI Titan TEM operating at 200 kV located at the Material Science Department of the North Carolina State University (NCSU). The only difference between this microscope and the Talos F200X microscope is the fact that this microscope is fitted with a spherical aberration corrector to improve the point resolution limit.

The *Figure 3.65* shows EDX elemental maps acquired for a selected region. The investigation was initially performed on a large region with a length of approximately 150 nm and a width of 300 nm from the surface of the sample. On the HAADF image, elongated particles are readily observed with dark contrasts within the depth of 100 nm from the surface of the sample, which represents the implanted region. The maps show a depletion of Fe and an enrichment in Cr as well as some O presence in these particles. Whilst the imaging of O posed several challenges in the ChemiSTEM mapping using the previous microscope, O mapping could be easily achieved using this microscope. The elemental maps acquired for Y and Ti as well as C appeared quite homogeneous. The Cr and O presence, also observed in EFTEM, suggest the formation of Cr-O particles.

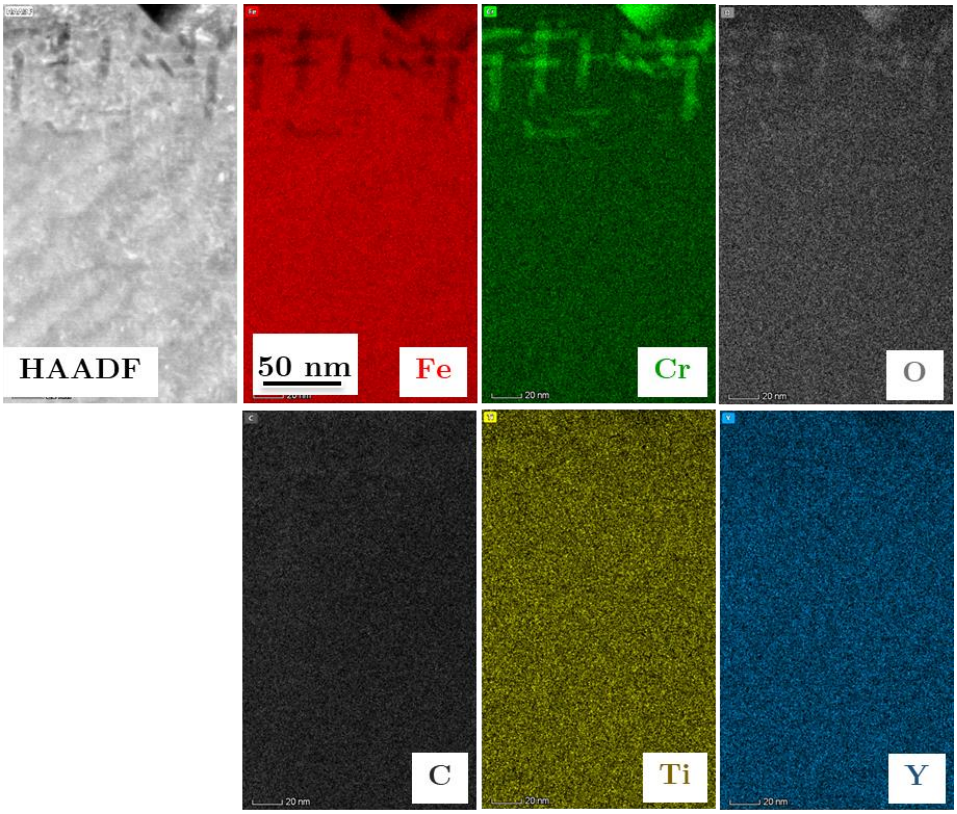

Figure 3.65 ChemiSTEM-EDX imaging at low magnification of FIB lamella extracted from Ti, Y and O ion-implanted FeCr sample and annealed at 800°C. High Angle Annular Dark Field (HAADF) image together with Fe, Cr, O, C, Ti and Y elemental maps as indicated. EDX mapping was performed for a duration of 15 – 20 minutes.

A STEM-EDX investigation was performed at a higher magnification on a region including particles. The *Figure 3.66* shows the HAADF image for this selected region with particles appearing with a much darker contrast as compared to the matrix. As in the previous investigation at low magnification, the particles display a depletion in Fe and an enrichment in Cr and O. In contrast to the previous elemental maps for Y and Ti which appeared quite homogeneous, the particles are observed to be depleted in Y and Ti.

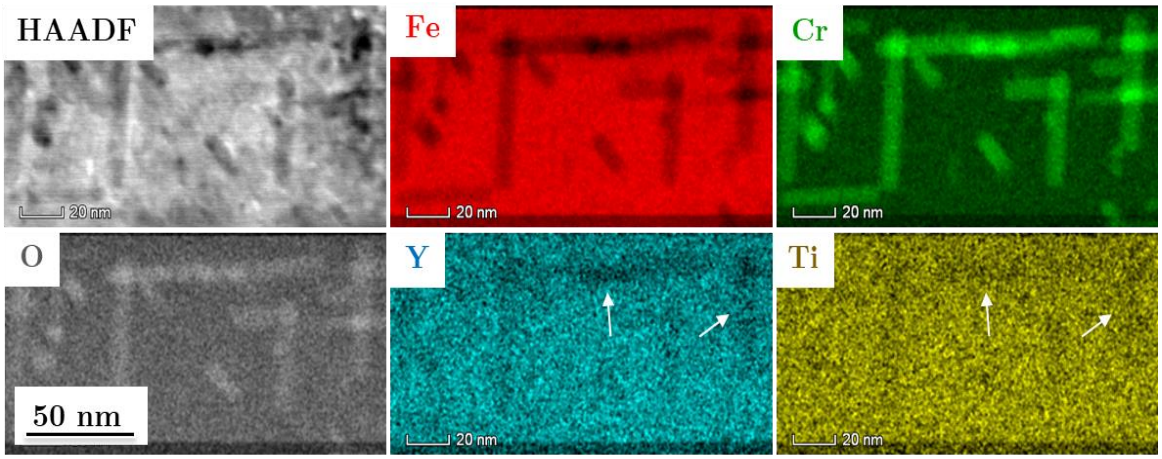

Figure 3.66 STEM-EDX imaging at high magnification of FIB lamella extracted from Ti,Y and O ion-implanted FeCr sample annealed at 800°C. High Angle Annular Dark Field (HAADF) image together with Fe, Cr, O, C, Ti and Y elemental maps. EDX mapping was performed for a duration of 15 – 20 minutes

Two distinct particles were selected for a higher magnification mapping and 1-D line scan imaging. HAADF images highlighting the two selected particles at low and high magnifications are shown in the *Figure 3.67* together with the elemental maps. The line scans through the two particles as imaged in the Cr map are reported in *Figure 3.68*. The results are identical to those of the *Figure 3.66* previously detailed, i.e. depletion in Y and Ti in the nanoparticles, and presence of Cr and O.

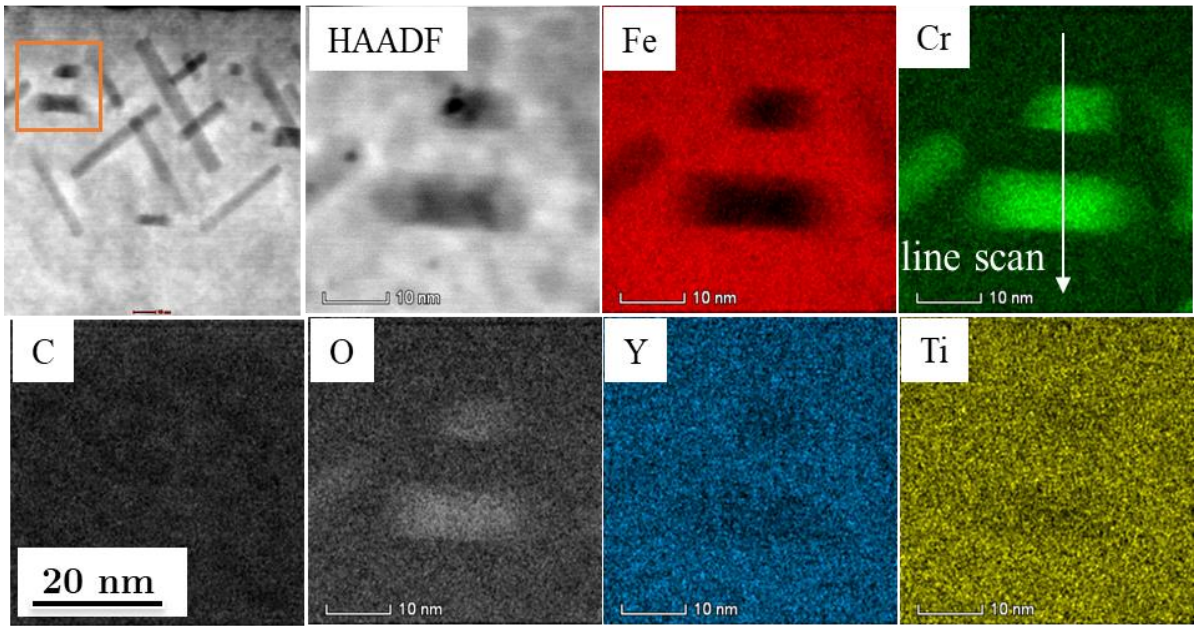

Figure 3.67 STEM-EDX imaging at high magnification of two distinct particles within the FIB lamella extracted from Ti, Y and O ion-implanted FeCr sample annealed at 800°C. (a) Low magnification High Angle Annular Dark Field (HAADF) image (b) high magnification HAADF image of the two particles together with Fe, Cr, O, C, Ti and Y elemental maps. An illustration of the trace of the 1-D line scan is shown on the Cr elemental map.

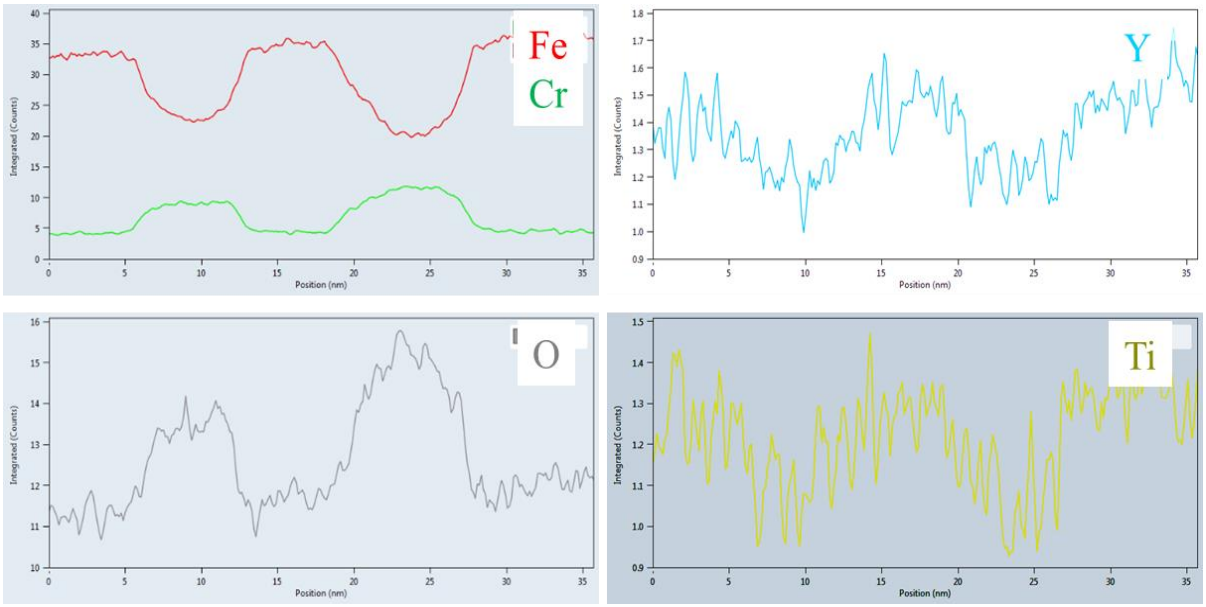

Figure 3.68 Line scans extracted from STEM-EDX imaging at high magnification of two distinct particles within the FIB lamella extracted from Ti,Y and O implanted sample annealed at 800°C. An illustration of the trace of the 1-D line scan is shown on the Cr elemental map. The 1-D lines are shown for Fe, Cr, O, Y and Ti elements.

It can thus be concluded from the different analysis performed on the Ti -> Y -> O implanted FeCr sample annealed at 800°C that the elongated particles formed are Cr_2O_3 particles without any Ti or Y presence.

3.3.2.2 Y -> Ti -> O annealed at 800°C

The very small nature of the nanoparticles formed after Y-> Ti -> O implantation and annealing at 800°C, as shown in the bright field image in *Figure 3.60(b)*, made it difficult to investigate using conventional TEM imaging techniques as well as EFTEM.

An elemental investigation was thus performed using STEM-EDX with the ChemiSTEM (Talos FX200 STEM). In the *Figure 3.69* is a low mag BF image indicating the region from which the ChemiSTEM maps were acquired. The HAADF image and the corresponding BF images for this region are given in the *Figure 3.69(b)* and *(c)*. The Fe elemental map displays a depletion in patches corresponding to nanoparticles observed in the BF images. The Cr as well as C and O display homogeneous elemental maps. The Y map is enriched at patches corresponding to these particles. It is however unclear with respect to Ti map if indeed there is some Ti enrichment. A line scan running through two particles is reported in the *Figure 3.70* highlighting these results. These particles can thus be said to be composed of Y so far.

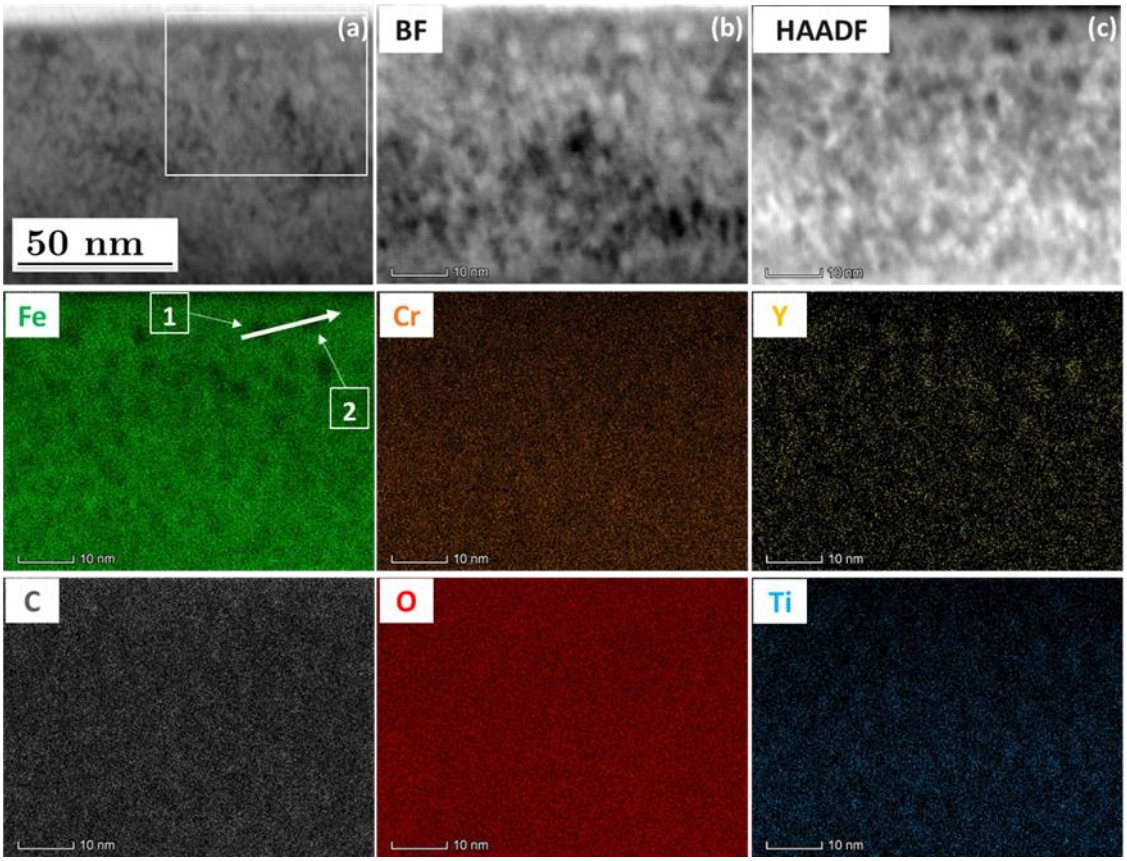

Figure 3.69 STEM-EDX elemental mapping using ChemiSTEM technology of FIB lamella extracted from Y-> Ti -> O bulk FeCr specimen implanted at RT followed by annealing at 800°C. (a) Bright Field (BF) image indicating the selected region (b) the corresponding Bright Field (BF) and (c) High Angle Angular Dark Field (HAADF) image together with elemental maps for Fe, Cr, Y, C, O and Ti. The mapping was performed for a total duration of 40 minutes at a count rate of 40k counts/second.

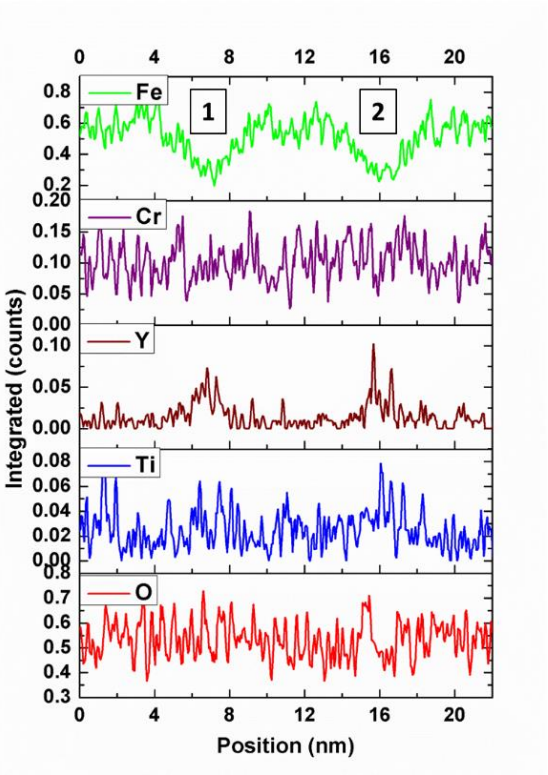

Figure 3.70 STEM-EDX 1-D line scans using ChemiSTEM technology through two particles 1 and 2 within the FIB lamella of Y-> Ti -> O bulk FeCr specimen implanted at RT and annealed at 800°C. The two selected particles are highlighted in Figure 3.68.

The uncertainty with respect to the composition especially in the case of Ti implies the fact that additional characterization using a different technique is required to provide additional elemental information. In conventional fabrication of ODS steels, as detailed in section 1.2.5, nanoparticles formed with sizes less than 5 nm have been characterized in detail by the use of Atom Probe Tomography. Hence, Atom Probe Tomography has been implemented to characterize and provide supplementary information for the nanoparticles observed in this sample.

3.3.2.3 Atom Probe Tomography (APT) characterization of Y-> Ti -> O sample annealed at 800°C

3.3.2.3.1 Distribution of ions in APT sample

Three tips made from the sample were analysed. The mass spectrum used in the reconstruction of the APT data shows peaks of the elements (Fe, Cr, Ti, Y, O, C, N) as well as molecular ions in the sample. Three tips made from the sample were analysed. A 1-D line profile for the distribution of ions for each element within the three analysed volumes is given in *Figure 3.71*. As explained in section 2.5.1, as a result of tip preparation, the surface of the tip may not exactly correspond to the surface of the implanted and annealed bulk specimen. Differences in the results from one tip to another may thus arise depending on the location of the tip with respect to the surface of the bulk specimen. On the line scans in *Figure 3.71*, the Fe and Cr are dominant with concentrations of approximately 90% and 10at% respectively far away from the surface of the tip, as expected. A significant Fe deficiency is recorded close to the surface. Inset are magnified images of the profiles closest to the surface of the tip. All the profiles

display a trend with a higher concentration of implanted-elements towards the surface. This is coherent with the data from the single element diffusion of Ti obtained by SIMS where ions were diffusing towards the surface of the sample at a temperature of 800°C. Y was however not observed by SIMS to diffuse significantly at this temperature. As explained above, the high concentration of implanted elements close to the surface of the tip may also result from the elimination of the close surface of the bulk specimen during the tip preparation. Indeed, the Ti has a varying concentration of 1-3% in the various APT tips and Y has a concentration of <2%, which is lower than expected from SRIM calculations. Hence, it is likely that the close surface of the bulk specimen has been removed during the preparation of the tips.

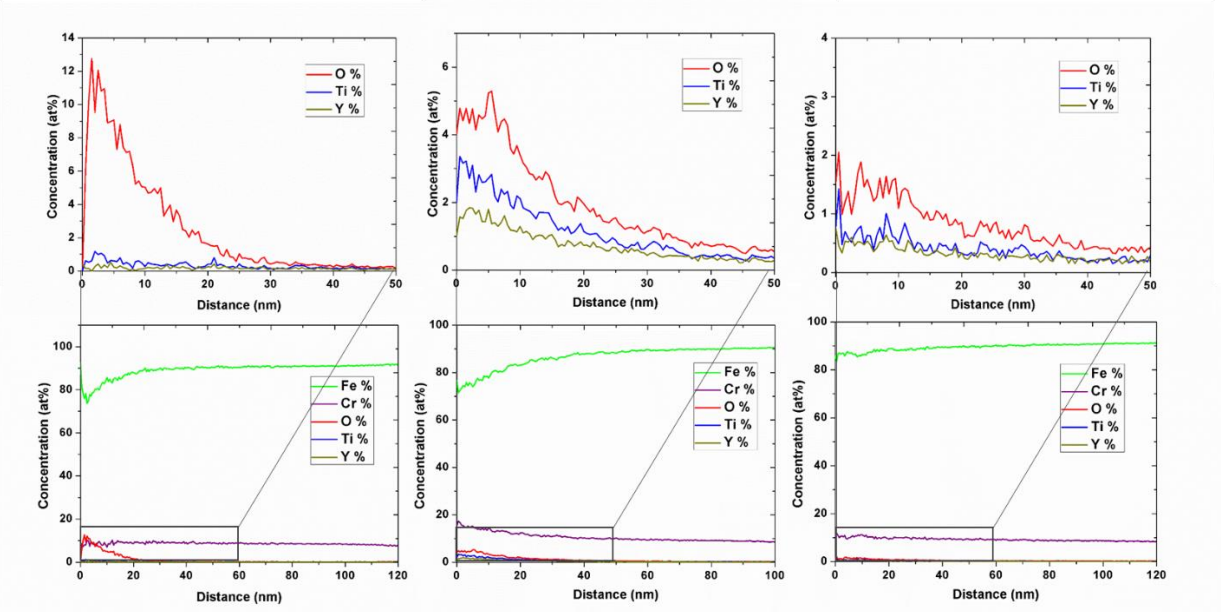

Figure 3.71 1-D elemental concentration profiles for the reconstructed volume along the z-axis of the Y->Ti->O ion-implanted FeCr sample annealed at 800°C. Inset are the magnified profiles of the elements with minimal concentrations. The profiles represent the three APT tips (a) R30_10306 (b) R30_10307 and (c) R30_10308.

The 3-D reconstructed volume of one of the analysed tips is shown in *Figure 3.72* for the main ions to display the distribution of these ions. In addition to the implanted ions and the matrix elements, CrO, TiO, YO and TiN molecular ions were observed in the mass spectra. The distributions of the ions in all the three APT tips (i.e. R30_10306, R30_10307 and R30_10308) appear quite similar. Hence, only the distribution of ions in R30_10306 is shown in *Figure 3.72*. The distributions of the ions in the two remaining specimens are given in Annex VI. The Fe, Cr, C and O distributions appear quite homogeneous. A more dense distribution of the O ions is observed close to the surface (this is observed clearly in the ion distribution of R30_10307 in the Annex VI), which suggests a surface oxide formation, as seen by TEM. The Y ions distribution appears less homogeneous with a more dense distribution observed close to the surface and patches which suggests possible cluster formation. For the Ti ion distribution, patches are more pronounced suggesting Ti cluster formation within the specimen. In the case of the molecular ions, the YO ion is not quite homogeneous, neither is any cluster formation clearly visible. The TiN ion distribution clearly has clusters observed at the same positions of the Ti clusters thereby confirming that Ti clusters are present with some N. Finally, the TiO ion distribution is the clearest indication of the cluster formation with a high number of clusters observed which are more concentrated close to the surface of the tip. APT thus appears to

indicate the presence of Ti and O in the clusters formed in the Y-> Ti -> O sample annealed at 800°C. To establish in detail the nature and composition of these clusters, a study of these clusters has been performed.

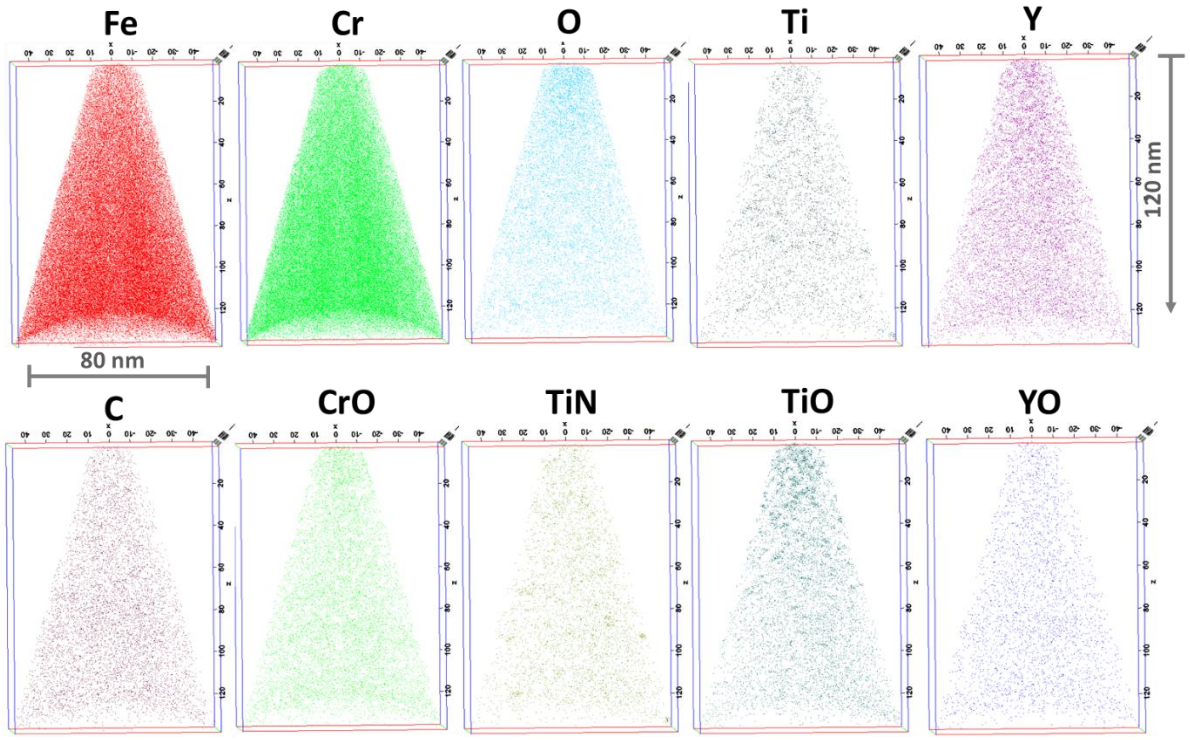

Figure 3.72 The 3-D APT reconstructed tip of the Y, Ti and O bulk sample implanted at room temperature followed by annealing at 800°C (tip R30_10308) showing the distribution of the evaporated Fe, Cr, O, Ti, Y and C elements as well as CrO, TiN, TiO and YO molecular ions.

3.3.2.3.2 Cluster analysis of Y-> Ti -> O sample annealed at 800°C

The analysis of these clusters has been achieved using the cluster analysis algorithm known as the maximum separation method as detailed in section 2.5. Ti-rich clusters have been used for the cluster analysis. The clusters are defined by the nearest-neighbour atoms and atoms within a maximum distance d_{max} are described as part of clusters. Atoms outside this distance are not counted as part of the cluster. The minimum number ions N_{min} required to form the cluster is also prescribed to avoid any misinterpretation of occasional density fluctuations of solid solution atoms as clusters. Using the count distribution provided by this algorithm, the d_{max} was determined as 0.9 nm and the minimum number of ions N_{min} required to form the cluster as 10. Any atoms found to be surrounding this cluster at a distance of 0.8 nm from the core atom, was counted and considered as part of the cluster.

The cluster analysis has been performed in detail and the result for specimen R30_10307 is given. A total of 90 particles were identified during the cluster analysis. The sizes of these clusters were estimated using the Guinier radius R_G. This is related to the radius of gyration Rg by the expression:

$$R_G = \sqrt{\frac{5}{3}}\, Rg$$

Detailed description of this Guinier radius and radius of gyration is given in section 2.5.5.

The *Figure 3.73* shows the size distribution using the Guinier radius of the particles. The radius ranges between 0.5 and 2.5 nm with an average radius of 1 nm. This size is in the same order of magnitude as the size of the particles observed in the conventional TEM images with an average size of 2 nm. This is not a peculiar case as Williams *et al.* [Williams 2010] confirmed that the sizes of clusters given by the Guinier radius is comparable with the sized estimated by TEM characterization techniques. The choice of parameters such as the N_{min} and d_{max} could affect the size of clusters determined.

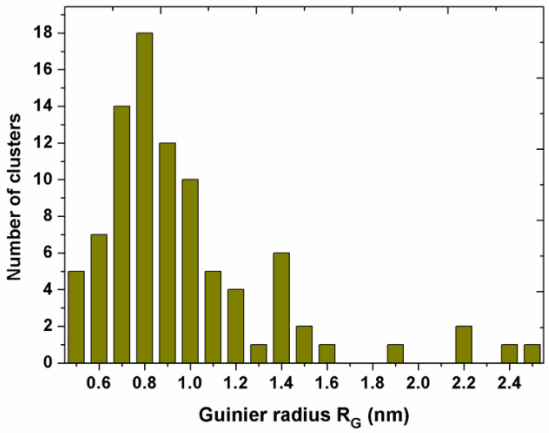

Figure 3.73 Size distribution of clusters within the APT specimen R30_10307. The Guinier radius R_G is used to represent the sizes of the clusters.

3.3.2.3.3 Chemical composition of clusters

The clusters identified by the cluster analysis were then isolated using interfaces to enable the calculation of their composition. It is possible to construct a 1-D line spectrum running through a particular cluster and get a composition profile. This has been performed for 2 particles for each of the 3 APT specimens. In *Figure 3.74*, the composition in Y, Ti and O of the two clusters from the 3 APT tips are displayed. The size of all the particles is approximately 2 nm. The recorded concentrations in each cluster are roughly the same with O, Ti and Y concentrations determined as roughly 4-6, 5-7 and 1-3 at%, respectively. The average composition of all the clusters was then performed.

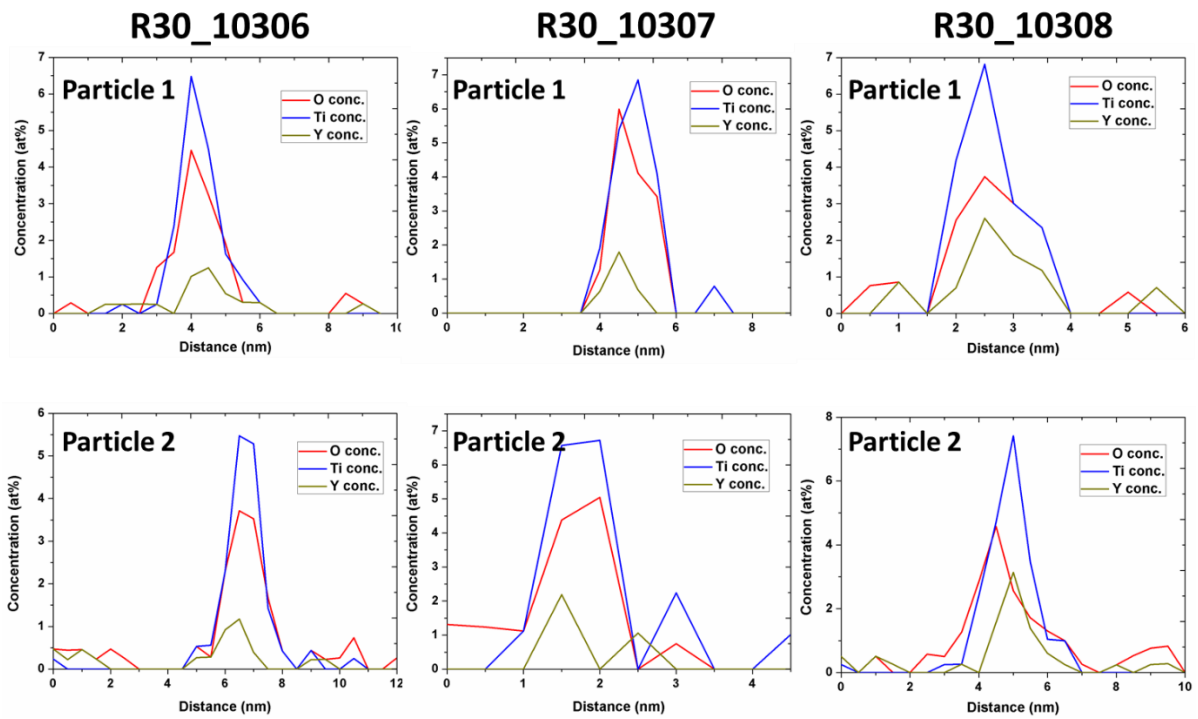

Figure 3.73 1-D line scan through two particles in each of the three investigated APT tips (a) R30_10306 (b) R30_10307 and (c) R30_10308.

The *Table 3.4* is the average composition of all the clusters identified in the three APT specimens. Considerable amount of Ti and Cr is found in the clusters ranging between 7 to 10 at% for Ti and 7 to 13 at% for Cr respectively with O presence ranging between 20 and 30 at%. Only a small Y presence in the range of 1.3 to 1.6 at% is recorded with minute contributions from C and N. There is therefore a reasonably low Y/Ti ratio of about 0.12-0.22. Noticeably, a high amount of Fe around 50 at% is recorded in the clusters.

.

Element	Composition (at%)		
	R30_10306	R30_10307	R30_10308
Fe	52.1285	53.9740	56.6091
Cr	7.0981	13.0108	8.0375
O	30.3088	23.029	22.4398
Ti	7.4744	7.9374	10.8527
Y	1.6599	1.4695	1.3264
C	0.0355	0.1609	0.08160
N	0.4643	0.4183	0.6528

Table 3.4 Average compositions of the clusters in the three investigated APT tips

Such a high presence of Fe in the clusters is not expected but is frequently observed in APT studies of ODS steels. This is usually explained as a result of artefacts from trajectory aberrations [please refer to section 2.5]. Simulations of field evaporation have showed that, such artefacts are present due to the low field evaporation of the oxide particles as well as

their insulator nature. This results in trajectories overlaps and artificial introduction of atoms from the neighbouring environment. Some atoms may also not be detected due to preferential evaporation. These artefacts can strongly modify the measured chemical composition with an over atomic density in the core of the particles. For example, a large amount of Fe and Cr was detected by APT in ODS nanoparticles that were actually identified as being pure in Y, Ti and O and surrounded by a Cr shell [Hatzoglou 2018]. Analytical models have been developed to correct and rectify such chemical biases but they imply the knowledge of some parameters such as the concentrations of elements in the matrix surrounding the particles [Hatzoglou 2018, Williams 2010] which cannot be accurately determined in our case.

From the previous APT studies [Hatzoglou 2018, Williams 2010], the particles can be considered as almost free from Fe. However, there is the possibility of low Cr presence in these particles as ChemiSTEM results from previous investigations revealed Cr presence within or around the particles in the form of a shell.

The results from these APT investigations revealed the presence of Ti and O in these clusters. From ChemiSTEM, it can also be confirmed that there is Y presence in these clusters. It can therefore be concluded that these clusters are (Y,Ti) oxides or have a Y-Ti-O composition. The exact structure of these nanoclusters cannot however be ascertained but the reasonably low Y/Ti ratio suggests a formation of a non-stoichiometric (Y,Ti) oxide.

3.3.3.3 Summary of RT sequential implantation of Ti->Y->O and Y->Ti->O annealed at 800°C

The order of implantation of the metallic element (i.e. Y and Ti) appear to be quite important in the formation of the nanoparticles. The Ti->Y->O order of implantation revealed the formation of elongated nanoparticles with a size ranging from 5 to 20 nm. These particles possessed a chromium-oxygen and possibly Ti composition with the corundum hexagonal crystal structure of the type Cr_2O_3. Few $FeCr_2O_4$ structured particles were also observed close to the surface of the sample.

On the other hand, the Y-> Ti-> O order of implantation revealed the formation of very small nanoclusters with sizes of 2-3 nm. The very small nature of these nanoclusters made it almost impossible to resolve the crystallographic structure of these clusters. However, the result from ChemiSTEM EDX as well as APT investigations revealed that these clusters were predominantly enriched in yttrium, titanium, oxygen and possibly chromium. A summary of these two conditions is presented in the *Table 3.5*.

Bulk room temperature implanted sample	Annealing Temperature	Particle size (nm)	Composition		Structure		Identification
			Technique	Chemical composition	Technique	Crystallographic structure	
Ti->Y->O	800°C	5-20	EFTEM	Fe depletion Cr and O enrichment Ti quite homogeneous Y completely homogeneous	HRTEM	Particle 1: Corundum hexagonal of the type Cr_2O_3 Particle 2: *fcc* crystal structure of the type $FeCr_2O_4$	Particle 1: Chromium oxide particles with the Cr_2O_3 structure Particle 2: Few Iron-chromium oxide particles with the $FeCr_2O_4$ observed close to the sample surface
Y->Ti->O	800°C	2-3	ChemiSTEM EDX APT	Y-Ti-O and probably Cr	HRTEM	Unidentifiable	

Table 3.5 Summary of chemical composition and crystallographic structure of nanoparticles observed in the Ti->Y->O and Y->Ti->O ion-implanted samples annealed at 800°C

Chapter 4: Discussions

4. Discussions

Ion beam synthesis is envisaged as a potentially very powerful tool for the investigation of nanoparticle formation and nucleation in ODS steels. In this study, the formation of (Y,Ti) nano-oxide particles by ion beam synthesis has been presented in detail. The experimental investigation has been performed following three different modes:

(i) Ti and O ion implantation : synthesis of Ti oxides

(ii) Y and O ion implantation : synthesis of Y oxides

(iii) Ti, Y and O ion implantation : synthesis of Y,Ti oxides

In all the three modes of experimentation, no visible nanoparticles were formed directly after room temperature ion implantation. Irradiation is known to enhance the mobility of solute atoms by the production of a high number of point defects (i.e. vacancies and interstitials). Even with the high number of point defects created in the implanted samples, as predicted by SRIM simulations, no visible cluster segregation is observed after room temperature implantation by using Transmission Electron Microscopy. Hence, as in conventional ion beam synthesis, high temperature annealing was required to force the formation of nanoparticles in all three experimentally investigated modes. The high temperature annealing was performed from 600 to 1100°C under vacuum, except for the last (iii) mode where only annealing at 800°C was performed. For each of these implantation modes and annealing conditions, nanoparticles were observed and their crystallographic structure and chemical composition were characterized in details by TEM (see chapter 3).

In the following sections, the reasoning behind particular oxide formation and the driving force leading to the formation of oxides for the various stages of each mode will be addressed using the obtained results and data from existing literature. The factors affecting the precipitation and/or nucleation of the clusters have been detailed in section 1.4 and these include the diffusivity of the implanted elements, the thermodynamical stability of the new oxide phases and the binding between the implanted elements, matrix components and the defects created. Finally, from all the results presented in Chapter 3 using the factors affecting the precipitation of the clusters as well as the deductions made in this chapter, mechanisms to help understand the early formation stages of oxide nanoparticles in ODS steels are dicussed.

4.1 Ti and O implanted and annealed samples

The Ti and O as-implanted samples as detailed in section 3.1 revealed no visible nanoparticle formation after room temperature implantation even though significant amount of vacancies are created as estimated by SRIM. Annealing was therefore required to promote the formation of nanoparticles. The Ti and O room temperature implanted samples were therefore annealed at 600°C for 2 hours where chromium oxide Cr_2O_3 were observed to be formed. An enrichment in Ti of these particles was eventually observed after annealing at temperatures of 800°C and above.

4.1.1 The first formation stages

O is known to have a low solubility limit in Fe and FeCr matrices [Meijering 1995]. The metallic element-oxygen (M-O, i.e. M = Titanium, iron, chromium in this case) cluster may be possibly formed since such elements interact with O to form oxides. Iron oxides are known to be formed as part of a surface oxide protection layer for FeCr steels (see section 3.1.2) with a corrosion layer comprising an outer Fe_3O_4 layer, an inner layer of mixed iron-chromium oxide spinel and a diffusion layer containing Cr rich precipitates. In our ion-implanted and annealed thin foils, only a iron-chromium oxide spinel has been observed to be formed as surface oxide (the iron-chromium oxide formation is comprehensively detailed in section 3.1). The formation of this spinel iron-chromium oxide was not observed within the FIB lamellae extracted from the bulk samples after annealing at 600°C. The spinel structure of the oxides induces a density decrease, which is favourable for formation on the surface or close to the surface of steels, as observed, but is probably very difficult within the bulk of the sample. Hin *et al.* [Hin 2009] found by kinetic Monte Carlo methods that the first stage of oxide formation in Fe matrices, prior to the formation of more stable Y or Ti oxides, is the formation of Fe_2O_3 which is eventually enriched in Y or Ti (this precipitation mechanism has been detailed in section 1.2.9). In the present case of FeCr matrix, although Fe is present in much larger concentration, Cr has a higher affinity for O compared to Fe (see table of enthalpy of oxides per mole of M-O bond, section 1.4). The precipitation of Cr enriched oxide clusters instead of Fe oxides may therefore be expected with similar mechanisms as those reported by Hin *et al.*. Ti and Cr both have low binding energies to O and vacancies in the 1nn distances (see table 1.4). The affinity of Ti for O is higher than the one of Cr for O (see enthalpy per mole of M-O bond, section 1.4) and hence, a Ti oxide could be expected. The kinetics of the nucleation and growth of nanoclusters also partly depends on the diffusivities of Ti and Cr. The diffusion coefficient of Ti in *bcc* Fe at 800°C was measured to be higher than the diffusion coefficient for Cr (see table 1.6), which would also favour the formation of Ti oxides. However, the diffusivities of species may largely differ in the presence of a high concentration of point defects in ion implanted FeCr. In addition, Cr is present in higher concentration compared to Ti and consequently has to diffuse over a lower distance. This probably explains the formation of Cr_2O_3, which is the most stable chromium oxide (see table 1.7), instead of Ti oxides. The mobile Cr atoms could be trapped by vacancies or any O-V pairs formed. The strong O-V pair binding (see section 1.3.6) and mobile Cr atoms may influence the early stages of nanoprecipitation in Ti and O implanted samples.

4.1.2 The role of Cr

Chromium is believed to play no major role in the formation of nanoparticles in ODS steels. These particles are mostly Y based and may contain Cr but the formation of the nanoparticles is not reported to be influenced by the Cr presence. There is very little information on the influence of Cr on early precipitation stages of clusters in ODS steels. However, Williams *et al.* [Williams 2013] observed a first step Cr_2O_3 nanoparticle at grain boundaries after annealing at 800°C. Details of this investigation will be readdressed in section 4.1.4. These particles evolved to Ti, Y and Cr enriched oxides upon further treatment. The formation of Cr_2O_3 as the first step nanoparticle formation in our Ti and O implanted samples indicates that Cr plays a major role in the early stage nanoparticle formation in the present study, and may play a major role in nanoparticle formation in Y free alloys.

4.1.3 The role of Ti

The mobility of solute ions in the matrix plays an essential role in the precipitation of any clusters in the material. At an annealing temperature of 500°C, Ti does not appear to diffuse significantly by SIMS and at 600°C, it is not observed to be part of the particles and thus does not seem to affect or play any role in the first step of oxide formation. The ToF-SIMS experiments demonstrated however that Ti appears to be significantly mobile at 800°C. At this temperature, the observed nanoparticles have a chromium-titanium-oxygen composition with a corundum hexagonal Cr_2O_3 type structure. A relatively high affinity of Ti for O as compared to the Cr for O may induce the Ti trapping at oxide particles. The Ti may form a shell around Cr_2O_3 particles before being a part of the core of the particles at higher temperatures as reported by Williams *et al.* [Williams 2013] for grain boundary Cr_2O_3 particles. Enhanced Ti diffusion was observed by ToF-SIMS after annealing at the temperatures of 1000°C and 1100°C. Even though no elemental quantitative analysis has been achieved, it is likely that the enhanced diffusion of Ti would promote more mobile Ti atoms being trapped in these clusters and as a result, leads to the increase in Ti content in these particles. At the temperature of 1100°C, two types of particles are observed: chromium-titanium oxide particles with corundum structure and particles with a Ti oxide core and a shell enriched in Cr. The formation of these latter particles could arise from two different paths: The particles could be totally new oxides formed from oxidation of mobile Ti atoms, or they could be oxides evolving from the previously observed chromium-titanium oxides. The coexistence of these particles with Cr_2O_3 particles as well as their relatively large size >10 nm (apparently larger than Cr_2O_3 particles) indicate that the latter is more probable. In section 2.4.2, the temperature evolution during the *ex situ* annealing is displayed. This shows that for annealing at 1000 and 1100°C, a temperature of 800°C is achieved within a duration of 20 minutes. The heating rate of the performed annealings is therefore relatively slow. Hence, for annealing at these temperatures where Ti has been indicated to be mobile, the chromium oxide Cr_2O_3 may be formed even before the Ti becomes mobile. It would be interesting to conduct such annealing with a much higher heating rate, such as a Rapid Thermal Annealing (RTA), where both Ti and Cr atoms could become mobile within a few minutes. It is unclear if the slightly higher Ti binding energy to O in the 2nn position would aid the formation of a Ti oxide before the formation of Cr oxide.

4.1.4 The Core/shell structure

Klimenkov *et al.* [Klimenkov 2008] and Marquis *et al.* [Marquis 2008] were the first to report the formation of the core/shell structure of particles observed in ODS alloys (details are given in section 1.2.8.). This core/shell structure has become a common feature for most ODS steels. Two theories have been proposed by Williams *et al.* [Williams 2013] to explain core/shell structure formation. The first theory suggests that the shell is a result of segregation to the particle/matrix interface after the particle has been formed. The second theory is based on the reasoning that the shell could be essential to the formation of the particle, and may act as an interfacial phase, lowering the surface energy of the particle, and thus enabling the particle to form. Cr is reported to possess a repulsive interaction with Ti in iron at binding energies of -0.15 and -0.11 eV in the 1nn and 2nn separations respectively. Hence, in our Ti and O implanted samples, it is unclear if such an interaction exists between the Cr and Ti in the oxide phase. However, the stronger Ti bonding with oxygen should be favourable for collecting Ti atoms within the oxide together, pushing Cr to the periphery. As a result, Cr would tend to concentrate in a shell around the particle after annealing at 1100°C, with the formation of a more thermodynamically stable Ti oxide in the core of the particle. The earlier theories to explain the core/shell structure are therefore not applicable in this instance. Further investigations may be required to fully understand the reason and formation of this core/shell structure. The core/shell structure of chromium oxides have been reported by Williams *et al.* [Williams 2013] where grain boundary Cr_2O_3 nanoparticles were observed with a shell enriched in Ti, Cr, O. The evolution of nanoparticles to gain the core/shell structure in ODS steels by experimental techniques has also been reported by Ribis *et al.* [Ribis 2017]. The kinetic precipitation pathway displayed a three step nanoparticle evolution for ODS particles formation [Ribis 2017]. The first step is the formation of a non-stoichiometric oxide followed by the formation of nanoclusters with a core/shell structure (with a Y,Ti,O enriched core and a Cr enriched shell). The formation of chromium-titanium oxides leading to the formation of non-identifiable Ti oxides with a Cr enriched shell in our case could represent the first two stages of nanoparticle formation as given by Ribis *et al.* [Ribis 2017]. In their study, the final step annealing was performed at 1300°C where the Cr shell was rejected leading to the formation of stoichiometric oxides. In our investigation, no high temperature annealing close to 1300°C has been performed. Such an annealing may therefore be required to investigate the likely evolution to a possible stoichiometric Ti oxide without the Cr enriched shell.

4.1.5 Comparison with conventional ODS steels

The present investigation addresses the formation of probable Ti oxides in FeCr alloy that does not contain yttrium. Pure Ti oxides are normally not used for strengthening of ferritic-martensitic steels because Ti oxides are usually less stable as compared to the Y oxides and produce a less homogeneous distribution of oxides as compared to Y. Hence, there is very little data relating to Y-free ODS alloys. *Table 4.1* shows the results of a few investigations conducted on Y free ODS alloys produced by the conventional MA technique. These Y-free alloys contain comparable composition of Cr to our specimens, even though other alloying elements are present. The formation of Ti-rich oxides is revealed. From this, it was concluded that Ti oxides could be formed within the grains of alloys that do not contain Y. The sizes of these particles are usually less than 20 nm and ≈10 nm, which is exactly comparable with the Ti oxides with a Cr-enriched shell observed after annealing at 1100°C in our study. No particular precipitation mechanism was suggested in these investigations to ascertain whether or not these oxides also evolved from chromium oxides.

	Alloy	Fabrication condition and characterization method	Treatment	Composition	Structure	Particle size (nm)
Miller 2006	14WT	MA - APT	HE 850°C ann. 1 hr at 1000°C	Ti-O		4 nm increase to 10 nm
2007 Hoelzer	14WT	MA – APT	HE 850°C	Ti-O		8.7 ± 4.5 nm
This study	FeCr - Ti+O	IBS - TEM	Annealed at 1100°C	Ti-O with Cr shell + Cr-Ti-O	Unidentified structure + Cr_2O_3	≈ 10 nm

Table 4.1 Summary of the characteristics of observed particles in Y-free ODS alloys as well as in the Ti and O implanted samples annealed at 1100°C from this investigation.

The formation of the chromium oxides or Cr enriched precipitates is not new to ODS steels. Cr_2O_3 have been observed in several ODS investigations. They are usually not formed uniquely in ODS alloys but formed in addition to other nano-oxide particles. It is unclear what are the favourable conditions for the formation of Cr_2O_3. Cr_2O_3 may be formed together with the conventional nanoparticles within the grains as reported by Castro *et al.* [Castro 2011]. Cr segregation at grain boundaries is a known phenomenon and hence the formation of Cr_2O_3 at grain boundaries has been reported [Chen 2007, Williams 2013, Auger 2011]. The evolution of chromium oxide Cr_2O_3 to Ti oxides or other oxides as observed in this study is not unusual, either. Such an evolution has been reported by Williams *et al.* [Williams 2013]. In their study, they investigated Fe-14Cr ODS steels. After annealing at 800°C for 10 minutes, grain boundary particles ranging between 8-15 nm and average size of 12 nm were observed. The measured compositions of these particles were ≈35%Cr and 55%O with a structure consistent with corundum Cr_2O_3. Each particle had a shell of ≈2 nm thickness enriched in Ti, Cr and O. In the case where the powders were annealed at 800°C for 2 hours, the observed particles had an average size of ≈15 nm with a Ti rich shell increased to size of 4-5 nm. Interestingly after consolidation (1100°C, 100 h), particles with the sizes ranging from 5-15 nm had a similar Ti-Cr-O composition. However, the particles greater than 15 nm possessed a core enriched with Ti as well as Y but with a structure no longer matching the Cr_2O_3. These results are explained to suggest that the initial oxide to form at grain boundaries is Cr_2O_3, and that a Ti-rich shell forms at the interface between the chromium oxide and the matrix on annealing. During consolidation, the core of the particle then transforms to a Y-Ti based oxide. This shows close similarities with our results showing Ti-oxide particles with a Cr shell apparently evolving from Cr_2O_3 particles at high temperature annealing. From the evolution of the nanoparticles in Ti and O implanted samples in the present study as well as the Cr_2O_3 evolution in several other studies, it is clear that Cr_2O_3 formation could be responsible for the very early formation stages of nanoparticles in ODS steels in the absence of Y.

4.1.6 Synopsis of the particle precipitation pathway

During the ion implantation, significant amount of point defects including vacancies that may contribute to the precipitation mechanisms are produced in the matrix. O has the strongest binding energy with such vacancies of 1.65 eV [Murali 2010] as compared to the other elements (see table 1.4). It is therefore not surprising that Fu *et al.* [Fu 2007] stated that nano-oxide cluster formation is defined by the formation of an O-V pair. This precipitation mechanism has been described in detail in section 1.2.9. The O-V pair would enable the formation of O-enriched clusters that attract other metallic elements with a strong O affinity leading to the formation of nanometallic oxide particles. The oxide formation could be facilitated by the fast diffusing O probably forming an O-V pair as proposed by Fu *et al.* [Fu 2007]. Ti appears to play no important role at this stage of nanoparticle formation. From the results presented in Chapter 3.1 as well as the discussions above, it is evident that the first step of oxide formation in Ti and O implanted samples is the formation of chromium oxide Cr_2O_3, which is achieved in the room temperature implanted samples after annealing at 600°C. The average size of such particles is estimated to be approximately 6 nm. The diffusion of Ti has been reported after annealing at the temperature of 800°C. The mobile Ti atoms are most probably captured at the surface of already nucleated Cr_2O_3 particles resulting in the particle enrichment with Ti. These particles are larger than those observed at 600°C with a size of approximately 10 nm. Annealing at even higher temperature of 1000°C produced very similar Cr-Ti oxides with the same corundum structure. The sizes of these particles are also very similar to the size of particles observed for the previous annealing condition, i. e. 800°C. Finally, the annealing performed at 1100°C resulted in the formation of Ti oxides with a Cr enriched shell in addition to the Ti-Cr oxides with Cr_2O_3 structure. The Ti oxides seem to evolve from the previously formed Cr oxides by condensation of Ti in the core and the rejection of Cr to the shell region around the particle. It is unclear whether the core part is a pure Ti oxide and in which form. TiO_2 oxide is the most frequently reported among existing titanium oxide, but its known structures are very different from that of corundum so that the internal phase transformation in the core should be strongly suppressed. Most probably the core region remains the same corundum $(Cr, Ti)_2O_3$ with the strong enrichment in Ti. It is also unclear if an annealing at higher temperature will result in the disappearance of the Cr enriched shell as observed in previous ODS studies [Ribis 2017]. A schematic representation of the evolution of the particles is represented in *Figure 4.1*.

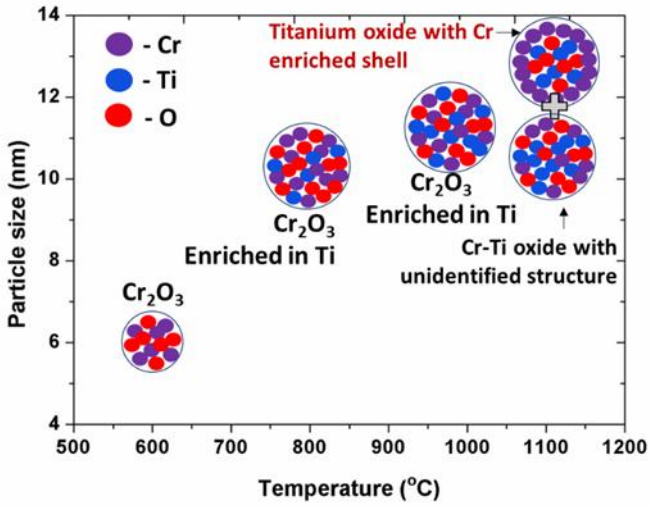

Figure 4.1 Steps involved in nanoparticle formation of Ti and O implanted and annealed samples

4.2 Y and O implanted and annealed samples

The as-implanted Y and O samples revealed no nanoparticle formation after room temperature implantation. The Ti, which is a smaller sized atom compared to Y and which is known to diffuse faster than Y in bcc-Fe [Murali 2011], is shown to migrate (ToF-SIMS results) and participate in the oxide particles only at the temperature of 800°C. It is therefore expected that the slower diffusing Y atom would not diffuse significantly at an annealing temperature below 800°C. Hence, the first annealing of the Y and O implanted samples was conducted at 800°C in contrast to the Ti and O implanted samples where the first annealing was conducted at 600°C. At this temperature very small 2-3 nm unidentifiable nanoclusters that appear to be spherical are observed. Enhanced annealing at 1100°C resulted in the formation of Y_2O_3 particles with a yttrium enriched core and a chromium enriched shell.

4.2.1 The first step formation stages

The nanoclusters observed after annealing at 800°C are measured to be approximately 2-3 nm in size. The very small size of these particles made it impossible to determine the elemental composition by the available TEM characterization techniques. Similarly, HRTEM characterizations were unable to identify the structure of these very small clusters. However, the shape and size of the particles strongly differ from the shape and size of particles observed for the same annealing condition in the case of Ti and O implantation. Hence, the structures and compositions of the particles are very likely to differ in the two cases. Therefore, Cr_2O_3 particles are unlikely, while particles of Y oxides or Y-Cr oxides are probable.

The diffusion coefficient of Cr in *bcc*-Fe has been reported to be much higher than the diffusion coefficient of Y. Based on these diffusion coefficients alone, Cr oxide particles would thus be expected to form faster. Y is also not observed to significantly diffuse at 800°C in our ToF-SIMS experiments (see *Figure 3.49* from Chapter 3), but this probably does not impede local rearrangements of Y atoms.

Y is known to have a strong binding with O in the 2nn [Claisse, Murali 2010]. Also, Y binds strongly to vacancies in the 1nn and 2nn directions. This very strong binding of Y to vacancies and O could be the basis for the formation of Y-oxides in the FeCr matrix. Y is believed to diffuse, like many other substitutional solutes, by the vacancy mechanism, where the atoms diffuse by successive position exchanges with vacancies. However, recent DFT calculations have shown an atypical behaviour for oversized solute atoms, including Y, in *bcc* and *fcc* Fe [Bocquet 2017]. The strong Y-V pairwise attraction is found to be so large that the pair is no longer stable and relaxes spontaneously towards a new configuration where the Y atom sits in the middle of two half-vacancies (V/2). The diffusion of Y, as other oversized solute atoms, cannot consequently be described by the standard vacancy mechanism according to this study. While the latter statement is definitely true, the prediction that Y atom diffuses faster than Fe at all temperatures by orders of magnitude in thermal equilibrium conditions [Bocquet 2017] is hard to trust because the efficient vacancy-mediated diffusion in iron starts already at 500°C, while our ToF-SIMS measurement do not show any noticeable Y diffusion below ≈800°C. This prediction is also contrary to most experimental investigations where Y is described as a slow diffuser. The significant amount of vacancies and oxygen present in the experimental samples, which strongly bind to Y, additionally slow down its diffusion. Recent ab initio VASP calculations by Mastrikov *et al.* [Mastrikov 2018] have shown that Y solute atoms are stabilized by vacancies in Fe creating the basis for the growth of Y oxide particles.

Newer expressions for the diffusivity of Y in the Fe matrix have been proposed and Boulnat *et al.* [Boulnat 2016] calculated that the nucleation of Y oxides (Y_2O_3 and $Y_2Ti_2O_7$) in Fe was attained at nearly 600°C during a non-isothermal heat treatment process. It is therefore conceivable that Y-enriched clusters are formed within our experimental investigation at 800°C. The strong Y-V and Y-O pairwise interactions, which probably provide the basis for Y cluster formation, may at the same time inhibit the formation of chromium oxides observed in the Ti and O implanted samples. With chromium diffusion and formation of chromium oxides at temperatures of around 600°C, it could therefore be assumed that the formation of some precursors of yttrium clusters occurs below this temperature. The most daring prediction could be the formation of Y oxide precursors already during the room temperature implantation. This hypothesis is supported by He *et al.* [He 2014] where they propose the formation of V-Y and/or Y-X (X = Y,O etc.) complexes could be the earliest formation stage of nanoclusters in ODS steels after implantation of Y and O into Fe base matrix at room temperature and characterization by PAS.

The clusters formed after annealing at 800°C with an average size of 2 nm are thus proposed to evolve from such precursors to form the Y enriched clusters. As various TEM investigations were unable to arrive at neither the composition nor the crystallographic structure, complementary characterizations preferably by APT could be ideal to clarify the composition of these clusters.

4.2.2 The role of Cr

We will recall that in the Ti and O implanted samples, chromium oxide particles are formed already after RT implantation and annealing at 600°C. Even though the compositions of the particles were enriched in Ti after annealing at 800°C, the typical corundum hexagonal structures were observed until 1000°C. On the other hand, for the Y and O implanted samples, even after RT implantation and annealing at high temperatures of 800°C, there is no evidence of the formation of such typical Cr_2O_3 type structures. The strong Y-V and Y-O binding may, as described earlier, promote the precursors for the cluster formation. Hence, in contrast to the Ti and O implanted and annealed samples, where Cr plays an important role in the early formation stages of nanoparticle formation, it appears that Cr, even though its presence is not excluded in the nanoparticles, does not seem to play a major role in the early formation stages of nanoparticles obtained after annealing of Y and O implanted samples. It is therefore conceivable that most ODS investigations overlook the role of Cr in nanocluster formation.

4.2.3 The role of Y as compared to Ti

Y-V, Y-O and/or Y-V-O clusters are proposed to be the precursors of nanoparticle formation within the Y and O implanted samples. Annealing at high temperatures resulted in enhanced diffusion of Y above 1000°C as demonstrated by the SIMS experiment. This enhanced Y diffusion as well as the fast diffusing O atoms ensure that Y as well as O may be trapped by these precursors. The nanoparticles are observed with an increase in size from 2 nm after annealing at 800°C, to the 5 nm sized Y_2O_3 nanoparticles after annealing at 1100°C. Y therefore appears to play a significant role in the early formation stages and growth of the particles.

The nanoparticle formation in the case of Y and O implanted samples appears quite different from the Ti and O implanted samples. Firstly, Cr plays a vital role in the first formation stages of nanoparticle formation in Ti and O implanted samples with the formation of Cr_2O_3 but the

role of Cr is less important in the Y implanted samples. In contrast to the Ti and O implanted samples where Ti appears to play no significant role in the early formation stages of nanoparticle formation, Y plays a vital role by inhibiting the formation of the chromium-oxides while promoting the formation of yttrium(-chromium) oxides.

4.2.4 The comparison with conventional ODS steels

The ODS steels obtained by the standard mechanical alloying have been widely investigated. Table 4.2 gives the characteristics of some of the particles observed in Ti-free ODS alloys in the literature. The nature of the nanoparticles has been mentioned to depend on the composition of the alloying elements and the fabrication route utilized. Upon all the available information on the types of ODS steels, Sakasegawa *et al.* [Sakasegawa 2009] divided the nanoparticles formed into two main groups: the non-stoichiometric Y-, Ti- oxides and the stoichiometric Y-, Ti- oxides. The non-stoichiometric Y-, Ti- oxides usually have a size ranging between 2 and 4 nm and are mostly formed after annealing at 850°C. The stoichiometric Y-, Ti- oxides usually have sizes >5 nm and are formed after consolidation at temperatures of 1100°C and above. The evolution of the nanoparticle formation reported by Sakasegawa *et al.* is coherent with the study by Ribis *et al.* [Ribis 2017] where they predicted that the nanoparticle formation is, as already mentioned above, in three stages. (i) The formation of Y-, Ti-, Cr- non-stoichiometric oxide, (ii) the formation of stoichiometric $Y_2Ti_2O_7$ with a Cr enriched shell after annealing and (iii) the elimination of the Cr enriched shell after enhanced annealing at 1300°C. By comparison with the first two stages of the nanoparticle formation described by Ribis *et al.*, in our study at the annealing temperature of 800°C, and in the absence of Ti, a yttrium-chromium oxide would be likely to be formed. Annealing at a temperature of 1100°C would lead to rejection of Cr to the shell to form yttrium oxides as observed in the samples investigated in this study. More information is required on the composition and structure of the particles observed after annealing at 800°C to confirm the similarities between this study and the study on ODS alloys.

It is seen from the section 3.2.3 where Y and O were implanted at an elevated temperature of 500°C, that particles readily form during the implantation stage, requiring no additional thermal annealing and providing particle sizes similar to those of the particles obtained after annealing at 1100°C. Although with the same Y_2O_3 structure, these particles clearly contain Cr in contrast to the Y and O RT implantation and annealing at 1100°C (but Cr is not completely excluded, neither after annealing at 800°C nor 1100°C). It therefore appears that the Y and O implantation at the temperature of only 500°C favored both the nucleation and growth of the nanoparticles. It implies that the ion implantation promoted yttrium diffusion at a temperature where yttrium was observed to be immobile during annealing (SIMS experiment). This mechanism appears to differ from the Y and O RT implantation and annealing at 1100°C where nucleation of the clusters first occurs before the eventual growth at very high temperatures. For the lower temperature annealing of the Y and O RT implanted sample, the 2-3 nm clusters observed could be the intermediate stage prior to Y_2O_3 particles with Cr shell at 1100°C and could be similar in composition and structure to the particles obtained after implantation at 500°C, i.e. Y-Cr-O with Y_2O_3 structure (then Cr is repelled out of the core and form a shell).

	Alloy	Condition	Treatment	Characterization technique	Composition	Structure	Particle size (nm)
Kueeh 2002b	Fe12Cr-0.25Y_2O_3	MA	HE at 1150°C	TEM	Y-O	Y_2O_3	10-40
Lindau 2002	EUROFER97	MA	HIP	TEM	Y-O	Y_2O_3 cubic	2-10 nm, avg 4 nm
Miller 2003	12YW	MA	HE at 1150°C, 200 MPa, ann. 1 h at 1050°C	APT	Y-O		5 nm
Klimenkov 2007	ODS-Eurofer	MA	HIP	TEM	Y-O	No defined crystalline structure	Bimodal distribution 5 – 18 nm And 5 nm
Klimenkov 2009	ODS-Eurofer	MA	HIP	TEM	Y-O with a Cr-V shell	Y_2O_3	8 nm
Ramar 2009	ODS EUROFER97	MA	HIP at 980°C	TEM	Y-O	Y_2O_3	10 – 30 nm
Ratti 2009	Fe18Cr1W	MA		TEM			6 nm
Brocq 2010		MA		TEM			
Sakuma 2004	FeCr unspecified	IBS	Annealing 600 – 1000°C	TEM	No given composition		6.5 nm
This study	FeCr - Y+O	IBS	Ion implantation at 500°C	TEM	Y-Cr-O Possible Cr enriched shell	*fcc* Y_2O_3	6 nm
This study	FeCr - Y+O	IBS	RT ion implantation - Annealed at 1100°C	TEM	Y-O (Y-Cr-O not excluded) Cr enriched shell	Particle 1:*bcc* Y_2O_3 Particle 2: *fcc* Y_2O_3	≈ 5 nm

Table 4.2 Summary of the conditions of Ti-free ODS alloys as well as the Y and O implanted samples from this investigation annealed at 1100°C as well as Y and O implantation at 500°C.

4.2.5 The proposed precipitation pathway

The precipitation of nanoclusters in Y and O implanted and annealed samples has been demonstrated to commence by the formation of very small clusters of the order of 2-3 nm after annealing at 800°C. The small sizes of these clusters make it quite difficult to obtain elemental information by various TEM techniques. APT is known to be quite useful for obtaining elemental composition for such very small clusters. Similar clusters studied in various investigations using APT in literature have a composition of yttrium, oxygen and probably chromium. It is therefore expected that the clusters observed after annealing at 800°C will have a similar composition, although it must still be confirmed by further investigations using advanced analysis techniques. Enhanced high temperature annealing performed at 1100°C to ensure the growth of these clusters up to approximately 5 nm has allowed to identify yttrium and chromium as particle constituents, with chromium forming a shell around a predominantly yttrium-enriched core. A schematic representation of the nanoparticle formation is illustrated in *Figure 4.2*. Some of the particles were determined to have crystal structures matching either *bcc-type*, or *fcc-type* yttrium oxide. The presence of two forms of oxide is quite unusual, because the macroscopic Y_2O_3 has the only known structure with the *fcc* ordering of metal atoms. Otherwise, the size and shape of the particles is directly comparable with the nanoparticles formed by the conventional MA employed in the ODS steels fabrication (see table 4.2 for Ti-free ODS alloys) and it is therefore likely that the small particles observed after annealing at 800°C are non-stoichiometric Y-Cr oxide particles that evolve with further annealing by repelling the Cr out of the core. It is unclear whether the hypothesis from Ribis *et al.* [Ribis 2017] where the Cr enriched shell disappears after annealing at 1300°C is applicable in our case. Hence, a high temperature annealing of Y and O samples implanted and annealed at 1300°C is proposed to be performed.

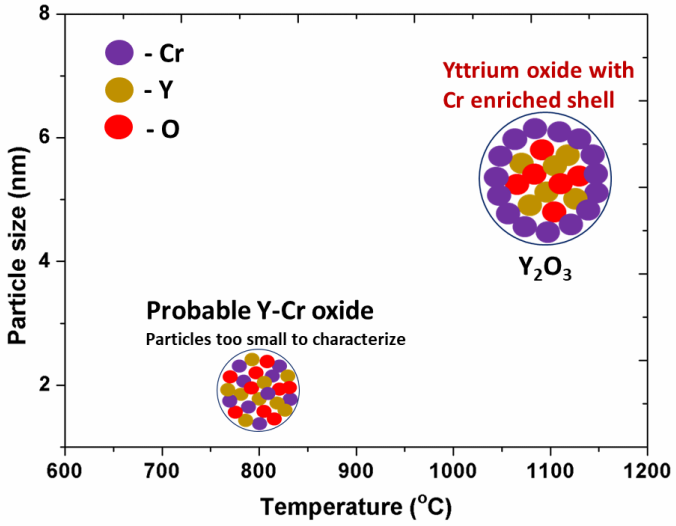

Figure 4.2 Steps involved in nanoparticle formation of Ti and O implanted and annealed samples.

4.3 O, Ti and Y implanted and annealed samples

Conventional ODS fabrication is performed by the simultaneous mixing of all the alloying elements. In our ion beam experiments, however, implantation of the ions has been performed sequentially. The order of implantation appears to be crucial in the oxide formation. The implantation starting with Ti and followed by Y, and then O revealed the formation of elongated chromium oxide (Cr_2O_3) particles as well as iron-chromium oxide ($FeCr_2O_4$) particles. On the other hand, Y implantation followed by Ti and then O revealed the formation of very small nanoclusters of Y-Ti (and possibly Cr) oxide after annealing at 800°C. In both previous implantation modes with metal+oxygen pairs, no nanoparticles were visible after room temperature implantation; they only became visible after annealing at high temperatures. These observations prompt the conclusion that the nanoparticle nucleate and grow during the annealing process. The implantation of Y inhibited the formation of Cr oxides that was observed in Ti and O implanted samples. The two sequential implantations Ti -> Y -> O and Y -> Ti -> O were followed by annealing using the same annealing parameters and at the same temperature (the specimens were actually annealed together during the same annealing experiment). The high sensitivity of the final results to the order of metal ion implantation forces one to conclude that, the atomic-scale processes determining the subsequent particle nucleation pathways operate already during implantation at room temperature. The implanted and alloy elements are very likely to bind differently to implantation-induced defects depending on the order in the sequence of implantation, which probably affects their diffusivity and reactivity in the nucleation process during subsequent annealing. Next, we will attempt to look at the individual RT implantations.

In the case of Ti first implantation (Ti -> Y -> O), the results are similar to those obtained after annealing at the same temperature of Ti and O implanted samples, except for the seemingly absence of Ti in the Cr_2O_3 particles. The Ti thus appears to play no significant role in the early formation stages of oxide nanoparticles. A high number of vacancies are however created during the Ti implantation. The subsequent Y implantation arrives at a time where there is a high number of vacancy-type defects, such as small vacancy clusters. Due to the strong affinity between Y and vacancies, Y could be trapped at such vacancy clusters that impede Y diffusion. The final stage then involves the O implantation and high temperature annealing. With possible Y movement impeded by its binding to vacancy clusters, Cr diffusion may promote the formation of chromium-oxide and hence the observation of Cr_2O_3 oxide in the samples implanted with Ti,Y,O annealed at 800°C.

The results of Y-first implantation (Y -> Ti -> O) seem similar to the results obtained after annealing at the same temperature of Y and O implanted samples, as far as we can judge from the general particle appearance with no information on the composition of the particles in this latter case. The Y has been mentioned to have a strong binding energy to O and vacancies. It might be that Y-V cluster precursors have time to collect during the Y implantation stage, though they must be quite small, being invisible in the microscope. In this situation, the subsequent Ti implantation has no effect on the early formation stages of nanoclusters.

Implantation of O would then likely fix the Y-vacancy precursors and not sufficient free oxygen will be available to promote the precipitation of chromium oxide clusters with the available Cr content in the alloy matrix. Hence, the system follows the cluster evolution trends, characteristic for the Y+O implantation case. At the temperature of 800°C, the Ti diffusion is triggered predictably and Ti enriches the tiny Y oxide particles to evolve into Y-Ti oxides.

It is evidently clear that the defect creation and its interaction with the implanted elements, mostly Y it seems, affects significantly the formation of nanoparticles in our FeCr alloys. Hence, 6 MeV Au ion irradiation has been performed in high purity FeCr followed by Y and O implantation at room temperature and subsequent annealing to investigate the role of the vacancies in the formation of nanoparticles and eventually exclude any role of the Ti in the nucleation process.

Experiments of Y and O ion implantation in Fe, preceded or not by Au ion irradiation, should also enable to conclude on the influence of Cr.

5. Summary and Conclusions

Oxide Dispersion Strengthened (ODS) steels are being developed as the ideal candidate structural material for Generation IV nuclear reactor systems (notably the Sodium Fast Reactor SFR) as well as fusion reactors. The most important feature of these steels is the fine distribution of metallic oxide particles, which serve as point defect recombination sites, He traps and obstacles to mobile defects thereby improving their creep and irradiation resistance. Even though numerous investigations of the microstructure of these steels have been conducted, there is no consensus on the exact mechanism of precipitation of the nanoparticles. This thesis was therefore aimed at using an alternative experimental technique known as ion implantation, contrary to conventional ball milling, to produce oxide nanoparticles in an attempt to understand the mechanisms involved in the formation of the nanoparticles in ODS steels. The implantation of Y, Ti and O ions at low energies into a high purity Fe10wt%Cr alloy has therefore been performed with the aim of producing oxides of either Y, Ti, or Y and Ti, in model high purity Fe10wt%Cr alloys. To this end, experimental investigations have been conducted following three different ion implantation experiments, mostly performed at room temperature :

(i) Ti and O ion implantation,
(ii) Y and O ion implantation,
(iii) Ti, Y and O ion implantation.

For all the implantations conducted at room temperature, no visible nanocluster was observed to be formed directly after the room temperature implantation by using TEM techniques. Annealing was therefore required to enhance the nucleation and/or growth of nano-oxides. The as-implanted samples were annealed at temperatures ranging from 600°C to 1100°C for the cases of dual ion implantation (i.e. Ti and O as well as Y and O ion implantations). The annealing of samples implanted with Ti, Y and O ions was only conducted at 800°C. Each annealing was performed for a duration of, or close to, 2 hours. The resulting microstructure and nanoparticles were characterized using a combination of TEM techniques, CTEM and HRTEM as well as analysis methods such as EFTEM and ChemiSTEM.

Firstly, Ti and O ions have been implanted directly into FeCr TEM thin foils at room temperature where no visible nanoparticles appeared to be formed. In situ annealing of the as-implanted thin foils at 500°C revealed the formation of precipitates with an average size of approximately 5 nm. These precipitates were clearly composed of Cr and O. The structure of these nanoparticles was identified to correspond to a mixed iron-chromium oxide spinel. With no typical Ti oxides formed, a further in situ annealing was performed at a temperature of 600°C. Nanoprecipitates similar in size to the precipitates observed at 500°C as well as much larger oxide patches were observed. Both of these newly formed phases were identified to be formed on the surface of the sample and grew in time to cover thicker regions. They had a composition of Cr and O and a crystal structure corresponding to a mixed iron-chromium oxide spinel crystal structure. Such oxides have been reported to be formed as part of the surface oxide layer in most FeCr steels. The oxygen provided to form this surface oxide layer is believed to be supplied by the oxygen remaining inside the vacuum chamber of the TEM after pumping during annealing as well as the oxygen present in the air which contributes to oxidation immediately after the final stage of sample preparation by electropolishing. Ti was

observed to diffuse at a temperature of around 800°C by ToF-SIMS experiments and hence, annealing of Ti and O thin foils was performed at 800°C. Again, similar to the previous annealing condition of 600°C, both small nano-precipitates of a size between 5 and 10 nm as well as large patches of the order of hundreds of nanometres were observed. The diffusing Ti appeared to enrich the nanoparticles, which were composed of Cr, Ti and O whilst still displaying the iron-chromium oxide spinel crystal structure.

The formation of these oxides with the spinel structure at the sample surface appeared to inhibit the possibility of observing nanoparticles beneath the sample surface. Hence, experiments performed on annealed TEM thin foils were abandoned in favour of experiments on cross section FIB lamellae extracted after implantation and annealing of bulk samples.

For the first set of experiments on Ti and O implanted bulk samples, nanoparticles with an average size of approximately 6 nm were observed after annealing at 600°C. These were identified as chromium oxides with the corundum crystal structure of the type Cr_2O_3. Some orientation relationships between the Cr_2O_3 nanoparticles and the matrix were deduced from HRTEM, which could suggest at least a partial coherence. After annealing at 800°C where Ti was observed to diffuse, Cr_2O_3 nanoparticles enriched in Ti were observed with an average size of approximately 11 nm. The diffusing Ti atoms thus appeared to be captured by the Cr_2O_3 nanoparticles to form these Ti enriched Cr_2O_3 nanoparticles. Annealing at enhanced temperatures of 1000°C revealed similar Ti enriched chromium oxides with the corundum Cr_2O_3 crystal structure and a similar size. Orientation relationships were again found between the nanoparticles and the matrix for both the annealing conditions of 800 and 1000°C. The final annealing was conducted at 1100°C, this temperature corresponds to the exact temperature implemented in the final thermal treatment of conventional ODS steels. Here, two types of nanoparticles were evident. The first type of particles was similar to Ti enriched Cr oxide with the corundum Cr_2O_3 crystal structure. In addition to these particles, Ti oxide particles with a Cr enriched shell were also evident. The crystallographic structure of these nanoparticles remained unidentified, as these did not match the Cr_2O_3 structure type particles or any known and likely metallic oxide. These Ti oxide particles are understood as being formed from the Cr_2O_3 particles that are enriched in Ti. Hence, contrary to the common perception that Cr plays no essential role in nanoparticle formation in ODS steels, Cr is likely to play an essential role in the nanoparticle formation within Y free alloys.

For the second set of experiments on Y and O implanted bulk samples, small clusters with sizes of approximately 2-3 nm were observed after annealing at 800°C. The sizes of these particles made it impossible to determine both the elemental composition and crystallographic structure by the various available TEM techniques. However, the difference in terms of shape and size between the precipitates in Y and O and in Ti and O implanted samples after similar annealing at 800°C suggests that a pure Cr oxide is excluded in this case, and a Y, or Y-Cr, oxide is likely. Cr_2O_3 being observed to be formed at 600°C in the case of Ti and O ion implantation, it could be assumed that a precursor for these Y oxides is already created at temperatures lower than 600°C. Annealing at a temperature of 1100°C revealed the formation of much larger nanoparticles with an average size of approximately 5 nm. ToF-SIMS investigations indicate that Y does not long-range diffuse at 800°C but diffuses significantly at the temperature of 1000°C and above, which could facilitate the nucleation and growth of the nanoparticles. The crystallographic structure of these nanoparticles was determined to correspond to either a *bcc* crystal structure of Y_2O_3 or an *fcc* crystal structure of Y_2O_3. These particles display a core/shell structure where the core is enriched in Y and probably Cr and

O, whilst the shell is composed of predominantly Cr. The size, structure and composition of the particles are directly comparable with the oxide particles formed by conventional fabrication of ODS steels. Here, contrary to the Ti and O ion implanted samples where the oxide formation is dictated by the Cr, the presence of Y suppresses the formation of any pure Cr oxides. The Y thus plays the most important role in the precipitation and limits the role of Cr in the oxide formation even though the presence of Cr within the core cannot be discounted. Y and O ions were also implanted into the high-purity FeCr matrix at the temperature of 500°C. The observed nanoparticles possessed an average size of approximately 6 nm with a structure coherent with the *fcc* crystal structure of Y_2O_3. Whereas Y and O room temperature implantation required an annealing at a temperature of 1100°C to form typical yttrium oxide particles (Y_2O_3) of a similar size, such particles can already be observed after the implantation of Y and O at 500°C. Ion implantation at elevated temperature therefore significantly enhances the mobility of the species including yttrium, which favors the nucleation and growth of the yttrium oxide nanoparticles.

The final set of experiments involved the implantation of Ti, Y and O ions. In this case, the ion implantations were performed in two different sequential orders : (i) a Y first implantation followed by Ti and then O ion implantation (Y->Ti->O), and (ii) a Ti first implantation followed by Y and then O ion implantation (Ti->Y->O). For both of the implantation schemes, no nanoparticles appeared to be formed directly after implantation. Bulk samples from both of these conditions were then annealed at 800°C. The Y->Ti->O implantation experiment led to the formation of very small nanoparticles of the size 2-3 nm whose crystallographic structure could not be identified by HRTEM. They were however identified as Y-Ti oxide particles using ChemiSTEM and APT. Elsewhere, the Ti->Y->O implantation experiment led to the formation of nanoparticles with sizes ranging from 5 to 20 nm. These nanoparticles were identified as chromium oxide particles with a corundum hexagonal structure of the type Cr_2O_3 similar to the samples implanted with Ti and O ions. The order of implantation is thus obviously crucial in the determination of structure and composition of oxide that will precipitate and grow during subsequent annealing. These results show that precursors driving the oxide formation in both conditions are already created during the room temperature implantation. This probably implies that the implanted metallic elements bind differently to implantation-induced defects depending on the order in the sequence of implantation, which would affect their diffusivity and reactivity in the nucleation process during subsequent annealing.

The formation of oxides of Ti, Y and mixed Y-Ti oxides has thus been achieved by ion implantation and subsequent thermal annealing in this study, with, in some cases, nanoparticle characteristics that are close to those reported in the literature of ODS alloys. Detailed characterization of observed nanoparticles has been presented for the three sets of experimental investigations. The formation of pure Ti oxides appears to be suppressed at annealing temperatures below 1000°C in Ti and O ion implanted specimens, with the formation of corundum Cr_2O_3 oxide particles. This Cr_2O_3 oxide formation is suppressed in the Y and O implanted samples where Y may interact with the O and vacancies at the implantation stage to form some precursors for Y oxide formation during subsequent annealing. The different oxide particles formed during the two sequential Y, Ti and O ion implantations buttresses the point that precursors are already formed during the room temperature implantation stage. It is therefore conceivable that precursors of the nanoparticles formed by conventional ODS steels fabrication are formed during the mechanical alloying stage. The observation of the formation of Y clusters after room temperature implantation would be ideal to confirm this hypothesis.

A summary of features of the nanoparticles observed in the implanted and annealed ion implantation samples for the various experimental conditions are presented in *Table 5.1.*

Implantation condition	2 hour annealing (°C)	Average particle size (nm)	Composition	Crystallographic structure
Ti+O RT implantation	600	≈6	Cr, O	Corundum Cr_2O_3
	800	≈11	Cr, Ti, O	Corundum Cr_2O_3
	1000	≈12	Cr, Ti, O	Corundum Cr_2O_3
	1100	≈10	Particle 1: Cr, Ti, O Particle 2: Ti, O enriched core Cr enriched shell	Particle 1: Corundum Cr_2O_3 Particle 2: Unidentified structure
Y+O RT implantation	800	≈2-3	Probable Y, O, (Cr) enrichment	Unidentifiable structure
	1100	≈5	Y, O enriched core Cr enriched shell	Particle 1: *bcc* Y_2O_3 Particle 2: *fcc* Y_2O_3
Y+O implantation @ 500 °C		≈6	Y, Cr, O enriched core Cr enriched shell	*fcc* Y_2O_3
Ti+Y+O RT implantation	800	≈5-20	Cr, O	Corundum Cr_2O_3
Y+Ti+O RT implantation	800	≈2-3	Y, Ti, O (Cr)	Unidentifiable structure

Table 5.1 Summary of characteristics of obtained nanoparticles in implanted and annealed samples for the three sets of ion implantation experiments.

6. Perspectives and Future Research

The investigations performed in this PhD study contribute to understanding the nanoparticle formation in FeCr model alloys for ODS steels purposes. There however remain a few questions, where future research could provide clarifications. There are few complementary investigations to the three sets of implantation experiments, which could help answer the questions pertaining to certain conditions.

In the case of the Ti and O implanted samples;

- Rapid Thermal Annealing (RTA), which implies reaching the desired high-temperature of annealing within a few minutes, instead of the relatively slow ramp of heating in the annealing performed in this PhD study, could be used.
  With Cr oxide forming already at 600°C, the slow ramp of heating probably ensures its formation before Ti becomes mobile and enrich the Cr_2O_3 particles. However, a rapid thermal annealing would lead to a competition between the Ti and Cr for the oxide formation and help establish if the corundum Cr_2O_3 type nanoparticles would still be formed.
- Annealing at 1300°C could be performed to see if the Cr rich shell formed around the Ti oxide particles disappears.
  Ribis *et al.* [Ribis 2017] indeed demonstrated that oxide particles formed after annealing at 1100°C displayed a Cr enriched shell which eventually disappears after annealing at 1300°C. Such an experiment could help understand a probable final stage of oxide evolution in the Ti and O implanted samples.

In the case of the Y and O implanted samples;

- Experiments performed in the same conditions as in the present study but on pure Fe could enable to observe any influence of Cr on the precipitation of nano-oxide particles.
- A detailed elemental composition characterization of the Y and O sample implanted at 800°C could be performed using Atom Probe Tomography for example, as well as a quantification of the elemental composition of the oxide nanoparticles for each implantation and annealing condition, if possible.
- Similar to the Ti and O implanted samples, annealing at 1300°C would enable to observe or not the disappearance of the Cr shell and elaborate a final oxide stage evolution.

In the case of the O, Ti and Y implanted samples;

- Annealing at 1100°C and probably 1300°C would enable to establish an evolution of the oxide structure and composition and may bring information on the exact role of the order of implantation of the elements.
- Similar experiments performed in the two orders of sequential implantation but with an ion irradiation (vacancy creation without ion implantation) instead of Ti

implantation, would enable to observe any effect of the presence of Ti in the oxide precipitation.

In addition to the suggested complementary investigations, some additional perspectives could be important to investigate :

1. From the various implantation experiments, and especially the Y and O, and Y, Ti and O ion implantation experiments, there appears to be an interaction between implanted species and vacancies to promote the formation of precursors at the implantation stage. Hence, an investigation of the interaction between the implanted elements and the vacancies by Positron Annihilation Spectroscopy (PAS) for example, which would be ideal to establish the various interaction mechanisms between the implanted elements and the vacancies.
2. In all the experimental investigations, a sequential implantation where the metallic ion was first implanted was implemented. But as has been demonstrated, there appear to already be some interactions between the implanted elements and the vacancies, especially with the Y which suppresses the formation of Cr oxide in the Y implanted samples where Y is implanted at first. A simultaneous implantation of the metallic ion and the oxygen could help understand the exact mechanisms ongoing during the implantation stage. A simultaneous implantation of Y and Ti ions, followed by O ion implantation, could also give some valuable information.
3. An ion irradiation performed on the implanted and annealed Y samples displaying the presence of Y_2O_3 oxide nanoparticles would give information on the stability of these oxides.
4. With Zr suggested to form a more homogeneous distribution of oxide nanoparticles, it could be possible to replace Ti with Zr and/or Al to evaluate the oxide formation in such conditions.

7. Annexes

Annex I: The as-implanted thin foil annealed at 600°C (complementary characterization)

Complementary characterization was performed for the samples implanted with Ti and O ions at RT and then *in situ* annealed at 600°C (see section 3.1.3.1 for initial characterization). Diffraction patterns were acquired for the two unique regions where the region A corresponds to the white contrast regions and the region B corresponds to the region further away from this white contrast region described in section 3.1.3.1. The diffraction patterns acquired for both the A and B regions are given in the *Figure 7.1(a)* and *(b)*, respectively. Only one 'network structure' observed in *Figure 7.1(a)* corresponds to an *fcc* crystal structure with an orientation B = [-112]. An estimate of the lattice parameter was determined as 0.836 nm from the inter-planar spacing which matches the theoretical lattice parameter of $FeCr_2O_4$ which is a = 0.845 nm. The diffraction pattern of region B, outside the white contrast region, shows two sets of diffraction spots. The first set of spots interconnected with yellow corresponds to the *bcc* crystal structure of the base matrix. The second set of spots interconnected with green appears to correspond to an *fcc* crystal structure with an orientation B = [-111]. The obtained lattice parameter again matches with $FeCr_2O_4$.

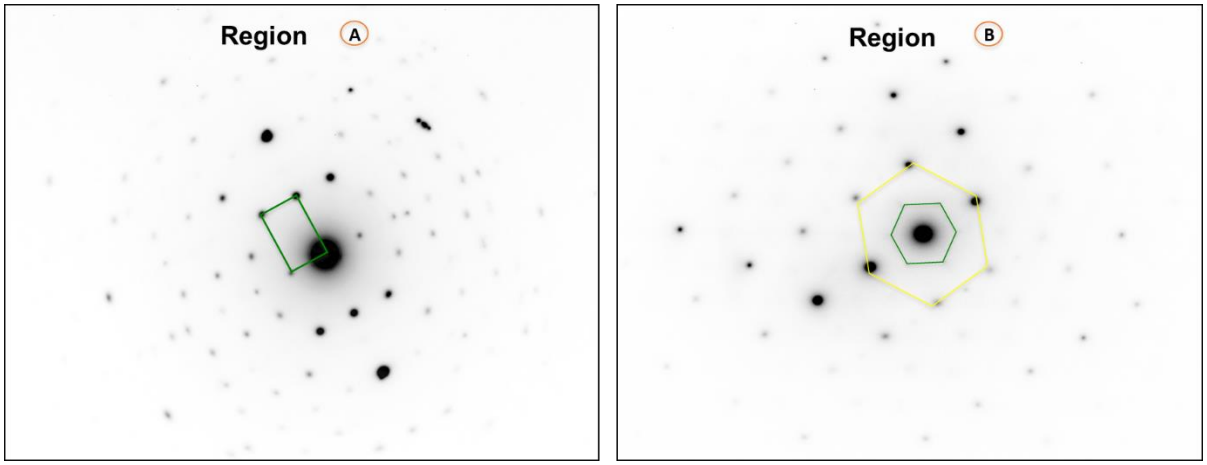

Figure 7.1 Diffraction patterns corresponding to (a) the region A with white contrast as observed in Figures 3.7 and 3.9 from chapter 3 section 3.1.2.2 with an orientation B = [-112] and (b) the thicker region B much further away from the hole.

Electron-Energy Loss Spectroscopy (EELS) investigation was performed comparing the white contrast regions (region A/ rectangular patches) to the region B outside this region. The obtained spectra are displayed in *Figure 7.2*. The thickness of the region A was determined by EELS measurements to be close to 15 nm. The corresponding core loss spectrum indicates intense Cr, O and Ti peaks. The core-loss spectrum of the region B outside the white contrast regions shows remarkable differences: the Fe peak is much more intense whilst peaks for Cr, Ti and O are weaker. This quite corresponds to the EFTEM results with a region A depleted in Fe. The thickness of this region measured by EELS was determined as about 38 nm.
The quantification from EELS spectra is given in *Table 7.1* for these two regions. This quantification, although not very accurate, confirms the presence of $FeCr_2O_4$ in region A. In region B, the ratio of Fe and Cr concentrations is characteristic of the FeCr matrix. The amount of oxygen in this region is however much higher than expected.

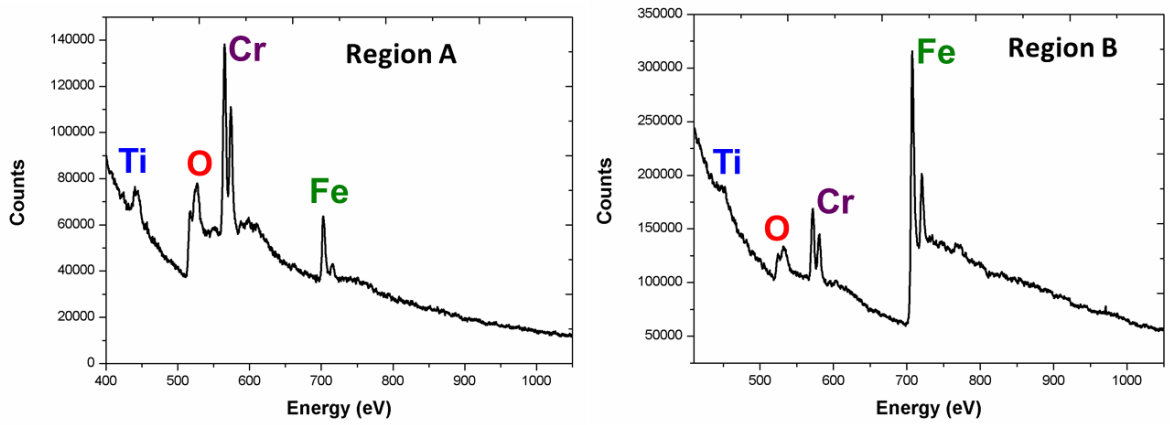

Figure 7.2. Electron Energy Loss Spectroscopy (EELS) investigation for (Ti,O) ion-implanted and annealed thin foil at 600°C comparing (a) spectrum for thin white contrast regions to (b) spectrum for much thicker regions outside this white contrast region.

Element	Fe	Cr	Ti	O
Zone A concentration (at%)	8-10	14-15	1.5-2.0	70-75
Zone B concentration (at%)	60-65	6-7	1.5-2.0	30-35

Table 7.1 EELS quantification of thin foil implanted with Ti and O ions at room temperature and *in situ* annealed at 600°C.

Annex II: HRTEM imaging of the matrix annealed at 1000 and 1100°C

For the FeCr base matrix with approximately 10wt%Cr, the phase transformation from the α-Fe bcc structure to the γ-Fe fcc structure occurs at a temperature of approximately 880°C (see the FeCr phase diagram in section 1.2.2). Hence, HRTEM imaging was performed to verify the crystallographic structure of the matrix after annealing at temperatures above 900°C. In the *Figure 7.3(a)* and *(b)* are HRTEM images acquired from bulk samples annealed at 1000 and 1100°C. The imaging was performed for a region outside the implanted region with the absence of any nanoparticles.

For the imaging of each of these conditions, the image labelled *(i)* is the HRTEM image of the selected region of the matrix, the image labelled *(ii)* is the high magnification image of the highlighted region and the image *(iii)* illustrates the fast Fourier transform (*fft*) of this region. The orientation of the selected regions of matrix as illustrated in both *fft* images was exactly the same. The interplanar distances for the (110) and (121) atomic planes were determined as 0.202 and 0.117 nm respectively. These values are exactly the same as the interplanar distances for the *bcc* FeCr crystal structure (where d_{110} = 0.203 and d_{121} = 0.117 nm). Elsewhere, the angles between the (110) and (2-11) atomic planes was measured as 73° and the angle between (2-11) and (1-21) was measures as 34°. These values also correspond exactly to the FeCr matrix. It can therefore be confirmed that the matrix retained the *bcc* FeCr crystal structure after annealing of the bulk samples at 1000 and 1100°C. It is expected that the *bcc* FeCr structure transforms to the *fcc* crystal structure beyond annealing temperatures of 800°C but the slow cooling of the samples after annealing as stated in chapter 2 section 2.4 may have promoted the transformation back to the *bcc* crystal structure.

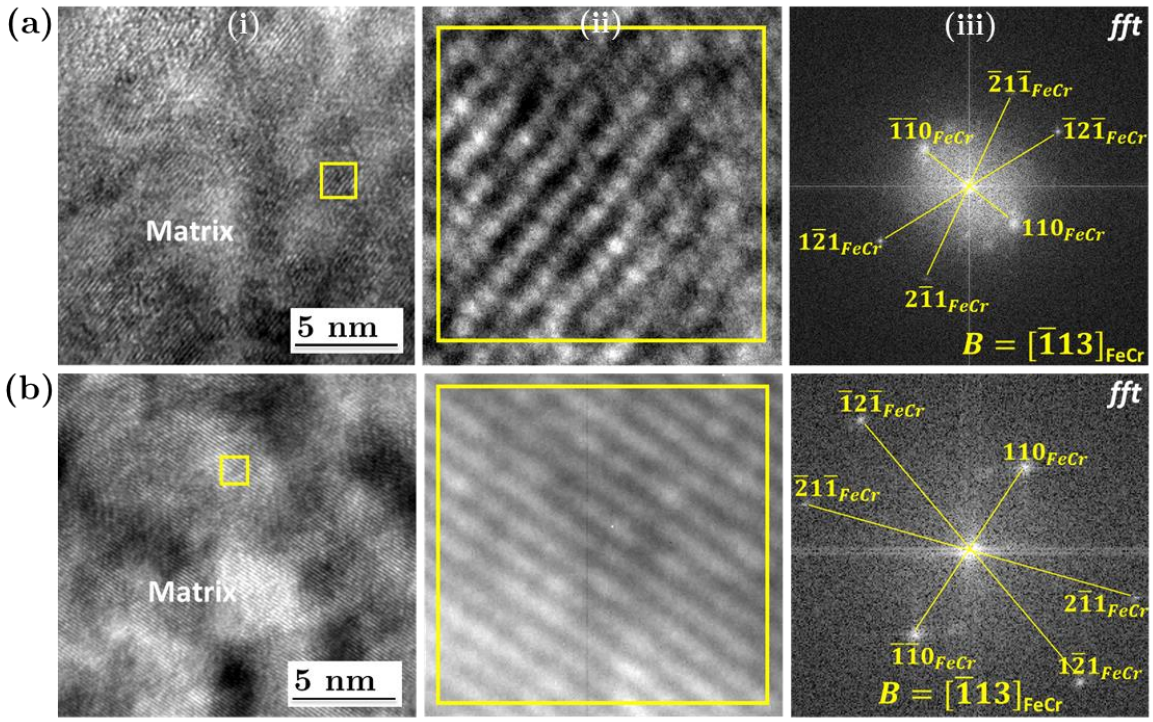

Figure 7.3 (i) High Resolution TEM (HRTEM) image of the the FIB lamella extracted after annealing at [a] 1000 and [b] 1100°C for 2 hours. (ii) Magnified image of the selected region of the matrix and the (iii) corresponding Fast Fourier Transform (*fft*) of the selected region of the matrix

Annex III: EFTEM compared to ChemiSTEM imaging of sample implanted with Y and O sample at 500°C

As briefly mentioned in the results section 3.2, elemental characterization of Y implanted samples was performed using EFTEM. However, this was quite difficult to image the Y. The reasoning attached to this is the fact that the position of the Y peaks in the EELS spectrum produce very weak signal for imaging. The two major Y edges in the EELS spectrum are the $L_{2,3}$ and the $M_{4,5}$ edges. The $L_{2,3}$ edge is positioned at an offset of 2155 eV. At such very high energies, only a small number of counts is recorded giving a weak signal for Y imaging. Elsewhere, for $M_{4,5}$ edge with an offset at 157 eV, this is positioned very close to the low-loss spectrum and at such a position, the background from the plasmon peak is quite high such that the Y signal may not be easily imaged. In the *Figure 7.4* is a typical example of EFTEM imaging of Y implanted samples.

The *Figure 7.4* shows a BF image of a chosen region for EFTEM imaging for the sample implanted with Y and O ions at 500°C. The Fe elemental map shows a depletion in patches, which correspond to observed particles in conventional TEM imaging. However, no Y presence is found for these particles with the Y map appearing quite homogeneous. Neither O nor Cr enrichment was equally observed for the nanoparticles with their elemental maps appearing quite homogeneous.

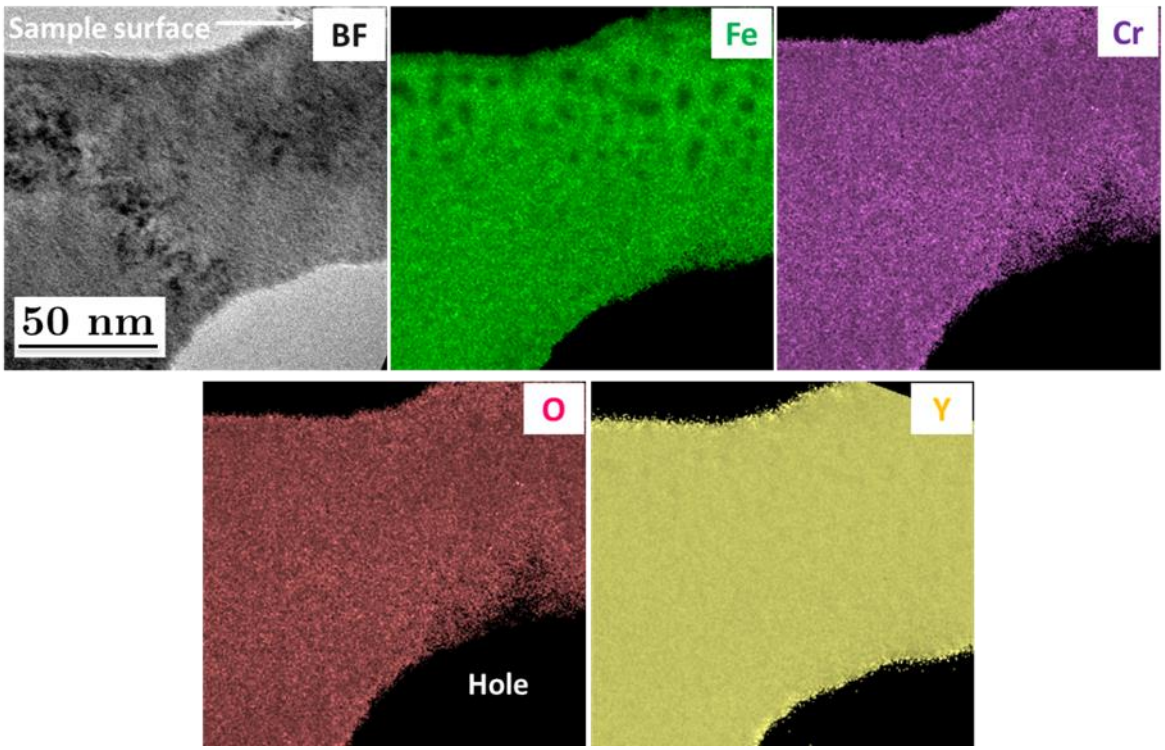

Figure 7.4 Energy-Filtered TEM (EFTEM) elemental characterization of the FIB lamella extracted after implantation of Y and O ions at 500°C. Bright Field (BF) image of the region chosen for EFTEM together with elemental maps acquired using the two-window jump ratio method in the vicinity of Fe-$L_{2,3}$ edge, Cr-$L_{2,3}$, O-K and Y-$L_{2,3}$ core loss edges.

With EFTEM appearing ineffective for the characterization of Y in the Y-implanted samples, STEM-EDX using the ChemiSTEM technology (description can be found in chapter 2 section 2.2.3.9) was adopted for the chemical characterization of Y implanted samples.

Mapping by ChemiSTEM was usually performed at both lower and much higher magnifications. The high magnification mapping has been showed in the results (section 3.3.2.1). In the *Figure 7.5* are images for the ChemiSTEM elemental mapping for the Y and O sample implanted at 500°C. A zone close to that used for the EFTEM was chosen for the mapping. The imaging was performed at a low magnification close to that used for EFTEM imaging in *Figure 7.4* using a count rate of 40k counts/second and the duration of the entire scan was 40 minutes.

The Fe elemental map shows a depletion in particles corresponding to particles observed in the conventional TEM imaging and this is coherent with the Fe elemental map in the EFTEM imaging. On the contrary, Cr and Y elemental elemental map showed an enrichment in patches corresponding to the formed nanoparticles. The O map appeared quite homogeneous with a reason for this given in section 3.1.3.1 So contrary to the EFTEM elemental mapping where only an Fe depletion is observed for the nanoparticles, STEM-EDX mapping using the ChemiSTEM technology has confirmed that these particles are composed of Y, Cr and probably O. This has been confirmed by the mapping performed at higher magnification as shown in chapter 3 section 3.2.4.

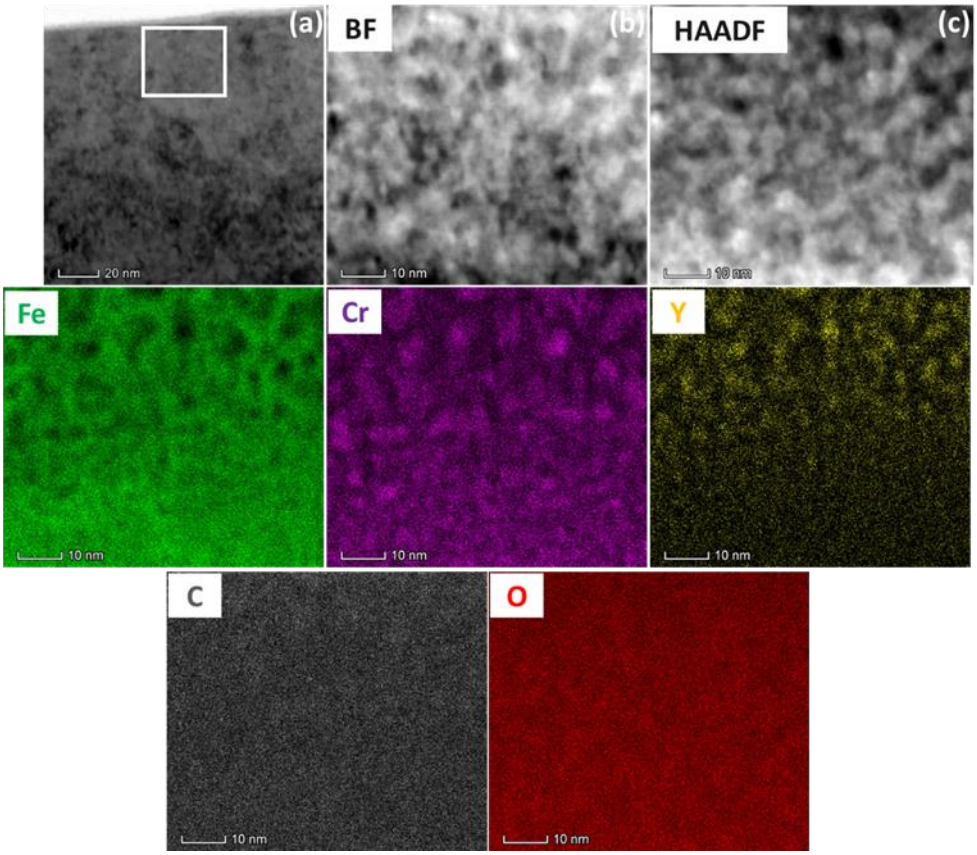

Figure 7.5 STEM-EDX elemental mapping of FIB lamella of Y+O sample bulk specimen implanted at 500°C using ChemiSTEM technology. (a) Bright Field (BF) image indicating the selected region (b) the corresponding Bright Field (BF) and (c) High Angle Angular Dark Field (HAADF) image together with elemental maps for Fe, Cr, Y, O and Cr.

As complementary to the ChemiSTEM imaging, spectrum imaging has been performed for a small region of about 5 nm by 5 nm. The zone 1 corresponds to region without any nanoparticle presence and the zone 2 corresponds to a region where a particle is found (as shown in the *Figure 7.6(a)*). The spectra from each of these regions is given in the *Figure 7.6(b)*. It is clearly evident that the spectrum for the zone 2 display Y peaks which are absent for the zone 1. Enhanced Cr peaks are also observed for the zone 2 as compared to the zone 1. This confirm the Y and probably Cr presence in the nanoparticles.

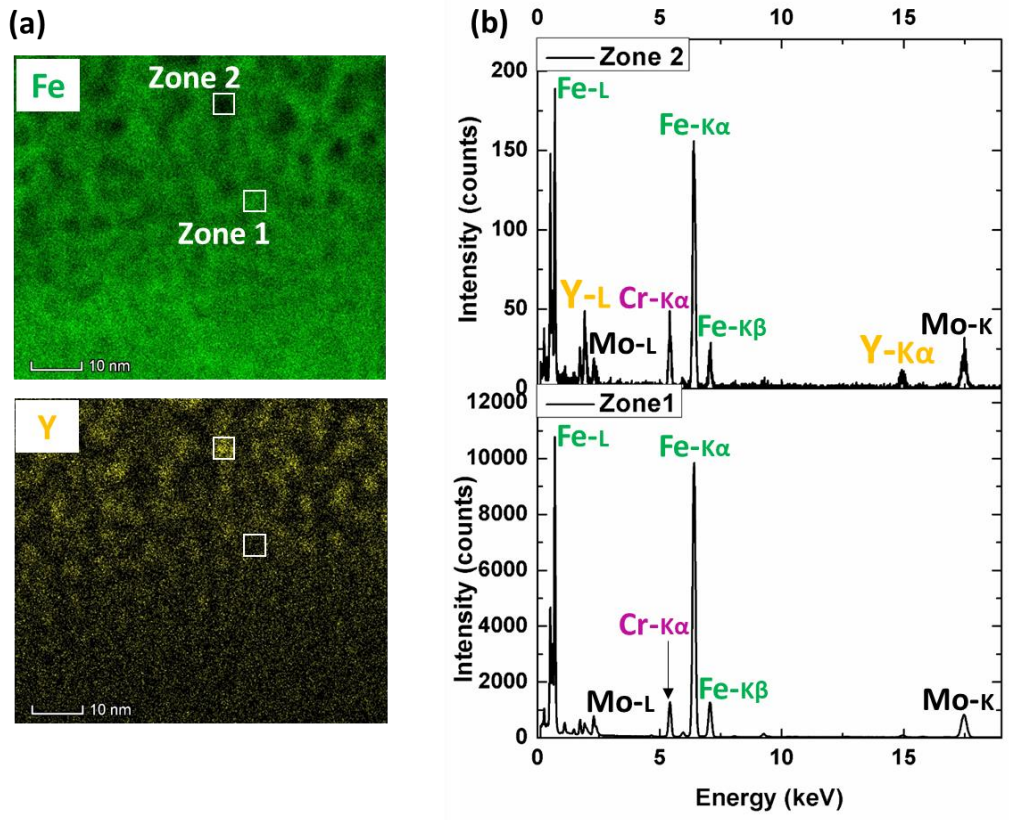

Figure 7.6 STEM-EDX elemental mapping of FIB lamella of Y+O sample bulk specimen implanted at 500°C using ChemiSTEM technology (a) Fe and Y elemental maps illustrating zones 1 and 2 for spectrum imaging and (b) EDX spectra acquired for regions 1 and 2.

Annex IV: High purity Fe sample implanted with Ti ions only

As performed for the high purity Fe sample implanted with Ti and O ions at room temperature followed by annealing at 800°C for 2 hours, the high purity Fe bulk sample was also implanted with Ti ions only and annealed at 800°C for 2 hours. A FIB lamella was extracted from the bulk sample only after RT implantation and a subsequent annealing. In the *Figure 7.7(a)* is the BF image of a selected region from the FIB lamella where no visible nanoparticles were evident. Diffraction patterns acquired for this region showed no additional reflections in the diffraction pattern (see *Figure 7.7(b)*). These observations were also found for many different regions investigated. These results therefore suggest the fact that there is no likely nanoparticle formation after the implantation at RT of Ti ions only into the high purity Fe sample and subsequently annealed at 800°C.

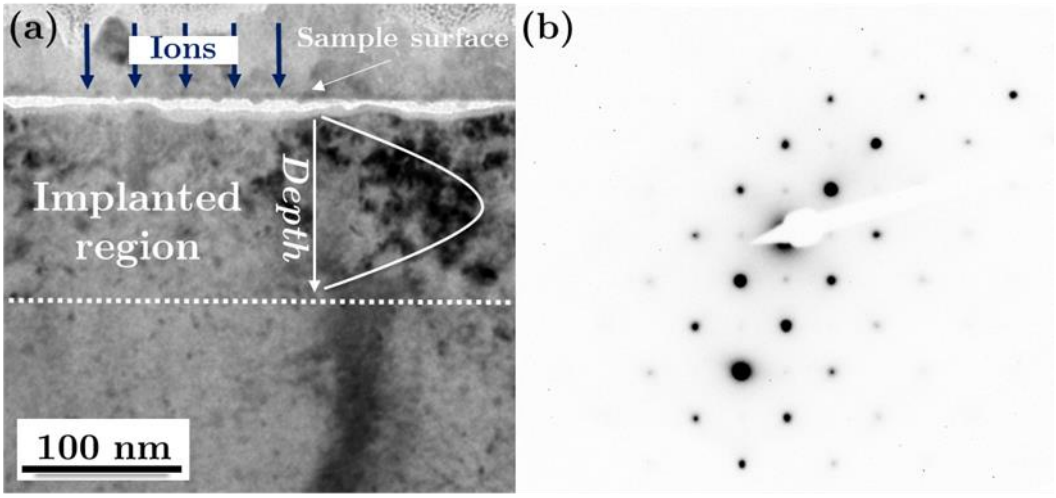

Figure 7.7 (a) Bright field image of the FIB lamella extracted from the high purity Fe sample implanted at RT with Ti ions only and annealed at 800°C for 2 hours (b) Diffraction pattern acquired for this region

It was observed however there was a formation of a surface oxide after annealing and this surface layer extended into the bulk sample a few nanometers from the surface of the sample (as shown in the *Figure 7.8(a)* and *(b)*). The crystallographic structure of this layer was investigated by HRTEM imaging. In the *Figure 7.8(c)* is the *fft* of the region highlighted in the *Figure 7.8(a)*. The crystal structure of this region appears to correspond to an *fcc* crystal structure of the type Fe_3O_4 or $FeCr_2O_4$ with the orientation B = [011]. With the alloy composition devoid of any Cr, it is evident that the structure corresponds to the Fe_3O_4 and not the $FeCr_2O_4$. The interplanar distances for the (200) and (111) atomic planes were determined as 0.42 and 0.48 nm respectively. The angle between the (111) planes was determined as 70° and the angle between the (200) and (111) atomic planes was determined as 55°. These parameters closely match the theoretical interplanar values of Fe_3O_4 where the (200) and (111) atomic planes are given as 0.418 and 0.483 nm respectively. Equally, the angle between the two (111) atomic planes and the angle between the (200) and (111) atomic planes are given as 70.52° and 54.74° respectively.

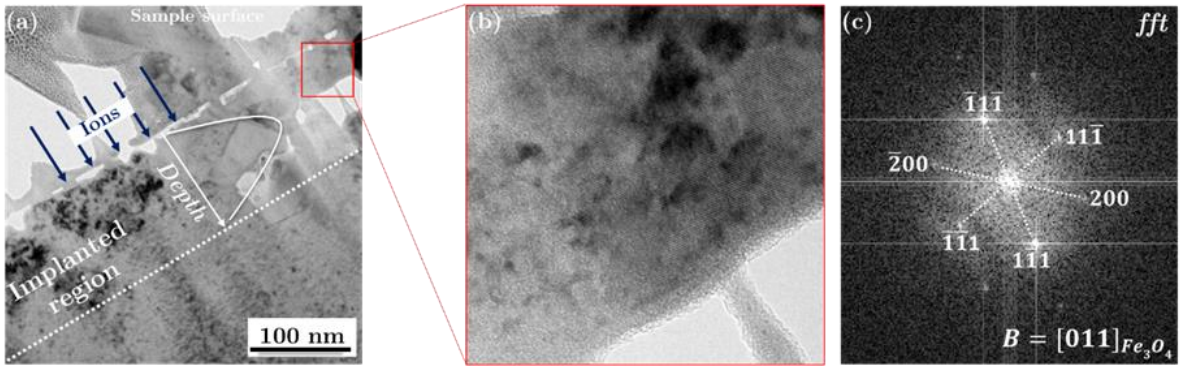

Figure 7.8 (a) Bright field image of the FIB lamella extracted from the high purity Fe sample implanted with Ti only and annealed at 800°C for 2 hours (b) Low magnification HRTEM image acquired for this region and the (c) corresponding *fft* for this region

Annex V: Thin foil annealing at 800°C of O, Ti and Y sample implanted at room temperature

The as-implanted thin foils just as with previous conditions have been observed to display no nanoparticle formation directly after room temperature implantation. With no visible nanoparticles formed after RT ion implantation, subsequent annealing has been conducted on the thin foils of Ti -> Y -> O and Y -> Ti -> O implanted samples at a temperature of 800°C for a duration of 2 hours. Both thin foils just as in the case of RT implanted samples appeared very similar. Hence, we chose to study in more details only the Y -> Ti -> O sample annealed at 800°C. BF imaging conducted at selected regions within the sample appeared to reveal the formation of nanoparticles not evident after just the RT implantation. In the *Figure 7.9* is the BF imaging of the sample showing the presence of particles (highlighted with arrows). The contrasts of these particles change from the underfocus to the overfocus condition.

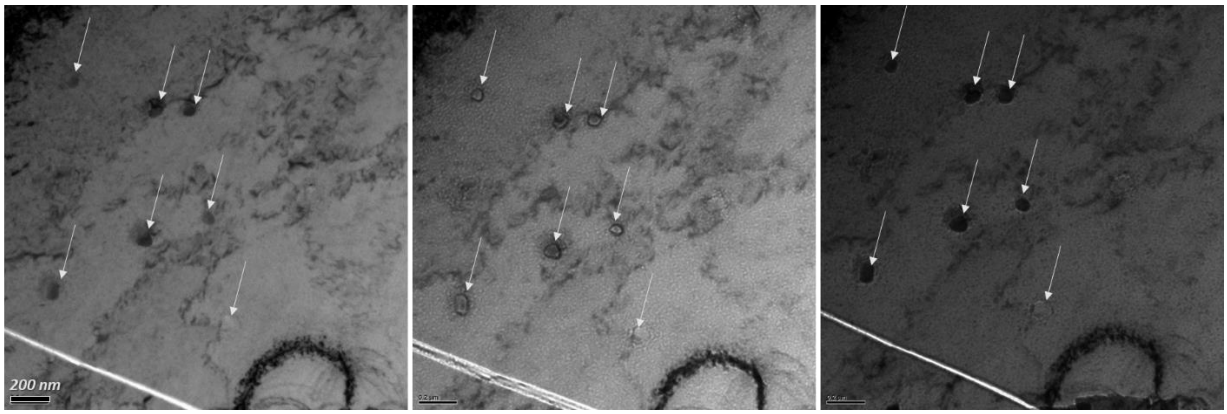

Figure 7.9 Bright Field (BF) TEM imaging of the as-implanted Y -> Ti -> O thin foil annealed at 800°C for 2 hours indicating the formation of particles (a) close to focus condition (b) in the underfocus condition and (c) overfocus condition.

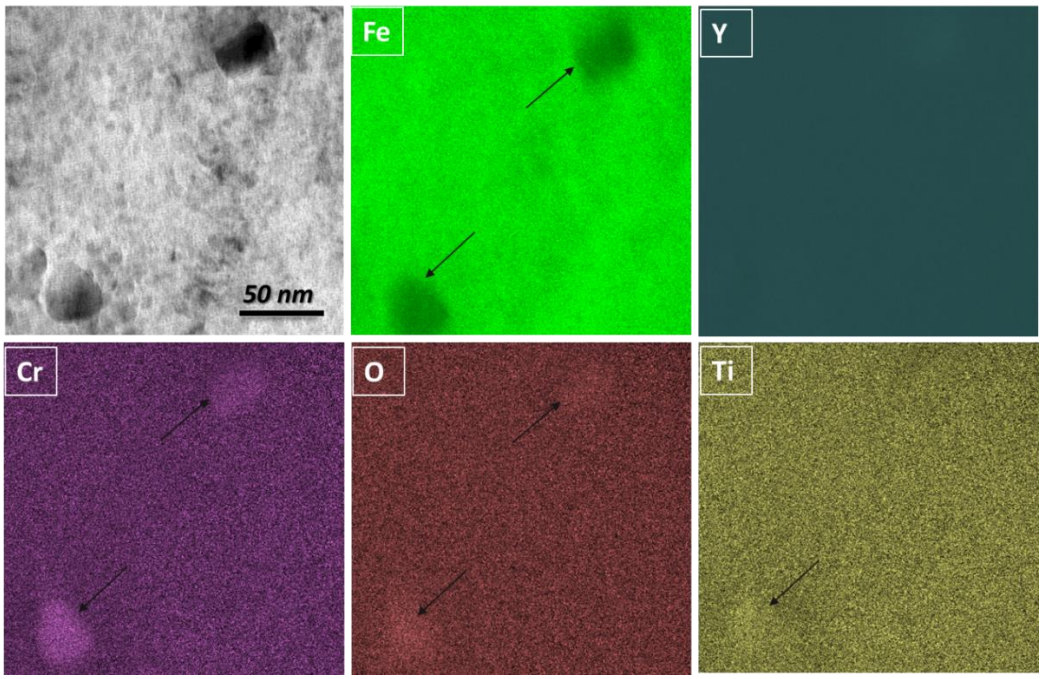

Figure 7.10. Energy-Filtered TEM (EFTEM) elemental characterization of the thin foil observed after implantation at room temperature and annealing at 800°C for 2 hours. Bright Field (BF) image of the region chosen for EFTEM together with elemental maps acquired using the two-window jump ratio method in the vicinity of Fe-$L_{2,3}$ edge, Y-$M_{4,5}$, Cr-$L_{2,3}$, O-K and Ti-$L_{2,3}$ core loss edges.

In order to determine the composition of these particles, EFTEM elemental maps were acquired for the various elements of interest. The BF image of the zone selected for the EFTEM imaging is given in the *Figure 7.10* showing two distinct particles of a size ≈ 50 nm. There appear to be a depletion in Fe in these particles. The Y elemental map however appeared quite homogeneous. Similar to most previous elemental compositions, the particles appear enriched in Cr and O as well as Ti.

Diffraction pattern (DP) image was acquired for this region containing these particles as given in the *Figure 7.11* Strong reflections are easily observed as have been highlighted in the yellow pattern. The measured interplanar spacings and angles were determined to correspond to the *bcc* crystal structure of the FeCr matrix with an orientation B = [013]. Many other additional reflections can also be observed and have been highlighted in the red pattern. These reflections evidently do not belong to the FeCr matrix. The interplanar spacings and angles for these additional reflections have been measured and appear to correspond to an *fcc* crystal structure. The distances closely match that of the inverse spinel $FeCr_2O_4$. It therefore becomes apparent there is the formation of a similar $FeCr_2O_4$ surface oxide as has been observed in the Ti and O implanted and annealed samples.

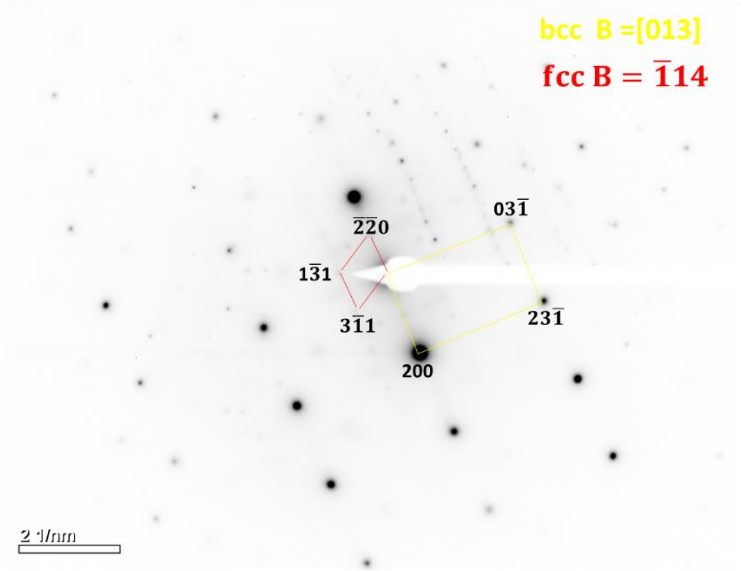

Figure 7.11 Diffraction Pattern (DP) of thin foil implanted at room temperature and annealed at 800°C for 2 hours with spots in the yellow pattern corresponding to the FeCr matrix with an orientation B = [013] and additional highlighted spots in red matching that of an fcc crystal structure of $FeCr_2O_4$ with an orientation B = [-114].

Annex VI: Complimentary Atom Probe Tomography (APT) Characterizations

In the Y, Ti and O sequentially implanted and annealed sample, APT has been used to characterize the very small nanoclusters observed in the sample (see section 3.3.2.3 for detailed characterization of this sample). Three APT tips were stated to have been prepared and displayed a very similar distribution of ions within the three different samples. The ion distribution within only one of the APT tips (labelled as R30_10308) was displayed in section 3.3.2.3.1. The distribution of ions within the two remaining APT tips labelled as R30_10306 and R30_10307 are illustrated in the *Figures 7.12* and 7.*13* respectively.

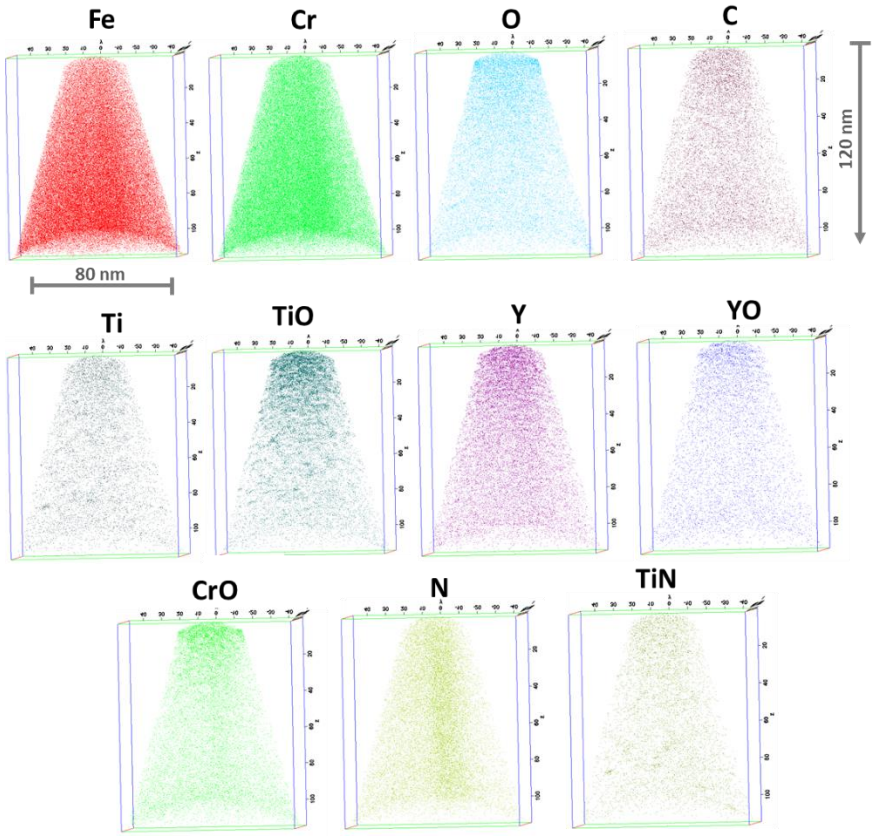

Figure 7.12 The 3-D APT reconstructed tip of the Y, Ti and O bulk sample implanted at room temperature followed by annealing at 800°C (tip R30_10307) showing the distribution of the evaporated Fe, Cr, O, Ti, Y, N and C elements as well as CrO, TiN, TiO and YO molecular ions.

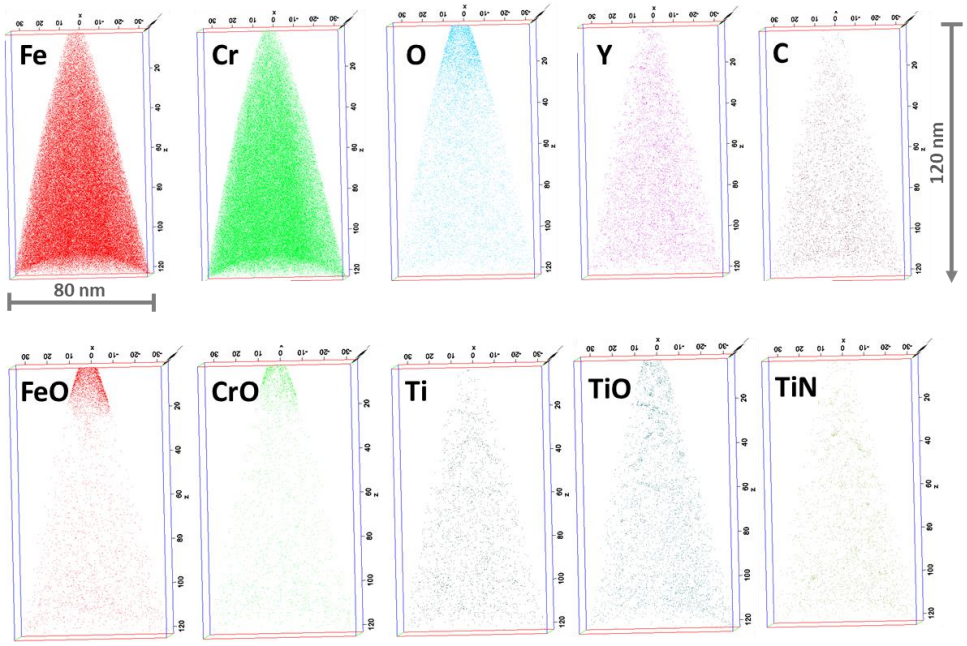

Figure 7.13 The 3-D APT reconstructed tip of the Y, Ti and O bulk sample implanted at room temperature followed by annealing at 800°C (tip R30_10307) showing the distribution of the evaporated Fe, Cr, O, Ti, Y and C elements as well as FeO, CrO, TiO and TiN molecular ions.

Annex VII: List of oxides

Based on the base matrix composition and the implanted elements, the list of possible oxide formation is given in the *Table 7.2*. The crystal structure and the lattice parameters for these possible oxide phases (obtained from Pearson Crystallographic book) are given. The crystallographic structure of any oxide formed was investigated by HRTEM and the structure verified to correspond to any of these oxides.

Oxide Phase	Crystal structure	Lattice parameter (nm)
Fe_2O_3	Cubic	a = 0.9393
Fe_3O_4	Cubic	a = 0.8396
$FeCr_2O_4$	Cubic	a = 0.8344
CrO_2	Tetragonal	a=b = 0.442 c = 0.292
Cr_2O_3	Corundum	a = b = 0.495 c = 1.358
TiO_2	Anatase Brookite - orthorhombic Rutile	a = b = 0.3785 c = 0.9514 a = 0.9185 b = 0.5447 c = 0.5145 a = b = 0.459 c = 0.296
$YCrO_3$	Orthorhombic	a = 0.552 b = 0.753 c = 0.524
Ti_2O_3	Corundum	a = 0.4991 b = 0.2879
TiO	Rock salt	a = b = c = 0.423
$Y_2Ti_2O_7$	Pyrochlore	a = b = c = 1.009
Y2TiO5	Orthorhombic	a = 1.035 b = 0.37 c = 1.125
Y_2O_3	Cubic	a = b = c = 1.06

Table 7.2 List of possible stoichiometric oxides of Fe, Cr, Ti and Y in the FeCr matrix

Annex VIII: Scientific Communications

Publications

- Thesis Manuscript in preparation, defence expected 26th September 2019

- Martin Owusu-Mensah, Stéphanie Jublot-Leclerc, Aurélie Gentils, Cédric Baumier, Joël Ribis, Vladimir A. Borodin, *In situ* TEM thermal annealing of high purity Fe10wt%Cr alloy thin foils implanted with Ti and O ions, Nuclear Instruments and Materials in Research Section B, submitted 2019.

- Martin Owusu-Mensah, Stéphanie Jublot-Leclerc, Aurélie Gentils, Joël Ribis, Ryan Schoell, Djamel Kaoumi, Vladimir A. Borodin, Study on the feasibility of synthesis of (Ti, O) nanoparticles in Fe10%Cr alloy by ion implantation, in preparation.

- Martin Owusu-Mensah, Aurélie Gentils, Stéphanie Jublot-Leclerc, Joël Ribis, Ryan Schoell, Djamel Kaoumi, Vladimir A. Borodin, Synthesis of yttrium oxide nanoparticles by ion implantation in a high purity Fe10%Cr alloy, in preparation.

- Martin Owusu-Mensah, Stéphanie Jublot-Leclerc, Aurélie Gentils*, Joël Ribis, Ryan Schoell, Djamel Kaoumi, Marion Descoins, Dominique Mangelinck, Vladimir A. Borodin, Understanding the first formation stages of (Y, Ti, O) nanoparticles in Fe10%Cr alloy by ion implantation, in preparation.

Conferences Attended

- March 2019
  The Minerals, Metals and Materials Society (TMS), 2019 Annual Meeting, San Antonio, Texas, United States of America
  Symposium: Materials Processing Fundamentals
  Contribution: Contributed oral presentation

- June 2018
  European Materials Research Society (E-MRS), Spring Meeting 2018, Strasbourg, France
  Symposium Y: New developments in the modeling and analysis of radiation damage in materials
  Contribution: Contributed oral presentation and conference assistant
  Award: Best oral presentation

- March 2018
  Microscopy of Irradiation Damage workshop, Oxford, United Kingdom
  Contribution: Poster presentation

- October 2017
  Groupe Utilisateurs de Microscopie electronique Philips-FEI (GUMP), Metz, France
  Contribution: Contributed oral presentation

- July 2017
  International conference on Radiation Effects in Insulators, REI-19, Versailles, France
  Contribution: Attendee and conference assistant

Annex IX: Résumé détaillé en français

Les aciers ferritiques-martensitiques renforcés par dispersion d'oxyde, dit ODS (Oxide Dispersion Strengthened), sont actuellement en cours de développement en tant que matériau de structure pour les réacteurs nucléaires du futur, que ce soit pour les systèmes de réacteurs nucléaires de génération IV (notamment le réacteur à neutrons rapides à caloporteur sodium SFR) ou pour les réacteurs à fusion. La spécificité de ces aciers est la distribution fine de nanoparticules d'oxydes métalliques, composées généralement de titane et yttrium, qui servent de sites de recombinaison de défauts ponctuels, de pièges à hélium ainsi que d'obstacles aux défauts mobiles, améliorant ainsi considérablement la résistance de ces aciers au fluage ainsi qu'à l'irradiation.
La fabrication conventionnelle de ces aciers implique le broyage mécanique de poudres d'alliage et d'oxydes suivi d'une consolidation à très haute température en utilisant divers procédés tels que l'extrusion à chaud (HE), la compression isostatique à chaud (HIP), ou bien plus récemment le frittage par procédé SPS (Spark Plasma Sintering). Des caractérisations détaillées de la microstructure des aciers ODS ont été réalisées dans différentes études ces vingt dernières années. Les nanoparticules sont généralement classées selon deux formes principales. Les nanoparticules typiques de Y-Ti-O, avec des tailles grandes supérieures à 10 nm, correspondent à des composés Y_2O_3, $Y_2Ti_2O_7$ et Y_2TiO_5. D'autres nanoparticules plus petites de Y-Ti-O, de taille inférieure à 10 nm, généralement de 1 à 3 nm de diamètre, ont été identifiées par tomographie à sonde atomique et sont décrites comme étant non stoechiométriques. La microstructure de ces aciers avant et après irradiation a également été abondamment rapportée dans la littérature. La nature et la composition de ces nanoparticules dépendent généralement de la composition de l'alliage et du procédé de fabrication exact.
Les étapes de formation de ces oxydes ont été rapportées par Hsuing et al. (2010) et Alinger et al. (2009). Cette formation d'oxydes peut être résumée en trois étapes principales comprenant la fragmentation de la poudre initiale d'Y_2O_3 au début de l'étape de broyage, l'agglomération et l'amorphisation des amas d'Y_2O_3 lors de l'étape de broyage, et une cristallisation des amas amorphes pour former de plus grandes nanoparticules d'oxyde avec une structure cœur/coquille pendant la consolidation à 1150°C. Plusieurs tentatives de calculs ont également été réalisées (Gopejenko 2010, Jiang 2009, Murali 2010) pour comprendre les mécanismes impliqués dans la formation des nanoparticules à l'échelle atomique. En outre, des efforts expérimentaux ont également consenti des efforts remarquables pour caractériser complètement les nanoparticules d'oxydes à différents stades de la production des aciers ODS, c'est-à-dire avant et après les traitements thermiques, afin d'obtenir des informations importantes pour comprendre les mécanismes sous-jacents (He 2014, Ribis 2017, Williams 2013). Malgré toutes ces tentatives, il n'existe pas de consensus sur le mécanisme exact de la précipitation de ces nanoparticules d'oxyde.
Cette thèse a donc pour objectif de contribuer à la compréhension des mécanismes impliqués dans la formation des nanoparticules dans les aciers ODS, en utilisant l'implantation ionique comme technique expérimentale alternative à la technique conventionnelle de broyage de poudres afin de produire des nanoparticules d'oxyde.

Cette technique expérimentale d'implantation ionique permet non seulement d'introduire de manière contrôlée les éléments nécessaires à la précipitation de nano-oxydes dans les aciers mais également de créer une quantité significative de défauts ponctuels et notamment de lacunes, de façon similaire à l'étape de broyage mécanique de la méthode conventionnelle de fabrication des aciers ODS. La technique d'implantation ionique a par ailleurs l'avantage de permettre un contrôle précis de divers paramètres tels que la nature des éléments implantés, l'énergie, la température et la fluence d'implantation, et ainsi de potentiellement isoler et identifier les mécanismes en jeu lors de la nucléation et croissance des nano-précipités.
L'implantation d'ions Y, Ti et O à relativement basse énergie, de l'ordre de quelques dizaines de keV à quelques centaines de keV selon l'ion, a ainsi été réalisée dans un alliage modèle Fe10wt%Cr de haute pureté dans le but de produire des oxydes d'Y, Ti ou Y-Ti. À cette fin, des études expérimentales ont été menées à la suite de trois séries d'expériences d'implantation ionique, réalisées principalement à température ambiante à l'aide de l'implanteur IRMA de la plateforme JANNuS-Orsay/SCALP du CSNSM à Orsay :

(i) implantation d'ions Ti et O,
(ii) implantation d'ions Y et O,
(iii) implantation d'ions Ti, Y et O.

Pour toutes les implantations ioniques conduites à la température ambiante, la microscopie électronique en transmission (MET) n'a révélé la présence d'aucun nanoprécipité directement après implantation ionique. Une étape de recuit thermique a donc été nécessaire pour favoriser la nucléation/croissance des nano-oxydes. Les échantillons implantés ont été recuits à des températures allant de 600°C à 1100°C pour les cas d'implantation ionique double (c'est-à-dire pour les implantations d'ions Ti et O, ainsi que d'ions Y et O). Le recuit d'échantillons implantés avec des ions Ti, Y et O n'a été effectué qu'à 800°C. Chaque recuit a été effectué sous vide pendant une durée de 2 heures. La microstructure et les nanoparticules résultantes ont été caractérisées à l'aide d'une combinaison de techniques de microscopie électronique en transmission, en mode conventionnel et haute résolution, ainsi que des méthodes d'analyse telles que l'imagerie filtrée en énergie (EFTEM) et l'imagerie élémentaire par détection de rayons X en mode ChemiSTEM.
En premier lieu, les ions Ti et O ont été implantés dans des lames minces de microscopie électronique en transmission à la température ambiante. Le recuit *in situ* à 500°C dans le microscope de ces lames minces implantées a induit la formation de nanoprécipités d'une taille moyenne d'environ 5 nm. L'analyse par EFTEM de ces précipités a montré qu'ils contiennent du Cr et de l'O. La diffraction électronique ainsi qu'une analyse quantitative en EELS ont permis d'identifier clairement un spinelle mixte d'oxyde de fer et de chrome. L'objectif attendu étant de faire précipiter des oxydes de Ti, un autre recuit *in situ* a été effectué à une température de 600°C. Des nanoprécipités de taille similaire aux précipités observés à 500°C ainsi que des plaques d'oxyde beaucoup plus grandes ont été observés. Ces plaques d'oxydes se forment préférentiellement sur les bords très minces de l'échantillon et se développent au cours

du recuit pour couvrir des zones de plus en plus épaisses, ce qui montre qu'il s'agit d'un phénomène de surface. Les analyses par EFTEM et par diffraction permettent de conclure que les nanoprécipités ainsi que les plaques sont des oxydes de Fe et Cr de structure spinelle qui croissent à la surface des lames minces de microscopie implantées aux ions et recuites. Il a en effet été rapporté que de tels oxydes faisaient partie de la couche d'oxyde de surface dans la plupart des aciers FeCr. L'oxygène nécessaire à la formation de cette couche d'oxyde provient possiblement de la colonne du TEM après pompage pendant le recuit, ainsi que très probablement de l'air qui contribue à l'oxydation du matériau immédiatement après la dernière étape de préparation de l'échantillon par polissage électrolytique. Des expériences ToF-SIMS ont montré la diffusion du Ti à partir d'une température d'environ 800°C. Par conséquent, un recuit des lames minces implantées aux ions Ti et O a été effectué à 800°C. De nouveau, comme dans la condition de recuit précédente à 600°C, des nano-précipités de taille comprise entre 5 et 10 nm ainsi que des grandes plaques de l'ordre de plusieurs centaines de nanomètres ont été observés. A cette température, l'oxyde formé en surface est toujours identifié comme étant un oxyde de Fe et Cr de structure spinelle mais il est cette fois-ci clairement enrichi en Ti, en accord avec l'observation de la diffusion du Ti à 800°C par ToF-SIMS.

La formation de ces oxydes de structure spinelle à la surface des lames minces de microscopie empêche l'observation de nanoparticules potentiellement formées sous la surface. Par conséquent, les expériences de recuit *in situ* effectuées sur des lames minces ont été abandonnées au profit d'expériences sur des échantillons en section transverses prélevées par FIB sur des échantillons massifs après implantation ionique et recuit thermique.

Pour la première série d'expériences sur des échantillons massifs implantés aux ions Ti et O, des nanoparticules de taille moyenne d'environ 6 nm ont été observées après recuit à 600°C. Celles-ci ont été identifiées par microscopie haute résolution et EFTEM comme étant des oxydes de chrome de structure cristalline corindon du type Cr_2O_3. Des relations d'orientation entre les nanoparticules de Cr_2O_3 et la matrice ont été déduites des caractérisations par microscopie à haute résolution, ce qui suggère une cohérence au moins partielle des nanoprécipités. Après recuit à 800°C et en accord avec les expériences précédentes sur les lames minces recuites *in situ*, les nanoparticules observées sont des nanoparticules de Cr_2O_3 enrichies en Ti et de taille moyenne d'environ 11 nm. Les atomes de Ti diffusants à 800°C semblent ainsi être capturés par les nanoparticules de Cr_2O_3 synthétisées au préalable pour former ces nanoparticules de Cr_2O_3 enrichies en Ti. Un recuit à une température de 1000°C induit également la formation de nanoparticules d'oxyde de chrome enrichies en Ti avec la structure cristalline du Cr_2O_3 sans variation notable de taille par rapport aux nanoparticules observées après recuit à 800°C. Des relations d'orientation ont à nouveau été identifiées entre les nanoparticules et la matrice pour les conditions de recuit de 800 et 1000°C. Un recuit final a été effectué à une température de 1100°C, cette température correspondant à la température du traitement thermique final des aciers ODS classiques. A cette température de recuit, deux types de nanoparticules sont observés. Le premier type de particules est similaire à l'oxyde de Cr enrichi en Ti avec la

structure cristalline du corindon Cr_2O_3. En plus de ces particules, des particules plus larges d'oxyde de Ti ayant une coquille irrégulière enrichie en Cr sont également visibles de façon évidente sur les cartographies élémentaires acquises en ChemiSTEM. La structure cristallographique de ces nanoparticules est non identifiée : celles-ci ne correspondent pas à des particules de type Cr_2O_3 ni à aucun autre type d'oxyde métallique connu et probable. Il semblerait que ces particules d'oxyde de Ti soient formées à partir des particules de Cr_2O_3 enrichies en Ti. Le Ti pourrait ainsi être collecté à la surface des particules de Cr_2O_3 avant d'en pénétrer le cœur et avant l'expulsion du Cr à la surface de la particule sous forme de coquille. Ainsi, contrairement à la perception commune selon laquelle le Cr ne joue aucun rôle dans la formation des nanoparticules dans les aciers ODS, le Cr est susceptible de jouer un rôle essentiel dans la formation de nanoparticules au sein d'alliages exempts d'Y. La figure 1 schématise les étapes de formation des nanoparticules d'oxyde observées dans cette étude dans les échantillons de Fe10Cr implantés avec des ions Ti et O après un recuit thermique subséquent.

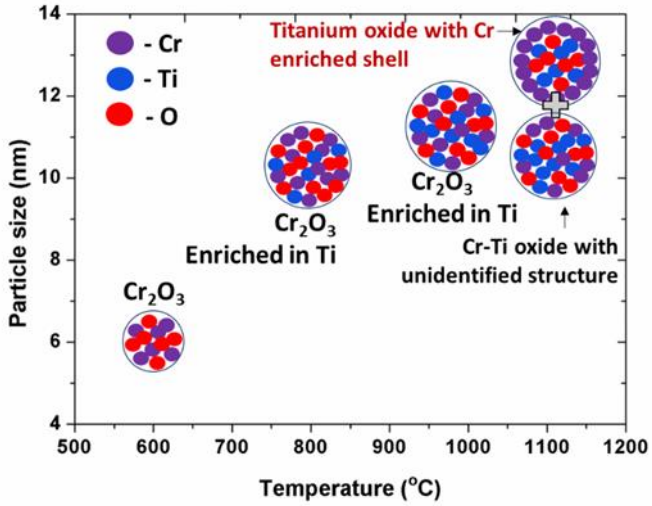

Figure 1 - Étapes de la formation de nanoparticules d'oxyde dans des échantillons de Fe10Cr implantés avec des ions Ti et O après un recuit thermique subséquent à la température indiquée.

Pour la deuxième série d'expériences effectuée sur des échantillons massifs implantés aux ions Y et O, des nanoparticules d'une taille d'environ 2 à 3 nm ont été observées après recuit à 800°C. La taille de ces nanoparticules ne permet ni la détermination de la composition élémentaire ni la détermination de la structure cristallographique par les différentes techniques de microscopie électronique en transmission disponibles. Cependant, les différences de forme et de taille entre ces nanoparticules et celles observées après recuit d'échantillons implantés aux ions Ti et O à température similaire suggèrent qu'un oxyde de Cr pur est exclu dans ce cas. Des nanoparticules d'oxyde d'Y ou Y-Cr sont par conséquent très probables. Dans le cas de l'implantation d'ions Ti et O, le Cr_2O_3 est déjà formé après recuit à 600°C. On peut donc supposer qu'un précurseur de ces nanoparticules d'oxyde d'Y ou Y-Cr est déjà créé à des températures inférieures à 600°C. Un recuit à une température de 1100°C induit la formation de nanoparticules beaucoup plus grosses, de taille moyenne d'environ 5 nm. Les études

réalisées par ToF-SIMS indiquent que l'Y ne diffuse pas à longue distance à 800°C mais diffuse de manière significative à une température supérieure à 1000°C, ce qui pourrait faciliter la nucléation et la croissance des nanoparticules. Deux structures cristallographiques sont observées pour ces nanoparticules : la structure cristalline *bcc* de l'Y_2O_3 et la structure cristalline *fcc* de l'Y_2O_3. Les analyses en ChemiSTEM montrent que ces particules présentent une structure coeur/coquille avec un noyau enrichi en Y et probablement en Cr et O, tandis que la coquille est composée principalement de Cr. La taille, la structure ainsi que la composition des particules sont directement comparables à celles des particules d'oxyde formées lors de la fabrication classique d'aciers ODS. Ici, contrairement aux échantillons implantés aux ions Ti et O où la formation des nanoparticules d'oxydes est dictée par le Cr, la présence d'Y supprime la formation d'oxydes de Cr purs. L'Y joue donc le rôle le plus important dans la précipitation et limite le rôle du Cr dans la formation d'oxyde, même si la présence de Cr dans le noyau ne peut pas être totalement exclue. Des ions Y et O ont également été implantés dans des échantillons de FeCr de haute pureté à une température de 500°C. Des nanoparticules sont observées directement après implantation à chaud. Elles possèdent une taille moyenne d'environ 6 nm et ont la structure cristalline *fcc* de l'Y_2O_3. Alors que l'implantation à température ambiante d'ions Y et O nécessite un recuit à une température de 1100°C pour former des particules d'oxyde d'yttrium Y_2O_3, des particules de taille similaire peuvent donc déjà être observées après l'implantation d'ions Y et O à 500°C. L'implantation d'ions à température élevée favorise donc considérablement la nucléation et la croissance des nanoparticules d'oxyde d'yttrium ce qui indique son action favorable sur la mobilité de l'yttrium. La figure 2 schématise les étapes de formation des nanoparticules d'oxyde observées dans cette étude dans les échantillons de Fe10Cr implantés avec des ions Y et O après un recuit thermique subséquent.

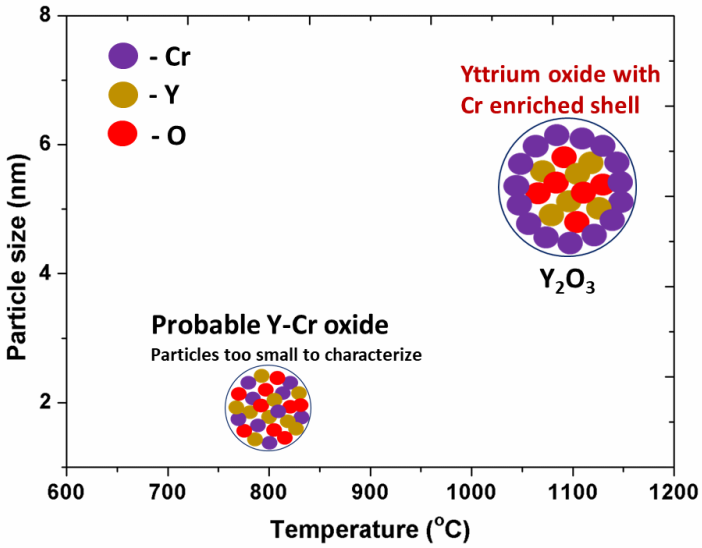

Figure 2 - Étapes de la formation de nanoparticules d'oxyde dans des échantillons de Fe10Cr implantés avec des ions Y et O après un recuit thermique subséquent à la température indiquée.

La dernière série d'expériences concerne l'implantation d'ions Ti, Y et O. Dans ce cas,

les implantations ioniques ont été réalisées dans deux ordres séquentiels différents : (i) une implantation d'ions Y suivie par une implantation d'ions Ti puis O (Y -> Ti -> O), et (ii) une première implantation d'ions Ti suivie d'une implantation d'ions Y puis O (Ti -> Y -> O). Pour les deux schémas d'implantation, aucune nanoparticule n'est visible par microscopie électronique en transmission directement après l'implantation. Des échantillons massifs implantés dans ces deux ordres séquentiels ont ensuite été recuits à 800°C. L'expérience d'implantation Y -> Ti -> O a conduit à la formation de très petites nanoparticules d'une taille de 2 à 3 nm dont la structure cristallographique n'a pas pu être identifiée par microscopie haute résolution. Elles ont cependant été identifiées comme étant des particules d'oxyde d'Y-Ti en utilisant le ChemiSTEM et la sonde atomique tomographique. L'expérience d'implantation Ti -> Y-> O a quant à elle conduit à la formation de nanoparticules de tailles allant de 5 à 20 nm. Ces nanoparticules ont été identifiées comme étant des particules d'oxyde de chrome ayant la structure hexagonale du corindon de type Cr_2O_3 similaire aux échantillons implantés avec des ions Ti et O. La figure 3 résume ces résultats dans le cas de l'implantation Ti->Y->O (partie supérieure) et Y->Ti->O (partie inférieure) en montrant notamment des images en champ clair de microscopie électronique en transmission sur lesquelles les nanoprécipités sont visibles en sous- et sur-focus. L'ordre d'implantation est donc de manière évidente crucial pour la détermination de la structure et de la composition de l'oxyde qui précipite et croît lors du recuit thermique ultérieur. Ces résultats suggèrent donc que des précurseurs à l'origine de la formation des nanoparticules d'oxydes dans les deux conditions sont déjà créés lors de l'implantation à température ambiante. Cela implique probablement que les éléments métalliques implantés se lient différemment aux défauts induits par l'implantation en fonction de l'ordre dans la séquence d'implantation, ce qui affecterait leur diffusivité et réactivité dans les processus de nucléation et croissance des nanoparticules lors du recuit ultérieur.

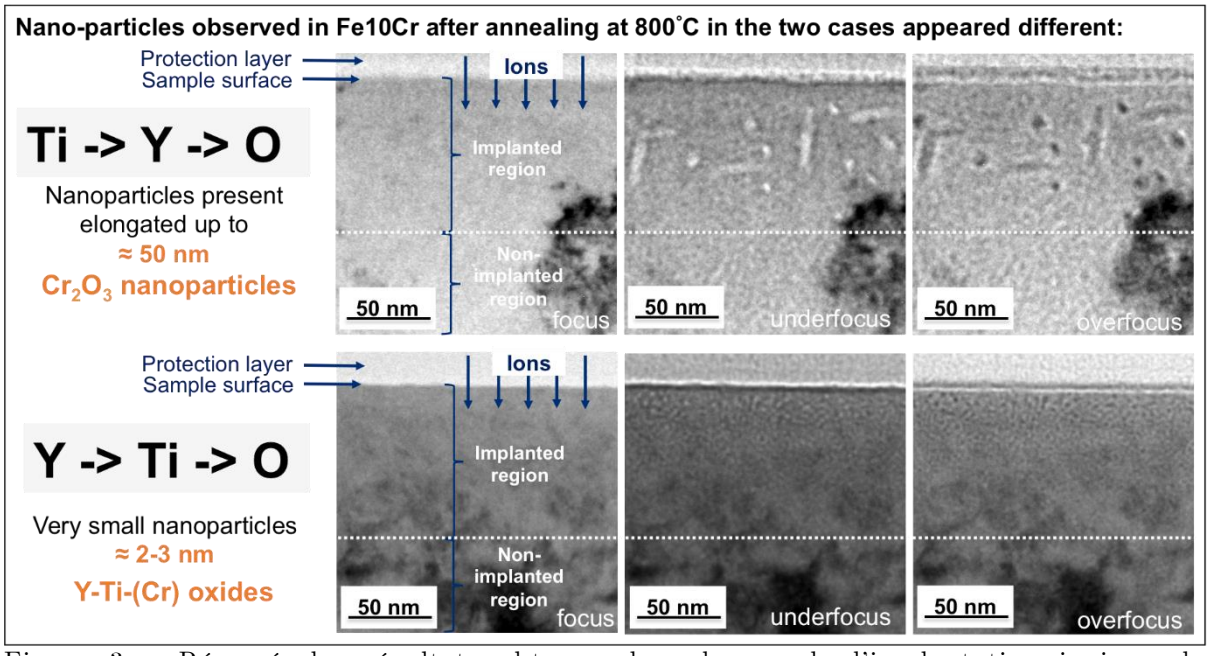

Figure 3 – Résumé des résultats obtenus dans le cas de l'implantation ionique de Ti->Y->O (partie supérieure de la figure) et Y->Ti->O (partie inférieure) dans un alliage

de Fe10Cr, qui montre la présence de nanoprécipités visibles sur des images de microscopie électronique en transmission en champ clair en sous- et sur-focus.

Dans cette étude, la formation d'oxydes de Ti, Y et d'oxydes mixtes d'Y-Ti a donc été réalisée par implantation ionique et recuit thermique subséquent, avec, dans certains cas, des caractéristiques de nanoparticules proches de celles rapportées dans la littérature sur les aciers ODS fabriqués de façon conventionnelle. Ceci confirme que la technique d'implantation ionique ou synthèse par faisceaux d'ions est une technique de choix pour étudier les mécanismes responsables de la nucléation et croissance de nanoparticules d'oxydes dans les aciers ODS. Une caractérisation détaillée des nanoparticules observées a été présentée pour les trois séries d'investigations expérimentales. La formation d'oxydes de Ti purs semble être supprimée aux températures de recuit inférieures à 1000°C dans les échantillons implantés avec des ions Ti et O, au profit de la formation de particules d'oxyde de Cr de structure corindon Cr_2O_3. Le Cr apparaît dont avoir un rôle essentiel dans la formation de nanoparticules d'oxydes en l'absence d'Y. Cette formation d'oxyde de Cr_2O_3 est supprimée dans les échantillons implantés aux ions Y et O, où Y peut interagir avec l'oxygène et les lacunes au stade de l'implantation ionique pour former des précurseurs de la formation d'oxyde d'Y lors du recuit ultérieur. Les différentes particules d'oxyde formées lors des deux séries d'implantations triple séquentielles d'ions Y, Ti et O renforcent l'hypothèse que des précurseurs se sont déjà formés au cours de la phase d'implantation à température ambiante. Il est donc concevable que des précurseurs des nanoparticules formées lors de la fabrication des aciers ODS classiques soient formés pendant la phase de broyage mécanique de poudres. L'observation de la formation d'agrégats d'Y après implantation à la température ambiante serait idéale pour confirmer cette hypothèse. Un résumé des caractéristiques des nanoparticules observées dans les échantillons implantés et recuits pour les différentes conditions expérimentales est présenté dans le tableau suivant.

Condition d'implantation	Recuit de 2 heures (°C)	Taille moyenne des particules (nm)	Composition chimique	Structure cristallographique
Implantation Ti + O à RT	600	≈ 6	Cr, O	Corindon Cr_2O_3
	800	≈ 11	Cr, Ti, O	Corindon Cr_2O_3
	1000	≈ 12	Cr, Ti, O	Corindon Cr_2O_3
	1100	≈ 10	Particule 1: Cr, Ti, O Particule 2: Ti, O noyau enrichi Coquille enrichie en Cr	Particule 1: Corindon Cr_2O_3 Particule 2: Structure non identifiée
Implantation Y + O à RT	800	≈ 2-3	Enrichissement probable en Y, O, (Cr)	Structure non identifiable
	1100	≈ 5	Noyau enrichi en Y, O Coquille enrichie en Cr	Particule 1: *bcc* Y_2O_3 Particule 2: *fcc* Y_2O_3
Implantation Y + O à 500°C		≈ 6	Noyau enrichi en Y, Cr, O Coquille enrichie en Cr	*fcc* Y_2O_3
Implantation Ti + Y + O à RT	800	≈ 5-20	Cr, O	Corindon Cr_2O_3
Implantation Y + Ti + O à RT	800	≈ 2-3	Y, Ti, O (Cr)	Structure non identifiable

Résumé des caractéristiques des nanoparticules obtenues dans des échantillons implantés et recuits pour les trois séries d'expériences d'implantation ionique.

Les recherches menées dans le cadre de cette thèse contribuent à la compréhension de la formation des nanoparticules d'oxyde dans des alliages modèles FeCr avec pour but d'améliorer la fabrication des aciers ODS. Il reste cependant quelques questions pour lesquelles des recherches futures pourraient apporter des éclaircissements. Il y a

d'abord des études complémentaires aux trois séries d'expériences d'implantation réalisées, ce qui pourrait aider à répondre aux questions relatives à certaines conditions, comme par exemple des recuits thermiques à plus haute température (1300°C) afin d'observer la présence ou l'absence de coquille de chrome, ou l'utilisation de traitements thermiques rapides (RTA, de façon à atteindre la température souhaitée en un court laps de temps, entrainant une compétition entre la diffusion de Ti et Cr). Outre ces investigations complémentaires, il pourrait être important d'étudier d'autres perspectives, en couplant par exemple ces expériences avec des modélisations et simulations numériques, en caractérisant expérimentalement la présence de lacunes et amas de lacunes-solutés, ou en implantant simultanément les éléments métalliques Y et Ti.

8. References

[Abram 2008] Abram, T. & Ion, S. Generation-IV nuclear power : A review of the state of the science. *Energy Policy* 36, 4323–4330 (2008).

[Ahn 2006] Ahn, C. C. Transmission Electron Energy Loss Spectroscopy in Materials Science and the EELS Atlas. *John Wiley & Sons*. (2006).

[Airiskallio 2010] Airiskallio, E. *et al.* High temperature oxidation of Fe–Al and Fe–Cr–Al alloys : The role of Cr as a chemically active element. *Corrosion Science* 52, 3394–3404 (2010).

[Alinger 2004] Alinger, M. J., Odette, G. R. & Hoelzer, D. T. The development and stability of Y–Ti–O nanoclusters in mechanically alloyed Fe–Cr based ferritic alloys. *Journal of Nuclear Materials* 333, 382–386 (2004).

[Alinger 2009] Alinger, M. J., Odette, G. R. & Hoelzer, D. T. On the role of alloy composition and processing parameters in nanocluster formation and dispersion strengthening in nanostuctured ferritic alloys. *Acta Materialia* 57, 392–406 (2009).

[ammrf, website] Australian microscopy & Microanalysis Research facility. Available at: *http://www.ammrf.org.au/myscope/analysis/eds.*

[Asteman 2008] Asteman, H. & Spiegel, M. A comparison of the oxidation behaviours of Al_2O_3 formers and Cr_2O_3 formers at 700°C – Oxide solid solutions acting as a template for nucleation. *Corrosion Science* 50, 1734–1743 (2008).

[Auger 2011] Auger, M. A. *et al.* Microstructure and mechanical properties of ultrafine-grained Fe–14Cr and ODS Fe–14Cr model alloys. *Journal of Nuclear Materials* 417, 213–216 (2011).

[Barnard 2012] Barnard, L., Odette, G. R., Szlufarska, I. & Morgan, D. An ab initio study of Ti–Y–O nanocluster energetics in nanostructured ferritic alloys. *Acta Materialia* 60, 935–947 (2012).

[Barnard 2015] Barnard, L., Cunningham, N., Odette, G. R., Szlufarska, I. & Morgan, D. Thermodynamic and kinetic modeling of oxide precipitation in nanostructured ferritic alloys. *Acta Materialia* 91, 340–354 (2015).

[Behr 1999] Behr, R., Mayer, J. & Arzt, E. TEM investigations of the superdislocations and their interaction with particles in dispersion strengthened intermetallics. *Intermetallics* 7, 423-436 (1999).

[Benninghoven 1973] Benninghoven, A. Surface investigation of Solids by the Statical Method of Secondary Ion Mass Spectroscopy. *Surface Science* 35, 427-457, (1973).

[Bhattacharyya 2012] Bhattacharyya, D., Dickerson, P., Odette, G. R., Maloy, S. A. & Misra, A. On the structure and chemistry of complex oxide nanofeatures in nanostructured ferritic alloy U14YWT. *Philosophical Magazine* 92, 2089-2107(2012).

[Bhattacharya 2016] Bhattacharya, A. Ion Irradiation effects on high purity bcc Fe and model FeCr alloys *Phd Thesis* Université Paris-Sud, France. (2016).

[Bischoff 2012a] Bischoff, J. & Motta, A. T. Oxidation behavior of ferritic–martensitic and ODS steels in supercritical water. *Journal of Nuclear Materials* 424, 261–276 (2012).

[Bischoff 2012b] Bischoff, J. & Motta, A. T. EFTEM and EELS analysis of the oxide layer formed on HCM12A exposed to SCW. *Journal of Nuclear Materials* 430, 171–180 (2012).

[Bocquet 2017] Bocquet, J., Barouh, C. & Fu, C. Migration mechanism for oversized solutes in cubic lattices : The case of yttrium in iron. *Physical Review B* 95, 214108(1)–(1)1 (2017).

[Boulnat 2015] Boulnat, X. *et al.* Acta Materialia Influence of oxide volume fraction on abnormal growth of nanostructured ferritic steels during non-isothermal treatments : An in situ study.

Acta Materialia 97, 124–130 (2015).

[Boulnat 2016] Boulnat, X., Perez, M., Cazottes, S. & Carlan, Y. De. Characterization and modeling of oxides precipitation in ferritic steels during fast non-isothermal consolidation. *Acta Materialia* 107, 390–403 (2016).

[BP Review 2017] BP Statistical Review of World Energy June 2017. (2017).

[Brandes 2012] Brandes, M. C., Kovarik, L., Miller, M. K. & Mills, M. J. Morphology, structure, and chemistry of nanoclusters in a mechanically alloyed nanostructured ferritic steel. *Journal of Material Science* 47, 3913–3923 (2012).

[Braun 1985] Braun, R. & Feller-Kniepmeier, M. Diffusion of Chromium in α-Iron. *Physica Status Solidi* 90, 553-561(1985).

[Bremaecker 2012] Bremaecker, A. De. Past research and fabrication conducted at SCK CEN on ferritic ODS alloys used as cladding for FBR's fuel pins. *Journal of Nuclear Materials* 428, 13–30 (2012).

[Brocq 2010] Brocq, M., Radiguet, B., Breton, Le J. M., Cuvilly, F., Pareige, P. & Legendre, F. Nanoscale characterisation and clustering mechanism in an Fe–Y_2O_3 model ODS alloy processed by reactive ball milling and annealing. *Acta Materialia* 58, 1806–1814 (2010).

[Brocq 2011] Brocq, M., Radiguet, B., Poissonnet, S., Cuvilly, F., Pareige, P. & Legendre, F. Nanoscale characterization and formation mechanism of nanoclusters in an ODS steel elaborated by reactive-inspired ball-milling and annealing. *Journal of Nuclear Materials* 409, 80–85 (2011).

[Brodrick 2014] Brodrick, J., Hepburn, D. J. & Ackland, G. J. Mechanism for radiation damage resistance in yttrium oxide dispersion strengthened steels. *Journal of Nuclear Materials* 445, 291–297 (2014).

[Capdevila 2010] Capdevila, C., Miller, M. K., Toda, I. & Chao, J. Influence of the α–α' phase separation on the tensile properties of Fe-base ODS PM 2000 alloy. *Materials Science and Engineering A* 527, 7931–7938 (2010).

[Carlan 2009] Carlan, Y. De *et al.* CEA developments of new ferritic ODS alloys for nuclear applications. *Journal of Nuclear Materials* 386–388, 430–432 (2009).

[Castro 2009] Castro, V. De *et al.* Microstructural characterization of Y_2O_3 ODS–Fe– Cr model alloys. *Journal of Nuclear Materials* 386–388, 449–452 (2009).

[Castro 2011] Castro, V. De, Marquis, E. A., Lozano-perez, S., Pareja, R. & Jenkins, M. L. Stability of nanoscale secondary phases in an oxide dispersion strengthened Fe–12Cr alloy. *Acta Materialia* 59, 3927–3936 (2011).

[Cayron 2010] Cayron, C., Montani, A., Venet, D. & Carlan, Y. De. Identification of new phases in annealed Fe –18CrWTi ODS powders. *Journal of Nuclear Materials* 399, 219–224 (2010).

[Chao 1998] Chao J., On some scale related aspects influencing the fracture behaviour at room temperature of preoxidized MA956 alloy. *Material Science and Engineering A* 242, 248-258 (1998).

[ChemiSTEM 2010] ChemiSTEM^{TM}: Technology A revolution in EDX analytics. (2010).

[Chen 2007] Chen, Y., Sridharan, K., Ukai, S. & Allen, T. R. Oxidation of 9Cr oxide dispersion strengthened steel exposed in supercritical water. *Journal of Nuclear Materials* 371, 118–128 (2007).

[Chen 2015] Chen, D., Kimura, A., Han, W. & Je, H. Age-hardening susceptibility of high-Cr ODS ferritic steels and SUS430 ferritic steel. *Fusion Engineering and Design* 98–99, 1945–1949 (2015).

[Cheon 2009] Cheon, J., S., Lee, C., B., Lee, B., O., Raison, J., P., Mizuno, T., Delage, F. & Carmack, J. Sodium fast reactor evaluation : Core materials. *Journal of Nuclear Materials* 392, 324–330 (2009).

[Cho 2007] Cho, H. S. & Kimura, A. Corrosion resistance of high-Cr oxide dispersion strengthened ferritic steels in super-critical pressurized water. *Journal of Nuclear Materials* 370, 1180–1184 (2007).

[Claisse 2013] Claisse, A. & Olsson, P. Nuclear Instruments and Methods in Physics Research B First-

principles calculations of (Y, Ti, O) cluster formation in body centred cubic. *Nuclear Instruments and Methods in Physics Research, B* 303, 18–22 (2013).

[CSNSM, website] CSNSM. Available at: *https://csnsm.in2p3.fr/Equipments.*

[Cunningham 2016] Cunningham, N. J., Alinger, M. J., Klingensmith, D., Wu, Y. & Odette, G. R. On nano-oxide coarsening kinetics in the nanostructured ferritic alloy MA957 : A mechanism based predictive model. *Material Science and Engineering A* 655, 355–362 (2016).

[Dade 2017] Dade, M., Malaplate, J., Garnier, J., Barcelo, F., Widen t, P. & Deschamps, A. In fl uence of microstructural parameters on the mechanical properties of oxide dispersion strengthened Fe-14Cr steels. *Acta Materialia* 127, (2017).

[Dai 2012] Dai, L., Liu, Y. & Dong, Z. Size and structure evolution of yttria in ODS ferritic alloy powder during mechanical milling and subsequent annealing. *Powder Technology* 217, 281–287 (2012).

[Dapeng 2011] Dapeng, Z., Yong, L., Feng, L., Yuren, W, Liujie, Z. & Yuhai, D. ODS ferritic steel engineered with bimodal grain size for high strength and ductility. *Materials Letters* 65, 1672–1674 (2011).

[Dawson 2014] Dawson, K. & Tatlock, G. J. Characterisation of nanosized oxides in ODM401 oxide dispersion strengthened steel. *Journal of Nuclear Materials* 444, 252–260 (2014).

[Deschamps 2016] Deschamps, A., Geuser, F. De, Malaplate, J. & Sornin, D. When do oxide precipitates form during consolidation of oxide dispersion strengthened steels? *Journal of Nuclear Materials* 482, 83–87 (2016).

[Dou 2011] Dou, P. *et al.* Effects of extrusion temperature on the nano-mesoscopic structure and mechanical properties of an Al-alloyed high-Cr ODS ferritic steel. *Journal of Nuclear Materials* 417, 166–170 (2011).

[Dou 2014] Dou, P. *et al.* TEM and HRTEM study of oxide particles in an Al-alloyed high-Cr oxide dispersion strengthened steel with Zr addition. *Journal of Nuclear Materials* 444, 441–453 (2014).

[Dou 2017] Dou, P., *et al.* TEM and HRTEM study of oxide particles in an Al-alloyed high-Cr oxide dispersion strengthened ferritic steel with Hf addition. *Journal of Nuclear Materials* 485, 189–201 (2017).

[Egerton 2009] Egerton, R. Electron energy-loss spectroscopy in the TEM. *Reports on Progresses in Physics* 72, 16501(1)-(25) (2014).

[Fischer 1978] Fischer, J. J. Dispersion Strebgthened Ferritic Alloy For Use In Liquid-Metal Fast Breeder Reactors (LMFBRS). *United States Patent* (1976).

[Fu 2007] Fu, C. L, Krcmar, M., Painter, G. S. & Chen, X. Vacancy Mechanism of High Oxygen Solubility and Nucleation of Stable Oxygen-Enriched Clusters in Fe. *Physical Review Letters* 99, 225502(1)–(4) (2008).

[Gale 2004] Gale, W. F. & Totemeir, T. C. Smithells Metals Reference Book. *Elsevier Butterworth-Heinemann* (2004).

[Gen IV Roadmap 2002] A Technology Roadmap for Generation IV Nuclear Energy Systems *U.S. DOE* (2002).

[Giancarli 2006] Giancarli, L. *et al.* Breeding Blanket Modules testing in ITER: An international program on the way to DEMO. 81, 393–405 (2006).

[Goldberg 2011] Goldberg, S. M. & Rosner, R. Nuclear Reactors : Generation to Generation. *American Academy of Arts and Science* (2011).

[Goldston 2002] Goldston, R. *et al.* A Plan for the Development of Fusion Energy. *Journal of Fusion Energy* 21, 61-111 (2003).

[Goo 2007] Goo, N. H. Formation of hard magnetic L1 0 -FePt / FePd monolayers from elemental multilayers. *Thesis* Max-Planck-Institut fur Metallforschung, Germany. (2007).

[Gopejenko 2010] Gopejenko, A., Zhukovskii, Y. F., Vladimirov, P. V, Kotomin, E. A. & Möslang, A. Ab initio simulation of yttrium oxide nanocluster formation on fcc Fe lattice. *Journal of Nuclear Materials* 406, 345–350 (2010).

[Gopejenko 2011] Gopejenko, A., Zhukovskii, Y. F., Vladimirov, P. V, Kotomin, E. A. & Möslang, A. Modeling of yttrium , oxygen atoms and vacancies in γ-iron lattice. *Journal of Nuclear Materials* 416, 40–44 (2011).

[Gopejenko 2018] Gopejenko, A., Mastrikov, Yu, A., Zhukovskii, Yu, F., Kotomin, E., A. & Vladimirov, P., V. Ab initio modelling of the Y, O, and Ti solute interaction in fcc -Fe matrix. *Nuclear Inst. and Methods in Physics Research, B* 433, 106–110 (2018).

[Hatzoglou 2018] Hatzoglou, C., Radiguet, B., Vurpillot, F. & Pareige, P. A chemical composition correction model for nanoclusters observed by APT - Application to ODS steel nanoparticles. *Journal of Nuclear Materials* 505, 240–248 (2018).

[He 2012] He, P., Klimenkov, M., Lindau, R. & Möslang, A. Characterization of precipitates in nano structured 14 % Cr ODS alloys for fusion application. *Journal of Nuclear Materials* 428, 131–138 (2012).

[He 2014a] He, C. W., Barthe, M. F., Desgardin, P., Akhmadaliev, S., Behar, M. & Jomard, F. Positron studies of interaction between yttrium atoms and vacancies in bcc iron with relevance for ODS nanoparticles formation. *Journal of Nuclear Materials* 455, 398–401 (2014).

[He 2014b] He, J., Wan, F., Sridharan, K., Allen, T. R., Certain, A. & Shutthanandan, V. Stability of nanoclusters in 14YWT oxide dispersion strengthened steel under heavy ion-irradiation by atom probe tomography. *Journal of Nuclear Materials* 455, 41–45 (2014).

[Heintze 2012] Heintze, C., Hernandez-Mayoral, M., Ulbricht, A., Bergner, F., Shariq, A., Weissgarber, T. & Frielinghaus, H. Nanoscale characterization of ODS Fe–9%Cr model alloys compacted by spark plasma sintering. *Journal of Nuclear Materials* 428, 139–146 (2012).

[Heintze 2016] Heintze, C., Bergner, F., Hernandez-Mayoral, M., Kogler, R., Muller, G. & Ulbricht, A. Irradiation hardening of Fe e 9Cr-based alloys and ODS Eurofer : Effect of helium implantation and iron-ion irradiation at 300 C including sequence effects. *Journal of Nuclear Materials* 470, 258–267 (2016).

[Hetherington 2004] Hetherington, C. Aberration correction for TEM. *Materials Today* 7, 50–55 (2004).

[Hilger 2016] Hilger, I. *et al.* Fabrication and characterization of oxide dispersion strengthened (ODS) 14Cr steels consolidated by means of hot isostatic pressing , hot extrusion and spark plasma sintering. *Journal of Nuclear Materials* 472, 206–214 (2016).

[Hin 2009] Hin, C., Wirth, B. D. & Neaton, J. B. Formation of Y_2O_3 nanoclusters in nanostructured ferritic alloys during isothermal and anisothermal heat treatment: A kinetic Monte Carlo study. *Physical Review B* 80, 134118(1)–(11) (2009).

[Hin 2010] Hin, C. & Wirth, B. D. Formation of Y_2O_3 nanoclusters in nano-structured ferritic alloys: Modeling of precipitation kinetics and yield strength. *Journal of Nuclear Materials* 402, 30–37 (2010).

[Hin 2011] Hin, C. & Wirth, B. D. Formation of oxide nanoclusters in nanostructured ferritic alloys during anisothermal heat treatment : A kinetic Monte Carlo study. *Materials Science & Engineering A* 528, 2056–2061 (2011).

[Hirata 2011] Hirata, A. *et al.* Atomic structure of nanoclusters in oxide-dispersion-strengthened dteels. *Journal of Nuclear Materials* 10, 922–926 (2011).

[Hirata 2012] Hirata, A., Fujita, T., Liu, C. T. & Chen, M. W. Characterization of oxide nanoprecipitates in an oxide dispersion strengthened 14YWT steel using aberration-corrected STEM. *Acta Materialia*

60, 5686–5696 (2012).

[Hoelzer 2000] Hoelzer, D. T., Pint, B. A. & Wright, I. G. A microstructural study of the oxide scale formation on ODS Fe-13Cr steel. *Journal of Nuclear Materials* 287, 1306–1310 (2008).

[Hoelzer 2007] Hoelzer, D. T., Odette, G. R. & Alinger, M. J. Influence of particle dispersions on the high-temperature strength of ferritic alloys. *Journal of Nuclear Materials* 370, 166–172 (2007).

[Hoelzer 2016] Hoelzer, D. T., Unocic, K. A., Sokolov, M. A. & Byun, T. S. In fl uence of processing on the microstructure and mechanical properties of 14YWT*. *Journal of Nuclear Materials* 471, 251-265 (2016).

[Hofer 1995] Hofer, F., Warbichler, P., Grogger, W. & Lang, O. On the application of enerfy filtering TEM in material science: I. Precipitates in a Ni/Cr-alloy. *Micron* 26, 377-390 (1995).

[Hofmann 2014] Hofmann, J. P. Recent advances in secondary ion mass spectrometry of solid acid catalysts: large zeolite crystals under bombardment†. *Physical Chemistry Chemical Physics* 16, 5465–5474 (2014).

[Holtkamp 2009] Holtkamp, N. The status of the ITER design. *Fusion Engineering and Design* 84, 98–105 (2009).

[Hsiung 2010] Hsiung, L. L. *et al.* Formation mechanism and the role of nanoparticles in Fe-Cr ODS steels developed for radiation tolerance. *Physical Review B* 82, 184103(1)–(13) (2010).

[Hu 2013] Hu, H. L., Zhou, Z. J., Liao, L., Zhang, L. F., Wang, M., Li, S. F. & Ge, C. C. Corrosion behavior of a 14Cr-ODS steel in supercritical water. *Journal of Nuclear Materials* 437, 196–200 (2013).

[Inkson 1996] Inkson, B. J. & Threadgill, P. L. Y_2O_3 Morphology in an Oxide Dispersion Strengthened FeAl Alloy Prepared by Mechanical Alloying. *Materials Research Society Proceedings* 460, 767 (1996).

[Inoue 2007] Inoue, M., Kaito, T. & Ohtsuka, S. Research and development of Oxide Dispersion Strengthened Ferritic Steels for Sodium Fast Breeder Reactor Fuels. (2007).

[IONTOF5, website] IONTOF5. Available at: *https://www.iontof.com/tof-sims-5-product-version-100mm-200mm-300mm.html.*

[Isselin 2010] Isselin, J., Kasada, R. & Kimura, A. Corrosion behaviour of 16%Cr–4%Al and 16%Cr ODS ferritic steels under different metallurgical conditions in a supercritical water environment. *Corrosion Science* 52, 3266–3270 (2010).

[Jiang 2009] Jiang, Y., Smith, J. R. & Odette, G. R. Formation of Y-Ti-O nanoclusters in nanostructured ferritic alloys : A first-principles study. *Physical Review B* 79, 064103(1)–(7) (2009).

[Johnson 1979] Johnson, D. E. Introduction to Analytical Electron Microscopy. (Plenum Press, 1979).

[Jouffrey 2012] Jouffrey, B. & Karlik, M. Etude des metaux par microscopie electronique en transmission (MET) - Formation des images. *Dossier Techniques de L'Ingenieur* (2012).

[Joy 1979] Joy, D. C., Egerton, R. F. & Maher, D. M. Progress in the quantification of electron-loss spectra. In: Scanning Electron Microscopy *SEM Inc.* 817-826 (1979).

[Juslin 2007] Juslin, N., Nordlund, K., Wallenius, J. & Malerba, L. Simulation of threshold displacement energies in FeCr. *Nuclear Instruments and Methods in Physics Research, Section B: Beam Interactions with Materials and Atoms* 255, 75–77 (2007).

[Kaito 2004] Kaito, T., Narita, T., Ukai, S. & Matsuda, Y. High temperature oxidation behavior of ODS steels. *Journal of Nuclear Materials* 333, 1388–1392 (2004).

[Kalokhtina 2012] Kalokhtina, Study of the Formation of Nano-particles in ODS and NDS Steels by Atom Probe Tomography. *PhD Thesis.* L'Université de Rouen, France. (2012).

[Kasada 2007] Kasada, R., Toda, N., Yutani, K., Cho, H.S., Kishimoto, H. & Kimura, A. Pre- and post-deformation microstructures of oxide dispersion strengthened ferritic steels. *Journal of Nuclear Materials* 367-370, 222-228 (2007).

[Kasada 2011] Kasada, R. *et al.* Anisotropy in tensile and ductile–brittle transition behavior of ODS ferritic steels. *Journal of Nuclear Materials* 417, 180–184 (2011).

[Kelly 2014] Kelly, J. E. Generation IV International Forum : A decade of progress through international cooperation. *Progress in Nuclear Energy* 77, 240–246 (2014).

[Kim 2014] Kim, J. H. *et al.* Effects of processing condition on the microstructural and tensile properties of 14Cr-based oxide dispersion strengthened alloys. *Journal of Nuclear Materials* 449, 300–307 (2014).

[Kimura 2011] Kimura, A. *et al.* Development of Al added high-Cr ODS steels for fuel cladding of next generation nuclear systems. *Journal of Nuclear Materials* 417, 176–179 (2011).

[Klimenkov 2009] Klimenkov, M., Lindau, R. & Möslang, A. New insights into the structure of ODS particles in the ODS-Eurofer alloy. *Journal of Nuclear Materials* 386–388, 553–556 (2009).

[Klimenkov 2012] Klimenkov, M., Lindau, R., Materna-Morris, E. & Möslang, A. TEM characterization of precipitates in EUROFER 97. *Progress in Nuclear Energy* 57, 8–13 (2012).

[Klimenkov 2017] Klimenkov, M., Lindau, R., Jantsch, U. & Moslang, A. Effect of irradiation temperature on microstructure of ferritic- martensitic ODS steel. *Journal of Nuclear Materials* 493, 426–435 (2017).

[Klimiankou 2003] Klimiankou, M., Lindau, R. & Moslang, A. HRTEM Study of yttrium oxide particles in ODS steels for fusion reactor application. *Journal of Crystal Growth* 249, 381–387 (2003).

[Klimiankou 2004] Klimiankou, M., Lindau, R. & Moslang, A. TEM characterization of structure and composition of nanosized ODS particles in reduced activation ferritic–martensitic steels. *Journal of Nuclear Materials* 333, 347–351 (2004).

[Klimiankou 2005] Klimiankou, M., Lindau, R. & Moslang, A. Energy-filtered TEM imaging and EELS study of ODS particles and Argon-filled cavities in ferritic–martensitic steels. *Micron* 36, 1–8 (2005).

[Klimiankou 2007] Klimiankou, M., Lindau, R. & Moslang, A. Direct correlation between morphology of $(Fe,Cr)_{23}C_6$ precipitates and impact behavior of ODS steels. *Journal of Nuclear Materials* 370, 173–178 (2007).

[Klueh 1992] Klueh, R. L., Ehrlich, K. & Abe, F. Ferritic/martensitic steels: promises and problems*. *Journal of Nuclear Materials* 191–194, 116–124 (2008).

[Klueh 2002a] Klueh, R. L., Gelles, D. S., Jitsukawa, S., Kimura, A., Odette, G. R., Schaaf, B. Van Der & Victoria, M. Ferritic/martensitic steels – overview of recent results. *Journal of Nuclear Materials* 311, 455–465 (2008).

[Klueh 2002b] Klueh, R. L., Maziasz, P. J., Kim, I. S., Heatherly, L., Hoelzer, D. T., Hashimoto, N., Kenik, E. A. & Miyahara, K. Tensile and creep properties of an oxide dispersion-strengthened ferritic steel. *Journal of Nuclear Materials* 311, 773–777 (2008).

[Klueh 2005] Klueh, R. L., Shingledecker, J. P., Swindeman, R. W. & Hoelzer, D. T. Oxide dispersion-strengthened steels: A comparison of some commercial and experimental alloys. *Journal of Nuclear Materials* 341, 103–114 (2008).

[Klueh 2007] Klueh, R. L. & Nelson, A. T. Ferritic/martensitic steels for next-generation reactors. *Journal of Nuclear Materials* 371, 37–52 (2008).

[Klugkist 1995] Klugkist, P. & Herzig, C. Tracer Diffusion of Titanium in α-Iron. *Physica Status Solidi* 148, 413-421 (1995).

[Kohyama 1996] Kohyama, A., Hishinuma, A., Gelles, D. S., Klueh, R. L., Dietz, W. & Ehrlich, K. Low-activation ferritic and martensitic steels for fusion application. *Journal of Nuclear Materials* 237, 138-

147 (1996).

[Kuksenko 2011] Kuksenko, V., Pareige, C., Genevois, C., Roussel, M. & Pareige, P. Effect of neutron-irradiation on the microstructure of a Fe–12at.%Cr alloy. *Journal of Nuclear Materials* 415, 61–66 (2011).

[Lackner 2002] Lackner, K., Andreani, R., Campbell, D., Gasparotto, M., Maisonnier, D. & Pick, M. A. Long-term fusion strategy in Europe. *Journal of Nuclear Materials* 311, 10–20 (2002).

[Larson 2001] Larson, D. J., Maziasz, P. J., Kim, I. S. & Miyahara, K. Three-dimensional atom probe observation of nanoscale titanium-oxygen clustering in an oxide-dispersion-strengthened Fe-12Cr-3W-0.4Ti+Y2O3 ferritic alloy. *Scripta Materialia* 44, 359-364 (2001).

[Lavergne 1994] Lavergne, J. L., Foa, C., Bongrand, P., Seux, D. & Martin, J. M. Application of recording and processing of energy-filtered image sequences for the elemental mapping of biological specimens: Imaging-Spectrum. *Journal of Microscopy* 174, 195-206 (1993).

[Leapman 1984] Leapman, R. D., Fiori, C. E. & Swyt, C. R. Mass thickness determination by electron energy-loss for quantitative x-ray microanalysis in biology. *Journal of Microscopy* 133, 239-253 (1984).

[Lee 1990] Lee, C., Iijima, Y., Hiratani, T. & Hirano, K. Diffusion of Chromium in α-Iron. *Materials Transactions.* 31, 255-261 (1990).

[Lee 2007] Lee, J. S., Jang, C. H., Kim, I. S. & Kimura, A. Embrittlement and hardening during thermal aging of high Cr oxide dispersion strengthened alloys. *Journal of Nuclear Materials* 370, 229–233 (2007).

[Lee 2011] Lee, J. H. *et al.* Influence of alloy composition and temperature on corrosion behavior of ODS ferritic steels. *Journal of Nuclear Materials* 417, 1225–1228 (2011).

[Lescoat 2011] Lescoat, M., Monnet, I., Ribis, J., Dubuisson, P., Carlan, Y. de., Costantini, J. M. & Malaplate, J. Amorphozation of oxides in ODS materials under low and high energy ion irradiations. *Journal of Nuclear Materials* 417, 266-269 (2011)

[Lescoat 2014] Lescoat, M. *et al.* Radiation-induced Ostwald ripening in oxide dispersion strengthened ferritic steels irradiated at high ion dose. *Acta Materialia* 78, 328–340 (2014).

[Li 2010] Li, H. & Chen, W. Stability of $MnCr_2O_4$ spinel and Cr_2O_3 in high temperature carbonaceous environments with varied oxygen partial pressures. *Corrosion Science* 52, 2481–2488 (2010).

[Li 2014] Li, S. *et al.* The influence of Cr content on the mechanical properties of ODS ferritic steels. *Journal of Nuclear Materials* 455, 194–200 (2014).

[Li 2017] Li, W. *et al.* The effect of Zr , Ti addition on the particle size and microstructure evolution of yttria nanoparticle in ODS steel 1100 C. *Powder Technology* 319, 172–182 (2017).

[Li 2018] Li, W. *et al.* Microstructural characterization and strengthening mechanisms of a 15Cr- ODS steel produced by mechanical alloying and Spark Plasma Sintering. *Fusion Engineering and Design* 137, 71–78 (2018).

[Lindau 2005] Lindau, R. *et al.* Present development status of EUROFER and ODS-EUROFER for application in blanket concepts. *Journal of Nuclear Materials* 79, 989–996 (2005).

[Lo 2009] Lo, K. H., Shek, C. H. & Lai, J. K. L. Recent developments in stainless steels. *Materials Science and Engineering R* 65, 39–104 (2009).

[London 2014] London, A. J. *et al.* Comparison of atom probe tomography and transmission electron microscopy analysis of oxide dispersion strengthened steels. *Journal of Physics: Conference Series* 522, 012028(1)-(4) (2014).

[London 2015a] London, A. J. *et al.* Acta Materialia Effect of Ti and Cr on dispersion , structure and composition of oxide nano-particles in model ODS alloys. *Acta Materialia* 97, 223–233 (2015).

[London 2015b] London, A. J., Lozano-perez, S., Moody, M. P., Amirthapandian, S. & Panigrahi, B. K. Quantification of oxide particle composition in model oxide dispersion strengthened steel alloys. *Ultramicroscopy* 159, 360–367 (2015).

[Loyer-Prost 2016] Loyer-prost, M. *et al.* High resolution Transmission Electron Microscopy characterization of a milled oxide dispersion strengthened steel powder. *Journal of Nuclear Materials* 479, 76–84 (2016).

[Mao 2015] Mao, X., Oh, H., Kang, H., Kim, K. & Jang, J. On the coherency of $Y_2Ti_2O_7$ particles with austenitic matrix of oxide dispersion strengthened steel. *Acta Materialia* 89, 141–152 (2015).

[Marquis 2008] Marquis, E. A. Fe–Cr alloys Core/shell structures of oxygen-rich nanofeatures in oxide-dispersion strengthened Fe–Cr alloys. *Applied Physics Letters* 93, 181904(1)–(4) (2008).

[Marquis 2009] Marquis, E. A. *et al.* Nuclear reactor materials With the renewed interest in nuclear energy , developing new. *Materials Today* 12, 30–37 (2009).

[Marquis 2011] Marquis, E. A., Lozano-perez, S. & Castro, V. De. Effects of heavy-ion irradiation on the grain boundary chemistry of an oxide-dispersion strengthened Fe–12wt.% Cr alloy. *Journal of Nuclear Materials* 417, 257–261 (2011).

[Martinelli 2015] Martinelli, L. *et al.* Comparative oxidation behaviour of Fe-9Cr steel in CO_2 and H_2O at 550°C : Detailed analysis of the inner oxide layer. *Corrosion Science* 100, 253–266 (2015).

[Mastrikov 2018a] Mastrikov, Y. A. *et al.* Nuclear Inst . and Methods in Physics Research B Ab initio modelling of the initial stages of the ODS particle formation process. *Nuclear Instruments and Methods in Physics Research B* (2018).

[Mastrikov 2018b] Mastrikov, Y. A., Sokolov, M. N., Kotomin, E. A., Gopejenko, A. & Zhukovskii, Y. F. Ab Initio Modeling of Y and O Solute Atom Interaction in Small Clusters within the bcc Iron Lattice. *Physica Status Solidi* 1800346(1)–(5) (2018).

[Mathon 2015] Mathon, M. H., Perrut, M., Poirier, L., Ratti., M., Herve., N. & Carlan Y. De. Development of new ferritic alloys reinforced by nano titanium nitrides. *Journal of Nuclear Materials* 456, 449–454 (2015).

[Mazen 2009] Abu-khader, M. M. Recent advances in nuclear power : A review. *Progress in Nuclear Energy* 51, 225–235 (2009).

[Miller 2003] Miller, M. K., Kenik, E. A., Russell, K. F., Heatherly, L., Hoelzer, D. T. & Maziasz Atom probe tomography of nanoscale particles in ODS ferritic alloys. *Journal of Nuclear Materials* 353, 140–145 (2003).

[Miller 2004] Miller, M. K., Hoelzer, D. T., Kenik, E. A. & Russell, K. F. Nanometer scale precipitation in ferritic MA/ODS alloy MA957. *Journal of Nuclear Materials* 333, 338–341 (2008).

[Miller 2006] Miller, M. K., Russell, K. F. & Hoelzer, D. T. Characterization of precipitates in MA/ODS ferritic alloys. *Journal of Nuclear Materials* 351, 261–268 (2008).

[Miller 2009] Miller, M. K. & Forbes, R. G. Atom probe tomography. *Materials Characterization* 60, 461–469 (2009).

[Miller 2011] Miller, M. K. & Hoelzer, D. T. Effect of neutron irradiation on nanoclusters in MA957 ferritic alloys. *Journal of Nuclear Materials* 418, 307–310 (2011).

[Mock 2017] Mock, M. & Albe, K. Diffusion of yttrium in bcc-iron studied by kinetic Monte Carlo simulations. *Journal of Nuclear Materials* 494, 157–164 (2017).

[Moses 2009] Moses, E. I. Ignition on the National Ignition Facility : a path towards inertial fusion energy. *Nuclear Fusion* 49, 104022(1)-(9) (2009).

[Mujahid 1994] Mujahid, M. & Martin, J. W. The effect of oxide particle coherency on Zener pinning in ODS superalloys. *Journal of Material Science Letters* 13, 153–155 (1994).

[Murali 2010] Murali, D., Panigrahi, B. K., Valsakumar, M. C., Chandra, S., Sundar, C. S. & Raj, B. The role of minor alloying elements on the stability and dispersion of yttria nanoclusters in nanostructured ferritic alloys: An ab initio study. *Journal of Nuclear Materials* 403, 113–116 (2010).

[Murali 2011] Murali, D., Panigrahi, B. K., Valsakumar, M. C. & Sundar, C. S. Diffusion of Y and Ti / Zr in bcc iron : A first principles study. *Journal of Nuclear Materials* 419, 208–212 (2011).

[Muroga 2014a] Muroga, T., Nagasaka, T., Abe., H., Kimura, A. & Okuda, T. Fabrication and characterization of reference 9Cr and 12Cr-ODS low activation ferritic/martensitic steels. *Fusion Engineering and Design* 89, 1717–1722 (2014).

[Muroga 2014b] Muroga, T., Chen, J. M., Chernov, V. M., Kurtz, R. J. & Flem, M. Le. Present status of vanadium alloys for fusion applications. *Journal of Nuclear Materials* 455, 263–268 (2014).

[Murty 2008] Murty, K. L. & Charit, I. Structural materials for Gen-IV nuclear reactors : Challenges and opportunities. *Journal of Nuclear Materials* 383, 189–195 (2008).

[Noh 2014] Noh, S., Choi, B., Kang, S. U. K. H. & Kim, T. K. Influence Of Mechanical Alloying Atmospheres on the Microstructures and Mechanical Properties of 15Cr ODS Steels. *Nuclear Engineering and Technology* 46, 857–862 (2014).

[Oka 2016] Oka, H. *et al.* Effect of thermo-mechanical treatments on nano-structure of 9Cr-ODS steel. *Nuclear Materials and Energy* 9, 346–352 (2016).

[Oksiuta 2009] Oksiuta, Z., Olier, P., Carlan, Y. De & Baluc, N. Development and characterisation of a new ODS ferritic steel for fusion reactor application. *Journal of Nuclear Materials* 393, 114–119 (2009).

[Oksiuta 2013] Oksiuta, Z., Lewandowska, M., Kurzydlowski, K. J. & Baluc, N. Effect of vanadium addition on the microstructure and mechanical properties of the ODS ferritic steels. *Journal of Nuclear Materials* 442, S84–S88 (2013).

[Olier 2012] Olier, P. *et al.* Chemical and microstructural evolution on ODS Fe–14CrWTi steel during manufacturing stages. *Journal of Nuclear Materials* 428, 40–46 (2012).

[Olier 2013] Olier, P., Couvrat, M., Cayron, C., Lochet, N. & Chaffron, L. Incidence of mechanical alloying contamination on oxides and carbides formation in ODS ferritic steels. *Journal of Nuclear Materials* 442, S106–S111 (2013).

[Pandey 2014] Pandey, A., Jayasankar, K., Debata, M., Mishra, B. K. & Saroja, S. Optimization of milling parameters , processing and characterization of nano-crystalline oxide dispersion strengthened ferritic steel. *Powder Technology* 262, 162–169 (2014).

[Pareige 2007] Pareige, P., Miller, M. K., Stoller, R. E., Hoelzer, D. T., Cadel, E. & Radiguet, B. Stability of nanometer-sized oxide clusters in mechanically-alloyed steel under ion-induced displacement cascade damage conditions. *Journal of Nuclear Materials* 360, 136–142 (2008).

[Ramar 2009] Ramar, A., Baluc, N. & Schäublin, R. On the lattice coherency of oxide particles dispersed in EUROFER97. *Journal of Nuclear Materials* 386–388, 515–519 (2009).

[Ramar 2013] Ramar, A. & Schäublin, R. Analysis of hardening limits of oxide dispersion strengthened steel. *Journal of Nuclear Materials* 432, 323–333 (2013).

[Ramunni 2015] Ramunni, V. P. & Rivas, A. M. F. Diffusion behavior of Cr diluted in bcc and fcc Fe : Classical and quantum simulation methods. *Materials Chemistry and Physics* 162, 659–670 (2015).

[Ratti 2009] Ratti, M., Leuvrey, D., Mathon, M. H. & Carlan, Y. De. Influence of titanium on nano-cluster (Y , Ti , O) stability in ODS ferritic materials. *Journal of Nuclear Materials* 386–388, 540–543 (2009).

[Ribis 2011] Ribis, J. *et al.* Stability of nano-oxides upon heavy ion irradiation of an ODS material. *Journal of Nuclear Materials* 417, 262–265 (2011).

[Ribis 2012a] Ribis, J. & De Carlan, Y. Interfacial strained structure and orientation relationships of the nanosized oxide particles deduced from elasticity-driven morphology in oxide dispersion strengthened materials. *Acta Materialia* 60, 238–252 (2012).

[Ribis 2012b] Ribis, J. & Lozano-perez, S. Orientation relationships and interface structure of α′-Cr nanoclusters embedded in α-Fe matrix after α–α′ demixing in neutron irradiated Oxide Dispersion Strengthened material. *Materials Letters* 74, 143–146 (2012).

[Ribis 2012c] Ribis, J., Bordas, E., Trocillier, P. Surreys, Y., Carlan, Y. De & Legris, A. Nuclear Instruments and Methods in Physics Research B Radiation-sustained nanocluster metastability in oxide dispersion strengthened materials. *Nuclear Instruments and Methods in Physics Research, B* 365, 22–25 (2015).

[Ribis 2013a] Ribis, J., Lescoat, M., Zhong, S. Y., Mathon, M. & Carlan, Y. De. Influence of the low interfacial density energy on the coarsening resistivity of the nano-oxide particles in Ti-added ODS material. *Journal of Nuclear Materials* 442, S101–S105 (2013).

[Ribis 2013b] Ribis, J. Structural and chemical matrix evolution following neutron irradiation in a MA957 oxide dispersion strengthened material. *Journal of Nuclear Materials* 434, 178–188 (2013).

[Ribis 2014] Ribis, J. & Lozano-perez, S. Nano-cluster stability following neutron irradiation in MA957 oxide dispersion strengthened material. *Journal of Nuclear Materials* 444, 314–322 (2014).

[Ribis 2017] Ribis, J., Thual, M. A., Guilbert, T., Carlan, Y. De & Legris, A. Relaxation path of metastable nanoclusters in oxide dispersion strengthened materials *Journal of Nuclear Materials* 484, 183-192 (2017).

[Rogozhkin 2016] Rogozhkin, S. *et al.* Nanostructure evolution in ODS steels under ion irradiation. *Nuclear Materials and Energy* 0, 1–9 (2016).

[Rouxel 2016] Rouxel, B., Bisor, C., Carlan, Y. De, Courcelle, A. & Legris, A. In fl uence of the austenitic stainless steel microstructure on the void swelling under ion irradiation. *EPJ Nuclear Sciences and Technologies* 30, 1–11 (2016).

[Sakasegawa 2009] Sakasegawa, H. *et al.* Correlation between chemical composition and size of very small oxide particles in the MA957 ODS ferritic alloy. *Journal of Nuclear Materials* 384, 115–118 (2009).

[Sakuma 2004] Sakuma, D., Yamashita, S., Oka, K., Ohnuki, S., Rehn, L. E., & Wakai, E.Y_2O_3 nano-particle formation in ODS ferritic steels by Y and O dual ion-implantation. in *Journal of Nuclear Materials* 329–333, 392–396 (2004).

[Schaublin 2006] Schaublin, R., Ramar, A., Baluc, N., Castro, V. De, Monge, M. A., Legeuy, T., Schmid, N., & Bonjour, C. Microstructural development under irradiation in European ODS ferritic / martensitic steels. *Journal of Nuclear Materials* 351, 247–260 (2006).

[Sickafus 2007] Sickafus, K. E., Kotomin, E. A. & Uberuaga, B. P. Radiation Effects in Solids, 235 *Mathematics, Physics and Chemistry* (2007).

[Smallman 1999] Smallman, R. E. & Bishop, R. J. Modern physical metallurgy and materials engineering. *Oxford: Elsevier.* (1999).

[Smith 1998] Smith, D. L., Billone, M. C., Majumdar, S., Mattas, R. F. & Sze, D. Materials integration issues for high performance fusion power systems. *Journal of Nuclear Materials* 263, 65-73 (1998).

[Smith 2005] Smith, C. L. The need for fusion. *Fusion Engineerig and Design* 74, 3–8 (2005).

[Steckmeyer 2010] Steckmeyer, A. *et al.* Tensile properties and deformation mechanisms of a 14Cr ODS ferritic steel. *Journal of Nuclear Materials* 405, 95–100 (2010).

[Sun 2012] Sun, Q. X., Zhang, T., Wang, X. P., Fang, Q. F., Hao, T. & Liu C. S. Microstructure and mechanical properties of oxide dispersion strengthened ferritic steel prepared by a novel route.

Journal of Nuclear Materials 424, 279–284 (2012).

[Suryanarayana 2001] Suryanarayana, C. Mechanical alloying and milling. *Progress in Materials Science* 46, 1-184 (2001).

[Swenson 2017] Swenson, M. J. & Wharry, J. P. Nanocluster irradiation evolution in Fe-9 % Cr ODS and ferritic- martensitic alloys. *Journal of Nuclear Materials* 496, 24–40 (2017).

[Takada 1986] Takada, J. U. N. Determination of diffusion coefficient of oxygen in α-iron from internal oxidation measurements in Fe-Si alloys. *Journal of Materials Science* 21, 2133–2137 (1986).

[Takaya 2009] Takaya, S. *et al.* Corrosion behavior of Al-alloying high Cr-ODS steels in lead – bismuth eutectic. *Journal of Nuclear Materials* 386–388, 507–510 (2009).

[Takaya 2012] Takaya, S. *et al.* Al-containing ODS steels with improved corrosion resistance to liquid lead – bismuth. *Journal of Nuclear Materials* 428, 125–130 (2012).

[Tan 2013] Tan, L., Yang, Y. & Busby, J. T. Effects of alloying elements and thermomechanical treatment on 9Cr Reduced Activation Ferritic–Martensitic (RAFM) steels. *Journal of Nuclear Materials* 442, S13–S17 (2013).

[Tan 2018] Tan, L., Katoh, Y. & Snead, L. L. Development of castable nanostructured alloys as a new generation RAFM steels*. *Journal of Nuclear Materials* 511, 598–604 (2018).

[Tanaka 2004]Tanaka, T. *et al.* Synergistic effect of helium and hydrogen for defect evolution under multi-ion irradiation of Fe – Cr ferritic alloys. *Journal of Nuclear Materials* 333, 294–298 (2004).

[Tavassoli 2014] Tavassoli, A. F., Diegele, E., Lindau, R., Luzginova, N. & Tanigawa, H. Current status and recent research achievements in ferritic / martensitic steels. *Journal of Nuclear Materials* 455, 269–276 (2014).

[Thomas 2002] Thomas, P. J. & Midgley, P. A. An introduction to energy-filtered transmission electron microscopy. *Topics in Catalysis* 21, 109-138 (2002).

[Tong 2010] Tong, Z. & Dai, Y. The microstructure and tensile properties of ferritic/martensitic steels T91, Eurofer-97 and F82H irradiated up to 20 dpa in STIP-III. *Journal of Nuclear Materials* 398, 43–48 (2010).

[Ukai 1993] Ukai, S. *et al.* Alloying design of oxide dispersion for long life FBRs core materials strengthened ferritic steel. *Journal of Nuclear Materials* 204, 5–73 (1993).

[Ukai 2000] Ukai, S., Mizuta, S., Yoshitake, T., Okuda, T., Fujiwara, M., Hagi, S. & Kobayashi, T. Tube manufacturing and characterization of oxide dispersion strengthened ferritic steels. *Journal of Nuclear Materials* 287, 702-706 (2000).

[Ukai 2002] Ukai, S. & Fujiwara, M. Perspective of ODS alloys application in nuclear environments. *Journal of Nuclear Materials* 307–311, 749–757 (2002).

[Unifantowicz 2013] Williams, C. A., Baluc, N. & Unifantowicz, P. Structure of complex oxide nanoparticles in a Fe-14Cr-2W-0.3Ti-0.3Y_2O_3 ODS RAF steel *Journal of Nuclear Materials.* 442, 158–163 (2013).

[Vamousse 2003] Vaumousse, D., Cerezo, A. & Warren, P. J. A procedure for quantification of precipitate microstructures from three-dimensional atom probe data. *Ultramicroscopy* 95, 215–221 (2003).

[Villars 1985] Villars, P. & Calvert, L. D. Pearson's Handbook of Crystallographic Data for Intermettalic Phases. *American Society for Metals.* (1985).

[Was 2007] Was G. S. Fundamentals of Radiation Materials Science. *Springer.* (2007).

[Wharry 2017] Wharry, J. P., Swenson, M. J. & Yano, K. H. A review of the irradiation evolution of dispersed oxide nanoparticles in the b.c.c. Fe-Cr system: Current understanding and future directions. *Journal of Nuclear Materials* 486, 11–20 (2017).

[Williams 2009] Williams, D. B. & Carter, B. C. Transmission Electron Microscopy: A textbook for Materials Science. *Springer Science+ Business Media, LLC.* (2009).

[Williams 2010] Williams, C. A., Marquis, E. A., Cerezo, A. & Smith, G. D. W. Nanoscale characterisation of ODS – Eurofer 97 steel : An atom-probe tomography study. *Journal of Nuclear Materials* 400, 37–45 (2010).

[Williams 2012] Williams, C. A., Smith, G. D. W. & Marquis, E. A. The effect of Ti on the coarsening behavior of oxygen-rich nanoparticles in oxide-dispersion-strengthened steels after annealing at 1200°C. *Scripta Materialia* 67, 108–111 (2012).

[Williams 2013] Williams, C. A., Haley, D., Marquis, E. A., Smith, G. D. W. & Moody, M. P. Ultramicroscopy Defining clusters in APT reconstructions of ODS steels. *Ultramicroscopy* 132, 271–278 (2013).

[Wu 2012] Wu, Y., Haney, E. M., Cunningham, N. J. & Odette, G. R. Transmission electron microscopy characterization of the nanofeatures in nanostructured ferritic alloy MA957. *Acta Materialia* 60, 3456–3468 (2012).

[Wu 2016] Wu, Yuan, Ciston, J., Kraemer, S., Bailey, N., Odette, R. & Peter, H. The crystal structure , orientation relationships and interfaces of the nanoscale oxides in nanostructured ferritic alloys. *Acta Materialia* 111, 108–115 (2016).

[Xia 2013] Xia, Y. P., Wang, X. P., Zhuang, Z., Sun, Q. X., Zhang, T., Fang, Q. F., Hao, T. & Liu, C. S. Microstructure and oxidation properties of 16Cr – 5Al – ODS steel prepared by sol – gel and spark plasma sintering methods. *Journal of Nuclear Materials* 432, 198–204 (2013).

[Xie 2017] Xie, R., Lu, Z., Lu, C., Li, Z., Ding, X. & Liu, C. Microstructures and mechanical properties of 9Cr oxide dispersion strengthened steel produced by spark plasma sintering. *Fusion Engineering and Design* 115, 67–73 (2017).

[Xu 2017a] Xu, H., Lu, Z., Ukai, S., Oono, N. & Liu, C. Effects of annealing temperature on nanoscale particles in oxide dispersion strengthened Fe-15Cr alloy powders with Ti and Zr additions. *Journal of Alloys and Compounds* 693, 177–187 (2017).

[Xu 2017b] Xu, H., Lu, Z., Wang, D. & Liu, C. Microstructure Refinement and Strengthening Mechanisms of a 9Cr Oxide Dispersion Strengthened Steel by Zirconium Addition. *Nuclear Engineering and Technology* 49, 178–188 (2017).

[Xu 2017c] Xu, H., Lu, Z., Wang, D. & Liu, C. Effect of zirconium addition on the microstructure and mechanical properties of 15Cr-ODS ferritic Steels consolidated by hot isostatic pressing. *Fusion Engineering and Design* 114, 33–39 (2017).

[Yamamoto 2011] Yamamoto, M., Ukai, S., Hayashi, S., Kaito, T. & Ohtsuka, S. Reverse phase transformation from a to c in 9Cr-ODS ferritic steels. *Journal of Nuclear Materials* 417, 237–240 (2011).

[Yamashita 2002] Yamashita, S., Oka, K., Ohnuki, S.Akasaka, N. & Ukai, S. Phase stability of oxide dispersion-strengthened ferritic steels in neutron irradiation. *Journal of nuclear Materials* 307-311, 283-288 (2002).

[Yamashita 2004] Yamashita, S., Akasaka, N. & Ohnuki, S. Nano-oxide particle stability of 9-12Cr grain morphology modified ODS steels under neutron irradiation. *Journal of nuclear Materials* 329–333, 377–381 (2004).

[Yamashita 2007] Yamashita, S., Akasaka, N., Ukai, S. & Ohnuki, S. Microstructural development of a heavily neutron-irradiated ODS ferritic steel (MA957) at elevated temperature. *Journal of Nuclear Materials* 367-370 A, 202–207 (2007).

[Yazawa 2004] Yazawa, Y., Furuhara, T. & Maki, T. Effect of matrix recrystallization on morphology, crystallography and coarsening behavior of vanadium carbide in austenite. *Acta Materialia* 52, 3727–

3736 (2004).

[Yutani 2007] Yutani, K., Kishimoto, H., Kasada, R. & Kimura, A. Evaluation of Helium effects on swelling behaviour of oxide dispersion strengthened ferritic steels under ion irradiation. *Journal of Nuclear materials* 367-373, 423-423 (2007).

[Yvon 2009] Yvon, P. & Carré, F. Structural materials challenges for advanced reactor systems. *Journal of Nuclear Materials* 385, 217–222 (2009).

[Zhang 2009] Zhang, L., Ukai, S., Hoshino, T., Hayashi, S. & Qu, X. Y 2 O 3 evolution and dispersion refinement in Co-base ODS alloys. *Acta Materialia* 57, 3671–3682 (2009).

[Zhang 2011] Zhang, C. H., Kimura, A., Kasada, R., Jang, J., Kishimoto, H. & Yang, Y. T. Characterization of the oxide particles in Al-added high-Cr ODS ferritic steels. *Journal of Nuclear Materials* 417, 221–224 (2011).

[Zhang 2014] Zhang, T., Vieh, C., Wang, K. & Dai, Y. Irradiation-induced evolution of mechanical properties and microstructure of Eurofer 97. *Journal of Nuclear Materials* 450, 48–53 (2014).

[Zhang 2015a] Zhang, H. *et al.* Processing and microstructure characterisation of oxide dispersion strengthened Fe-14Cr-0.4Ti-0.25Y_2O_3 ferritic steels fabricated by plasma sintering. *Journal of Nuclear Materials* 464, 61–68 (2015).

[Zhang 2015b] Zhang, G. *et al.* The microstructure and mechanical properties of Al-containing 9Cr ODS ferritic alloy. *Journal of Alloys and Compounds* 648, 223–228 (2015).

[Zhao 2017a] Zhao, Q., Yu, L., Liu, Y., Huang, Y., Guo, Q., Li, H. & Wu, J. Evolution of Al-containing phases in ODS steel by hot pressing and annealing. *Powder Technology* 311, 449–455 (2017).

[Zhao 2017b] Zhao, Q., Yu, L., Liu, Y., Huang, Y., Ma, Z., Li, H. & Wu, J. Microstructure and tensile properties of a 14Cr ODS ferritic steel. *Materials Science & Engineering A* 680, 347–350 (2017).

[Zheng 2015a] Zheng, C., Gentils, A., Ribis, J., Borodin, V. A., Kaitasov, O. & Garrido, F. Metal-oxide nano-clusters in Fe-10%Cr alloy by ion implantation. *Nuclear Instruments and Methods in Physics Research B* 365, 319-324 (2015).

[Zheng 2015b] Zheng, C. Metallic nano-oxide clusters synthesis by ion implantation in high purity Fe10Cr alloy. Université Paris-Sud, France. *PhD Thesis* (2015).

[Zhou 2019] Zhou, X., Ma, Z., Yu, L., Huang, Y. & Li, H. Formation mechanisms of Y–Al– O complex oxides in 9Cr-ODS steels with Al addition. *Journal of Materials Science* 54, 7893–7907 (2019).

[Ziegler 1996] Ziegler, J. SRIM website:https://www.srim.org (1996).

[Zinkle 2005] Zinkle, S. J. Advanced materials for fusion technology. *Fusion Engineering and Design* 74, 31–40 (2005).

[Zinkle 2009] Zinkle, S. J. & Busby, J. T. Structural materials for fission & fusion energy Structural materials represent the key for containment of nuclear fuel. *Materials Today* 12, 12–19 (2009).

université PARIS-SACLAY | ÉCOLE DOCTORALE PHENIICS

Titre : Compréhension des premiers stades de formation des nano-précipités (Y, Ti, O) dans les aciers ODS (Oxide Dispersion Strengthened)

Mots clés : Alliages Fe-Cr, implantation ionique, synthèse par faisceaux d'ions, aciers renforcés par dispersion d'oxydes (ODS), nano-oxydes, précipitation, recuit thermique, microscopie électronique en transmission (MET).

Résumé : Les aciers appelés ODS (pour Oxide Dispersion Strengthened), renforcés par une dispersion homogène de nano-oxydes, sont des matériaux de structure avancés pour les futurs réacteurs nucléaires de fusion et de fission. En effet ces nano-oxydes, à base d'Y et Ti, servent comme centres de recombinaison de défauts ponctuels et d'obstacles aux mouvements des dislocations, améliorant de ce fait leur résistance aux radiations et aux températures élevées. La fabrication conventionnelle des aciers ODS est réalisée par broyage mécanique suivi de traitements thermo-mécaniques, et ne permet pas facilement de comprendre les mécanismes physiques conduisant à la précipitation des nano-oxydes, ce qui serait potentiellement utile pour optimiser leur production. La cinétique de formation de ces nano-oxydes peut être étudiée en utilisant une technique alternative, à savoir la synthèse par faisceaux d'ions, qui présente de nombreux avantages, notamment le contrôle précis des paramètres expérimentaux et la possibilité de décorréler divers facteurs contribuant à la cinétique de précipitation.

Au cours de cette thèse, cette technique a été utilisée pour étudier la coprécipitation d'ions métalliques (Y et/ou Ti) et d'oxygène implantés dans un alliage modèle Fe-Cr de composition proche de celle typique des aciers ODS commerciaux. Des ions de Y, Ti et O à basse énergie ont été implantés dans des échantillons d'alliage Fe10wt%Cr de haute pureté à température ambiante. Les échantillons implantés ont ensuite été recuits à diverses températures entre 600 à 1100°C pour favoriser la précipitation de nano-oxydes, conformément au principe de cette technique. La microscopie électronique à transmission a été utilisée pour caractériser la structure cristallographique et la composition chimique des nano-oxydes formés lors de trois séries d'expériences. Tout d'abord, l'implantation séquentielle d'ions Ti et O a été mise en œuvre. Un recuit ultérieur a révélé qu'il n'y avait pas de précipitation d'oxyde de titane jusqu'à des températures inférieures à 1000°C, mais la présence de nano-oxydes riches en chrome avec une structure hexagonale de type corundum, qui contiennent une certaine quantité de Ti à des températures suffisamment élevées. Ce n'est qu'après le recuit à 1100°C que des nano-oxydes d'un autre type à cœur enrichi en Ti et coquille enrichie en Cr ont également été observés. Deuxièmement, l'implantation séquentielle d'ions Y et O a entraîné la formation à 800°C de nano-oxydes probablement riches en yttrium. Le recuit à 1100°C a favorisé la croissance des particules identifiées comme étant des nano-oxydes d'yttrium avec une coquille enrichie en Cr. Enfin, une implantation ionique séquentielle de deux ions métalliques (Y et Ti) a été réalisée, suivie d'une implantation d'O. L'ordre d'implantation des ions métalliques s'est révélé crucial pour la précipitation de nano-oxydes lors du recuit ultérieur. Lors de la séquence avec une implantation de Ti en premier, une précipitation d'oxyde riche en chrome de structure corundum hexagonale a été observée, très similaire au cas de l'implantation d'ions Ti et O. En revanche, la séquence avec une implantation d'ions Y en premier a produit des nano-oxydes d'yttrium-titane qui possèdent une structure non identifiable.

En résumé, l'étude a clarifié les détails de la formation de nano-oxydes de Y, Ti et (Y, Ti) par implantation ionique. La thèse présente la caractérisation détaillée de ces nano-oxydes, ainsi que certaines de leurs caractéristiques spécifiques, telles que la présence de relations d'orientation entre les nano-oxydes et la matrice FeCr, qui ont été observées même dans le cas de nano-oxydes de type corundum riches en Cr. Enfin, les résultats obtenus, combinés avec les données de la littérature, sont discutés pour une meilleure compréhension des mécanismes impliqués dans la formation des nano-oxydes dans les aciers ODS.

Université Paris-Saclay
Espace Technologique / Immeuble Discovery
Route de l'Orme aux Merisiers RD 128 / 91190 Saint-Aubin, France

université PARIS-SACLAY | ÉCOLE DOCTORALE PHENIICS

Title : Understanding the first formation stages of (Y,Ti) nano-oxides in Oxide Dispersion Strengthened (ODS) steels

Keywords : Fe-Cr alloys, Ion Implantation, Ion Beam Synthesis, Oxide Dispersion Strengthened (ODS) steels, Oxide nanoparticles, Precipitation, Thermal annealing, Transmission Electron Microscopy (TEM).

Abstract : Oxide Dispersion Strengthened (ODS) steels, that is steels reinforced with a homogeneous distribution of (Y,Ti) oxide nanoparticles, are advanced structural materials for nuclear applications. The oxide particles serve as point defect recombination centres and obstacles to dislocation motion thereby improving radiation resistance and high-temperature strength of these steels making them perfect candidate materials for future fusion and fission nuclear reactors. The conventional fabrication of ODS steels is achieved by mechanical alloying followed by thermomechanical heat treatments. This way of ODS steel production seems complicated to understand the physical mechanisms leading to the precipitation of nano-oxide particles. The kinetics of nanoparticle formation can be much better studied using an alternative technique of nanoparticle growth, namely Ion Beam Synthesis (IBS). This approach has many advantages including the precise control of experimental parameters and the ability to de-correlate various factors contributing to precipitation kinetics. A better knowledge gained in this way would be potentially helpful for optimization of ODS steel production routines.

In the course of this PhD study, the IBS approach was applied to investigate the co-precipitation of metal (Y and/or Ti) and oxygen ions implanted into a model Fe-Cr alloy with the composition close to those typical for commercial ODS steels. Following the standard IBS schedule, consisting of ion implantation followed by high-temperature heat treatment, ions of Y, Ti and O at low energies were implanted into high-purity Fe10wt%Cr alloy samples at room temperature. The implanted samples were then annealed at various temperatures ranging from 600 to 1100°C to promote the precipitation of nano-oxide particles. A range of Transmission Electron Microscopy techniques were used to characterize the crystallographic structure and chemical composition of the nanoparticles.

The study has been performed following three sets of experiments. First of all, the sequential implantation of Ti and O ions was implemented. Subsequent annealing at temperatures below 1000°C revealed that precipitation of titanium oxide was suppressed. Instead, chromium-rich nano-oxide particles with corundum hexagonal structure were found to precipitate. At sufficiently high temperatures these corundum particles were found to contain certain amount of Ti. Only after annealing at the highest temperature of 1100°C, particles of another type with Ti enriched core and Cr enriched shell were additionally fixed. Secondly, sequential Y and O ion implantation resulted in the formation of presumable yttrium-rich oxides at 800°C. Annealing at 1100°C promoted their growth to larger sized yttria (Y_2O_3) particles with a Cr enriched shell. Finally, sequential ion implantation of both metal ions (Y and Ti) was performed, followed by O implantation. The order of metal ion implantation has been found to be crucial for subsequent oxide precipitation at the annealing stage. With the Ti implantation first in the sequence, the precipitation of corundum hexagonal chromium-rich oxide was observed, very similar to the case of Ti and O implantation. In contrast, implantation starting with Y produced yttrium-titanium oxide particles with unidentifiable structure.

Summing up, the study has clarified the details of the formation of Y, Ti and (Y,Ti) oxides by ion implantation. The thesis presents the detailed characterization of the nanoparticles, as well as the discovered specific features of precipitated particles, such as the presence of orientation relationships between the particles and the FeCr matrix, which was observed even for the case of Cr-rich corundum particles. Finally, the implications of the obtained results, in conjunction with the already known data from the existing literature, for the better understanding of the mechanisms involved in the formation of nano-oxide particles in ODS steels are discussed.

Université Paris-Saclay
Espace Technologique / Immeuble Discovery
Route de l'Orme aux Merisiers RD 128 / 91190 Saint-Aubin, France